LBL-15091
c.2

Lawrence Berkeley Laboratory
UNIVERSITY OF CALIFORNIA

Materials & Molecular Research Division

RECEIVED
LAWRENCE
BERKELEY LABORATORY
OCT 7 1982
LIBRARY AND
DOCUMENTS SECTION

SUPERSONIC MOLECULAR BEAM ELECTRIC RESONANCE SPECTROSCOPY AND VAN DER WAALS MOLECULES

Henry Steven Luftman
(Ph.D. thesis)

September 1982

TWO-WEEK LOAN COPY
This is a Library Circulating Copy which may be borrowed for two weeks. For a personal retention copy, call Tech. Info. Division, Ext. 6782.

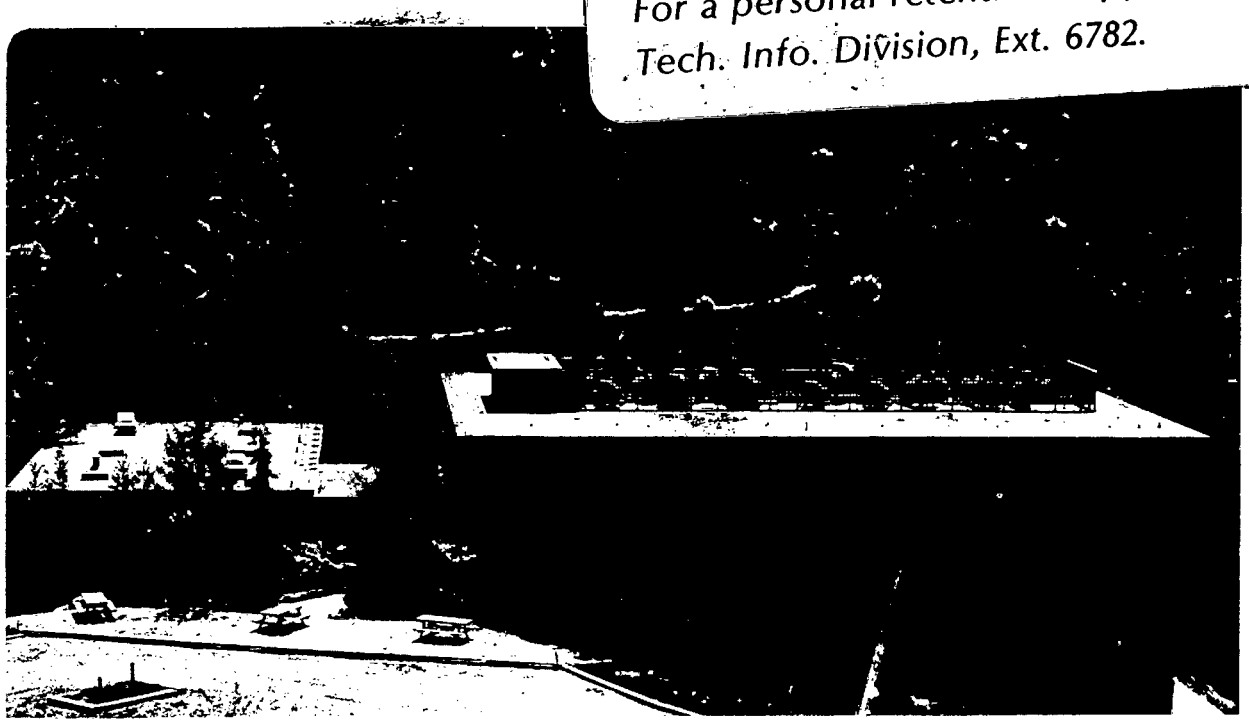

LBL-15091
c.2

Prepared for the U.S. Department of Energy under Contract DE-AC03-76SF00098

DISCLAIMER

This document was prepared as an account of work sponsored by the United States Government. While this document is believed to contain correct information, neither the United States Government nor any agency thereof, nor the Regents of the University of California, nor any of their employees, makes any warranty, express or implied, or assumes any legal responsibility for the accuracy, completeness, or usefulness of any information, apparatus, product, or process disclosed, or represents that its use would not infringe privately owned rights. Reference herein to any specific commercial product, process, or service by its trade name, trademark, manufacturer, or otherwise, does not necessarily constitute or imply its endorsement, recommendation, or favoring by the United States Government or any agency thereof, or the Regents of the University of California. The views and opinions of authors expressed herein do not necessarily state or reflect those of the United States Government or any agency thereof or the Regents of the University of California.

LBL-15091

SUPERSONIC MOLECULAR BEAM ELECTRIC RESONANCE SPECTROSCOPY AND van der WAALS MOLECULES*

Henry Steven Luftman

Ph.D. Thesis

Materials and Molecular Research Division,
Lawrence Berkeley Laboratory
and Department of Chemistry
University of California
Berkeley, California 94720

This work was supported by the Director, Office of Energy Research, Office of Basic Energy Sciences, Chemical Sciences Division of the U.S. Department of Energy under Contract No. DE-AC03-76SF00098.

Supersonic Molecular Beam Electric Resonance Spectroscopy and van der Waals Molecules

Henry Steven Luftman

Abstract

A supersonic molecular beam electric resonance (MBER) spectrometer was built to study the radiofrequency spectra of weakly bound gas phase van der Waals molecules. The instrument and its operating characteristics are described in detail. Sample mass spectra of Ar-ClF gas mixtures are also presented as an illustration of the synthesis of van der Waals molecules.

The Stark focusing process for linear polar molecules is discussed and computer-simulated using both second order perturbation and variational methods. Experimental refocusing spectra of OCS and ClF are studied and compared with these trajectory calculations. Though quantitative fitting is poor, there are strong qualitative indicators that the central part of a supersonic beam consists of molecules with a significantly greater population in the lowest energy rotational states than generally assumed. "Flop in" as opposed to "flop out" resonance signals for OCS are also numerically predicted and observed.

The theoretical properties of the MBER spectrum for linear molecules are elaborated upon with special emphasis on line shape considerations. MBER spectra of OCS and ClF under a variety of conditions are presented and discussed in context to these predictions. There is some uncertainty expressed both in our own modeling and in the manner complex MBER spectra

have been analyzed in the past. Finally, an electrostatic potential model is used to quantitatively describe the class of van der Waals molecules Ar-MX, where MX is an alkali halide. Energetics and equilibrium geometries are calculated. The validity of using an electrostatic model to predict van der Waals bond properties is critically discussed.

John S. Winn

DEDICATION

For Mom, Dad, Jack and Eric.

You were there.

ACKNOWLEDGMENTS

Professor John S. Winn has been both my mentor and a friend during my residence in Berkeley. His breadth of knowledge and general enthusiasm were at times awesome and often inspirational. Any experimental ability I may have now I credit to him. As for a general academic and research environment, I believe that there is none better than that offered by the Chemistry Department of the University of California at Berkeley and its affiliation with the Lawrence Berkeley Laboratories. I have been honored with the acquaintances of Profs. Y. T. Lee, C. B. Moore, H. L. Strauss and others, and I thank the faculty overall for their general approachability. I thank here the Regents of U.C. and L.B.L. for their financial support.

Little of the experimental work in this thesis would have been possible without the assistance of the members of the Winn research group. Brian Hale had much to do with the development of our detector system. Susan Sherrow aided with the apparatus development and made several contributions to this body of work, including being at the helm for our first observed transition. Michael Maier also played an important role in the obtaining of our early experimental results. The Chemistry Machine Shop, particularly George Webber, are heartfully thanked for their most professional help in the design and construction of our beam machine, and the electronic and woodshops for most everything else. All of the aforementioned have been much more than colleagoes. I thank Sue for our coffee and talk, Mike for his points of view and Brian for his kidding around. Also from our group I thank Jim Goble, Dennis Hartman, Will Hollingsworth and Dave Horak for their intellectual

stimulation and friendship. I thank George, Hoy Wong, Howard Wood, Steve Smiriga and the shops for supplying me with places to hide from the lab. Finally here I acknowledge and thank Cordelle Yoder, Nancy Monroe, Kathy McBride, and Gloria Pelatowski for their aid in the preparation of this tome.

Having been in Berkeley for more than a few years, one might expect that I would have made some friends. If in very little else, in this I have been more than successful. My apartment mates and neighbors Larry Dubois, Vera Mainz, Pauline Ho, Linda Young, Alison Abbate, Joan Frisoli, Steve Oblath, Greg Girolami, Dan Wachs and Steve Sandler have taught me, listened to me, laughed with me, fed me, included me -- in fact, have kept me driven on the brink of sanity. Geri Richmond, Kathy Mensler, Steve Sofen, Laura Lewin, Steve Sibener, Ann Hriciga, Steve Hansen and Jim Weishaar have done an incredible job in keeping my ego afloat. Ted Shifrin, Noreen Hickok and Katy Lebowitz humored me endlessly. Eileen Strauss, Jim Murdoch, Vicky Shannon and, again, Sue Sherrow have helped in seeing me through the end of my tenure here. The Pelatowskis and Beauregards, my West coast family, have also contributed much to the smile I can still wear. For the Chem Pistols, the bridge, the sailing, skiing and tennis, the parties, the drinking, the love -- I most gratefully acknowledge the above and all my other friends from my Berkeley experience. If any of you ever need a ride to the airport, just call.

TABLE OF CONTENTS

		Page
I.	INTRODUCTION	1
	A. Overview	1
	B. Van der Waals Molecules	3
	C. Molecular Beam Electric Resonance Spectroscopy	5
	References for Chapter I	12
II.	THE APPARATUS	13
	A. The Source Chamber	13
	1. Gases and Gas Handling	15
	2. The Source Can	17
	3. The Source and Buffer Chambers	21
	4. Some Source Operating Conditions	23
	5. Routine for a Nozzle Change	24
	B. The Spectroscopic Chamber	25
	1. The A and B Fields	26
	2. The C Field	28
	3. The Buffer Fields	31
	4. The Chamber	32
	5. Assembly of the Spectroscopy Region	34
	C. The Detector	37
	1. The Ionizer	39
	2. The Quadrupole Mass Filter and Particle Multiplier	43
	3. The Main Chamber	45
	4. The Detector Chambers	47
	5. Data Collection and Miscellaneous Electronics	49
	6. Detector Assembly	52

TABLE OF CONTENTS (continued)

Page

D. Apparatus Operation. 55

1. Chamber Preparation. 56

2. Tuning the Detector and Taking a Mass Spectrum . . . 57

3. Stark Focusing and MBER Spectroscopy 59

4. Shutting Down. 61

E. Source and Detector Characteristics - Mass Spectra . . . 63

1. Argon Beam Characteristics 63

2. ClF-Ar Mixtures and Cluster Formation. 67

3. Other Mass Spectra 73

F. The Apparatus - Parting Comments 74

Appendix - The Molecular Beam Interface Control. 77

Notes and References 81

III. STARK FOCUSING OF A MOLECULAR BEAM OF LINEAR POLAR MOLECULES 102

A. Theory 103

1. The Stark Effect 103

2. The Initial Molecule Distribution. 118

3. The Numerical Methodology. 133

B. Experimental and Numerical Results 141

1. Refocusing as a Function of the A and B Field Voltages. 143

2. Refocusing as a Function of Source Conditions. . . . 159

3. Transition Signal Intensity as a Function of the A and B Fields. 172

C. Discussion 181

1. Refocusing Spectra 181

2. Molecular Beam Energy Distribution 185

TABLE OF CONTENTS (continued)

Page

References and Notes 193

Appendix - The Computer Programs ABFELDV and ETABLE. 195

IV. RESONANCE SPECTRA OF LINEAR POLAR MOLECULES. 197

A. Theory - Stark and Nuclear Interactions in a Linear Molecule. 198

1. The Hamiltonian. 201

2. Relevant Basis Sets. 205

3. The Numerical Solution of Eigenstates and Energies . 212

4. Transitions. 223

B. Experimental and Numerical Results 235

1. OCS Data 235

2. ClF Data 246

3. Numerical Calculations 256

C. Discussion 259

References to Chapter IV 264

Appendix I - Rabi's Formula: Transitions in a Two-Level System. . 265

1. Classical View of Magnetic Resonance and Rabi's Formula 265

2. A Quantum Mechanic Derivation of Rabi's Formula. . . 287

3. MBER and Rabi's Formula. 293

References to Appendix I 301

Appendix II - The Computer Programs ω. vs. E and TWOSPIN 302

V. THE ARGON-ALKALI HALIDE MOLECULE SYSTEMS - AN ELECTROSTATIC MODEL 309

A. Introduction 310

TABLE OF CONTENTS (continued)

Page

B. The Electrostatic Theory 311

1. Coulombic Interaction. 312

2. Repulsive Interaction. 317

3. Dispersive Interaction 322

4. Calculation. 322

C. Results. 324

D. Discussion 346

E. Conclusion 354

References for Chapter V 355

Appendix - The Computer Program CLARNA 358

CHAPTER I

INTRODUCTION

A. Overview

The existing literature describing the structure and bonding of van der Waals molecules in the gas phase is quite recent and still largely incomplete when compared to what has been written on covalently bound molecules. Given the supposedly more complex interactions of this latter class of molecules, this may seem surprising. It is only recently that the technology has been available to study these weakly bound species by various spectroscopies. This thesis is primarily concerned with the method of molecular beam electric resonance (MBER) spectroscopy, a technique particularly well-suited for the study of many van der Waals molecules, and, as will be shown, a method that itself is intrinsically interesting. Besides describing the spectrometer and its development, the modeling of the experimental system for both of the general phenomena of the focusing of linear polar molecules with an inhomogeneous electric field and the radiofrequency resonance spectroscopy that is the immediate goal of MBER will be discussed. Comparisons of this modeling with experimental results for covalent linear molecules will be made as well. Due to a host of technical problems encountered during our development period, which, at the time of this writing, has not really concluded, very little in the way of spectroscopic results for van der Waals molecules have yet been obtained on our apparatus. Hopefully this will change in the coming year. However, as a result, no new spectroscopic data will appear in this thesis.

The remainder of this chapter serves as an introduction to the problems discussed in this thesis. Following this overview will be a brief discourse on the general topic of van der Waals molecules and the difficulties inherent to their study. The method of molecular beam electric resonance spectroscopy will then be described, with special emphasis on the solutions MBER offers to many of the problems of the van der Waals molecule spectroscopist. The rough procedural description given here will also serve as an overview for the reader when later reading about the details of the apparatus and the model simulations. The second chapter deals with the specific apparatus - its design, construction and use. Apart from just describing the present status of our MBER spectrometer, some of the "cul-de-sacs" encountered in the past few years will be indicated for future unwary users of this machine. Typical mass spectra for a variety of source gases and conditions will be presented as well as an empirical study of the formation of van der Waals complexes.

Chapter III will begin with a detailed discussion on the theory of Stark focusing for linear polar molecules. A model will be presented for the prediction of focusing patterns of a molecular beam. It is felt that refocusing studies as described here can serve as a good probe for transverse and longitudinal velocity and rotational energy distributions within the beam. Experimental refocusing patterns for OCS and ClF will be presented and discussed in this context. The theoretical details of resonance spectroscopy will be the topic of the first part of Chapter IV. The relevant quantum mechanics of the transitions we study will be summarized, followed by a prediction for the observable line shapes of MBER. Comparisons with experimentally obtained spectra for OCS and ClF will then be made.

The final chapter will return to the topic of weakly bound molecules. A classical electrostatic model is presented to describe and predict the bonding for the particular class of molecules Ar-MX, where MX is an alkali halide monomer. Included in the discussion of the calculated results is a more general topic of the possible importance of electrostatic forces in the entire class of van der Waals molecules.

B. Van der Waals Molecules

Loosely speaking, van der Waals molecules encompass those polyatomic species with at least one particularly weak intramolecular bond which springs from what are normally considered intermolecular forces. These forces include London dispersive (or induced dipole-induced dipole) forces, ion-induced dipole attractions, dipole-induced dipole attractions and weak Lewis acid-base interactions. Electron exchange, charge transfer and other effects generally attributed to covalent bonding are present in van der Waals bonds as well, but being orders of magnitude weaker here, they can be described more succinctly in classical terms. Several recent reviews[1-3] have been written which collect most of the experimental data on these molecules. Their binding energies have a wide range in terms of a logarithmic scale, from on the order of 10 cm^{-1} (HeNe, NeNa), through 100 cm^{-1} (e.g., Ar_2, XeH_2, ArHCl), to 1000 cm^{-1} (e.g., Ca_2, XeF), with a few more molecules spanning through the energy range to the covalent bond regime of 20,000 to 80,000 cm^{-1}. The diversity of van der Waals bond characteristics is less surprising when one realizes that a "nonchemical" binding well exists between any two neutral atomic or molecular species, with only ground state He_2 having a well too shallow to support abound state. Due to this diversity, a general description of the van der Waals bond is quite difficult. As an example,

vast differences in the bond directionality, determined as the ratio of stretching to bending vibrational frequencies of the relevant bond, are observed, indicating varying amounts of "chemical" behavior to what were once thought to be purely "physical" bonds.

Interest in van der Waals bonds and molecules transcends just the understanding of the previously described gas phase complexes. At temperatures below the condensation point for most substances it is the van der Waals forces that are responsible for the gas molecules' nucleation and for many of the dynamic processes within a liquid or molecular crystal. An understanding of the bonding in van der Waals gas phase molecules thus allows a better modeling for other phases. In heterogeneous systems, the phenomenon of surface physisorption (as opposed to chemisorption) may also be van der Waals-force controlled. A better understanding of gas phase bulk properties can be obtained with an improved picture of the intermolecular forces encountered in collisions and the dissociation mechanics of van der Waals bonds. Finally, as van der Waals forces tend to cause only a small perturbation to covalently bonded parts of a molecule, studies of van der Waals molecules can give useful information on the properties of that molecule's covalently bonded constituents (e.g., as in the determination of the direction of the ClF dipole moment[4]). In general, one would like to understand the potential energy surfaces governing these weak bond forces.

A particular source of information about these potential energy surfaces at distances of bond length order is structural data of the bonded van der Waals molecules. Spectroscopic methods are routinely used for covalent molecules to determine bond lengths and angles, stretching and bending constants, dipole moments and other molecule

characteristics. However, the very properties that distinguish van der Waals molecules from others make standard spectroscopic methods next to worthless for determining their structural properties. An obvious problem is that given the weakness of a van der Waals bond, the synthesis of such a molecule would require quite low temperatures, typically less than 50 K. The problem is one of having such a local temperature and yet still being in the gas phase. Secondly, given the shallowness of the binding well, any intermolecular collisions would destroy the bond. Furthermore, any method of synthesis of gas phase van der Waals molecules would at best produce a very low concentration of the species of interest amidst a large background of uncomplexed molecules. This, coupled with a partition of internal energy problem which would further divide this low population into many different states, would thereby produce very poor signal to noise characteristics in typical absorption or emission spectral methods.

C. Molecular Beam Electric Resonance Spectroscopy

A general method used in spectroscopy when standard absorption/emission techniques are inappropriate is to observe transitions by detecting a measurable change to the molecule of interest itself rather than to the photon field. This is the essence of such experimental techniques as photoionization, photoacoustic and mass spectroscopy, as well as molecular beam electric resonance spectroscopy. In MBERS, advantage is taken of the change in energy of a polar neutral molecule in an inhomogeneous electric field which alters its trajectory *en route* to a mass spectrometer, and the dependence of this energy on the molecule's rotational state. The basic method of MBERS was first developed by

H. Hughes[5] as a technique analogous to the method of magnetic resonance spectroscopy of Rabi,[6] in order to study spectroscopic details of alkali halide monomers. The method was improved upon by Trischka[7] and the technique has remained essentially the same since then.[8,9]

The physical process of molecular beam deflection will be described more completely in Chapter III. Briefly, as a result of the Stark effect, the energy of a polar molecule in an electrostatic field is dependent upon the strength of the field and the molecule's dipole moment, rotational constant(s) and particular rotational state. For a linear molecule, as an example, the change in energy due to an electric field as calculated by second order perturbation theory is

$$E = \frac{\mu^2 |\underset{\sim}{E}|^2}{B} \frac{J(J+1)-3M^2}{2J(J+1)(2J-1)(2J+3)}$$

$$= \frac{\mu^2 |\underset{\sim}{E}|^2}{B} f(J,M), \tag{1.1}$$

where $\underset{\sim}{E}$ is the electric field vector, μ and B the molecule's permanent dipole moment and rotational constant, and J and M the molecule's rotational quantum numbers. If one has a beam of such molecules in the presence of an inhomogeneous electric field, where $\underset{\sim}{E}$ has some radial dependence, then the molecules will experience a radial force,

$$\underset{\sim}{F} = -\underset{\sim}{\nabla} E = \frac{-\mu^2}{B} f(J,M) \underset{\sim}{\nabla}(\underset{\sim}{E}\cdot\underset{\sim}{E}). \tag{1.2}$$

The sign of this force is thus dependent upon the relative values of J and M.

Figure 1 presents a simplified picture of an MBER spectrometer. A beam of molecules enters an inhomogeneous electric field region (to be

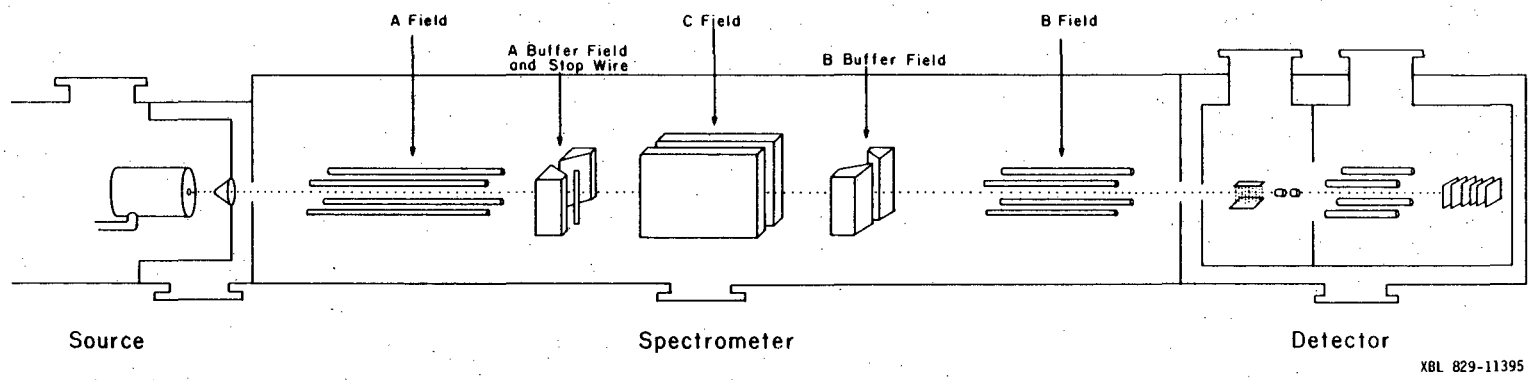

Figure 1.1. Molecular beam electric resonance spectrometer - schematic (beam travels from left to right).

referred to as the "A" field henceforth) for initial deflecting. Earlier work in MBER used a two-wire or dipole type field here,[8] as well as for the B field, discussed later. We have chosen to use quadrupole fields, which have a simple radial field strength expression

$$\underset{\sim}{E} = k'\underset{\sim}{r} \tag{1.3}$$

where $\underset{\sim}{r}$ is the position vector for a point in space drawn from the closest point on the quadrupole's axis, and k' is a constant dependent upon geometrical parameters of the field pieces and the applied voltages. For linear polar molecules, then, one has a radial force

$$\underset{\sim}{F} = \frac{-2\mu^2 k'^2}{B} \; f(J,M)\underset{\sim}{r} \, . \tag{1.4}$$

As can be inferred from Equations (1.1) and (1.4), linear molecules in rotational states (J,M) = (1,0), (2,0) and (2,±1), for example (henceforth to be referred to as "positive" Stark states) will experience negative forces, deflecting them toward the axis of the quadrupolar A field. Molecules in "negative" Stark states, such as (J,M) = (0,0), (1,±1), and (2,±2), will experience positive forces, i.e., will be attracted toward the greater field strength in the vicinity of the field pieces, and will diverge from the beam. Following the A field, the beam runs into a relatively small axial stopwire which blocks from the beam any nonfocusing molecules or molecules that remained too close to the field axis to experience sufficient deflecting forces. Thus, after the stopwire, the beam consists only of the focusing, "positive" Stark state molecules, particularly those in the best focusing low J states.

The beam then enters the C field region, where it is exposed to radiofrequency or microwave radiation, of energy sufficient to only cause

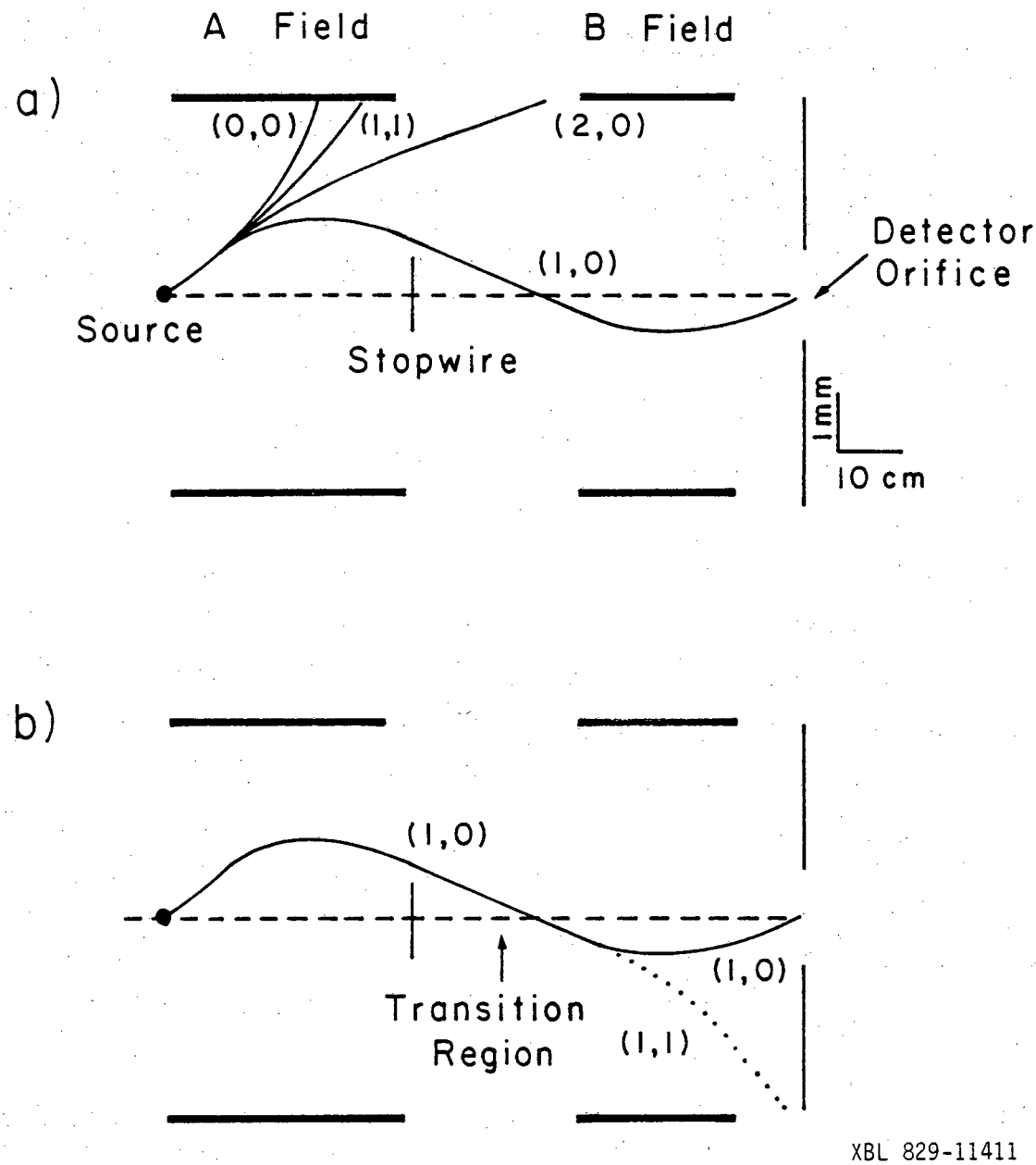

Figure 1.2. Beam trajectory simulations in MBERS. (J,M) rotational states as indicated. (a) State focusing for OCS with V_A (A field voltage) = 19 kV, V_B = 25 kV. All trajectories with the same initial velocity. Scale shown on right. (b) Trajectory change with (1,0) → (1,1) transition.

changes of the molecule's rotational state. It can be shown quantum mechanically that transitions between states of identical J quantum numbers require the presence of an electric field apart from that of the radiation. Thus, the C field also supplies a very homogeneous static electric field component. As the resonance frequency for a transition between two molecular states is dependent upon the strength of this static field, the degree of this field's homogeneity will play a very major role in determining the narrowness of the observed resonance. Following the C field, the beam then enters the B field region, which, as was the A field, is inhomogeneous, focusing positive Stark state molecules and defocusing negative Stark state molecules. In a typical MBER experiment, one tunes the A and B fields to obtain a beam of positive Stark state molecules focused onto the spectrometer axis at the exit end of the B field, where it then enters a mass sensitive particle detector, as illustrated schematically in Figure 2a. If one then tunes the DC field strength and radiation frequency in the C field region to cause a transition from a focusable positive Stark state to a defocusing negative Stark state, one would see a corresponding drop in the detector signal beyond the B field. Figure 2b illustrates the change in trajectory of a molecule if its rotational state is changed from (J,M) = (1,0) to (1,1). Thus, the resonance frequency for this transition is found by following the signal from the particle detector as a function of the radiating frequency in the C field, with a drop in signal corresponding to resonance. In general to induce a measurable transition between two molecular states, one first must create a difference from the equilibrium population distribution of these states, then radiate, and finally probe for a further change in the relative populations. In MBER, the A field creates the nonequilibrium population, the C field

delivers the radiation, and the B field with the particle detector analyzes for the change.

In a supersonic molecular beam expansion local temperatures lower than 10 K can be generated routinely while leaving the beam in a gaseous state. As shown by Klemperer, et al.,[10] this allows the necessary conditions for the synthesis of van der Waals molecules in a beam for MBER studies. Kantrowitz and Grey,[11] before this, suggested that such an adiabatic molecular expansion enhances the population in the low J rotational states of molecules within a beam, greatly alleviating the signal problem inherent in spectroscopy due to a wide distribution of populated molecular states. Other advantageous properties of the beam from a supersonic source expansion as compared to the more standard effusive source beam include an enhanced axial beam intensity, a tighter velocity distribution, and better control of a beam mean velocity with the appropriate choosing of a "carrier" gas. All of this will be discussed further in Chapter III. We have used a Campargue-type[12] design for our source, allowing a greater source pressure and thereby further enhancing our beam's intensity and cooling. In order to prevent collisional dissociation or rotational state scrambling of our weakly bonded molecules, the entire spectroscopic and detector regions of the MBER apparatus are maintained at pressures lower than 10^{-6} torr.

The particle detector on the far side of the B field consists of a Weiss ionizer[13] followed by a quadrupole mass filter, particle multiplier and collector. This allows a verification of the identity of the molecules which leave the spectrometer region, and, thereby, one can ensure that one is studying the transitions of the molecules of interest. Thus, the background problem of van der Waals molecule spectroscopy as discussed in the previous section is remedied.

REFERENCES for CHAPTER I

1. G. E. Ewing, Can. J. Phys. 54, 487 (1976); B. L. Blaney and G. E. Ewing, Ann. Rev. Phys. Chem. 27, 553 (1976); G. E. Ewing, Acc. Chem. Res. 8, 185 (1975).

2. W. Klemperer, J. Mol. Struct. 59, 161 (1980); W. Klemperer in Advances in Laser Chemistry, ed. by A. H. Zewail (Springer-Verlag, Berlin, 1978).

3. J. S. Winn, Acc. Chem. Res. 14, 341 (1981).

4. K. C. Janda, W. Klemperer, and S. E. Novick, J. Chem. Phys. 64, 2698 (1975).

5. H. K. Hughes, Phys. Rev. 72, 614 (1947).

6. I. I. Rabi, S. Millman, P. Kusch, and J. R. Zacharias, Phys. Rev. 55, 526 (1939).

7. R. G. Luce and J. W. Trischka, J. Chem. Phys. 21, 105 (1953).

8. N. F. Ramsey, Molecular Beams (Oxford Univ. Press, London, 1956), Chpt. 10.

9. P. Kusch and V. Hughes, Ency. of Phys. 37, 1 (Springer-Verlag, Berlin, 1959).

10. T. R. Dyke, G. R. Tomasevich, W. Klemperer, and W. E. Falconer, J. Chem. Phys. 57, 2277 (1972); T. R. Dyke, B. J. Howard, and W. Klemperer, J. Chem. Phys. 56, 2442 (1972).

11. A. Kantrowitz and J. Grey, Rev. Sci. Inst. 22, 328 (1951).

12. R. Campargue and A. Lebehot, Rarified Gas Dynamics, 9, c.11 (1974).

13. R. Weiss, Rev. Sci. Inst. 32, 397 (1961).

CHAPTER II

THE APPARATUS

The method of molecular beam electric resonance spectroscopy has been described in the previous chapter. As this is the first opportunity our laboratory has had to document the MBER spectrometer we have built, this chapter will serve as a somewhat detailed guide to the components, assembly and use of the machine. The first three sections presented here deal respectively with the source, spectroscopic chamber and detector chamber (Fig. 1.1). The text of these sections is reserved for descriptions of the present status of the apparatus[1] and current methods of assembly. The color involved with development problems and caveats to the user are reserved for the notes at the end of the chapter and can be safely ignored by the casual reader. The fourth section describes the preparation for a typical MBER experiment with particular emphasis on electrical tuning. The next section describes certain mass spectra we have obtained and some results on van der Waals molecule synthesis. In the concluding section are a few comments on the development of our MBER spectrometer and some suggested changes.

A. The Source Chamber

The required properties of a molecular beam which can carry van der Waals molecules for an MBER experiment formed the guide for our source's development (Fig. 1). The gaseous beam must have little translational random motion to allow van der Waals molecule synthesis, collimation of the beam and future ease in trajectory and spectral analysis. An appropriate amount of rotational cooling is required so that there will

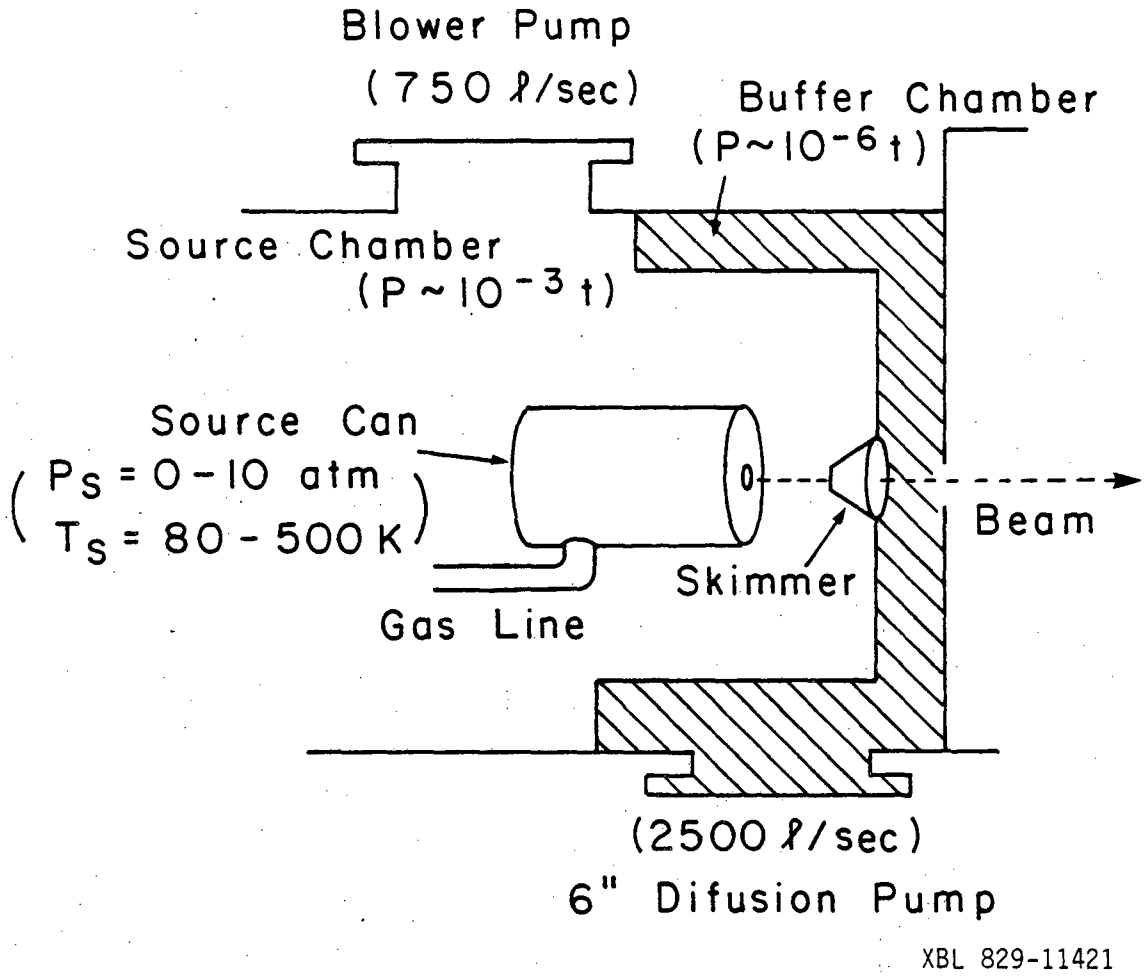

Figure 2.1. Source schematic.

be a substantial number of molecules in the most focusable states. A detailed comparison of the properties of a molecular flow with an effusive flow is reserved for the following chapter. The properties of a beam are determined during the expansion process, with the degree of cooling determined by the number of collisions participating molecules experience during that period.[2] The related design consideration is to have a large value for the ratio of the source orifice diameter to the mean free path of the molecules within the source, i.e., a large Knudsen number. To maintain such a beam, it is then necessary quickly to isolate the beam from background scattering, both by removing uncollimated molecules from the exterior region about the nozzle and by extracting the cooled part of the beam from the expansion region before it encounters the so-called Mach disc[2] or shock wave from the stagnant pressure of the background molecules, where nonadiabatic heating of the beam would begin. The former method involves the use of fast pumping outside the source. The latter technique involves the use of an appropriate aperture, the skimmer, to pass the cooled part of the beam into a lower pressure region without itself disrupting the beam, and the ability to change the distance between this aperture and the source nozzle for optimal cooling.

1. Gases and Gas Handling

Most of the work described here involved the use of argon, carbonyl sulfide[3] (OCS) and chlorine monofluoride[4] (ClF), and the occasional use of helium, hydrogen fluoride, hydrogen chloride, ammonia, chlorine and sulfur hexafluoride.[5] A portable gas cart was built for sample mixing and controlled pressure delivery to the source can.[6] This system consists of a 1/3 hp mechanical pump, 1/4" stainless steel tubing, stainless steel

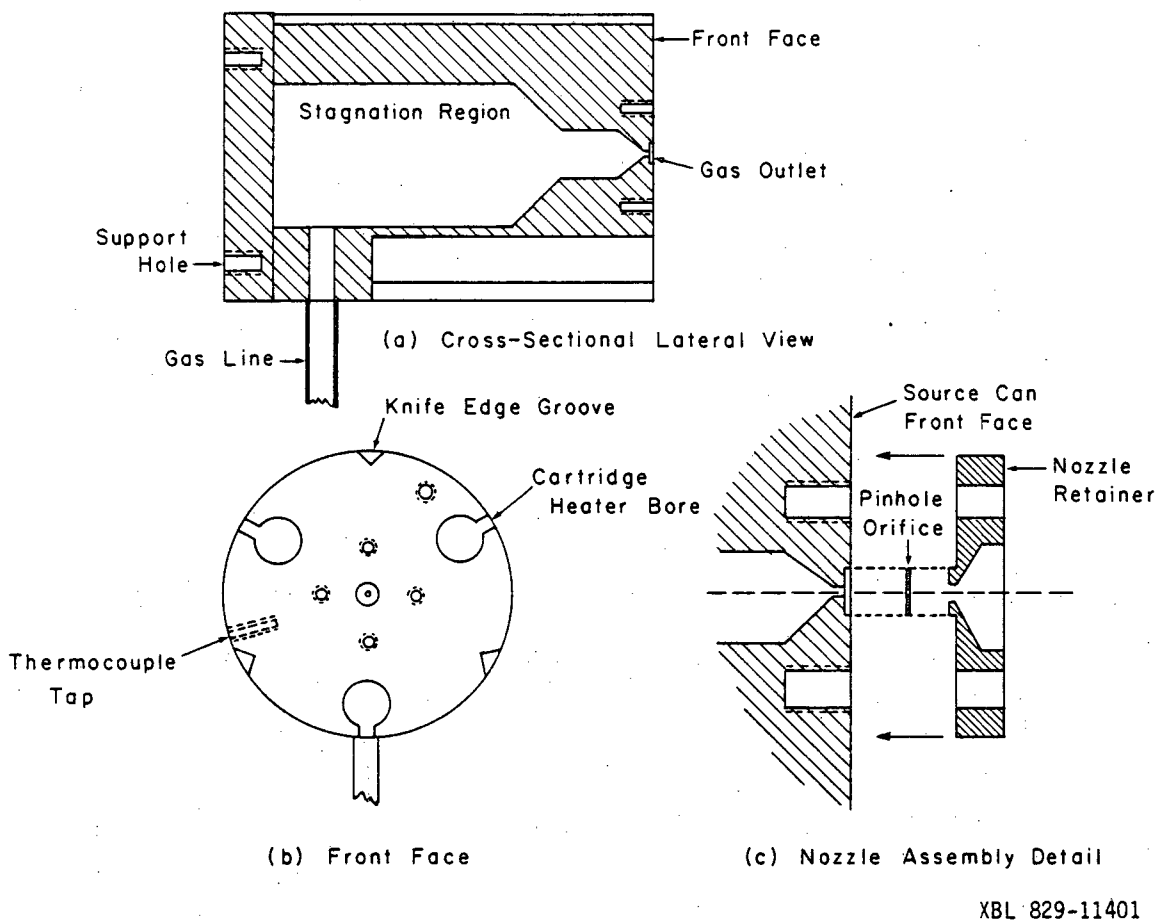

Figure 2.2. Source can.

valves[7] and pressure measuring gauges.[8] A 1/4" monel tubing line was prepared for ClF delivery to the gas cart. Before using ClF in an experiment, all lines and relevant sample cylinders were passivated for at least an hour with typically 200 t (torr) ClF. Special care was generally employed when using ClF (and HF) due to its toxicity.[9]

2. The Source Can

A longitudinal cross section and front view of the gas beam source is given in Figure 2.[10] A 2" long, 1½" O.D. monel cylinder was drilled out as shown with a 1/4" plate welded onto the back. The stagnation room inside this can allows equilibration of the gas with the source temperature. 1/8" diameter by 20 mil wall thickness monel tubing is welded to the can, which can be joined to stainless steel tubing within the source chamber, which, in turn is joined to a gas line vacuum feedthrough, a valve, and the delivery line from the gas cart. Three grooves run along most of the length of the can from the front face for the knife edges of the source can holder. Three 1/4" drilled and slotted holes are present for snugly fitting cartridge heaters. One of the face-tapped holes supports a source stop, which prevents the user from bringing the source against the skimmer and thereby damaging it. A side tapped hole supplies a place for attaching a temperature monitoring thermocouple. Threaded holes on the can's back are for the attachment of a cooling can and the position controlling rod.

The detail in Figure 2 indicates the normally used mode for nozzle assembly. A 3 mm disc[11] of nickel shim stock 40 μ thick with a centered hole of a diameter between 25 and 400 μ[12] is inserted into the central bore on the face of the source can, and held in place by a nozzle retainer with a 120° flared opening.[13] An alternate type of nozzle was

Figure 2.3. Source assembly

1. Motion rod
2. ℓ-N_2 vent tubing
3. ℓ-N_2 supply tubing
4. Motion rod connector
5. Insulating washers
6. ℓ-N_2 reservoir block
7. Source can
8. Gas supply tubing
9. Knife edged source holder
10. Source stop
11. Skimmer
12. Source-buffer snout

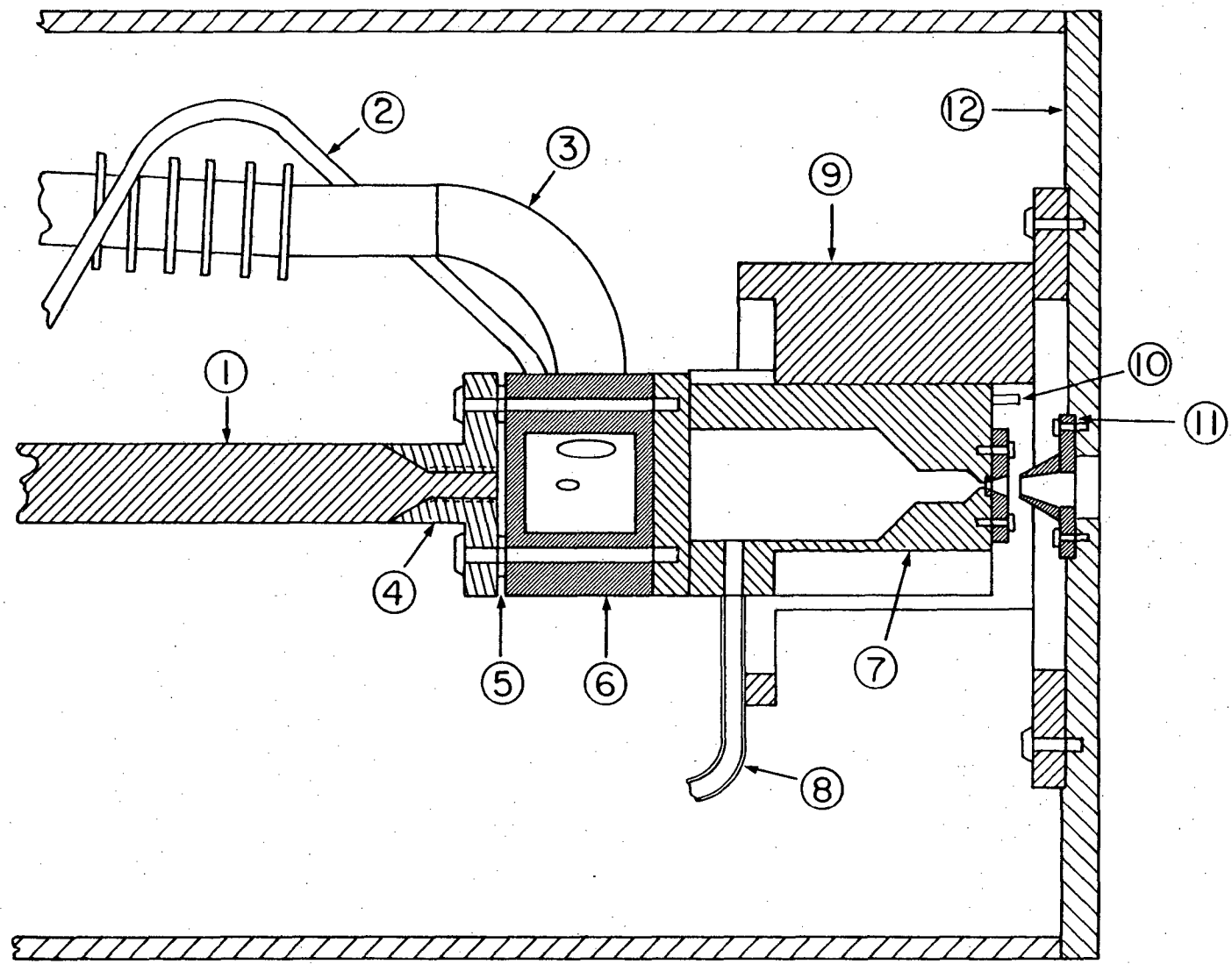

XBL 829-11419

also constructed, consisting of a single stainless steel piece which bolted onto the face of the source can, with a 75 μ hole drilled on its outer flat face.[14]

Heating of the source was accomplished with three 1/4" diameter, 1¼" long cartridge heaters.[15] They were connected in parallel and powered externally by a 0-132 volt, 2¼ amp current (maximum) Powerstat variable transformer. Cooling was done with liquid nitrogen, by attaching an ℓ-N_2 fillable copper block to the back of the source can.[16] An indium sheet was occasionally used between the block and source can to improve thermal contact. Liquid nitrogen was supplied to the block through 18 to 24" of 1/2" flexible stainless steel tubing from an ℓ-N_2 supply arm on the end source flange, and vented through 1/8" steel tubing coiled about the steel hose and also leading to the source flange. Temperature measurement was obtained by a spot-welded chromel-alumel thermocouple (ice-referenced) attached to the side of the source about 1/2" from the source can face.[17]

The assembly of the source can, cooling block and source positioning elements is indicated in Figure 3.[18] Teflon or Macor washers are inserted between the motion rod connector and the copper block for thermal insulation, and the connector, washers and block are held to the source can with four 6-32 screws. The control of distance between the source nozzle and skimmer is accomplished with a 40" stainless steel "push me-pull you" rod which runs from the source connector, through an axially aligned rod support with a Teflon sleeve about 14" from the source, and finally through a Wilson seal[19] on the end source flange. The position of the source is measured with an exterior dial indicator. Two different source holders[20] were used, each with three knife edges for the source

can to slide through, and a surface to key-in concentrically to the source-buffer wall. The second source holder is comprised of two parts, the key-in ring and the three jaw piece with an adjustable frame, to allow for the possible loss of centricity from thermal warping.[21] Its knife edges were made coaxially shorter with a leading cut-off edge for source assembly ease.[22]

3. The Source and Buffer Chambers

The source chamber is contained by a source chamber tee, source flange and source-buffer snout.[23] The tee, with 1/8" stainless steel walls, consists of a 10½" inner diameter cylinder, with a 10" entrance underneath (adaptable for a 10" diffusion pump) and a 6" port above. The source-buffer snout, also of 1/8" steel, is an 18" long, square prism with 6 1/8" interior sides. Key-in surfaces are on it for the skimmer, source holder and the source motion rod support. It, itself, keys into the buffer chamber piece.

The overall source design is of the Campargue type,[24] which, by using a larger source stagnation pressure than the more conventional molecular beam sources, and yet maintaining roughly the same ratio between pressures within the source and just past the nozzle, generates a significantly more intense beam with somewhat better cooling. To handle the gas load from the source requires a fast pumping system which can operate at relatively high pressures. A foreline of 6" inner diameter PVC tubing[25] ran from the port on top of the source tee to a 6" gate valve,[26] which in turn rested upon a mechanical turbine booster pump (800 l/sec) backed by a Triplex high vacuum mechanical pump (250 l/sec).[27,28] These large pumps were somewhat isolated from the remainder of the laboratory. With no gas load, these pumps could evacuate the source chamber to 15 μ.[29]

A skimmer was keyed and bolted to the inside of the source-buffer snout. The initially used skimmers were machined from nickel with a 50° internal and 60° external angle, with openings of 8, 20, and 25 mils. Later work used an electroformed nickel skimmer[30] with an opening diameter of 0.28 mm.

A pumped-out buffer region surrounds most of the source-buffer snout, and is the next area encountered by the beam for about 1" of its path when it emerges from the skimmer. It is contained by the source-buffer snout and the buffer shroud,[31] with a 10½" inner diameter and 1/8" stainless steel walls. It has key-in surfaces for the source-buffer snout, the spectrometer chamber and a collimating orifice on the buffer side. Both the snout and the shroud have fitted quartz windows for viewing the source can when assembled and in anticipation of future radiative excitation experiments with the molecular beam. The spectrometer side of the shroud has locating holes for the spectroscopic bench (next section), and there are locating holes on the bolt circle connecting the buffer shroud and spectroscopic chambers. The buffer region is pumped through a 2' long 6" diameter line and 6" gate valve by a 6" diffusion pump[32] (2400 l/s) backed by a beltless drive mechanical pump.[33] The pressure in this region is monitored with an ionization gauge.[34] Typical pressures during an experiment are on the order of 2×10^{-5} t.

The beam leaves the buffer chamber through a collimating orifice, presently consisting of one of our older skimmers,[35] and enters the spectroscopic chamber. A gate valve for the ½" bore through the buffer shroud is attached on the spectrometer side and controlled by a rod running through a Wilson seal on the right side of the spectrometer chamber (as looking from the source). When properly adjusted, a vacuum is maintained in either the buffer or spectrometer chamber when the other is vented.[36]

4. Some Source Operating Characteristics

The increase in beam cooling by increasing the source stagnation pressure or the diameter of the nozzle orifice was observed, and will be discussed in the following chapter. An increase in the background pressure within the source chamber or buffer chamber for a given stagnation pressure predictively decreases the beam intensity. The source and buffer chamber pressures are themselves dependent on the stagnation pressure and nozzle diameter.[37] At certain stagnation pressures, increasing the nozzle-skimmer distance from its minimum can increase the beam intensity by better than a factor of ten, a property particularly indicative of a molecular expansion.[24,38]

The characteristics of the cartridge heaters are somewhat dependent on how the source can is mounted.[39] The maximum temperature attainable before the heaters begin to burn out is on the order of 525°C. At temperatures above 200°C it becomes difficult to move the source can within its holder. When working at temperatures greater than room temperature, the heater powerstat is generally turned to an appropriate current and the source is allowed to equilibrate. For cooling, liquid nitrogen is fed to the cooling block adjacent to the source while the vent line is pumped on by the building vacuum line.[40] As the appropriate temperature is approached, the vent is turned to the atmosphere and then closed. Temporary fine tuning for cold temperatures is attained by briefly opening the vent line or with short heating pulses from the cartridge heaters. Temperatures as low as 100 K are obtainable, but our practical limit is determined by that temperature and pressure condition where the expanding gas condenses and clogs the nozzle (e.g., around 200 K for argon).

5. Routine for a Nozzle Change

This section is actually a long footnote to describe some of the procedural use of the source chamber. Before venting the source chamber, the gate valves to the spectrometer chamber, to the buffer chamber diffusion pump and to the blower should be closed. When turning off the large mechanical pumps, the blower should be turned off first and allowed to come to rest before venting and turning off the backing pump. Vent the source chamber with the valves under the source tee and on the buffer chamber line leading to its diffusion pump. Unbolt the PVC foreline from the top of the tee, unbolt the source tee from the source-buffer snout, and disconnect the gas cart line from the source. Unplug any electrical accessories on the source table. When the chamber is at an atmosphere, slide the source stand back from the buffer chamber about 10". Disconnect the source can motion rod support from the source-buffer snout, and then continue to pull back the source stand.

To make a nozzle change, take off the pinhole retainer from the source can and blow N_2 through the source gas line to remove the old nozzle. If it is needed to remove the source can, pull out the cartridge heaters, disconnect the interior gas line and remove the connecting screws from the back of the motion rod connector.[41] When reassembling the source, the gas line side points downward. The cooling block should be oriented so that the flexible hose enters from the upper right when viewed from the rear of the source to insure that the motion rod will need a clockwise twist when inserting the source into the holder.[42] It is occasionally a good idea to apply O-ring grease to the holder knife edges and the grooves on the source can. Reverse the aforementioned steps to reassemble the source chamber.[43] If the two piece source holder

is in use, it should be a simple matter to twist the source can into the correct orientation with the "push me-pull you" rod, and then slide the source into position. With the other holder, it is necessary to unbolt the source-buffer snout from the buffer shroud and slide the source stand back again. Carefully remove the quartz window from the side of the snout, and, with a long screwdriver, pry up the source can to match the knife edges of the holder while twisting and pushing the motion rod from outside the chamber, until the source can slides into the holder. Then finish reassembly.

B. The Spectroscopic Chamber

The processes in MBER, which have already been briefly discussed in Chapter I, determine the specifications of the spectroscopic region of our apparatus (see Fig. 1.2). The focusing A and B fields need to sustain high electric fields to induce deflections on linear or asymmetric top polar molecules where the Stark effect is only second order. The C field region, in which transitions are induced, must have a very homogeneous static field component to reduce inhomogeneous broadening of the measured spectral resonance lines and the field must be well characterized to allow a meaningful analysis of the data obtained. To reduce the effect of Majorana or nonadiabatic transitions as state selected molecules travel between fields of greatly different strength, buffer fields are placed on either side of the C field.[44] Obstacles, such as a stopwire or knife edge, are needed to remove most of the background signal. Molecular collisions must be minimized and the field components need to be aligned along the beam axis for optimal detection response.

1. The A and B Fields

Our focusing fields are quadupolar and are each made from four 1/4" stainless steel polished rods: 36.70 cm in length for the A field and 25.40 cm long for the B field.[45] Each set of rods is held in place equally spaced on a 0.500" diameter circle by 1/8" thick Macor discs,[46] which are in turn mounted in aluminum supports. A 3/32" hole has been drilled on each rod. 2" long 1/2" aluminum cylinders, rounded on both ends and polished all over, serve as the high voltage connectors. Diagonally opposing rods are connected with 3/32" aluminum rods running from these connectors into the corresponding bores on the quadrupole rods.

The voltage for the fields is supplied by two regulated module power supplies,[47] which with an inputted voltage of 24 VDC can output between 0 and 30 kV, controlled by an external ten-turn 5 KΩ potentiometer. They are mounted on a plexiglass board above the spectroscopy chamber.[48] From each power supply, the outputted voltage runs into an aluminum connecter to which two 1 GΩ resistors[49] are connected. One runs to a porcelain high voltage vacuum feedthrough[50] mounted on the top flange of the spectroscopic chamber, and serves to limit the current flow when the quadrupole fields arc. The second resistor leads to a 250 KΩ potentiometer and then to ground, in order to bleed the voltage from the quadrupoles and power supply when the voltage is turned down. The voltage drop from the brush of the adjusted potentiometer to ground serves as an indirect measure of the voltage being delivered to the quadrupoles.[51] A summarizing electrical schematic for the voltage delivery to a focusing field is given in Figure 4. The external connecting pieces, resistors, and feedthroughs are surrounded for safety with Teflon and plexiglass shielding.[52] Holes through the shielding have been made for testing the

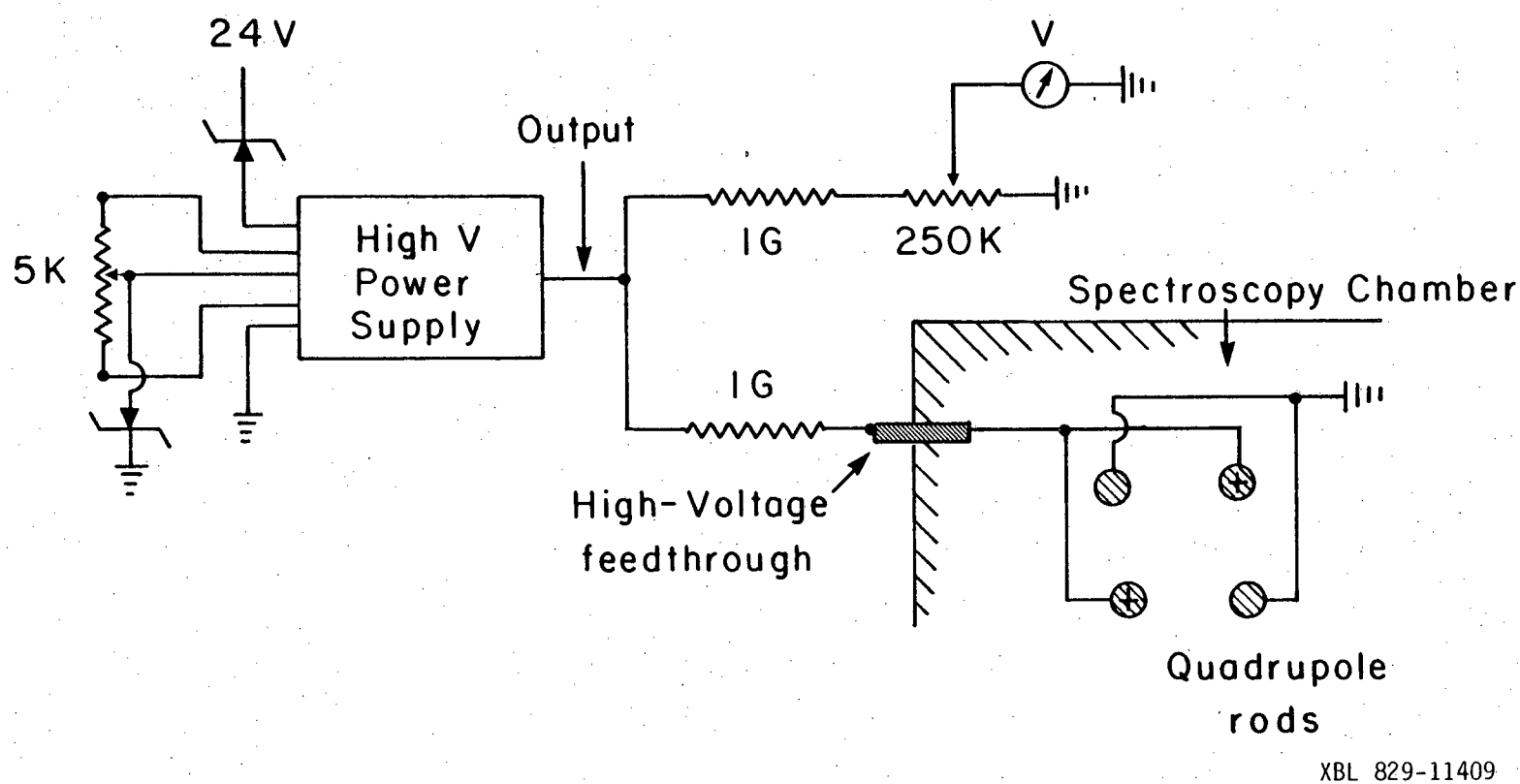

Figure 2.4. A and B field electrical schematic.

circuitry with a high voltage probe when trouble-shooting.[53] Within the spectroscopic chamber the voltage is delivered from the vacuum feed-throughs to the high voltage connectors on the quadrupole rods with high voltage cable.[54] Glass tubing surrounds the cable running to the B field to prevent arcing through its insulation to other metal components within the chamber.

2. The C Field

The assembled C field is represented in Figure 5. Two 4 x 8", 1" thick quartz flats were polished flat to within a quarter wavelength of the sodium resonance line along the 2" central region in the 4" direction, and within a half wavelength along the 6" central region in the long direction.[55] A thin gold coating was evaporated onto the polished faces over maskings for the electrical isolation of regions and for the plates separation spacers. The faces of these plates are indicated in Figure 5b. The coating is thin enough to be translucent to bright back lighting. The plates are kept apart by three 1.000 cm precision spacers and are compressed by Teflon capped alignment screws attached to the C field frame.[56]

A schematic of the circuitry associated with the C field is given in Figure 5c. In one mode of operation (the parallel-perpendicular mode) the regions indicated as 2 and 5 are supplied with a variable radiofrequency while all remaining regions are rf grounded, so that there will be rf field components in the central region between the plates running both from plate to plate and vertically.[57] In the parallel mode regions 4 and 5 receive the rf voltage, so that all rf field lines run from plate to plate. In both modes the entire plate with regions 4 and 5 is supplied with an adjustable static voltage while the opposing plate

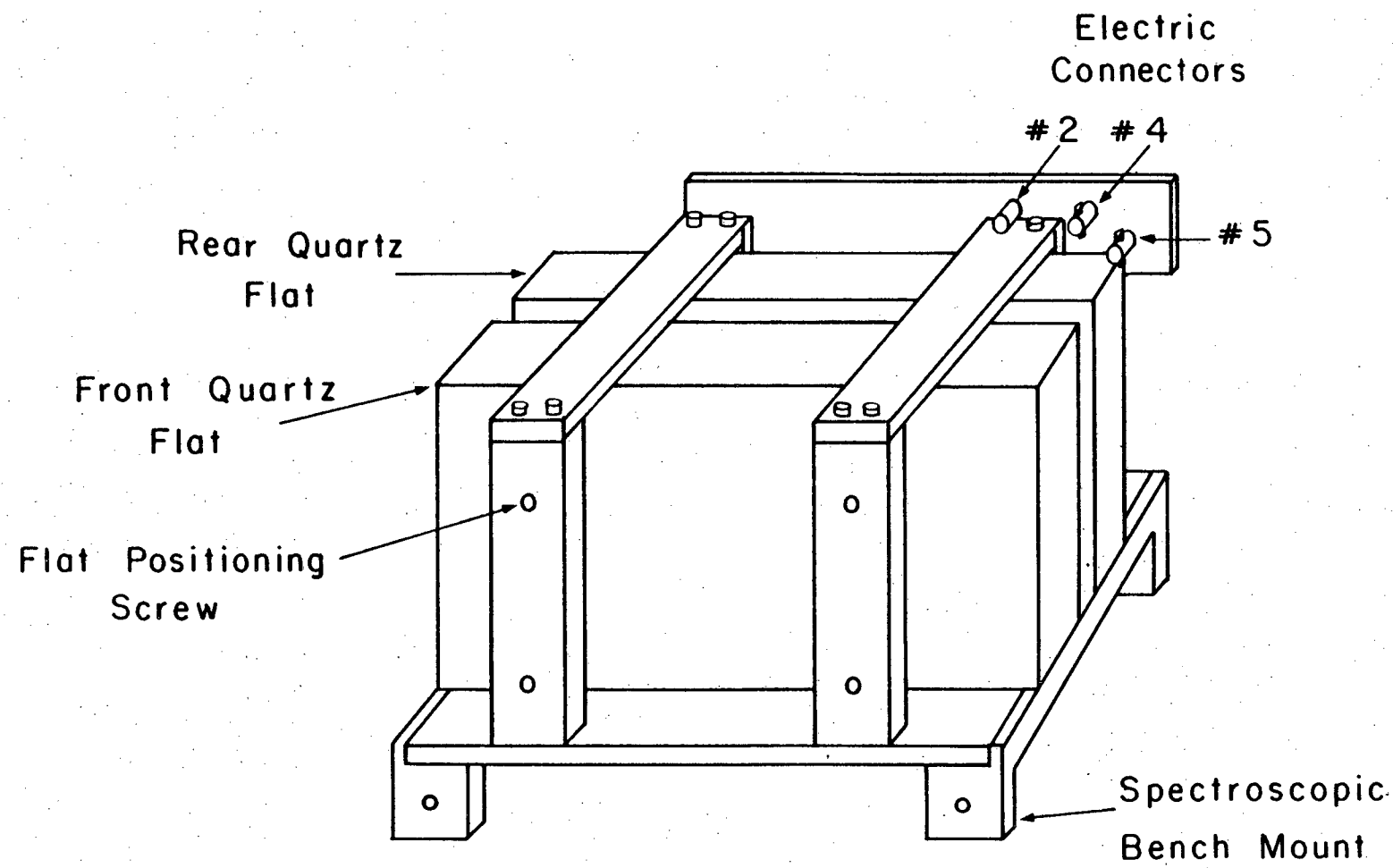

XBL 829-11420

Figure 2.5a. C field (assembled).

is dc grounded.[58] Electrical connections to the gold plated regions are made by gold ribbon wire silver painted to the surfaces.[59]

The positive static voltage is supplied from a 0-3 kV well regulated precision power supply[60] and is monitored by a differential voltmeter.[61] The dc voltage passes through a 10 MΩ current limiting resistor before joined to the circuitry of Figure 5. The rf voltage is supplied from a radiofrequency synthesizer[62] with a frequency range of 50 kHz to 80 MHz. The signal is then passed through two rf amplifiers.[63] The maximum voltage attainable is dependent upon the particular rf frequency, and ranges from about 2 to 80 volts peak to peak. When connected to the C field circuitry, an effective 50 Ω termination is added, reducing the rf voltage by 50%. Occasionally the rf signal is mixed with a noise source to broaden the signal's bandwidth.[64] This will reduce the outputted voltage by 16%. When the rf is passed through our molecular beam interface chopper (to be described in a later section) the rf intensity is reduced by a further 50%.[65]

3. The Buffer Fields

The general shape of the buffer field knife edges and orientation are indicated in Figure 1-2.[66] The knife edges are 1 3/8" wide stainless steel trapezoidal prisms cut at a 30° angle. The wide sides are spaced 0.40" apart on the buffer field mounts. They can slide perpendicularly to the direction of the beam along the spectroscopic bench on 1/8" Teflon rods. Their lateral position is controlled by 1/4" steel rods connected to bellows-type linear motion vacuum feedthroughs.[67] One knife edge on each of the buffer pieces is grounded to the buffer piece frame. The other edges are electrically connected to vacuum feedthroughs

is dc grounded.[58] Electrical connections to the gold plated regions are made by gold ribbon wire silver painted to the surfaces.[59]

The positive static voltage is supplied from a 0-3 kV well regulated precision power supply[60] and is monitored by a differential voltmeter.[61] The dc voltage passes through a 10 MΩ current limiting resistor before joined to the circuitry of Figure 5. The rf voltage is supplied from a radiofrequency synthesizer[62] with a frequency range of 50 kHz to 80 MHz. The signal is then passed through two rf amplifiers.[63] The maximum voltage attainable is dependent upon the particular rf frequency, and ranges from about 2 to 80 volts peak to peak. When connected to the C field circuitry, an effective 50 Ω termination is added, reducing the rf voltage by 50%. Occasionally the rf signal is mixed with a noise source to broaden the signal's bandwidth.[64] This will reduce the outputted voltage by 16%. When the rf is passed through our molecular beam interface chopper (to be described in a later section) the rf intensity is reduced by a further 50%.[65]

3. The Buffer Fields

The general shape of the buffer field knife edges and orientation are indicated in Figure 1-2.[66] The knife edges are 1 3/8" wide stainless steel trapezoidal prisms cut at a 30° angle. The wide sides are spaced 0.40" apart on the buffer field mounts. They can slide perpendicularly to the direction of the beam along the spectroscopic bench on 1/8" Teflon rods. Their lateral position is controlled by 1/4" steel rods connected to bellows-type linear motion vacuum feedthroughs.[67] One knife edge on each of the buffer pieces is grounded to the buffer piece frame. The other edges are electrically connected to vacuum feedthroughs

which are in turn connected to regulated power supplies which can supply up to 400 V.[68] The A buffer field piece is also supplied with a stopwire which is supported by adjustable screws to be centrally located between the two knife edges. Stopwire diameters typically vary from 0.06 to 0.15 cm, and have consisted of tool steel drill blanks or aluminum wire. The top retaining screw on the A buffer is connected to the high voltage side through a 1/2" voltage divider so that the stopwire will not seriously interfere with the buffer's field.

4. The Chamber

All the spectroscopic field pieces are attached to aluminum mounts which can slide along the spectroscopic bench and be hand screwed to lock them into position. The bench consists of a 36" long, 4" wide ground tool steel sheet, 3/8" thick with lateral edges cut inward at 70° for the aluminum sliders to bolt against. For rigidity, this sheet is bolted to a 1½" tall 1/4" thick aluminum channel that runs the length of the bench. Two dowel pins which can be inserted into the spectrometer face of the buffer shroud have matching locating holes bored to the bench. Table 2.1 indicates the approximate locations of the various field pieces when layed out on the bench.

The spectroscopic region is enclosed by the buffer snout, a stainless steel, 32" long spectroscopic chamber,[69] a stainless steel connecting chamber and a spectroscopic chamber shroud. The top flange of the spectroscopic chamber has the high voltage feedthroughs for the A and B fields, as well as other auxiliary parts for venting, time of flight electronics, etc. The right face, from the source side, has the motion control rod for the buffer-spectrometer chamber gate-valve. The front side is typically removed for work within the spectroscopy chamber. It

Table 2.1

Typical Spectrometer Field Piece Locations
(Distances in cm)

Source to A Field	4.
Length of A Field	36.7
A Field to Stopwire	1.9
Stopwire to C Field	1.9
Length of C Field	20.3
C Field to B Field	3.8
Length of B Field	25.4
B Field to Detector Aperture	10.3
Source to Detector Aperture	104.

has a plexiglass window for viewing the chamber when it is closed and a liquid nitrogen delivery arm which leads to an interior cooling copper block.[70] Bolted under the chamber is a 6" gatevalve, a liquid nitrogen trap[71] and a 6" diffusion pump[32] (2400 l/s) backed by a 1 hp mechanical pump.[72] Pressure is measured by an ionization gauge[34] mounted on the spectroscopic chamber, and under typical operating conditions is on the order of 10^{-7} torr.[73] The connecting chamber[74] has 1/4" walls and keys into the spectroscopic and main chambers. It is about 5" long, and when all is assembled, the C field sits inside of it. The spectroscopic bench is located somewhat by a bore inside this chamber and is bolted down here. On its left wall are the linear motion feedthroughs for the buffer fields. On the right wall are the electric vacuum feedthroughs for the C field and buffer electronics, and the C field external circuitry is mounted here.[75] A window port is located on the upper face of the connector. The spectroscopic chamber shroud is of 1/8" stainless steel and is keyed into the main chamber wall from inside the main chamber (discussed in the following section). The exterior face of the shroud has a bored surface for the possible use of a beam collimator.[76] The shroud has been designed to allow room for a full 90° motion of the detector arm in the main chamber.

5. Assembly of the Spectroscopy Region

Attach the connector chamber to the spectroscopy chamber.[77] The spectroscopy chamber is bolted to the buffer shroud using locating pins to guide the pieces together. Insert the bench locating pins into the shroud wall so that the off centered pumpout holes on the dowels are on the buffer side. Screw the tool steel bench top to the aluminum channel, and insert the lateral bench locating pins under the table. Slide the

table into place from the connector side of the apparatus so that the lateral locating pins fit through the corresponding grooves in the connector chamber and the dowels on the buffer shroud fit into the bench. The spectroscopic chamber assembly is then guided into the large port of the main chamber on the side opposite its door. Leveling adjustment of the spectroscopic chamber is handled by jacking screws on the spectroscopic chamber frame, until the connecting chamber keys into the main box. On initial assembly, alignment of the source, spectrometer and detector (described in the following section) can be checked with a cathetometer sighting through the buffer snout along the spectroscopic bench, with the source tee pulled out of the way. A special alignment flange keys into the snout, and sliders with beam alignment holes are available for the spectroscopic bench. The beam axis should remain true to within a few mils from buffer to detector.

Most of the assembly of the spectroscopic bench should be done wearing gloves, as, particularly the A and B fields, parts need to remain clean.[78] In assembling the B field, the high voltage connectors should be vertical to allow for clearance when inserting it into the spectroscopic shroud. The connector on the source end is wired to one of the retaining screws on the farther B field table slider.[79] A sufficiently long high voltage cable is attached to the other connector. It is held by an insulated spacer on the downstream B field slider on the front side of the field to keep the cable from the table. Glass tubing is then slid along the cable. The B field is then ready to be slid along the bench[80] until about 1/4" of the quadrupole rods emerge from the spectroscopic chamber shroud into the main chamber.[81] Hand tighten at least one slider screw. For the B buffer field it has been found easiest to

have the 1/4" motion control rod that will be parallel to the bench and its connectors initially connected to the feedthrough and tightened in place. Slide the assembled buffer piece into the chamber, with the open knife edge face pointing toward the source, to its appropriate position beyond the motion feedthrough. There should be about 1/4 - 1/2" between the knife edges and the B field.[82] Tighten the connection to the motion feedthrough,[83] hand tighten the slider to the table, and connect the B buffer voltage cable to the appropriate pin.[75] Check the motion of the B buffer, insuring that the position where it is centered on the bench is approximately the midposition in its movement range.

Place a 1/2" plexiglass spacer next to the B buffer slider. Place the assembled C field[84] carefully on the spectroscopic bench with its cable connection points toward the rear of the chamber. Lift the C field cables, previously connected to the electrical feedthroughs of the connecting chamber, with one hand and slide the C field down with the other. Cables 4 and 5 should be draped over the side edge of the rear frame. Attach these cables when they can reach their appropriate BNC jacks on the C field.[85] Slide the C field further in, connect cable #2, and then slide the C field up to the spacer. The A buffer is most easily inserted with all motion rods connected to the feedthrough. With the stopwire facing the C field, place the buffer in far enough to be able to connect it to its electrical feedthrough. Then continue sliding it toward the C field, fitting the short buffer rod into the motion connector. Adjust the position of the A buffer and stopwire laterally so that the stopwire will be centered at the midpoint of its lateral range, and then tighten the connection. There should be about a 1/4" between the buffer and the C field. The A field is assembled as the B field, with the

grounded connection on the downstream end.[82] With all fields now in place, adjust the glass tubing along the B field high voltage line and then attach the A and B high voltage cables to the vacuum feedthroughs on the top of the chamber. Check the beam flight path and the A field connectors, and then close up the chamber after rechecking electrical isolation and continuity with a high impedance ohmmeter.

In operation, the A and B fields will invariably arc on occasion.[86] A period of field conditioning[87] is suggested following every time the spectroscopic chamber is vented, and pumped down again which involves turning the fields up incrementally and leaving them on for awhile until arcing has mostly ceased. This should be continued up to about 30 kV on each field, and then the fields should generally be left on at 20 kV when the apparatus is pumped down but not in use.[88]

C. The Detector

The final aspect of an MBER experiment involves the measurement of the number of molecules of interest exiting the spectroscopy chamber along the beam axis.[89] In order to ascertain the identity of the molecules whose trajectory we are observing and to remove from the background all other molecular species present, the beam is passed through an electron bombardment ionizer and a quadrupolar mass spectrometer. The mass selected ions are then electrostatically led to the first dynode of a particle multiplier for signal gain. The main criterion for the design of this detector assembly is detection efficiency. Beam ionizers and associated focusing electronics are generally less than 1/4% efficient, so that very good vacuum conditions are required to prevent scattering of wanted ions, and ion focusing fields need to be optimized. Finally, the electron signal from the anode of the particle

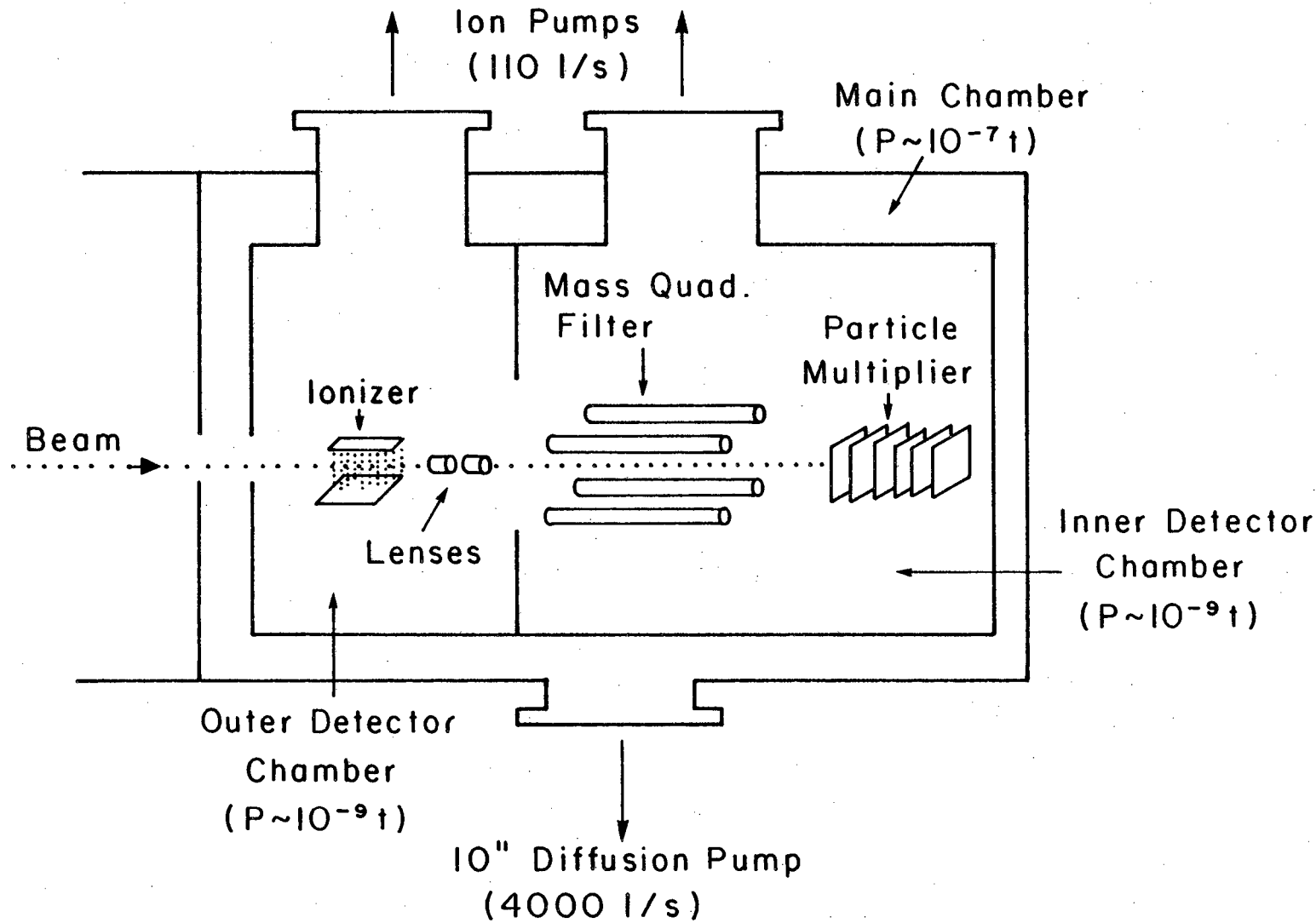

XBL 829-11408

Figure 2.6. Detector schematic.

multiplier is amplified and sent on to an electrometer or pulse counting electronics for data handling. The hardware and software for data handling and driving the experiment are designed to allow for speedy analysis and storage of the experimental results.

1. The Ionizer

Our universal electron bombardment ionizer was modeled after that of Weiss[90] to allow the possibility of generating and detecting both positive and negative ions.[91] In essence, electrons are boiled from a tungsten ribbon filament and pulled into the ionizing region through a positively charged accelerating grid, and allowed to strike a similarly charged collection plate on the opposite side of this region. The molecular beam travels parallel to the filament and between the grid and plate. Heuristically, electrons passing through the grid toward the plate are slowed down by preceding electrons until they get to the central region, where they are reaccelerated by succeeding electrons. This effective space charge in the center of the ionizing region both increases the electron density in the path of the molecular beam and creates a potential well for positive ions when they are formed. If the spacing between the plate and grid increases slightly along the direction of the beam, this potential trough deepens in the same direction, creating an effective ramp for positive ions towards the remaining detector electronics. The ionizer is followed by electrostatic lenses and ion-extracting fields. Weiss found his detector to have a detector efficiency of 1/400.

Our ionizer (see Fig. 7)[92] uses a thoriated 0.001" thick tungsten filament,[93] about 2" long and less than 1/4" wide.[94] It is spot-welded to two 3/16" diameter molybdenum posts,[95] which are in turn fitted into

Figure 2.7. Ionizer assembly.

1. Ionizer frame
2. Pin retaining plate
3. Macor pin holders
4. Electrical connection pins
5. Lens #2
6. Lens #1
7. Alumina rods
8. Support bars
9. Filament post
10. Filament post (split)
11. Post support plates
12. Pierce gun plate
13. Grid plate
14. Anode plate
15. Lock ring
16. Base plate
17. Copper ionizer housing
18. Detector chamber shaft

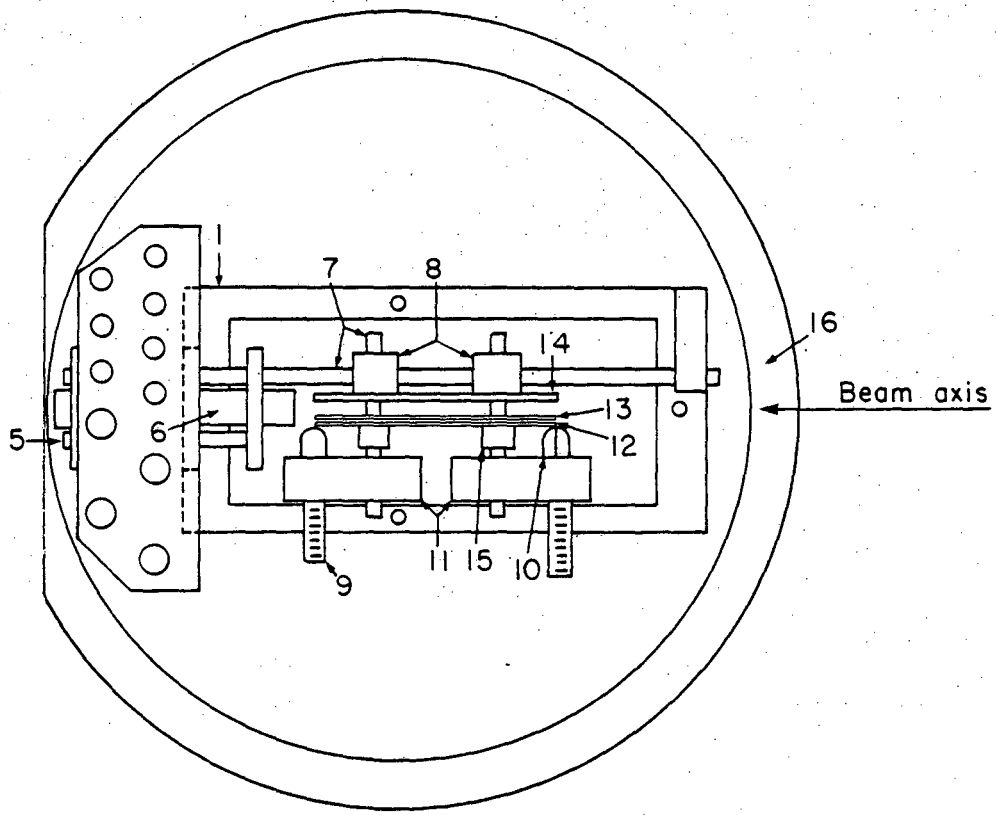

(a) Top view

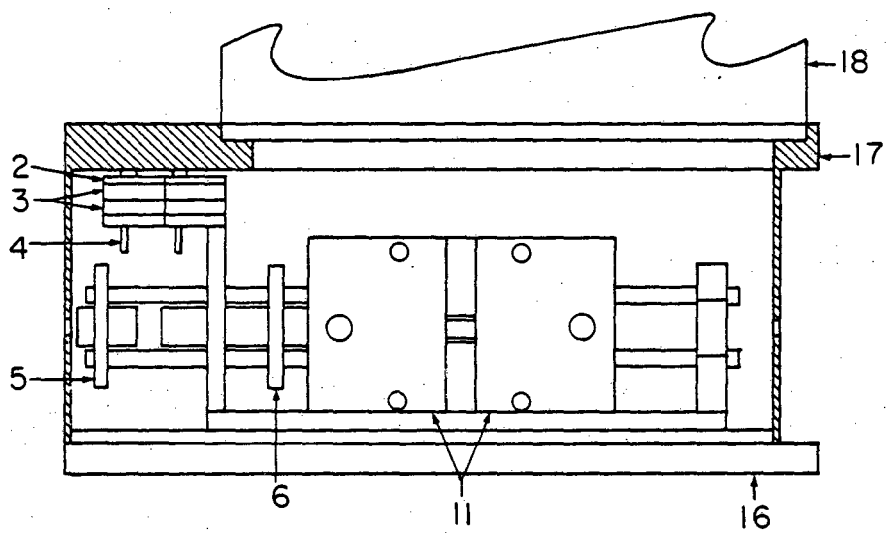

(b) Side view in housing

XBL 829-11400

molybdenum support plates. Two molybdenum 2" x 5/8" x 0.030" Pierce gun electrode plates are mounted on either side of the filament, which aid in the extraction of a beam of electrons from the filament. The grid is a molybdenum plate 2" x 1½" x 0.030" with a tungsten mesh spot-welded over a 1 7/8" x 0.28" centered slot.[96] The electron collecting anode plate is 2" x 1½" x 0.060" molybdenum, and is backed by two 1½" x 3/8" x 3/8" stainless steel support bars. The molybdenum pieces and the support bars are mounted on four 1/8" diameter alumina rods, with 1.2 mm ceramic washers separating the grid from the Pierce electrode pieces, 3.5 mm washers separating the grid from the plate and stainless steel lock rings to press the assembled elements from the electrode pieces to the anode plate against the support bars.[97] Two stainless steel cylinders[98] with 0.313" inner diameter, 1/2" and 1¼" long, are used as collimating lenses. These and the aforementioned assembly are mounted with alumina rods to a stainless steel mounting bracket, 5¼" long, 1 3/4" tall and 2" wide, as indicated in Figure 7. Sandwiched between two macor pieces and between the top face of this mounting bracket and another steel plate are six stainless steel pins used to make electrical connections between the ionizer and the outside world. The filament posts are electrically connected to two of the four larger pins (0.090" diameter) by pairs of 0.020" thick, 1/4" wide nickel strips, mechanically fastened to both the posts and the pins.[99] Steel wires are attached with stainless sleeves to the remaining large posts and spot-welded to the grid and plate pieces.[100] The two smaller posts (0.050" diameter) are connected with spotwelded steel wire to the two lenses. Other connections are made between the two Pierce electrode pieces and one of the filament mounting plates. The mounting bracket is itself

mounted onto a 6" outer diameter stainless steel base plate, which, in turn, is held by capture screws to the copper ionizer housing at the base of the detector chamber shaft (to be described in a later section). When assembled, the connection pins fit through holes on the upper surface of the ionizer housing and are attached with brass sleeves to bare copper wires running up along the detector shaft to vacuum feed-throughs above the chamber.[101]

The tungsten filament is resistively heated using a current regulated 0-20 amp power supply,[102] and typically requires 10 to 18 A at less than 6 V. The potentials on the grid and plate are maintained by individual voltage regulated power supplies,[103] typically in the range of 75 to 200 V with emission currents of up to 100 mA with the ionizer working. Lens 2 (the upstream lens piece) has recently been charged with negative potentials as high as -760 V,[104] while lens 1 is typically at a potential between -100 and 100 V.[105]

2. <u>The Quadrupole Mass Filter and Particle Multiplier</u>

The detailed theory behind quadrupole mass spectroscopy will not be dealt with here.[106] Our mass filter, obtained from Extranuclear Laboratories, Inc.,[107] consists of four 20 cm long steel rods of 9.5 mm diameter, very precisely aligned and housed in a 21.5 cm long by 4.7 cm diameter steel cylinder. This cylinder is mounted[108] concentrically inside a 5" outer diameter cylinder that houses part of the outer detector chamber. A steel aligning piece fits over the entrance end of the quadrupole can into the ionizer copper housing.[109] The other end is affixed to the multiplier housing. Two posts emerge from the detector can for electrical connections to the quadrupole.

A signal gain of up to 10^6 is attained with a twenty one stage copper-beryllium venetian blind particle multiplier.[110] It is housed in a steel can 15.4 cm long with an 8.2 cm diameter, which is held by a steel supporting bar within the detector chamber. The entrance to the first dynode is off axis from the ionizer and mass filter to prevent secondary electron emission from nonfocusable metastable molecules or photons. The front end or Faraday plate also has an orifice on axis to permit a line of sight from the end of the detector along the apparatus' beam axis. The Faraday plate can itself be put at a potential for either improved ion focusing to the multiplier or to measure directly the ion current from the preceding detection electronics.[111]

The relevant potentials for the quadrupole mass filter are supplied by a quadrupole control and radiofrequency power source unit to a hi-Q head and then to electrical feedthroughs mounted on top of the main chamber of our apparatus (further described in the next section).[112] Within the main chamber, two shielded cables[113] connect these feedthroughs to copper rods mounted on the detector chamber housing, which are in turn electrically connected to the posts from the quadrupole mass filter can. Control over mass selection and resolution is at the quadrupole control unit. Mass ranges can automatically be swept by the introduction of a voltage ramp signal to the control unit.[114] The mass filter can also be electrically floated relative to the rest of the detector electronics.[105]

For positive ion collection a negative potential of ca - 3 kV,[115] supplied by the power supply that accompanies our fast electrometer,[116] is delivered to the first dynode of the particle multiplier, to extract the appropriate ions from the mass filter, and to allow a sufficient

voltage drop from the grounded anode to the first dynode for the desired electron cascade. This dynode is connected to a vacuum feedthrough on the back flange of the detector chamber, which in turn is connected by a shielded cable to a feedthrough on the top of the main chamber. A triax connector on this same back flange is connected to the signal anode and referenced to the voltage of the last dynode within the detector chamber, and is connected with an insulated coaxial cable to a triax feedthrough connector[117] on the main chamber roof. This cable's shielding is referenced directly to ground for positive ion collection. Negative ion collection will be discussed later. Finally, a pin on the detector flange[118] is connected interiorly to the Faraday plate, and exteriorly to a feedthrough on the main chamber triax flange. The Faraday plate is typically floated between 0 and +220 V.[105]

3. The Main Chamber

When the molecular beam leaves the spectroscopic chamber it enters the main chamber region and travels about 2" before entering the surrounded detector regions. The main chamber is bounded by the "main box"[119] an aluminum door, the spectroscopic shroud and a 24" outer diameter rotatable lid.[120] The box is made of 304 stainless steel with 1½" thick sides and bottom, and a 2½" thick top wall and internal dimensions of 43" wide, 43" deep, and 23" tall.[121] With the detector chamber assembled to the rotating lid, the detector assembly can be rotated a full 90° from the detector orifice pointing toward the spectroscopic chamber to its pointing in the direction of the left wall of the main box (as viewed from the source and spectroscopic chambers). The large wall thickness prevents deformation of the key-in surfaces' alignment when

the chamber is pumped out.[122] The rear side of the main chamber is sealed with a 49½" x 31" x 1½" thick aluminum door, the removal of which allows access to the interior of the main box and the detector chamber.[123] The left wall of the box has a 6" and 10" port, the latter of which is concentric with the detector axis when the detector is rotated 90° from pointing toward the spectrometer.[124] For our use, this port is covered with a plexiglass flange to allow visual inspection of the detector. The right wall has an 18", 6" and two 4" ports. A liquid nitrogen delivery arm is mounted to a flange for the 6" port, which is internally connected to a copper cold wall[125] that covers most of the floor of the main chamber. The front wall has a 6" utility port and a 10" port. It is through this latter opening that the molecular beam in our experiment travels. The connective spectroscopic chamber keys in and bolts to the outer side of this port, while the spectroscopic shroud is attached to its inner side. The bottom wall has an 11", 7", 5½" and 3/8" port, the last of which is centered about an axis perpendicular to the axes of the 10" ports on the front and left walls. The main chamber is pumped through the 11" port and connecting steel spool by a 10" diffusion pump[126] (4200 l/s), which is backed by a 1 hp mechanical pump.[72] Under typical operating conditions the pressure of the main chamber, as monitored by an ionization gauge,[34] is between 10^{-7} and 10^{-6} torr. All ports mentioned, unless otherwise specified, are sealed with steel or aluminum flanges.[127]

The roof of the main box has a single 24" orifice that is centered over the 3/8" port on the bottom of the chamber. Its inner circumferential surface is grooved for two sealing gaskets, a pump out region between them and a 24" bearing ring.[128] A stainless steel rotatable ring fits into this assembly and the lid bolts over a gasket into this

ring.[120] It is scribed with angle indicating markings to correspond to a stationary ring bolted to the top of the main box about the rotatable one for lid orientation indication. A toothed gear ring bolts onto the rotatable ring, which can be turned by a chain linkage from a smaller gear bolted to the back right corner on the top of the box. The lid itself is made from 1½" thick stainless steel. It has three 3½", two 2½" and one 3/8" ports, the last of which is centrally located. A six sided stainless steel shaft with 1/2" thick walls drops 17 5/8" from under a 7½" conflat port on the upper lid surface, and partly houses the outer detector chamber. The detector housing, described in the previous section, keys into a 5" port near the end of this shaft. This port and a 0.15" beam entrance orifice on the shaft's opposite face are concentric to the apparatus' beam axis on assembly. A motor and gear driven aperture wheel assembly[129] fits over the beam orifice, permitting the use of 0.01, 0.03, 0.06, 0.10, or 0.15" apertures. Of the ports on the lid, one is sealed with the signal triax and Faraday plate feedthrough flange, another with a flange with four copper feedthroughs used for the quadrupole mass filter and particle multiplier high voltage connections,[130] and a third with auxiliary feedthroughs, some of which are connected to the aperture wheel motor and indicators. The bottom of the lid shaft is sealed with a steel plate.[131]

4. <u>The Detector Chambers</u>

The inner detector region which houses the ionizer is contained by the detector shaft,[132] which fits within the lid shaft and is fastened to the 10" conflat surface on the lid's top. The outer detector region, housing the particle multiplier and mass filter, is contained by the outer surface of the detector shaft, the inner surface of the lid shaft

and the detector arm.[108] The overall detector chamber design is similar to that of Lee, et al.,[122] with the exclusion of their outer detector buffer region. The detector shaft is a double walled cylinder, the bottom of which is welded to the OFHC copper ionizer housing. The top is welded to an outer cylinder, which has exterior ports for the inner and outer detector region ion pumps (110 l/s);[133] liquid nitrogen supply and venting to the inner wall and ionizer regions; and three 1½" diameter ports, two of which we sealed with electric feedthrough flanges for the ionizer. The remaining port and the top of the detector shaft are sealed with conflat flanges.[135] The copper ionizer housing has 0.15" orifices through its front and back surfaces for the molecular beam to enter and leave the ionizing region.[136] Holes are drilled through the upper part of the housing, not directly under the detector shaft, which correspond to the electric connection pins of the assembled ionizer. The ionizer base plate screws into holes about the open base of the housing. The inner detector chamber generally operates at 10^{-9} to 5×10^{-8} t.

Most of the characteristics of the outer detector chamber were described in the mass filter and multiplier section. In MBER experiments, the detector arm extends ~16" from the outer wall of the lid shaft.[137] The four inner ports of the high current vacuum feedthrough[101] are connected with steel rings to 0.083" diameter copper wire which run parallel to the inner cylinder to just above the ionizer housing. The seven steel wires emerging from the other electric feedthrough on the detector shaft's outer sylinder are strung through two macor spacing discs. Three of these (#4, 5 and 6) are spotwelded to thinner copper wires which also run down to the ionizer. The rear flange of the

detector arm[118] has three electric feedthroughs for the nonionizer detector electronics and a centered quartz window to allow a line of sight along the molecular beam axis. The typical operating pressure of the outer detector region is 1 to 2 times that of the inner region.

5. Data Collection and Miscellaneous Electronics

The equipment primarily used for data collection and handling from the signal anode include a fast preamp electrometer, a PET microcomputer, a specially designed molecular beam interface board and a pulse discriminator, giving us the versatility to collect data using both analog and pulse counting techniques. Though in principle we should have been capable of negative ion detection, in practice we had very little success, so that the related electronics and circuitry will not be discussed in detail here.[138]

When using the electrometer,[116] the signal from the anode is first passed through a preamplifier[139] connected to the triax feedthrough by a ~4" long coaxial cable. The electrometer measures and indicates the voltage drop induced by the amplified signal across one of three possibly chosen input resistors of 10^5, 10^7, and 10^9 Ω.[140] Depending upon the user's choice of meter sensitivity, full scale deflection can range from 10 mV to 10 V, so that in principle analog signals can be measured from 10^{-11} to 10^{-4} A. The electrometer signal's time constant can be adjusted from nearly 0 to 300 msec, or longer by adding appropriate capacitors across jacks indicated on the back of the electrometer. In typical work the electrometer signal is taken from a 1000 mV full scale jack, and passed to a strip chart recorder, an X-Y recorder[141] and/or to the analog jack on the rear of the molecular beam interface board.

Several possible jobs can be performed by the molecular beam interface.[142] Three BNC jacks on the front panel lead to an rf mixer which can be used to mix a noise background with the rf synthesizer signal to form a broadened frequency line for the C field.[64] For digital analysis of the electrometer's analog signal, an A to D converter based on a voltage to frequency conversion circuit is also included.[143] The other two main features are controlled by a PET minicomputer.[144] The software considerations are left for this chapter's appendix. A 10 MHz reference clock signal is introduced to the interface, typically from our rf synthesizer.[62] The interface can then be programmed to generate its own clock signal at particular lower frequencies (e.g., 10 and 100 Hz). The rf signal going to the C field can be modulated on and off at this set clock frequency. The second remaining feature is two pulse counters which are "and" gated with the clock signal so that one can count pulses (either from the A to D converter or directly from a discriminator) when the clock pulse is high and the other when it is low.[145] The PET driving program can allow these registers to accumulate counts for a preset number of clock cycles, read the counters and store their values in computer memory, rezero them, and have them start counting again. Furthermore, the PET can control the rf synthesizer along an IEEE bus line, and, therefore, step the C field rf frequency in the time between reading the counters and restarting them. In this way, a time modulated MBER spectrum can be taken as a function of the C field rf frequency.

If pulse counting is desired, a discriminator circuit[146] is connected to the triax signal feedthrough. Powered by a 15 V power supply,[147] the discriminator amplifies the anode signal and transmits pulses of 3 V amplitude, 2 μsec wide for each pulse that it detects of voltage

above a set threshold. The discriminator has an upper limit of 10^6 counts per second due to its internal response time, so signals of this order or greater cannot be measured by pulse counting. A 50 Ω terminating resistor is required when directly measuring pulses with the molecular beam interface.

A few remaining comments are in order for the electronics of the MBER apparatus. Presently, one ionizer lens, the Faraday plate and the A buffer field voltage, as well as the quadrupole mass filter floating voltage are supplied through a lens board, which can output between -400 and +400 V to each device.[148] The power supplies for the B buffer field, the lens board, the plate, the grid, and the dc C field component, as well as the quadrupole mass spectrometer control and fast electrometer are all plugged into a single 20 A fused plug strip, which, for both equipment and personal safety, is wired through a relay controlled by one of the ion pump controls. The ion pumps themselves turn off if the pressure in a detector chamber rises above 10^{-5} t, so that the aforementioned devices cannot be turned on if the pressure is unduly high.[149] The PET, rf synthesizer, rf amplifiers and molecular beam interface are mounted away from the remaining electronics to help protect them from the effects of the A or B fields' arcing.[150] Cables for the pumps, pump interlocks and pressure measurements, with the exception of the ion pump cables, are run along the floor into a slightly elevated wooden platform and to their controlling units. All other cables are run over the laboratory lighting fixtures between the controlling units and their corresponding devices. All electronic cabinets, the main and spectroscopic chambers, and electronic devices are grounded commonly to the laboratory water pipes. Finally, other equipment used in conjunction with the PET

for data analysis include a second minicomputer, a printer-plotter, a printer and floppy disc drive.[151]

6. Detector Assembly

In this section the routine for ionizer assembly and closing up the detector is briefly described. It is assumed that the lid and detector shaft elements are assembled and in place and that the detector arm with its enclosed particle multiplier and mass filter are also already assembled.[152]

Tungsten filaments are thoriated by cataphoresis in a thoria solution of finely ground 8 g. ThO_2 and 0.12 g $Th(NO_3)_4 \cdot 4H_2O$ in 150 ml ethanol and 20 ml water.[153] A 0.001" thick tungsten strip cut approximately 2¼" x 3/16" should be straightened and cleaned in ethanol. It is then electrically connected to the negative terminal of an appropriate power supply and submerged into the thoria suspension. A second polished and cleaned tungsten ribbon may be used for the other electrode. Assuring that the filament to be thoriated is not touching any surfaces, approximately 50 mA (~200 V) is passed through the cell for about 45 seconds. The filament is then removed and allowed to dry. A clean white coating should be on both sides of the filament where it was submerged. The filament should be cut to a final length of about 1 7/8", and the thoria on both sides should be scraped off with a knife about 1/4" from the ends for eventual spotwelding.

Figure 7 and the previous section on the ionizer can be used as partial guides for the ionizer assembling. All pieces of the ionizer, including the screws, should be cleaned in ethanol before assembly, and once cleaned no parts should be handled without using either lint free gloves or tweezers. Alumina rods may have metal plated on them which

should be sanded off before cleaning. The four 1½" alumina rods are to be inserted through the outer pair of holes on each of the two plate support bars, and tightened into place with set screws. The following pieces should then be slid down these rods to the bars in the given order and orientation: the plate, flat side first; the 3.5 mm ceramic washers; the assembled grid; the 1.2 mm ceramic washers; the Pierce electrode pieces, in a direction perpendicular to the bars with their flat sides facing away from the grid; the steel retaining rings; and the filament support plates with the filament posts already mounted, such that the threaded parts of the posts are pointing away from the grid and are on opposite ends of the assembly from each other. In the assembly of these mounts, the threaded ends of the posts emerge from the flat sides of the support plates and should be fastened in place each by one nut. The split mounting post should be positioned so that the part connected to the threaded portion of the post is closest to its plate's nearer edge.[154] The retaining rings are tightened such that the gun pieces are pushed snugly back toward the plate support bars and so that the ring set screws will be accessible in the finished ionizer. The filament plates should also be temporarily tightened in place.

Affix the mounting bracket onto the ionizer base plate. Two long alumina rods[155] are guided through the bracket from the end opposite from where the electric connecting pins are to be inserted. These rods are then guided through, in the following order, the inner holes on the support bars of the assembled ionizer elements, so that the assembly lies over the bracket and that the split filament post end is entered first; the long lens, with its shorter end pointing toward the assembled section and its longer end already inserted through the bracket hole on

the pin end; the corresponding holes on the pin end of the bracket; and the second lens, with its longer end pointing toward the assembly. Position the ionizer and lenses using Figure 7 as a guide, and then tighten in place.[156] Place one Macor insulating plate on top of the pin plate of the bracket, so that the counter bores are pointing up and the holes on the plates are aligned. Insert the four larger pins into the larger holes and thinner pins into the two smaller holes on the opposite end of the plates, all with their shorter ends down. Sandwich these with the other insulating plate and the steel hold down plate, and fasten the pin assembly together with a screw, nut and washer through one of the unused holes. Insure that the holes on these pieces are properly aligned so that the pins, if wiggled, will not touch any metal surfaces.

Spotweld 1 cm^2 pieces of tantalum foil to the rounded ends of the filament posts, so that they are particularly well attached at points on the outer sides of these posts near the ends.[157] Spot weld the ends of a thoriated tungsten filament to the tantalum strips so that the filament is as tight as possible. Carefully slide the post support plates toward the grid until the filament is almost between the electrode pieces, and then tighten the plates to the alumina rods.[158] See notes 99-101 and the ionizer section for the other electric contacts to be made. Make sure that the bare wires do not touch any surfaces that they are not supposed to touch. With an ohmmeter, check all electric connections for continuity and lack of shorts. There should be little resistance between the filament posts.

Before mounting the ionizer into the detector chamber, the four captive screws should be threaded through the ionizer base plate, and the brass sleeves used to attach the ionizer connecting pins to the

detector wires should be already attached to those wires. Bring the ionizer under the copper housing with the pins toward the detector arm opening. Carefully maneuver the ionizer upward until the connecting pins emerge through the top of the housing,[158] and then loosely connect the base plate to the housing with the capture screws so that the ionizer is still about 1/8" below its eventual position. Loosen the brass sleeves from the wires and slide them over the exposed ionizer connection pins. Then tighten the captive screws, and connect the pins to the wires with the sleeves. With an ohmmeter, check out the high current feedthrough above the main chamber for continuity between the filament posts and that nothing else is shorted.[101] The bottom plate of the lid shaft may now be attached, and the detector arm is keyed in and bolted to the lid shaft such that the triax connector on its rear flange is pointing down. The two quadrupole cables, and the signal, Faraday plate and particle multiplier cables are now connected to their appropriate terminals.[118] The shielding of the quadrupole, Faraday plate and particle multiplier cables should be connected to ground, typically with wires soldered to the shielding and in turn held against the detector arm by conflat bolts. Check that the shieldings of the cables are not in contact with their inner wires on either end and that the shielding of the signal cable is connected appropriately to the underside of the triax flange. Finally, it is often convenient to rotate the aperture wheel to its 0.15" orifice to allow faster pumping down of the detector chamber. Remove all tools from within the main chamber and then close it up.

D. Apparatus Operation

As is the case with most large apparatus and as indicated in the preceding sections, the procedure required for doing an experiment with our

MBER machine can appear quite involved to the uninitiate. This description of its operation does not intend to take the place of experience for the user, but merely to be a guide for initial use, and to suggest where problems may occur. For the more casual reader, this section includes some of the detailed experimental conditions not already discussed. As with the order of events in a typical experiment, this section is subdivided into parts on the chamber preparation, obtaining a mass spectrum and other detection tuning, obtaining an MBER spectrum, and shutting down. Comments on the operation characteristics are largely empirical, with little attempt made here to explain why our machine has behaved as it has.

1. Chamber Preparation

With the chamber assembled and all ports closed,[127] the mechanical pumps backing the main, the spectroscopic, and the buffer chamber diffusion pumps are opened to their respective chambers.[159] When the pressures in these regions have dropped to about 100 μ, the diffusion pumps and their respective interlocking protection devices are turned on.[160] After about 2 hrs the main and detector chamber pressures should be below 10^{-5} t, and the ion pumps may be started. Typically about 5 amps are also run through the ionizer filament both to bake out the detection region and help prepare the filament for later use.[161] Warming up times of various amounts are also required for the A and B fields (for quadrupole rod conditioning), the dc power supply for the C field, the electrometer and the counting head power supply, if it is used.

About an hour prior to actual experimenting, the liquid nitrogen trap of the detector chamber should be filled. Initially, the lN_2 vent line on the detector shaft is pumped on by the house vacuum line until

it has become visibly frosted due to lN_2 passing all the way through the cold trap. The vacuum is then turned off and the vent line is opened partially to the atmosphere so that just a vapor spray emerges from the vent.[162] This trap must be kept sufficiently full whenever the ionizer filament current is above 5 A and particularly when doing experiments.[163] With the trap cooled, the ionizer current may be gradually turned up during the next 20 to 30 min.[164] The grid and plate are each supplied with about 100 V so that emission current from the filament can be detected. The filament is near operating condition when the plate emission current is on the order of 30 mA.[165] Fill the ℓ-N_2 trap under the spectroscopic chamber, it requiring about 30 min to equilibrate. Turn on the source backing pump (its water cooling line previously opened), open the pump to source chamber gate valve and then the source blower. With the buffer chamber gate valve still closed, valve off the buffer chamber diffusion pump backer from the diffusion pump, and open it directly to the buffer chamber. When this chamber's pressure is below 100 μ, close this valve, reopen the mechanical pump to the diffusion pump and open the diffusion pump gate valve. Initial adjustments for source temperature may be done now, as well.

2. Tuning the Detector and Taking a Mass Spectrum

The detector is generally tuned with the mass filter set for a species in a molecular beam so that the focusing parameters are suitable for a directed beam. The quadrupole mass filter is previously tuned and balanced, as described in its operation manual.[166] Zero the fast electrometer using the "V" and "A" controls and then turn the particle multiplier voltage slowly to about -3.2 kV for positive ion detection.[167]

Turn the remaining detection electronics to settings previously found workable. Examples of typical detector settings which we have used can be found in the Notes. Open to the source the gas[168] on which you plan to tune the detector and open the buffer to spectroscopic chamber gate valve. With the mass filter set appropriately and the electrometer on a more sensitive scale, a signal on the electrometer should be evident that can be almost zeroed by closing the aforementioned gate valve. If this is not the case, check the beam path.[169] If this appears clear and no other problems are evident, gross retuning may be necessary. Background peaks should also be evident at 28 (N_2^+) and 16 (O^+) amu. Once the beam signal is assured, maximize its intensity by adjusting the source to skimmer distance and the lid orientation.[170]

For electronic optimization of the detector signal, some choice has to be made between signal intensity and resolution. First fine tuning should be done with the filament current. A couple of sharp signal maxima may occur, but the setting for the lower filament current is preferable both to increase the filament's lifetime and to reduce the magnitude of the filament background peaks.[171] Of the remaining controls, lenses one and two, the grid, the plate and the Faraday plate tend to primarily affect signal amplitude, while the mass filter's resolution, ΔM and floating voltage will affect the mass peaks' relative intensities, shapes and, to a small extent, locations. All of the tuning controls are mutually coupled, so some diddling is required. The grid voltage should be slightly greater than that of the plate, while the emission current to the plate should exceed that to the grid.[172] These, the filament, the lenses, and Faraday plate should be adjusted using the electrometer signal as a reference. The remaining adjustments are best made taking rapid mass scans and using a scope.

Mass spectral scans are obtained using a sawtooth generator[114] to drive the mass filter and the electrometer to measure signal strength.[173] During tuning, to scan a single peak, the ramp is set at 0.1 sec/sweep, and the quadrupole mass filter is set at a suitably low width interval about the mass peak of interest. The "Resolution" and "ΔM" controls of the mass filter are strongly coupled. A lower "Res" setting increases the intensity of high mass signals relative to lower masses. The floating voltage control has the largest single effect on relative peak sizes and will show several signal maxima during tuning. With the peak shape as desired, the ionizer controls should be readjusted for final optimization. A full mass spectrum can then be taken, normally changing the sawtooth scan rate to 1 sweep/100 sec and appropriately increasing the scanned mass range.

3. Stark Focusing and MBER Spectroscopy

The gas to be studied is now introduced to the source in its preprepared mixture at the desired source pressure, the source temperature having already been established. The appropriate mass spectral peak can be found with the aid of background mass spectra taken with the buffer-spectroscopy gate valve closed. The source to skimmer distance should be readjusted for the different source conditions.[174] The detector will require some retuning to optimize the signal for the particular mass peak, especially needing a change in the mass filter floating voltage. The identity of the mass peak should then be rechecked by gating the source.

The A buffer stopwire should then be introduced into the beam path. If at least 95% of the mass signal cannot be occluded, then either the stopwire diameter is too small, the detector orifice is too large or

there is too high a background pressure in the spectroscopy chamber.[175] Now turn up the A and B field voltage to refocus the blocked beam.[176] Details of the refocusing process are left for the next chapter. Here it is pointed out that most of the refocusing is done with the A field. If more than one maxima is attainable in refocusing, the appropriate one is that which gives the best transition signal. For $J = 1$ transitions this will correspond to the lowest voltage maximum. The chosen dc voltage for the C field should be set, and the A and B buffer fields should be set to 200 and 450 V, respectively.[177] The final refocus tuning is to be done once the desired resonance frequency is found.

The three main methods used to scan for transition frequencies involve the direct manual use of the rf synthesizer and indirect control with the PET microcomputer with and without the molecular beam interface chopper. Aside from continuous manual control of the output frequency and amplitude, the synthesizer has also the built-in ability for 50 sec scanning over a desired frequency range. With the use of our laboratory's program "Synthesizer Sweep",[178] similar scans with more flexibility in time range and outputting are allowed. For 50 sec sweeps, the dc ramp output of the synthesizer is connected to the X drive of the XY recorder, and the half X scale point is set to correspond to the central rf frequency of the scan. For multiple scanning and a digital recording of a spectrum, the program "Fast MBER" or "MBER"[179] should be used in conjunction with the molecular beam interface. The memory extension board of the interface is inserted into the PET computer, and the 50 Ω rf output of the synthesizer is passed through the interface chopper before going through the rf amplifiers.[180]

To find a resonant frequency requires fast scanning over a wide region.[181] Due to the narrowness of the line width of radiofrequency transitions (<5 kHz), noise broadening of the rf synthesizer output is advisable, either through the use of the rf noise generator and interface mixer[64] or by the dither routine in "Synthesizer Sweep".[178] Once a resonance is located, the chopper routine of "Synthesizer Sweep" is convenient for optimizing the focusing field voltages, the rf frequency amplitude[182] and any of the other apparatus parameters before taking detailed spectra.

4. Shutting Down

For just stopping experimentation and not opening the chamber, turn off the gas source and pump out the source can with the gas cart pump. Close the blower and backer pump gate valve and turn off the blower. In a minute, the large pumps can be vented and the backer turned off. The high voltage on the particle multiplier should be turned down and off. The ionizer filament current can be turned down to 3-5A. The mass filter should be switched to standby and the C field voltage turned down somewhat to protect the unattended flats. The rf amplifiers should be turned off. Finally, the stopwire is moved from the beam path[183] and the buffer-spectrometer gate valve is closed.

If either the main or spectroscopic chambers will require opening, the ℓ-N_2 from the detector trap should be blown out.[184] Detector power supplies should be turned off. Both ion pumps and the main and spectroscopic chamber diffusion pumps can then be turned off and the interlocks set to "Calibrate".[105] After about 45 min, the chambers can be vented with dry N_2 and the backing mechanical pumps valved off. If only the source chamber needs to be vented, it suffices to close the buffer diffusion pump gate valve before opening the source to the atmosphere.

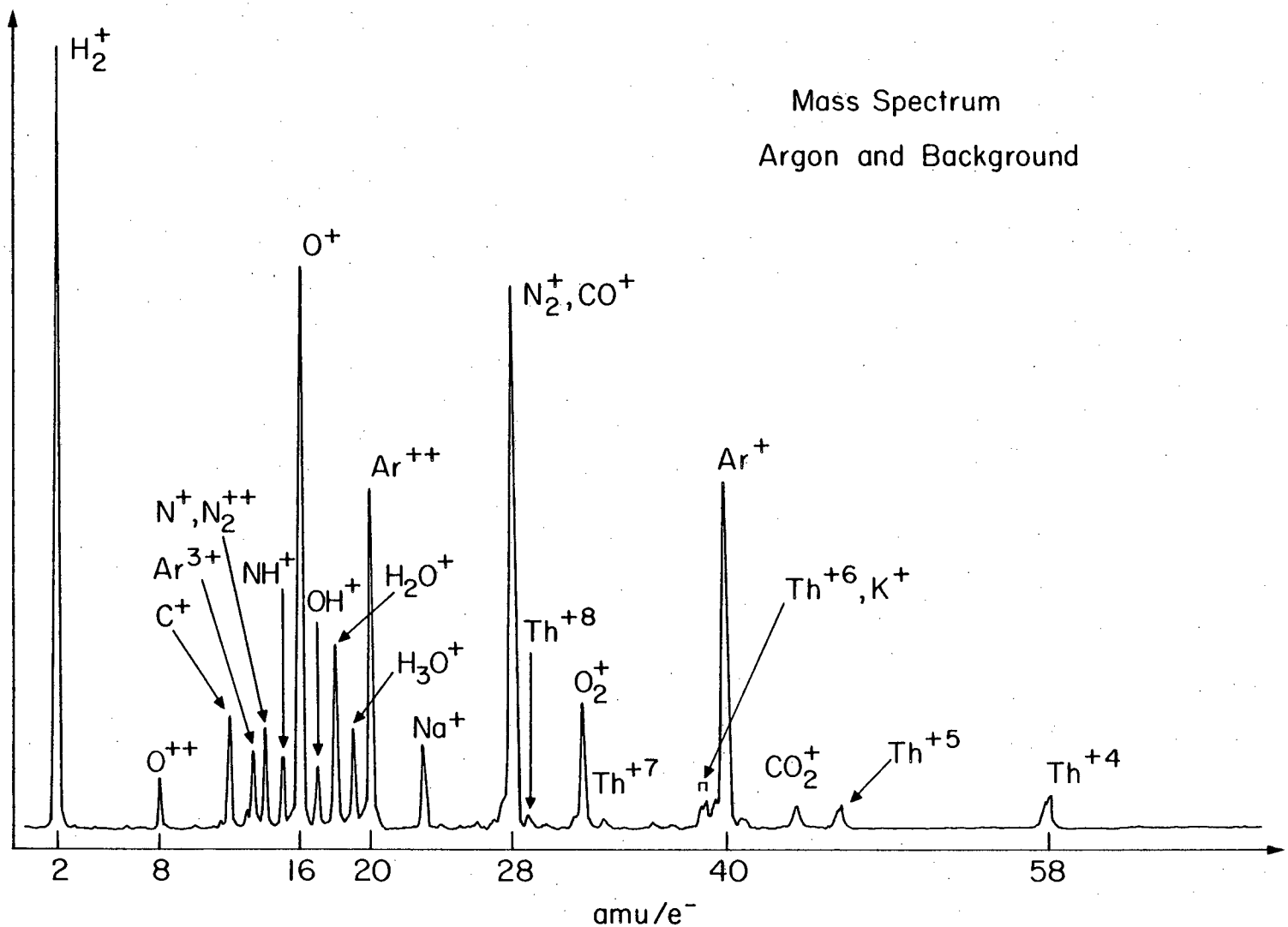

XBL 829-11402

Figure 2.8. Mass spectrum - Ar(P_s = 5.7 atm, T_s = 23°C)[186].

E. Source and Detector Characteristics - Mass Spectra

1. Argon Beam Characteristics

Figure 8 presents a mass spectrum covering mass to charge ratios from 0 to 60 for an Ar beam at room temperature and a source pressure of 68 psig.[186] An identification of the peaks is made under the spectrum. The low magnitude of the Ar-40 peak (~40 nA) relative to the background peaks at 28 (N_2^+, CO^+) and 16 (O+) could be dramatically changed by re-adjustment of the mass filter float voltage to about 5 times larger. Ar^{+2} - 20 is always evident in Ar mass spectra, though its magnitude is typically <2/3 that of the parent peak. This spectrum also presents a good example of the background. As this was made with a relatively hot ionizer filament, there are quite noticeable peaks associated with thorium, sodium and potassium, which may not be present with cooler ionizers. The general baseline noise is on the order of 0.05 nA, which is typical for all of our mass spectra and serves as a limit for detectability. In general it has been found that with a fixed detector setting the Ar-40 peak remains proportional with the argon source pressure only to a few hundred torr, and then does not rise as quickly. Time of flight measurements made on Ar beams[187] have indicated an effective beam path of length 117 cm as compared to a measured path from the skimmer to the detector of 104 cm. The difference has been largely attributed to the detector time response and a triggering offset in the TOF experiments.

In a measurement with pulse counting on a 20 t, room temperature Ar beam, 4.5×10^5 counts/sec were measured and a signal current of 720 nA. If one assumes that the pulse count is a somewhat accurate representation of the number of Ar^+ ions reaching the particle multiplier, a crude

estimate of the detection efficiency can be made. The beam flux is estimated by assuming an effusive flow from the source,

$$Q = \bar{v}\, n\, A_s/4 \tag{2.1}$$

where Q is the source flux (molecules/sec), $\bar{v}$ the mean velocity of the particles in the source, n the source number density and A_s the area of the source orifice. For 100% efficiency every molecule in the beam which strikes the detector orifice would be detected. This flux, N, can be estimated via

$$N = Q\,\frac{A_d}{2\pi l^2} \tag{2.2}$$

where A_d is the detector orifice area; l, the distance between the source and detector; and $A_d/2\pi l^2$, the fraction of the effusive beam's hemispherical flux that strikes the detector. Assuming a Boltzmann distribution within the source,

$$N = \frac{1}{8\pi}\,\frac{3kT}{m}\,\frac{P}{kT}\,\frac{A_s A_d}{l^2} \tag{2.3}$$

where k is the Boltzmann constant, P and T the source pressure and temperature, and m the mass of a beam particle. The detection efficiency can then be estimated by

$$\varepsilon = S/N \tag{2.4}$$

where S is the measured counts/second. The aforementioned experiment was performed with a source orifice diameter of 0.005", a detector orifice diameter of 0.15" and a separation of 104 cm, giving an estimated flux into the detector $N = 8.5 \times 10^{10}$/sec and a measured detection efficiency

$\varepsilon = 5.2 \times 10^{-6}$.[188] In fact, the source and beam are not effusive but more directed, which would increase the effective value of N. On the other hand, the particle multiplier has an upper operating limit on the order of 1 MHz, so a fraction of the Ar^+ reaching the particle multiplier are not counted. This is further indicated by the calculated multiplier current gain in this experiment of 10^7 (determined by the ratio of the electrometer current to counted pulses) which is a factor of 10 greater than that estimated by the manufacturer. Finally, Ar^{++} signal is not included in this analysis. The calculated efficiency given here is felt to be within an order of magnitude of the true detector efficiency. This compares quite poorly with the 2.5×10^{-3} predicted efficiency of the Weiss detector,[90] or the estimated 10^{-5} efficiency of the Klemperer MBER apparatus.[187] This will be discussed further in a later section.

As will be discussed in further detail in Chapter III, the beam temperature of a supersonic source decreases with a decrease of source temperature, an increase of source pressure and an increase of the source aperture diameter. This is manifested in an Ar beam with the formation of argon clusters which would only be stable at temperatures significantly lower than the generally used source temperatures. Figure 9 shows an example of Ar cluster formation for a source at 20 psig pressure, -110°C temperature and with a 100 μ diameter nozzle.[190] No clusters were evident under similar conditions at room temperature. Though peaks here are seen out to Ar_5^+, we have seen argon clusters up to Ar_{10}, which has been the upper mass limit of our detector. Again, changing the mass filter float voltage changes relative peak heights. For example, with an 84 psig beam at -25°C, the peak intensity ratios of

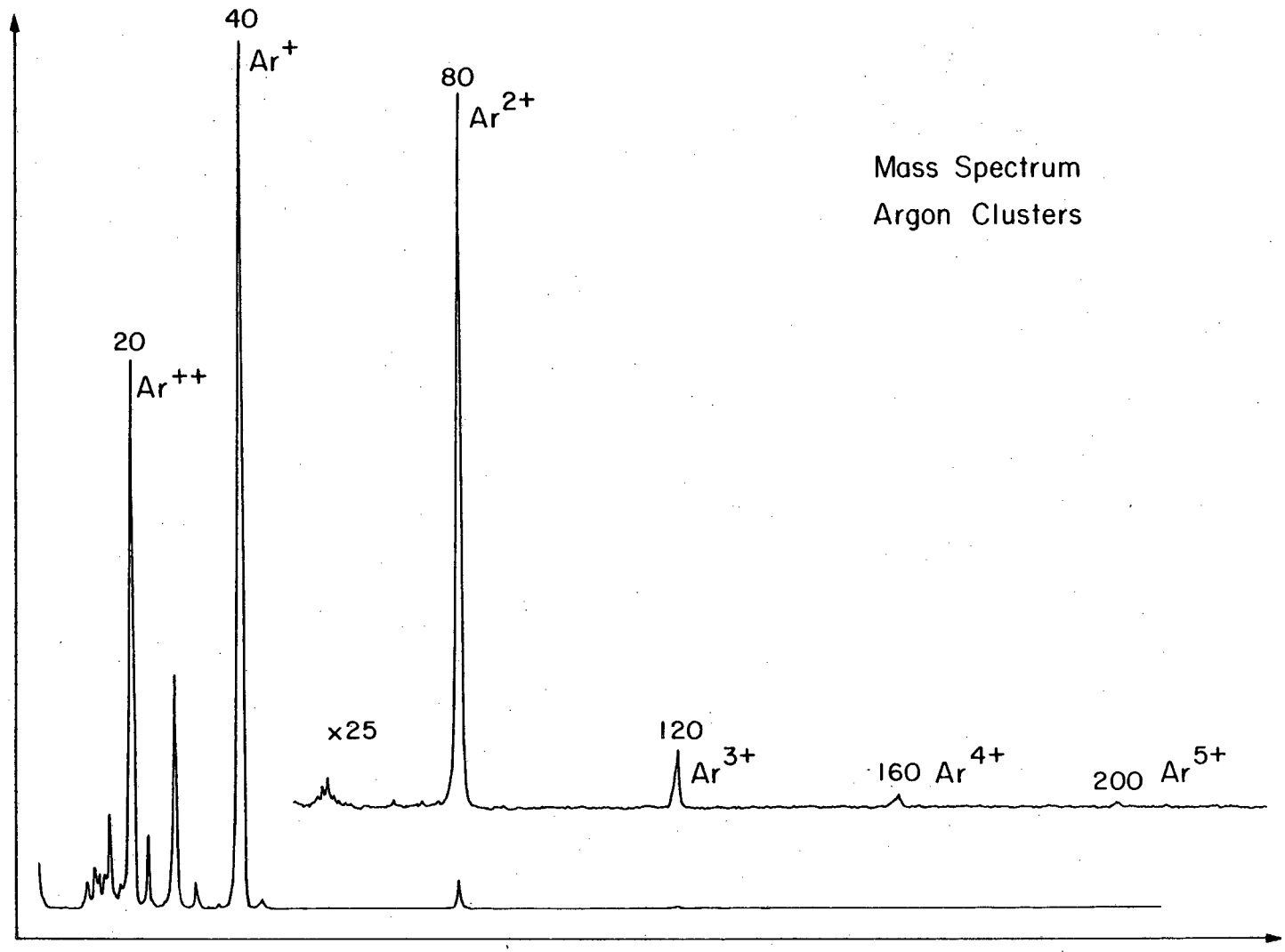

Figure 2.9. Mass spectrum - Ar(P_s = 2.3 atm, T_s = -110°C)[190]. XBL 829-11403

Ar^+ to Ar_2^+ to Ar_3^+ to Ar_4^+ were 21:1(62nA):0.04:0.006 when tuned to maximize the signal at 40, and 9:1(15nA):0.02:0.008 when tuned on peak 80.[191] Thus little can be said of a quantitative nature on the relative concentration of argon species. As anticipated the quantity of Ar_2 detected relative to Ar increases with source pressure and a decrease of source temperature. The relative amounts of the other polymers increase with respect to Ar_2 similarly. Ar was found to clog the source at source temperatures below -140°C.

2. <u>ClF-Ar Mixtures and Cluster Formation</u>

For a somewhat more detailed example of van der Waals molecules formation we studied the mass spectra of ClF-Ar mixtures as functions of the source gas composition, pressure, temperature and source nozzle diameter. A sample mass spectrum illustrating the typically observed clusters and fragments is given in Figure 10.[192] The source conditions were a temperature of -20°C and pressure of 50 psig (~4½ atm) of 15% ClF in Ar (P_{ClF} ~ 525 t), with a 100 μ nozzle. The major mass peaks observed with mass to charge ratios less than 130 are listed in Table 2.2, with the background and argon peaks listed separately. The identification of the ClF cluster and fragment peaks was facilitated by knowing the 3:1 natural distribution of the chlorine 35 and 37 isotopes. These peaks arose from such species as Cl^+, Cl_2^+ (their source pressure dependence indicates that these do not arise mainly from Cl_2 impurity in the beam), ClF^+, ClF_2^+, Cl_2F^+, Cl_3^+, $(ClF)_2^+$ and Cl_3F^+, as well as some fluorine and hydrated fluorine fragments. It is not obvious from our studies what parent molecules are unambiguously responsible for these peaks individually before the molecules are fragmented by the ionizer.

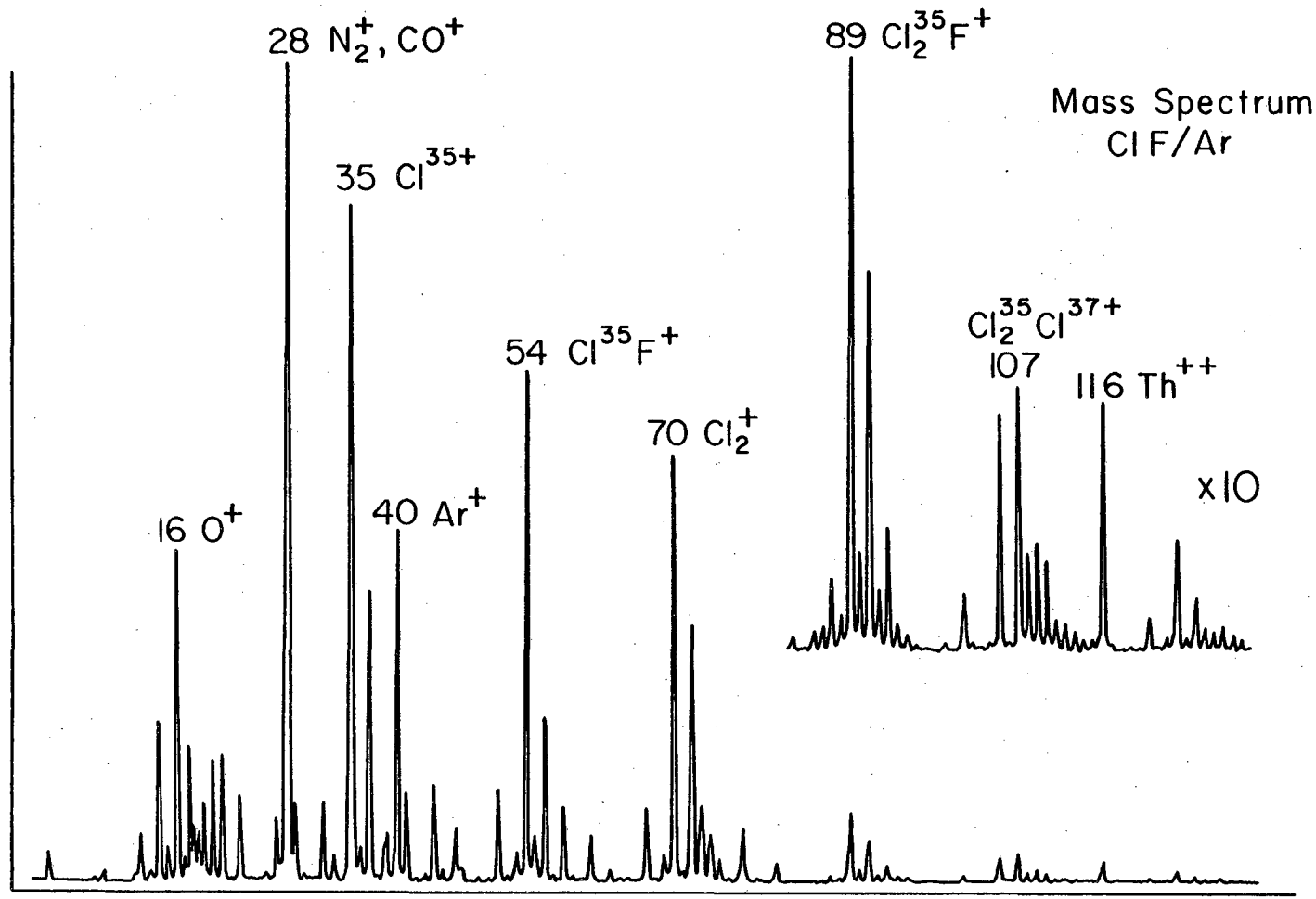

XBL 829-11572

Figure 2.10. Mass spectrum - ClF/Ar (P_s = 4.5 atm, P_{ClF} = 525 t, T_s = -20°C, D_s = 100 μ)[192]. See Table 2.2 for peak identification.

Table 2.2

ClF/Ar Mass Spectrum Peaks of Figure 2.10 (Relative Intensity of Larger Peaks Indicated)

P_s = 50 psig, P_{ClF} = 525 t, T_s = -20°C, D_s = 100 μ[192]

Background and Argon		ClF	
2	H_2^+	17.5	Cl^{35++}
8	O^{++}	18.5	Cl^{37++}
12	C^+	19	F^+
14 (0.19)	N^+, N_2^{++}	21	H_2F^+
15	NH^+	35 (0.82)	Cl^{35+}
16 (0.40)	O^+, O_2^{++}	36	$Cl^{35}Cl^{37++}$
17	OH^+	37 (0.35)	Cl^{37+}
18	H_2O^+	41	$(HF)_2H^+$
20	Ar^{++}	51	FO_2^+, $Cl^{35}O^+$
23	Na^+	53	$Cl^{37}O^+$
26	Th^{+9}	54 (0.62)	$Cl^{35}F^+$
27		56 (0.20)	$Cl^{37}F^+$
28 (1.0)	N_2^+, CO^+	61	$(HF)_3H^+$
29	Th^{+8}	67	$Cl^{35}O_2^+$
32	O_2^+	69	$Cl^{37}O_2^+$
33	Th^{+7}	70 (0.52)	Cl_2^{35+}
39	K^+, Th^{+6}	72 (0.32)	$Cl^{35}Cl^{37+}$
40 (0.43)	Ar^+	73	$Cl^{35}F_2^+$
44	CO_2^+	74	Cl_2^{37+}
46.5	Th^{+5}	81	$(HF)_4H^+$
55	$(H_2O)_3H^+$	87	
58	Th^{+4}	89 (0.09)	$Cl_2^{35}F^+$
63	Cu^{63+}	90	

Table 2.2 (continued)

Background and Argon		ClF	
65	Cu^{65+}	91	$Cl^{35}Cl^{37}F^{+}$
77.3 (0.07)	Th^{+3}	92	
116	Th^{++}	93	$Cl_2{}^{37}F^{+}$
124	ThO^{++}	101	$(HF)_5H^{+}$
		105	$Cl_3{}^{35+}$
		107 (0.04)	$Cl_2{}^{35}Cl^{37+}$
		108	$(Cl^{35}F)_2{}^{+}$
		109	$Cl^{35}Cl_2{}^{37+}$
		110	$Cl^{35}FCl^{37}F^{+}$
		121	
		126	$Cl_2{}^{35}Cl^{37}F^{+}$

It was interesting to us that there appear essentially no Ar cluster peaks in spectra as in Figure 10, whereas Ar_n^+ signals are quite apparent for n at least up to 3 for spectra taken under similar Ar conditions without ClF in the beam. At the time we were particularly looking for Ar_nClF species, which are present to only a very small extent in Figure 10. The magnitude of Ar_n and Ar_nClF peaks were found to have a strong dependence on the partial pressure of ClF (P_{ClF}) in the source. Some of our measurements of peak heights for Ar_2^+, Ar_3^+, ClF^+, Cl_2F^+, $ArClF^+$ and Ar_2ClF^+ are presented in Table 2.3 for various source conditions as functions of P_{ClF}.[193] In general, little argon clustering is seen with P_{ClF} greater than 100 t. As P_{ClF} is lowered, Ar_n and Ar_nClF grow in concurrently. The Ar_nClF peaks grow both absolutely and relatively compared to the other ClF fragments. A somewhat satisfactory explanation for this phenomenon is that the exoergicity of pure ClF cluster formation causes local beam heating during its expansion, thereby making Ar containing clusters thermodynamically unstable, so that only at lower ClF concentrations can the beam produce the Ar species. For example, reactions such as $Ar_2 + 2ClF \rightarrow Ar + ArClF + ClF \rightarrow 2Ar + (ClF)_2$ occur. In our studies with source pressures in the range of 1 to 4 atm and temperatures between -60 and 20°C, $ArClF^+$ and Ar_2ClF^+ peaks were found to maximize at P_{ClF} between 3 to 8 torr. It was less interesting to note that the intensity of the Cl_2F^+ peaks tracked the P_{ClF} significantly better than the ClF^+ peaks at $P_{ClF} > 8$ t.

In general the remaining source conditions had the expected effects on cluster formation. Clusters were somewhat enhanced by lower source temperatures and higher source pressures. In our range of conditions, no cluster formation was observed with a 25 μ diameter nozzle. Two

Table 2.3

Mass Spectra Peak Intensities for Ar-ClF Gas Mixtures

	Signal (relative, within each section)					
$P_{ClF}(t)$	Ar_2^+	Ar_3^+	ClF^+	Cl_2F^+	$ArClF^+$	Ar_2ClF^+
	T_s = -50°C		P_s = 3.7 atm		d_s = 100 μ	
110.	0.2		10.	3.2	0.10	
29.	2.5		9.5	3.6	0.24	
18.	5.0		8.5	2.6	0.44	
8.	9.0		8.1	1.7	0.67	
3.6	12.		4.4	0.68	0.52	
1.6	12.		2.2	0.28	0.28	
0.7	13.		1.0	0.09	0.12	
	T_s = -40°C		P_s = 1.7 atm		d_s = 75 μ	
30.	1.8	0.	7.2	4.4	0.20	0.
18.	4.2	0.13	7.4	4.0	0.40	0.13
10.8	6.6	0.55	6.0	3.8	0.65	0.25
6.5	9.4	0.88	4.8	2.4	0.88	0.20
3.9	10.8	1.4	4.0	1.2	0.78	0.38
2.3	12.0	1.6	2.8	0.56	0.75	0.30
1.4	14.0	2.5	1.8	0.25	0.60	0.30
0.0	14.5	2.4	0.	0.	0.	0.
	T_s = -70°C		P_s = 1.7 atm		d_s = 100 μ	
20.	1.6	0.23	8.3	2.8	0.20	0.
12.	6.0	0.60	9.0	4.5	0.70	0.08
7.2	8.9	1.2	8.9	2.7	0.80	0.16
4.3	8.9	1.6	8.0	1.6	0.80	0.17
2.6	9.0	1.9	5.8	0.80	0.80	0.15
1.6	9.0	1.9	3.7	0.38	0.58	0.11
0.9	9.0	2.0	2.2	0.10	0.38	0.11

special points should be made. The cluster formation was enhanced by our 75 μ nozzle over that of our 100 μ nozzle. This is attributed to the special design of the former, previously discussed (see the "Source Can" Section and Note 14). Secondly, our prime objective during this Ar-ClF survey was to generate a beam of ArClF and Ar_2ClF to use in MBER experiments. It was found during these studies that generally those conditions that best favored the creation of these van der Waals molecules, particularly high total source pressure, allowed for quite poor Stark focusing for both these species and ClF itself. The best conditions found were with source pressures between 1 and 1.8 atm and P_{ClF} between 3 and 8 torr (a little lower for Ar_2ClF optimization), where, though with poor total signal, up to 100% refocusing of ArClF about the A buffer stopwire was observed. This problem of opposing requirements for MBER cluster studies will be discussed further in later sections.

3. Other Mass Spectra

This section is to serve as a brief survey of the characteristics of mass spectra of some of the other molecular species run through our apparatus.

ClF/He. Under similar conditions as the ClF/Ar studies, no He-ClF clustering was observed. The ClF clusters disappeared at higher P_{ClF} values than in the argon carried beams.

NH_3/Ar. With 680 t NH_3 and a total source pressure (P_s) at 50 psig, peaks were observed at 17(NH_3^+), 18(NH_4^+ and background H_2O^+), 35, 52, and 69($(NH_3)_nH^+$ for n = 2,3,4). Cluster peaks were enhanced at lower source temperatures.

OCS/Ar. Significant peaks at 32, 60(OCS^+), 64(S_2^+, SO_2^+), 120 ($(OCS)_2^+$), and 100($ArOCS^+$). The peaks at 32, 60 and 100 are Stark focusable, so that 32 is probably a daughter S^+ fragment of OCS. The other peaks did not deflect. Pressure studies comparing the intensities of 60 and 64 indicate that 64 is from a cluster fragment.

SF_6. Observed peaks in decreasing order of magnitude were at 127(SF_5^+), 54(SF_4^{++}), 89(SF_3^+), 108(SF_4^+), 51(SF^+), 70(SF_2^+), and 63.5(SF_5^{++}). The S^+ peak (32) may have been masked by background O_2^+. No peak was found for SF_6^+. An attempt at detecting negative ions was made, but nothing reproducible was observed over the background.

HF/N_2. HF-20 peaks were in general difficult to detect due to background Ar^{++}. With 33% HF at P_s = 12 psig, there was slight increase in the 20 peak (HF^+), and peaks at 19, 41, 61, and 81($(HF)_nH^+$). HF could not be made to refocus.

HF/SF_6. A 30% HF mixture in SF_6 was tried to see if the HF could be slowed down enough for Stark focusing. Instead, no HF peaks were visible. Apparently the HF is ejected from the center of the beam by a mass effect of the SF_6.[2]

F. The Apparatus - Parting Comments

As previously mentioned, to date we have not been able to find previously undiscovered spectral peaks of van der Waals molecules with our MBER apparatus, for which it was designed. As will be noted in Chapter IV, we have not even been able to see all the reported peaks for covalently bonded ClF. Part of this is due to the relatively short time our machine has been in workable condition.[1-193] The other difficulties

will be more easy to point out in retrospect on a day the spectrometer is performing well. In the following paragraphs a few places for modification are suggested to aid in the attaining of that day.

The most serious problem we feel presently exists with the detection system. Given that van der Waals molecules are never synthesized in great quantity and that Stark focusing conditions for a beam further reduce the amount of weakly bound clusters present, the detector must be quite sensitive. The efficiency indicated in the previous section is probably not adequate. Alterations are required, most probably involving the design of the ionizer. It has been suggested that ions once formed are not extracted efficiently from the ionizing region by the present arrangement of lenses, and that even those ions which do leave have a transverse energy too great to allow focusing by the mass filter. If a suitable lens arrangement cannot be found, we suggest that either a surrounding magnetic field be used to aid in the restraining of the ions' transverse motion, or that a Brink's ionizer design be used.[91]

There has always been some ambiguity in the molecular beam's direction as it leaves the source chamber, due to the method by which the source can is held in place. Though we are not in the habit of creating more beam handling parameters than are needed, it is felt that a redesign of the source chamber may be in order to allow more degrees of freedom for the location and orientation of the source, or at least an alternate method of holding the source can which does not have the present "wiggle". The large blower and backing pumps acting on the source chamber have not been of the best operational quality. Some reduction of the source background pressure with better pumps would be desirable. The flat nozzle design of our 75 μ nozzle seemed to have

good cluster forming properties. Further experimentation with such nozzles seems to be called for. Finally, for the source chamber, the supposed value of high quality skimmers has not been obvious to the author. Though ultimately we feel these will be important, the other probable difficulties with the source should be addressed first.

At this time no significant suggestions can be made referring to the spectroscopic region. The field pieces seem to work well within the constraints already discussed. Eventually a dipole type field for the B region is advisable to explore flop-in type processes better, but only after at least detection problems are repaired. A stronger rf amplifier would also be useful to explore better rf power dependence of spectra and to probe for weak transitions.

MBER spectroscopy as a whole has made significant contributions to the study of van der Waals molecules, as indicated in the first chapter. The more recent method of Fourier transform electric resonance spectroscopy of Flygare[194] has also been shown to be quite powerful, and, for many molecules, a faster technique. The advantages of supersonic MBER will remain in the relative simplicity of spectra obtained for gas systems where many molecular moieties exist and, in conjunction with Campargue sources, the possible formation and study of very weakly bonded molecules, such as helium containing clusters. We feel that these criteria should be a guide in choosing systems to study for structural and binding information.

APPENDIX

THE MOLECULAR BEAM INTERFACE CONTROL

This appendix describes in some detail the programming required for the use of the molecular beam interface in phase modulated MBER experiments. The other aspects of the interface, namely its analog to digital converter and its rf mixer, will not be discussed here. A short sample program to drive the interface with an 8K PET is included at the end of this section. The current laboratory programs "Fast MBER" and "MBER" have this included in different forms. The interface was built and designed by the U. C. Berkeley Chemistry Department Electronics Shop.

The essential components of the circuit include a programmable chopping clock based on a constant 10 MHz input signal, a programmable gate (LS7474) and two 32 bit binary up counters (LS7060, with a counting rate of up to 10 MHz). The circuit is connected to a memory expansion board for a Commodore 8 K PET microcomputer which serves as the master controller. (A 32 K PET and compatible memory extension board may also be used. However, all the succeeding memory addresses indicated need to be incremented by 7168_{10}.) The PET may access these boards either through BASIC's POKE and PEEK commands or through direct machine language code. What follows is a description of the relevant memory addresses. All numbers, unless otherwise indicated, are given in base 10.

<u>28723 and 28727</u>. The two IO ports of the interface need to be designated by software as either 4 or 8 bit ports, and each subport needs to be designated either as input or output. In the MB interface the ports are each divided to four 8 bit subports with the first two

subports input and the third output with respect to the PET. At the start of a controlling program a value of 146 (92_{16}) must be sent to each address.

28722. The chopping frequency is input here by the user, using bits 0-5, with bits 0-2 determining the number of times the base chopping frequency of 1 MHz is halved, and bits 3-5 the number of times it is divided by 10. For example, to obtain a chopping rate of 5 Hz, enter 51_8 or 41 into this address, as 1 MHz $\div 10^5 \div 2^1 = 5$ Hz.

28726. Bits 2-7 are used here to control the gates and counters. Bit 7 (128) presets the counters before a measurement. Bit 6 communicates to the hardware of the interface that the software is ready for the counting to start, which will begin on the rising edge of a clock pulse and stop on another rising edge when instructed by sending a 0 to that bit. Bits 5 and 4 when on are "not load" instructions to counters 1 and 2, and are generally on in the normal step mode. When 0's are transmitted to them, the counters' output can then be accessed and their stored values are cleared. Bits 3 and 2 are used for scanning counters 1 and 2, respectively. Upon transmitting a 0 to bit 5 (or 4), the least significant 8 bits of the stored count in counter 1(2) is accessible from address 28720(28725). The next more significant 8 bits of counter 1(2) will be accessible upon the transmission of a 0 followed by a 1 to bit 3(2), and so on, until all 32 bits of the counter have been read.

28720 and 28725. These are the interface output addresses for the counters. Their use was described in the preceding paragraph. Counter 1 (28720) contains data measured when the clock pulse was high and the

rf signal was transmitted to the C field, and counter 2 when it was low and the rf blocked.

28724. This is an output address indicating the status of the counting gate and clock. Bit 4, when loaded with a 1 by the interface, indicates that the gate voltage is low and that counting is in progress. Its status should be verified immediately after starting a scan and before unloading the counters' results after a scan. The reverse is true with it reading 0. Bit 3 indicates whether the clock pulse is high (1) or low (0). Thus, in the software, a chosen number of up-down clock cycles can be designated for each counting scan before the scan is stopped and read.

In general, the timing sequence of a measurement involves clearing the counters, instructing the counters to run, wait for the gate signal to be low, count for the desired number of clock cycles, instruct the counter to not run, wait for the gate signal to be high, and then output the values of the counters. A sample program which does this follows. In typical MBER experiments, the C field rf frequency is incremented after each measuring cycle.

Program: Interface ... for the 8 K PET

```
  5    N = 4:  REM DESIRED NUMBER OF CLOCK PULSES PER SCAN
 10    POKE 28723, 146:  POKE 28727, 146
 20    POKE 28722, 41:  REM SELECT 5 HZ CHOPPING
 30    POKE 28726, 48 OR 128:  POKE 28726, 48:  REM RESET
 50    POKE 28726, 48 OR 64:  REM START COUNTING
 60    IF (PEEK (28724) AND 16) THEN 60:  REM WAIT UNTIL TEST GATE OPEN
 70    FOR I = 1 TO N
 80    WAIT 28724, 8:  WAIT 28724, 8, 8
 90    NEXT:  REM COUNT CLOCK PULSES
100    POKE 28726, 48:  REM STOP COUNTING
110    IF (PEEK (28724) AND 16) = 0 THEN 110:  REM WAIT UNTIL TEST GATE
         CLOSED
120    POKE 28726, 0:  POKE 28726, 48:  REM LOAD COUNTING LATCHES
130    C1 = 0:  C2 = 0:  FOR I = 0 TO 3:  REM READ COUNTERS
140    C1 = C1 + (PEEK (28720) * (256 ↑ I))
150    C2 = C2 + (PEEK (28725) * (256 ↑ I))
160    POKE 28726, 48 or 12:  POKE 28726, 48:  REM SCAN TO NEXT DIGIT
170    NEXT
180    PRINT C1, C2:  GO TO 30
```

NOTES and REFERENCES for CHAPTER II

1. Most of our MBER spectrometer was designed either by Professor John S. Winn or this author. The construction of the nonelectric parts of the apparatus was largely done by the University of California College of Chemistry Machine Shop, and most of that by George Webber.

2. J. B. Anderson, R. P. Andres, and J. B. Fenn, Adv. Chem. Phys. 10, 275 (1966).

3. 97.5% pure, Matheson Co. Delivery was handled with an 11-330 Matheson regulator, with stainless steel internal parts.

4. Ozark-Mahoney, Co. Delivery was handled with a B15-679 Matheson two-stage regulator with monel internal parts.

5. Matheson, research grade.

6. Mechanical drawings GC1 to GC11. (Referenced mechanical drawings are to be found in the files of J. S. Winn.)

7. Seven Nupro valves and a Granville-Phillips thousand turn leak valve for flow control.

8. U. S. Gauge 33022 (PSI resolution, up to 100 PSIG), Matheson 63-5601 (torr resolution to 760 t), and Varian Thermocouple gauge (micron resolution).

9. Initial lessons in the care and keeping of ClF were given by Dr. F. Tanzella. A monel sample cylinder was degreased with toluene and acetone and then dry heated in a nitrogen atmosphere. The ClF regulator[4] was fitted with one lead and several teflon gaskets. The line and cylinder were passivated for an hour and then evacuated before actually charging the sample cylinder. His laboratory was also equipped with the soda-lime traps to protect the pumps. Our typical handling scheme was somewhat less carefully treated. A single lead gasket is used in the regulator. As our gas cart is not in a vacuum hood, small line leaks are readily sensed when using ClF during passivation. For a tabulation of some of ClF's unhealthy properties, see closely related pamphlets on HF.

10. Mechanical drawings S045-2 and S087-1.

11. Utility pinholes, Ealing Co. (S. Natick, Mass.).

12. Nozzle orifice diameters typically used varied from 50 to 200 μ. The choice for a particularly sized nozzle is generally based on cooling considerations and on the conservation of the gas in the sample cylinder for a practical duration. The same considerations are used in choosing the source stagnation pressure.

13. The initial nozzle holder designed had a 60° conical opening. It was found that the restriction in available expansion space had adverse effects on the beam's adiabatic cooling, probably from local turbulence.

14. Mechanical drawing S088-1. The effect of an essentially 180° opening were quite good for cooling. This nozzle type should have probably been used somewhat more, but the flexibility of the pinholes caused it to remain mostly shelved.

15. Chromalox cartridge heaters, 100 watt, 120 volt. The manufacturer suggests that to acquire the highest temperatures, one wants to choose the heater to have a close circumferential fit and the lowest possible power surface density (watt/in.^{2}) in order to reduce the internal temperature gradient of the heaters, and, thereby, increase their lifetime and range.

16. Mechanical drawing S054-3.

17. F. Rosebury, Handbook of Electron Tube and Vacuum Techniques (Addison-Wesley Pub. Co., Reading, Mass., 1965) 525 ff.

18. The source can also be assembled without the copper cooling block by directly attaching the "push me- pull you" rod connector to the rear of the source can with shorter screws.

19. F. Rosebury, op. cit., 383

20. Mechanical drawings S052, S093, and S094.

21. Some drift of the center point of our first holder was noticed with time, leading to the development of the second holder. Its assembly is described in pages 3.9 to 3.11 in this author's laboratory notebook. Essentially, the tension of the knife edge piece is first set by two controlling screws, balanced so that the source will not wiggle too much, but can also slide easily. Its locating ring is then centered using crosshairs on the ring and the location of the source can nozzle in the knife-edge piece as a guide, and bolted to the knife edge piece.

22. Due to source wiggle, there is a possibility that the angle between the emerging beam axis and the spectrometer axis is nonzero and changes with the position of the source in the holder. This problem is of more significance with the second holder, as its knife edges are shorter.

23. Mechanical drawings S004-4, S035-4, and S049-3.

24. R. Campargue and A. Lebehot, Rarefied Gas Dynamics, 9, C.11 (1974).

25. Certainteed, Inc. Junctions and mating PVC flanges were connected with standard PVC solvent. The vacuum characteristics of this material have seemed quite adequate.

26. The gate valve should be placed so that it closes toward the PVC line if one wishes to maintain a vacuum in the source chamber with the booster pump off. Otherwise, the pressure in the source chamber rises to several hundred torr within minutes of valving and turning off the large pumps.

27. Kinney, Inc., KMBD1601 Mechanical Booster Pump and KT500 Triplex High Vacuum Pump. These were kindly lent to us by Prof. G. Pimentel. They had been used in a series of HF experiments, which had caused a considerable deposition of crud inside the backing pump, as well as a significant deficiency in performance. B. Hale and this author cleaned out the pump with kerosene and ethanol. Internal gaskets and the discharge valves were replaced, and considerable time was spent on the shaft seal, with much assistance from The Chemistry Machine Shop.

28. These pumps required power from a 3 phase 60 hertz 440 volt line. A 6 gallon/min water flow for cooling was supplied through a Hayes Sure-Flo water current regulator interlocked to the pumps control. The booster is also interlocked so as not to turn on at a pressure greater than 1 torr.

29. Specifications of the pumps suggest a 0.2 μ limit, which was unattainable by us. The greatest problem lied with the backer pump which at best could bring pressures to 400 μ.

30. Beam Dynamics, custom made to specifications of M. Maier. See also W. R. Gentry and C. F. Giese, Rev. Sci. Inst. 46, 104 (1975). Upon microscopic inspection chips were found on the interior surface of the machined skimmers, which were thought to be responsible for poor cooling characteristics in our expansion.

31. Mechanical drawing S028-4.

32. Varian VHS-6. Our diffusion pumps are interlocked for overheating, waterflow (via Hays Shur-Flo regulators) and over pressure in the foreline (via Varian 0531 TC Vacuum Gauges and NRC 810 meters).

33. Alcatel (ZM2030).

34. Either a Varian 0563-K2466-304 or an Electron Technology, Inc. #4336P. The gauge is in turn monitored with a Varian NRC 840 Ionization Gauge Control.

35. Initial design of this orifice involved 1/16" thick discs with 5, 10, and 100 mil drill-thrus. These were replaced with 1/32" flared out flanges with 10 and 25 mil drill-thrus, made to key into the shroud wall. Using one of the old skimmers greatly improved the measured beam intensity by reducing the local turbulence. The author acknowledges M. Maier's contribution here.

36. Properly adjusting this gate valve is somewhat difficult. As the higher pressure tends to be on the buffer side, it is unfortunate

that there was not sufficient room to have this valve on the other side of the wall. Upon opening and closing the valve, small pressure "bursts" are observed within the spectroscopy chamber, but have posed no problems.

37. For example, with a 400 μ nozzle, the source pressure is approximately (in μ) 40 + 15 * P_s (PSIG), where P_s is the stagnation pressure.

38. The typical skimmer-nozzle separation is on the order of 1 cm. With a 100 μ nozzle, the optimum beam signal for argon is found with the source can against the beam stop for any stagnation pressure less than 1 atm. At 20 PSIG, and 60 PSIG, the signal is optimized with the source ~0.05" and ~0.20" back. At greater pressures, no significant improvement is gained by further moving of the source. With a 400 μ nozzle, optimized source positions for 0, 20, and 60 PSIG are approximately at 0.40", 0.50", and 0.53" back from the source fully in, with little change in position for P_s > 20 PSIG. We have noticed that twisting the source can may change the measured beam intensity. Referring to this and to Note 22, it is difficult for us to know how much of this intensity peaking from the source nozzle position is due to expansion effects or due to alignment effects.

39. In one series of measurements, powerstat currents of 1/2, 1 and 1¼ corresponded to equilibrium source temperatures of 295, 365, and 420°C respectively. The time required for equilibration can be up to two hours.

40. When one initially tries cooling the source this way, there is an initial temperature increase at the source of about 2°C. The temperature then quickly drops at a rate up to -3°/min, taking less than an hour to get to -80°C. If one does not pump on the vent, but just leaves it open to the atmosphere, the cooling rate will not exceed -0.7°/min.

41. If an indium gasket has been used and the source has been heated, it may be necessary to either pry or torch the cooling copper block from the back of the source can.

42. Otherwise, the rod may be unscrewed.

43. Two particular warnings. First, remember to reinsert the cartridge heaters and check the thermocouple connection. Secondly, when sliding the source stand back toward the source-buffer snout, be careful not to pinch the flexible steel hose or ventline between the chambers. This has been found to be a fine way to generate leaks into the source chamber.

44. N. F. Ramsey, Molecular Beams (Oxford O.P., London, 1956), 115, 401; R. G. Luce and J. W. Trischka, J. Chem. Phys. 21, 105 (1953).

45. The A field rods have been shortened a couple of times because of spacing problems within the spectroscopic chamber. As will be seen, arcing has been the major difficulty in the development of our spectroscopic chamber.

46. Obtained from Leed Plastics. Macor is a glass, easily machined and cleaned, with very good dielectric properties. Teflon discs were tried but broke down quickly. When the A and B fields arc, it occurs primarily along the faces of the Macor discs, leaving "burned" brown streaks. These surface streaks have increased conductivity, so that the Macor needs to be lightly sanded occasionally.

47. Spellman FRM30 P1500 DX 826 Regulated Module Power Supplies. These were particularly chosen because of their specified ability to work when in a vacuum. With 24 VDC input, they draw $15 + 5 * V_o$ (kV) mA of current, where V_o is the outputted voltage.

48. The initial design had these power supplies mounted within the chamber. Considerable arcing occurred both outside each power supply, between the quadrupole rods and between some of the external circuitry, as well as within each power supply, although they were fully potted with RTV. Several methods of protecting the external circuitry were attempted, including the surrounding of all exposed metal ports, except for the field pieces themselves, with potting compound and with teflon sleeves. Zener diodes were added to protect the power supplies from burning out, which happened several times. The high voltage output cables, which had run through grommets mounted on the exterior metal box of the supplies, were redirected to come through the uncovered tops of the Spellman's to prevent arcing with the exterior casing. Besides the visible aspect of the arcs, this problem would also manifest itself in the intensity of the signal of a refocused beam. For example, in one experiment, tuning the A field to ~24 kV with a ClF beam gave a gradually enhanced signal. Further increasing the voltage, the refocus signal suddenly disappeared and could not be reattained until the power supply was turned off and then on again. It was eventually discovered that the internal and most of the external arcing problems disappeared if the power supplies were used in atmospheric conditions. Though the reason for this is not known, it has been suggested that under vacuum the Spellman's suffered either from problems associated with heat dissipation or with the internal pressure of some components. Much assistance on this problem was supplied by the Chemistry Electronic Shop.

49. The outer surfaces of these resistors need to be kept clean to prevent lower resistance electrical paths along the resistors' exteriors.

50. Our two feedthroughs tested satisfactorily to 30 kV after being left under ethanol in an ultrasonic cleaner for several hours. They were attached to the aluminum flange with epoxy.

51. A voltage following circuit, employing a 471 opamp, was designed to measure this high impedence signal. However, the opamps were destroyed each time the fields arced. As a result, the voltage is measured directly with a voltmeter which itself has a high enough internal impedence.

52. Mechanical drawing S096-3. The method of assembly is described on pages 3.29-3.30 of the author's laboratory notebook.

53. We have generally used a 0-30 kV probe with an internal impedance (R_I) of 600 MΩ. If one probes at a point beyond the current limiting 1 GΩ resistor that leads to the feedthrough, one needs to correct for the probes internal impedence via $V_o = V_n * (1 + 1\ G\Omega/R_i)$, where V_n is the indicated voltage and V_o the actual voltage. When testing the quadrupole voltage with the spectrometer chamber open, the rods will begin to arc at about 8 kV.

54. The high voltage connectors on the quadrupole rods have frequently fallen off the field rods due to vibrations from the pumps. When assembled, they need to be pushed quite firmly into their corresponding bores on the rods, and the cable connections need to be somewhat slack.

55. The flat construction was done by the Lawrence Berkeley Laboratory machine shop. The flats may deform temporarily with a temperature change, but should reflatten when they thermally equilibrate.

56. The actual spacing between the flats is determined from the analysis of MBER spectra of a known molecule, like OCS. This is described more fully in Chapter IV. We have determined this to be 0.991 cm. Paralleling the plates is done with an interference technique. A sodium arc lamp is placed behind one of the flats and the field is oriented until the images of the lamp become aligned. Diffraction fringes can then be seen about the lamp image. The teflon capped screws are then alternately tightened until the number of fringes has become minimized. Electrical connections are not made until after this process.

57. The effective spectroscopic region of the C field is in a 3/8" tall region about the vertical center line of the flats, along a 6" long path. 1" on each end of the C field serves as a buffer region so that molecules will not experience a resonant excitation while the dc field voltage it experiences is changing.

58. Thus, in the parallel mode, the rf and C field components are in the same direction, while in the parallel-perpendicular mode. These are rf field components both parallel and perpendicular to the dc field direction.

59. The gold on the surfaces of the C field flats can flake off very easily and should therefore always be treated with the greatest of respect. The silver paint serves not only to mechanically and electrically attach the gold wire to these surfaces, but whenever the C field happens to arc, it happens primarily at the silver paint and the paint flakes off, breaking the circuit and ceasing the arcing without damage to the gold surface.

60. Hewlett Packard 6110A dc Power Supply. It has been tested and shown to be stable to within 10 mV over an 8 min period. It does require about half an hour warm up time to attain a stable voltage. The actual operating range is limited to about 2 kV, as the C field arcs at stronger field strengths.

61. Fluke Differential Voltmeter Model 825AA1AG. The measured voltage is first passed through a 1:10 precision voltage divider to increase the effective measuring range. This voltmeter should always be left on.

62. HP3335A Synthesizer/Level Generator. The line width is ~0.001 Hz. The output voltage is referenced to a 50 Ω internal termination. This synthesizer has an IEEE interface and can be therefore controlled by our microcomputer system.

63. Amplifiers supplied by Lawrence Berkeley Laboratories. Together these can amplify an inputted rf signal by 40-50 times before they cease amplifying and just distort the waveform. These amplifiers are the source of the frequency dependence in the maximum attainable rf voltages.

64. Noise Generator DWG959A1, built by The Chemistry Department Electronics Shop. When used the noise signal should be introduced through the central BNC jack of the mixer on the molecular beam interface panel, whereas the rf input and output lines can be attached to either of the remaining jacks. When tuned to full amplitude, the mixer will broaden the inputted rf signal from 200 to 1500 kHz FWHM.

65. The actual rf power delivered to the region between the C field flats cannot be directly measured and can only be inferred from spectral results. This will be further discussed in Chapter IV. It has been found that there is a significant power drop (~90%) at 30-40 MHz due to some resonance within the C field circuitry.

66. Mechanical drawings S058-S063.

67. Mechanical drawings S076-S083. See also Reference 19. Dial indicators are mounted to the feedthroughs outside the chamber to note the positions of the buffer pieces. Calibration can be performed either with the source and buffer chambers removed and sighting the location of the buffer pieces with a cathetometer or, more roughly, by using a molecular beam in the closed apparatus. The motion of the pieces is controlled by exterior thinly threaded brass rods, which can easily freeze. Occasional spraying with a silicone based antifreezing agent is suggested.

68. Each buffer piece is placed in the spectrometer so that the end where the opposing knife edges are closest is on the side of the A or B field. The direction of the fields or the buffers should be the same as that of the dc field in the C field region.

69. Surplus chamber given to us by Prof. Y. T. Lee. The buffer and detector sides were remachined for alignment and compatibility with the rest of the apparatus.

70. In the initial design, a copper cold shield was bolted to this block inside the chamber to aid in maintaining a vacuum. However, the cooling of this shield proved to be very inefficient and has therefore no longer been used.

71. 6" Varian Cryo-Baffle Model # 0362-K1531-306.

72. Welch 1397 DuoSeal Vacuum Pump.

73. This pressure should not change when a beam is introduced. The effect of a leak in this chamber on a beam has been studied. As the stagnant pressure within this chamber increases the detected signal intensity of a full beam drops and that of a refocused beam drops somewhat faster. The percentage of a full beam occluded by a stopwire can drop from virtually 100% (for an appropriately sized stopwire and detector orifice) to 60% with a stagnant pressure of 10^{-5} t.

74. Mechanical drawing S019-3.

75. Facing these feedthroughs from inside the chamber, and considering the four arranged in a diamond configuration, the top pin corresponds to connection #5 on the C field, the lower to #4, the right to the A buffer field and the left to the B buffer field. The remaining, type N connector is for region #2 of the C field.

76. No collimator has been used here recently as the pressure differential between the spectroscopic and main chambers has not warranted it. As will be soon noted, in assembly the B field is made to emerge slightly through this port.

77. Here, as always when connecting chambers, do not forget the O-ring.

78. Before assembling the A and B fields, the rods and the Macor spacing discs should be degreased and rinsed with ethanol. We have then typically left these piece in an ultrasonic cleaner under ethanol for a few hours, followed by a period of drying in a vacuum oven. Fingerprints on the rods create wonderful new sites for arcing.

79. Until recently, this connector had a long high voltage cable running along the back of the spectrometer chamber which was then grounded to one of the A field sliders. This worked equally easily for the author.

80. Actually, the sliders do not slide very well, so that the B field is actually held above the bench until it is in position.

81. Check again that the high voltage connectors are still firmly on the rods. Be careful in the remaining assembly not to pull too hard on any B field cable.

82. One has to be careful that there is sufficient space between the focusing field pieces and neighboring pieces. Pump vibrations can cause the quadrupole rods to slide slightly, requiring that the high voltage cable be slack and that the connectors are firmly seated into the rods.

83. On both motion controls for the buffer fields, it is particularly important to have tightened those connections which hold rods perpendicular to the bench. If these become loose one can no longer move the buffer fields from the outside.

84. Hopefully it will rarely be necessary to clean the C field faces. The suggested method of removing oil from their faces is by dripping m-xylene down the surfaces and then rinsing lightly with ethanol.

85. The jack and cable for pin 5 are painted with red spots. Be careful when connecting and moving the C field not to let anything touch the inner flat faces and not to tear off the gold ribbon wires. Also, when connected, insure that the wires are not grounding to the BNC plugs.

86. This is noticed not only by beautiful lightening within the chamber, but by most electronic meters associated with detection jumping and occasional downing of the computer system.

87. R. Hawley, Vacuum 10, 310 (1960).

88. Due to the risk of damage if the spectroscopic chamber suddenly rises in pressure when the fields are on, it would be a good idea in the future to have the A, B and C field power supplies interlocked with the spectroscopic chamber's diffusion pump.

89. All of the experiments we have done to date have been done in the "flop out" mode, i.e., a transition is detected by a drop in the intensity of the measured beam. An alternate method would be to have the beam detector slightly off axis and look for an increase of beam strength from a transition, where the B field defocuses the newly created negative Stark state molecules from the beam axis. This "flop in" method has better signal-to-noise characteristics in principle, but requires a detector more sensitive than ours when dealing with radially symmetric focusing fields.

90. R. Weiss, Rev. of Sci. Inst. 32, 397 (1961).

91. For other commonly used ionizer designs, see, for example, G. O. Brink, Rev. Sci. Inst. 37, 857 (1966); Y. T. Lee, J. D. McDonald, P. R. LeBreton, and D. R. Herschbach, Rev. Sci. Inst. 40, 1402 (1969); R. W. Bickes, Jr. and R. B. Bernstein, Rev. Sci. Inst. 41, 759 (1970).

92. See also Mechanical Drawings D048-D064. B. Hale and S. Sherrow made many significant contributions to the present design of this ionizer.

93. Thoriation reduces the work function of tungsten, allowing a particular electron emission current at lower filament temperatures. See, for example, H. A. Jones and I. Langmuir, General Electric Review 30, 310 (1927).

94. The steady-state temperature of a resistive element of resistance R with a current I flowing through it is proportional to the power P of the circuit, which is given by I^2R. Thus, to minimize the required current for electron emission, the filament is made thin and narrow to increase its resistance.

95. The initial design of our ionizer called for one of these posts to be spring mounted to keep a fixed tension on the filament while the ionizer elements moved in response to the required high operating temperature. Unfortunately, the spring lost its elasticity under these conditions, so that this feature is not extant.

96. Spotwelding of tungsten to molybdenum, as with the filament and grid, require intermediate strips of tantalum foil to make mechanically strong connections. Typically, if the ionizer is not allowed to overheat, the spotwelds holding on the filament strengthen with time.

97. Due to the metal's expansion at elevated temperatures, the holes on the ionizer pieces for the support rods drift relative to each other. Before these holes were enlarged, the brittle alumina rods would be snapped by this motion, particularly at the steel support bars. Also, pyrex spacing washers were initially used, but were found to melt and fuse to the rods at our temperatures.

98. A third lens piece between what is now lens 2 and the ionizer was once used, with a cylinder outer diameter that allowed it to be placed somewhat within the ionizing region to improve ion extraction. However, many of the ions were found to be extracted to the walls of this piece, so it was removed to improve detection efficiency. Also note that the focusing effect of these lens cylinders actually occurs in the region between them.

99. Portions of several steel wires which were initially used in place of these nickel strips were vaporized when the ionizer was first used. Spotwelds do not work well for these strips, so they are hole-punched on one end to be fitted over the back ends of the filament posts, and on the other end to have a small screw with washers and a nut sandwich each pair of strips about their respective connecting pins. Before their first use, the nickel strips were cleaned as according to F. Rosebury, op. cit., 14.

100. Tantalum foil shrouds are spotwelded over the connections to the plate and grid to help maintain the connection.

101. Looking down on the assembled ionizer with the lenses toward the observer, the large pin furthest to the right and in the rear is connected to the split filament post, the next one (in the front) to the other filament post, the next one to the grid, and the last large pin to the plate. When appropriately connected to the wires along the detector shaft, then the four sockets on the high current feedthrough flange mounted on the upper part of the shaft, starting from the top socket and going clockwise, correspond to the grid (A), the split, upstream filament post (B), the downstream filament post (C) and the plate (D). Again looking at the ionizer, the pin to the far left is connected to the upstream

lens piece (lens 1), and the pin forward and to the right is connected to lens 2. Again, when all electric connections are made, these correspond to wires #5 and #4 respectively on the seven-wire feedthrough mounted to the upper part of the detector shaft.

102. N.J.E. Model 5Y36-20, 0-36 V, 0-20 Amp.

103. Lambda Regulated P.S. Model 71, 0-500 V, 0-200 mA.

104. Power Designs Pacific, Inc., High Voltage Regulated D.C. Power Supply, 1-3000 V, 20 mA. Presently only works from 0- -1000 V, due to the voltage breakdown limits of feedthroughs.

105. Powered from our lens panel, described in a later section.

106. See for example, Dawson and Whetten, Adv. Electronics and Elect. Phys. 27, 59 (1969).

107. Extranuclear Laboratories, Inc. ELFS Quadrupole 9.5 mm x 20 cm Model #4-162-8, with the associated Quadrupole Control and Radio-frequency Power Source, and High Q Head Models 011-13 and 15. See the manufacturer-supplied operating manuals for a detailed account of characteristics, assembly and usage.

108. Mechanical Drawing D034-4 for detector layout, and drawings D022, 28, 31-33, and 39 for parts.

109. Badly split mass spectral peaks that we originally obtained were partially due to a slight misalignment between the mass filter and ionizer axes, which this aligning piece corrected.

110. Extranuclear Laboratories, Inc. Particle Multiplier Model # 051-5. See the manual for a detailed description.

111. The Faraday plate cannot be allowed to float electrically , as a defocusing space change develops on its surface, greatly reducing the overall detection efficiency.

112. To reduce mutual interference between the mass filter's rf current and other detection related electrical lines, the rf power source is mounted above our main chamber, about 4' from the hi Q head. The hi Q head is mounted on a wooden platform on top of the detector shaft directly above the QMS electric feedthroughs to minimize the required length of cabling from the head to the quadrupoles, thereby minimizing the line impedance. This impedance determines the upper limit of the detectable mass to charge ratio for a given hiQ head.

113. The QMS, Faraday plate, particle multiplier voltage delivery and signal cables within the main chamber are coaxial with the outer insulation removed. The shielding of the former three are internally grounded to the detector housing.

114. Supplied from a sawtooth generator (DWG 930 AI) built by the Chemistry Electronics Shop.

115. -3.2 kV has been found to be about the optimal voltage for operating the particle multiplier. Working at significantly more negative voltages has caused arcing between the dynodes, both damaging them and the opamps within the detecting electrometer.

116. Extranuclear Laboratories, Inc. Preamp Electrometer Model 031-3. The power supply included puts out from -5 to +5 kV.

117. See Extranuclear Laboratories, Inc., Triax Flanges Models #062-1 and the associated manual.

118. Facing the external face of the rear detector flange, the BNC jack under the window is the triax connection for the detector signal and particle multiplier floating voltage. The larger pin to its left is connected to the first multiplier dynode, and the pin to its right to the Faraday plate.

119. Mechanical drawings M004-M011.

120. Mechanical drawings M002, M003, and M030.

121. This box was built by Allied Engineering Corp, Alameda, CA. It sits on a steel frame (drawing M001) roughly 46" off the laboratory floor. All other chambers are on stands to match the designed beam axis of this chamber to be 60" above the floor.

122. Many of the characteristics of the main box were designed for future experiments involving crossed molecular beam work and differential scattering measurements. J. Winn's design for this chamber was adapted from the design of a mirror image chamber of Y. T. Lee, J. D. McDonald, P. R. LeBreton and D. R. Herschbach, Rev. Sci. Inst. 40, 1402 (1969).

123. A chain operated mechanical hoist is used in removing this door from the box. The pulley mechanism rides on an I-beam appropriately connected to the laboratory's ceiling and running parallel to the molecular beam axis along most of the MBER apparatus. A three hooked adapter is fit on the hoist's larger hook when it is used to lift the main box door, the detector chamber insert or rotating lid. The hoist is also used in the removal of the spectroscopic chamber door.

124. This side of the main box has been used for cluster photoionization and other experiments by B. Hale. A separation chamber has been built which can be mounted within the box from the inside of this 10" port and which can be independently pumped on through a gate-valve and cold trap by a 6" diffusion pump[32] mounted to the bottom of the box. This pump shares the backing pump and controls of the 6" pump on the spectroscopic chamber, so that only one of these should be used concurrently.

125. The cold wall was adapted from one given to us by Y. T. Lee. It has not been found particularly useful for MBER experiments, as the beam does not travel far in the main chamber region.

126. Varian 10" NRC Diffusion Pump. See also Note #32. Fittings for a thermocouple pressure gauge and for venting the main chamber are on the 10" DP foreline.

127. One blank flange, typically one covering a 4" port on the right wall, is left loose to serve as a safety release for the main chamber when venting with a positive pressure of N_2. Given no other safety valve, the rotating lid will, as it has, lift off the main box and serve as a vent.

128. Fluorocarbon Co., Tec Rings (2) #A00487A and Keene Corp., Reali-Slim Ball Bearing 25.000" bore KG250XPO.

129. Mechanical drawings D009-D026 and D040-D042. The wheel is also supplied with a windowed aperture. It was initially hoped that with the wheel in a closed position that the vacuum within the detector chamber could be maintained when the main chamber was vented. This has not been found to be the case. Early problems were caused by the aperture wheel freezing in place when the chamber was in operation. These were eventually solved by flattening sides of appropriate pinions where they were coupled to gears and by shimming between the lid shaft and parts of the wheel driving assembly to relieve tension on the wheel. Electrical digital indicators are also attached to the wheel apparatus, originally to indicate externally the position of the wheel without actual visual inspection. These have been of questionable value to this author.

130. These pins are housed by a metal box. The QMS cables from the Hi-Q head pass through grommets on this box and connect to two of the pins. The other pins are shielded from the QMS pins and are connected to MHV connectors on the side of the junction box, to one of which the particle multiplier voltage is supplied when detecting positive ions.

131. Both the detector arm to lid shaft and the bottom plate to lid shaft junctions were originally to be sealed with indium gaskets. However, due to the relatively frequent necessity of accessing the detector chamber during the apparatus' development period, these gaskets have not been used.

132. Mechanical drawings D001-D008.

133. Perkin - Elmer Ultek D-I Pumps, Model 207-0060. These are each operated by a P-E Ultek 350 mA Ion Pump Control Dual Voltage, Model 222-0520.

134. Parts of the ionizer fall apart much more readily if it is operated without lN_2 cooling.

135. All conflat seals require the use of a clean copper gasket. Bolts should be tightened in a "starwise" manner to allow a good seal.

136. The location of these holes was determined with the ionizer liquid nitrogen trap full so that they would be concentric to the beam axis under operating conditions. This region moves up a few mm when the chamber is cooled. Thus, aside from the reason in Note 133, the detector trap needs to be filled just to have the detector aligned with the beam.

137. There is an alternate assembly of the detector-region for other types of experiments where the ionizer is not required. The detector shaft is removed and part of the detector arm can is also taken off. In this arrangement, when the arm is fastened to the lid shaft, the mass filter sits largely within the shaft. The 10" conflat surface on top of the lid shaft is covered with a 10" to 8" conflat adapter and one of the ion pumps.

138. Briefly, for negative ion detection we used an Extranuclear Laboratory, Inc., Neg/Pos Ion Current Preamplifier 0324, which was mounted on the wooden platform on top of the detector shaft next to the Hi-Q head. A high positive voltage for the particle multiplier, about 1½ times the magnitude of the negative voltage used for positive ion detection, is required and was supplied by the detection electrometer.[116] The MHV jack normally attached to the particle multiplier voltage supply is now grounded through a 10 MΩ resistor. The voltage is supplied to the Neg/Pos preamp and passed to the multiplier through the shielding of the signal cable running from the preamp to the triax flange. The ion current signal is referenced to the particle multiplier voltage. Details on hookups for analog and pulse counting techniques for negative ions are given in the triax flange Extranuclear manual. Ideally, the spacing between the grid and plate in the ionizer should narrow in the direction of the beam to improve space-charge effects, and the polarities of the lenses, Faraday plate and QMS float should be reversed. When, in fact, all this was attempted for observing negative ion fragments of SF_6, which were seen for a brief period, something (?) arced in the multiplier, destroying several opamps in the electrometer. Negative ion detection has not been reattempted.

139. Extranuclear Laboratory Preamp 032-5. Because of the high internal impedance of the unamplified anode signal, it is important that the preamp be close to the triax connection.

140. Besides affecting the electrometer sensitivity, the choice of input resistance also affects the detection maximum frequency response. Specifically, the 10^7 Ω input resistor allows a maximum frequency response of 2 kHz and the 10^9 Ω resistor one of 20 Hz. This should be an important consideration when choosing a chopping rate for an MBER experiment.

141. Hewlett-Packard 7044A X-Y Recorder.

142. Molecular Beam Interface 956AI. This panel was built by the Chemistry Department Electronics Shop.

143. The circuit is based on a LM331 National Semiconductor Voltage to Frequency chip, following their "precision" circuit (p. 8-162 in their catalog). The conversion goes as 93 kHz output per volt input with a maximum output at 100 kHz. The outputted pulses are TTL with an approximate 25 μsec width.

144. Commodore PET Computer Model 2001. 8 K memory.

145. The original interface was built with a single up-down counter. Problems occurred resulting with spurious bits being triggered, requiring signal filtering and other now unnecessary data handling techniques.

146. Typically, Extranuclear Laboratories, Inc. Preamp Counting Head #032-3.

147. The discriminator generally requires a warming up period. The optimal dial setting has been found to be about 1.26. Lower settings allow through much noise, while higher settings begin filtering out true signal. The "DC Out" jack of the discriminator can be connected to the preamp and electrometer for simultaneous analog measurements.

148. The lens panel can power up to five devices. Of the two columns of front panel banana plug sockets, the top five jacks on the left are for cables leading to the devices. The matching jacks on the right are to be jumped to one of the lower six jacks depending upon whether the corresponding device requires a positive or negative potential. The magnitude of the delivered potential is fixed by the setting of a corresponding 10 turn 500 KΩ potentiometer. The jacks on the left of the panel can be connected to a voltmeter to measure the delivered voltage to a particular device, with the appropriate setting of the function switch near those jacks. The panel is powered by two power supplies (Lambda Regulated P.S. C-481 and 28).

149. This plan was prompted by the event of the author once trying to remove an ionizer from the detector while voltage biases were being applied to the lenses, and another occasion where the author vented the main chamber while the particle multiplier was still charged, thereby essentially destroying the multiplier. One does learn, eventually.

150. Among the more disturbing effects of a focusing field arcing is the possible loss of control over the PET or the interface, which can only be regained by turning off and then restarting the device. This is normally accompanied by a loss of collected data and time.

151. Commodore PET-CBM Computer Model 2001, 32 K; Hewlett-Packard Plotter-Printer Model 7245A; CBM Tractor Printer Model 2022; and CBM Dual Drive Floppy Model 8050.

152. For a detailed description for the insertion of the lid and detector shaft, see the author's laboratory notebooks, p. 1.55-59 and 1.72-3. For other assemblies, refer to J. Winn.

153. T. E. Hanley, JAP 19, 583 (1948). (Thoria compounds supplied respectively by Alfa Products and Mallinckrodt.) It is convenient to make and store this solution in a 180 ml electrolytic beaker. The solution, or rather the colloidal suspension, should be well stirred just before use, but not during the cataphoresis process, as spotting on the filament will result. The suspension should be stored covered.

154. See note 95. Presently, the retaining nut on the split post can not be tightened to the supporting plate without a spring. Therefore, there is a little play in the position of this post in the assembled ionizer.

155. Occasionally the ionizer has been assembled with broken long alumina rods. The breaks then need to be strategically located so as not to significantly weaken the ionizer structure.

156. Short alumina rods have been used threaded through the remaining holes on the two lenses and the bracket. These are optional.

157. What is easily said in one sentence is often quite hard to do. Extra hands may or may not be helpful here. What is important is that the posts and the tantalum pieces be thoroughly degreased and clean. If the first few attempts at spotwelding are not successful, take a moment to polish off burn spots before continuing.

158. This can also be tricky. If the first few times the ionizer has been raised it has not been threaded through the housing holes, recheck your orientation. Furthermore, wires may become disconnected when the ionizer has been bumped around, so after a few unsuccessful attempts, recheck for electric continuity.

159. The 1/3 hp pumps assigned for the gas cart and rotating lid are generally left on and pumping those regions. The source blower and backing pump are left off to reduce wear when they are not in use.

160. Generally it takes 45 min of mechanical pumping for the pressure in the main chamber to be low enough so that there will not be pressure surges in its diffusion pump foreline after it has been turned on. The diffusion pump interlocks[32] should be set to "OPERATE" mode, and the pressure relays to about 150 μ. Failure to do so can and has had catastrophic effects if something should malfunction such as a cooling water line or a backing mechanical pump, causing decomposed diffusion pump oil to be deposited over the interior of the apparatus. Periodic inspection of the interlock panels' light switches and replacement of burnt out bulbs are strongly encouraged.

161. After recent venting, a filament generally requires about 15 hrs of operation time to remove the effects of recent atmospheric exposure. These effects include nonsteady emission currents and a higher required operating temperature. Particularly a new filament will require at least twice this time and the initial mass spectra will show large background peaks of standard atmospheric gases as well as of sodium and potassium (23 and 39 amu). The time for filament conditioning can be shortened by running currents larger than 5 A through it, i.e., running it at a higher temperature, but then the detector cold trap should be filled.

162. This procedure is to allow both for adequate cooling of the detector and conservation of l-N_2, the former being the more important. If the vent line does not frost exteriorly within 15 min of pumping, it may be blocked on the inside by frozen water. In that event, blow out as much as possible the l-N_2 that has already been poured into the trap, and then heat the vent line with, for example, a hot air gun, while still pumping on the line until it clears.

163. This is for ionizer protection, beam alignment (see note 136) and better pumping. If the trap runs low during operation, the beam signal will typically drop and background peaks particularly at 28 (N_2) and 44 (CO_2) amu grow in.

164. Particularly with a new filament, a fast temperature increase can either cause it to buckle and short to the grid or even cause it to become disconnected.

165. A few experienced ionizer problems and their symptoms are mentioned here. If there is no current passing through the filament when the filament power supply indicates a voltage drop, either the filament has become internally disconnected or you have forgotten to plug the output of the power supply to the high current feedthrough above the chamber lid. If the filament current is positive with no voltage drop across it, it has fallen off and shorted to ground. If the filament shorts to the grid, a current surge will pass through the grid power supply and trip it off if it is set to a nonnegative voltage. This problem may not require ionizer removal, for the filament may unshort itself if it is allowed to cool, and shorting may be avoided if the filament is heated more gradually the next time. If there is emission current but the grid or the plate voltage has no effect, one of these is disconnected. Finally, if there is emission current but no mass spectra are produceable, the filament may be in contact with a Pierce electrode or in some other way misaligned.

166. See note 107. Currently, the high calibration is set to 2.89 and the low to 0.00. With this tuning, the numbers on the mass tuning knob and the low mass knob for mass spectral sweeps correspond to 1/40 of the QMS passed mass fragment. For example, the 40 amu peak for Ar^+ is passed at a setting of 1.00 on the manual mass knob. If the rf or dc balance meter reads far from 0, the QMS

either needs rebalancing or there may be a short along the power cables. If good resolution is unattainable from the QMC control, the coarse resolution control on the HiQ head may need readjustment.

167. See notes 115 and 116 for the manual reference for the zeroing method and a warning on particle multiplier settings. If the electrometer does not zero, the electrometer may need replacing of its Zeltex 13303 operational amplifier. If while turning up the particle multiplier the electrometer behaves erratically with a 10^5 input resistor setting, the signal cable shielding may be disconnected from the triax connection or may just not be referenced correctly to ground.

168. We have generally used Ar at 20 PSIG source pressure for tuning. With a new filament, however, there may be interference in the mass spectrum from a background peak at 39 amu from K.

169. The points along the beam path to check include that all relevant gas cart valves are open, the source can is held correctly by its knife edge holder, the pressures in the source, buffer and spectroscopic chambers are appropriate, the buffer-spectrometer gate valve is open, the buffer fields and stopwires are not blocking the axis, no cables are obviously blocking the beam in the spectroscopy chamber, the detector aperture wheel is correctly opened and the lid is in correct orientation. Source operation can be checked by noting the effect of a source gas load on the buffer chamber pressure. Use the QMS to check for background peaks to insure that the detector is working.

170. The best lid orientation is generally near 180.5°.

171. Besides the K and Na peaks mentioned, thorium peaks can become quite evident and large if the filament current is greater than 15 A. These include Th^{+n} peaks at 232, 116, 77 1/3, 58, 46.4 and on to $n = 10$, and a ThO^{++} peak at 124.

172. The plate current becomes greater than the grid current when the plate's voltage is still roughly 50 V less than that of the grid. A little time should be spent finding the best settings for these electrodes for a given filament current. Fixing either the plate or grid voltage and just adjusting the other will always produce a local maximum in detector signal, but much improvement may be possible. Certain otherwise optimal settings produce a beating (on the order of 60 Hz) in the detector signal which are likely due to a space charge oscillation within the ionizer. In such cases, the grid and plate need to be slightly detuned.

173. For electrical hookups, the "Output Sync" and "Output" jacks of the sawtooth generator can be attached to the trigger input of an oscilloscope and the X drive of an XY recorder respectively. The Y inputs of both of these devices have been connected to the 1000 mV output in back of the electrometer. A rear connection is made between the sawtooth output and the QMS control ramp input.

For single peak scanning during tuning, the sawtooth is set for 0.1 sec/sweep, the QMS scan width at ~0.2 and the low mass at ~0.96 (for Ar). The scope signal time constant is controlled by the scope knob on the electrometer. The 10^9 Ω input resistance cannot be used at this scanning rate. For mass spectra recordings, slower scan rates are used, the QMS scan width is increased (5.4 ~ 120 amus, 8.0 ~ 160 amus), and the low mass is readjusted appropriately. With the QMS control in the "Sweep" mode, the sawtooth can also be used to tune individual mass peaks with it in the "DC" mode. This is often useful for peak identification purposes as well as giving an alternate means of sitting at a particular mass for MBER experiments.

174. It has been observed that all the components of a particular beam are optimized with a single nozzle to skimmer separation.

175. Suggested stopwire diameters for the various detector orifices are (all dimensions in cm) 0.185 for the 0.380 (0.15") orifice, 0.133 for the 0.253 (0.10"), 0.09 for the 0.151, 0.06 for 0.074, and 0.04 for the 0.049 orifice. See also note 73.

176. If no refocusing is seen, either something is wrong with one of the fields, you are attempting to refocus a molecule which is not polar enough for its mass and rotational constant, or the beam is rotationally too cold to have a significant population in a refocusable state.

177. The buffers and the C field dc voltage have on occasion been found to effect total refocusing up to 20%.

178. "Synthesizer Sweep" was written by J. Winn. As our RF synthesizer[62] is equipped with an IEEE bus line, it can be addressed and controlled by a PET microcomputer. Options of this program include sweeping over a desired frequency range at a selected rate, chopping the rf output between two different frequencies and "dither" sweeping over a particular frequency range, i.e., have the outputted frequency oscillate quickly about a slowly increasing central frequency to allow artificial band broadening. This program is used in conjunction with an XY plotter, with its X direction controlled either by its internal time base or by a voltage ramp outputted by the rf synthesizer.

179. "Fast MBER", written by J. Winn, drives the interface and the rf synthesizer at selected chopping and scanning rates and stores the digitized difference signals in up to 200 channels of memory per spectrum. The control addresses for the interface and a rough description of the operation of this program and its forebearer "MBER" are left for this chapter's appendix. The collected data can be stored on tape or transmitted through the controlling PET's user port to a 32 K PET running the "ER Output" program which in turn can transmit them to disc or tape storage, massage the data and plot spectra over our HP printer-plotter.[151]

Choice between modes of detection is dependent upon the signal-to-noise requirements and time duration desired for the spectrum. It should be remembered that chopping the rf with the interface reduces its amplitude by about 50%, and so a correspondingly longer scanning time is required to get the magnitude of signal obtained in more direct scanning.

The upper limit for reasonable chopping rates is determined by the time delay of a molecule undergoing a transition in the C field and its being detected. This delay stems both from the flight time of the molecule and electronic response time. Chopping at 10 Hz in one experiment lost about 10% of the transition signal to the background measurement because of this phase problem.

180. One should use an oscilloscope to monitor the final rf signal going to the C field, both to make sure it is there and to measure its amplitude.

181. It is, of course, advisable to have a very good idea of where to look. There are so many other parameters involved with the MBER apparatus that finding a new transition is in itself an artform. As of this writing no unknown transitions have yet been found on our machine.

182. As will be discussed in Chapter IV, the transition intensity and line shape depend in a nontrivial manner on the rf amplitude.

183. Or you may spend an extra 20 minutes next time trying to find a beam signal.

184. Leaving the filament on will help boil out the N_2. It has been found by some that blowing out the detector trap after each experimental run helps prevent ice blockage in the vent line. The ion pumps and diffusion pumps can be turned off while the trap is warming.

185. As much of the detector electronics are interlocked with the ion pumps, turning off the pumps turns off those power supplies. However, it is probably not a good policy, and for some power supplies definitely not good to activate these devices at nonzero voltages.

186. Spectrum #1, 12/12/79: This was taken (by B. Hale) with three lenses in the ionizer and a freely floating Faraday plate. Settings were filament: 22A, plate:97 V (24 mA), grid:113 V (18 mA), lens 1:42 V, lens 2:-38 V, lens 3:-255 V, QMS float:72 V, resolution:4.00, ΔM:3.4. (In notes, lenses are numbered from the downstream end.)

187. Performed by M. Maier. Results to be published.

188. Other detector conditions include filament: 16.5 A, plate:138 V (20 mA), grid:149 V (22 mA), lens 1:66 V, lens 2:-1 V, QMS float: 5 V, Faraday plate:157, resolution:2.93, ΔM:3.7, particle multiplier:-3.4 kV. Our three lens ionizer, under similar conditions, had an efficiency $\varepsilon = 3.8 \times 10^{-6}$.

189. K. Bowen, Ph.D. Thesis, Harvard University (1980). As an aside this document is a good source for relevant references to MBER and cluster formation, as well as for presenting all the characteristics of the Harvard MBER apparatus.

190. Spectrum #7, 9/15/79. The Ar_2^+ peak is 16 nA. All cluster peaks disappear when the beam is blocked, while there remain residual Ar^+(40) and Ar^{++}(20) peaks, illustrating that these clusters require a direct path to the detector.

191. Spectra #2-4, 12/18/79.

192. Spectrum #7, 1/12/79. Ionizer conditions: filament:22 A, grid: 138 V, plate:170 V, lens 1:-142, lens 2:25, lens 3:-250, float: 100 V, resolution:4.41, ΔM:3, particle multiplier:-3.5 kV.

193. From spectra #13-19, 2/26/80; #17-24, 3/26/80; and #2-8, 314/80. Due to day to day fluctuations in signal intensity, direct quantitative comparisons between different sets of data are of limited value.

194. T. J. Balle and W. H. Flygare, Rev. Sci. Inst. 52, 33 (1981); E. J. Campbell, L. W. Buxton, T. J. Balle, and W. H. Flygare, J. Chem. Phys. 74, 813 (1981).

CHAPTER III

STARK FOCUSING OF A MOLECULAR BEAM OF LINEAR POLAR MOLECULES

The process of deflecting neutral polar molecules with inhomogeneous electrostatic fields, briefly described in Chapter I, is useful to understand more quantitatively for several reasons. Our first purpose was to aid in the interpretation of the resonance spectra line shapes to be discussed in detail in the following chapter. Such an analysis was done by Dyke, et al.[1] on a beam of HCN, but the effect on their beam's initial velocity distribution by the focusing fields was neglected.[2] Stark focusing treats a molecular beam's transverse velocity, longitudinal velocity and rotational distributions in separate ways, so that the analysis of the refocusing properties of such a beam can probe these distributions[3,4] and test for their mutual dependence. Numerical simulations of refocusing can also be used to improve the design characteristics of an MBER apparatus[5] and aid in troubleshooting an existing spectrometer. Finally, deflection experiments alone have been used to determine dipole moment magnitudes and give some structural information of molecules,[6,7] a purpose which will not be discussed further in this thesis. In this chapter a series of experiments involving the measuring of refocused beam signals on our MBER spectrometer as functions of the source conditions and the focusing fields' voltages will be discussed. A numerical simulation model is first developed however, to predict the experimental results and aid in their analysis.

The process of polar molecule focusing[8] and approaches for analyzing individual trajectories have been discussed elsewhere.[9,10] Toennies, et al.[3] have done rotational temperature studies by seeding CsF in a Xe

beam and simulated the anticipated refocusing as a function of their field voltage. They used Gaussians for the individual rotational states, and both Monte Carlo and convolution techniques to introduce the beam's velocity distribution. A sophisticated graphical simulation technique was used by English and Gallagher,[5] involving a phase space approach to the beam molecule ensemble and following this "cloud's" deformation through an MBER arrangement. In the section that follows, our theoretical treatment will be presented in some detail. The Stark focusing quantum mechanical effect and various approximations will be discussed, followed by a review on supersonic molecular beam distributions mixed with a few changes from the standard perspective, and that followed by a summary of our numerical treatment. The next section presents some of our more interesting numerical results. Experimental results from the focusing of various linear molecules are presented in this section as well with special emphasis on OCS studies. The beam properties indicated by a comparison of these results and other MBER focusing phenomena will then be elaborated.

A. Theory

1. The Stark Effect

In classical mechanics the energy of an electric dipole, $\underset{\sim}{\mu}$, in a vector electric field $\underset{\sim}{E}$ is given by

$$E = -\underset{\sim}{\mu} \cdot \underset{\sim}{E}. \tag{3.1}$$

If the dipole is held stationary, the direction of the dipole with respect to the field determines the sign of this energy, and its magnitude increases with an increase in the magnitude of the field, $(\equiv|\underset{\sim}{E}|)$. Molecular dipoles, however, are not stationary and rotate with the

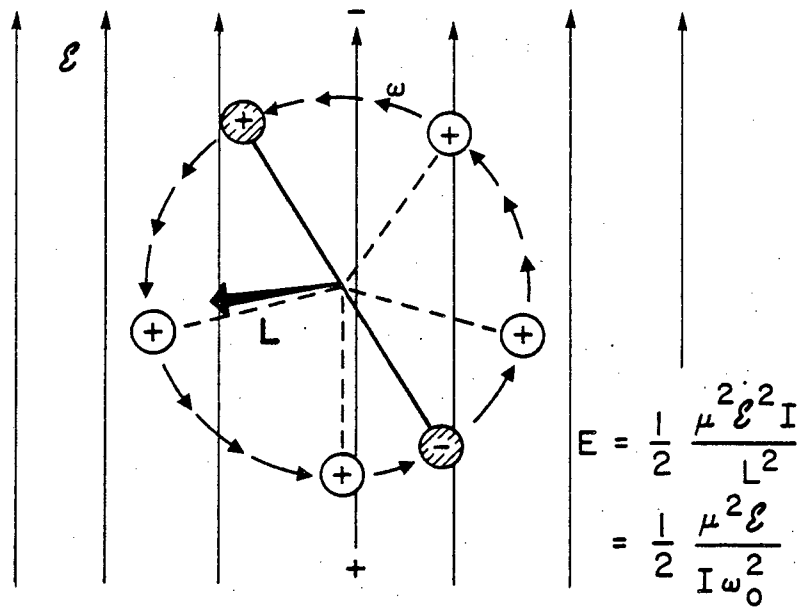

a) Angular momentum (L) perpendicular to the electric field ($\mathcal{E}$).

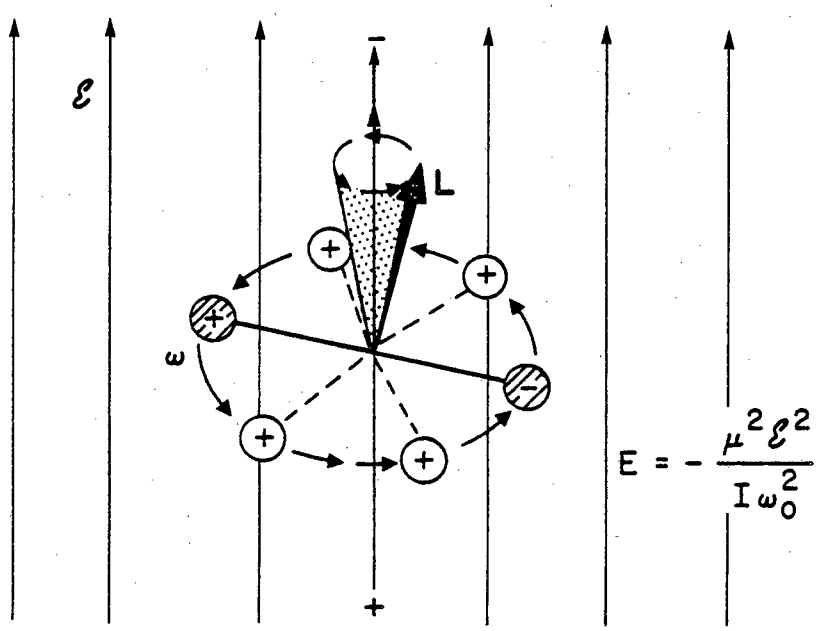

b) Angular momentum parallel to the electric field.

XBL 829-11551

Figure 3.1. Motion of a linear dipole in an electric field.

molecule. A freely rotating nonlinear molecule can generally have components of $\underset{\sim}{\mu}$ remain fixed with respect to $\underset{\sim}{E}$. A symmetric top's interaction with a field is largely first order in $\underset{\sim}{E}$, while an asymmetric top molecule has first order components. Linear molecules, however, rotate about an axis perpendicular to their $\underset{\sim}{\mu}$, so that the time averaged value of $\underset{\sim}{\mu}$ for an unperturbed rotation is zero. Classically, the effect of the field on a linear molecule must come from a perturbation of its rotational motion. If, for example, a molecule is rotating such that its angular momentum vector is perpendicular to $\underset{\sim}{E}$ (Fig. 3.1a), the molecule will rotate faster as its positive and negative ends are attracted toward the negative and positive directions of the field, respectively, and decelerate as the continued rotation brings the dipole into opposition with the field. Thus, on the average, the dipole spends more time in opposition to $\underset{\sim}{E}$ than not, and the dipole's potential energy will increase if the field's magnitude is increased. For the other extreme, if the molecule's rotational axis is parallel to $\underset{\sim}{E}$ (Fig. 3.1b), the field will exert a torque on the rotating dipole causing its rotational axis to precess at some small angle about the field direction so that the negative and positive ends are marginally twisted toward the positive and negative field directions. As the dipole is somewhat aligned with the field, the potential energy by (1) is negative. In both of these cases the amount of perturbation to the rotating motion caused by $\underset{\sim}{E}$ is proportional to its magnitude, E, so that the effective $\underset{\sim}{\mu}$, i.e., the dipole's time averaged value, is also proportional to E, and then the potential energy E, by (1), is proportional to E^2. It can be shown generally[11] that for a linear molecule with moment of inertia I, a permanent dipole μ (i.e., the dipole that would be measured in a frame rotating with the molecule),

rotating with an angular momentum L with its axis of rotation at an angle ϕ to an electric field $\underset{\sim}{E}$, the classical potential energy expression is

$$E = \frac{\mu^2 E^2 I}{2L^2} (3 \cos^2\phi - 1) \tag{3.2}$$

with this order of perturbation to the rotator's motion.

The quantum mechanical aspect of the Stark effect has been discussed several places,[9,10,12] and a short review of wavefunctions, Hamiltonians and basis sets is left for the next chapter. The Hamiltonian for a linear rigid rotor unperturbed by an external field is given by

$$\hat{\mathcal{H}}^0 = B \, \hat{\underset{\sim}{J}}^2 \tag{3.3}$$

where $\hat{\underset{\sim}{J}}$ is the total angular momentum operator, and B the molecule's rotational constant, given by

$$B = \frac{h}{8\pi^2 I} , \tag{3.4}$$

with I the rotor's moment of inertia. Restricting our attention to molecules with only nuclear orbital angular momentum, the allowed energies, i.e., eigenvalues, of (3.3) are

$$E^0_{J,M} = BJ(J+1) \tag{3.5}$$

with corresponding wavefunctions

$$\psi^0_{JM}(\theta,\phi) = N_{JM} \, P^M_J(\cos\theta) \, e^{-M\phi}. \tag{3.6}$$

Rotation is described by the two spherical coordinate variables θ and ϕ, and the wavefunctions and energies are characterized by the quantum labels J, where $\sqrt{J(J+1)}\hbar$ is the rotor's measurable angular momentum, and

where $M\hbar$ is the observable projection of this momentum on a chosen space-fixed axis. J may take any nonnegative integral value, and, for a given J, M takes any of the $2J+1$ integral values $-J, -J+1, \ldots, J-1, J$. In (3.6), $P_J^M(\cos\theta)$ is an associated Legendre function, and N_{JM} is a normalization constant given via

$$N_{JM} = \frac{1}{\sqrt{2\pi}} \left[\frac{(2J+1)(J-|M|)!}{2(J+|M|)!}\right]^{\frac{1}{2}} . \tag{3.7}$$

With the presence of an external electric field, $\underset{\sim}{E}$, a second term is added to the rotor's Hamiltonian,

$$\hat{\mathcal{H}}' = -\hat{\underset{\sim}{\mu}} \cdot \underset{\sim}{E} \tag{3.8}$$

where $\hat{\underset{\sim}{\mu}}$ is the dipole operator summed over all particles,

$$\hat{\underset{\sim}{\mu}} = \sum_i q_i \hat{\underset{\sim}{r}}_i \tag{3.9}$$

with $\hat{\underset{\sim}{r}}_i$ the position vector for each point charge q_i. It is of interest here to note that the expectation value of $\hat{\underset{\sim}{\mu}}$ in field free space for a linear "polar" molecule is, in fact, zero and that what one typically refer to as a molecule's dipole moment μ, as suggested in the previous paragraph, is actually the expectation value measured in a molecule-fixed rather than space-fixed frame. A standard method of determining the effect of $\hat{\mathcal{H}}'$ on the state energies of the full Hamiltonian

$$\hat{\mathcal{H}} = \hat{\mathcal{H}}^\circ + \hat{\mathcal{H}}' = B\hat{\underset{\sim}{J}}^2 - \hat{\underset{\sim}{\mu}} \cdot \underset{\sim}{E}, \tag{3.10}$$

assuming the effect of $\hat{\mathcal{H}}'$ is small compared to $\hat{\mathcal{H}}^\circ$, is via perturbation theory, in which the effects of $\hat{\mathcal{H}}'$ are treated as small corrections to the $\overset{\circ}{E}_{JM}$ and $\overset{\circ}{\psi}_{JM}(\theta,\phi)$ of Equations (3.5) and (3.6). The first order correction to the eigenvalues of $\hat{\mathcal{H}}^\circ$ is given by

$$E_{JM}^{(1)} = \int_0^{\pi} \sin\theta \, d\theta \int_0^{2\pi} d\phi \; \psi_{JM}^{*}(\theta,\phi)(-\hat{\underset{\sim}{\mu}}\cdot\underset{\sim}{\mathcal{E}})\psi_{JM}(\theta,\phi)$$

$$\equiv -\langle JM|\hat{\underset{\sim}{\mu}}\cdot\underset{\sim}{\mathcal{E}}|JM\rangle$$

$$= -\mathcal{E} \; \langle JM|\hat{\mu}_z|JM\rangle, \tag{3.11}$$

where $\hat{\mu}_z$ is the component of $\hat{\underset{\sim}{\mu}}$ along the direction of $\underset{\sim}{\mathcal{E}}$, taken to be along the z axis. Expression (3.11), however, is just the expectation value for $\hat{\mu}_z$ for state $\overset{\circ}{\psi}_{JM}(\theta,\phi) \equiv |JM\rangle^{\circ}$, which, as was previously implied, is zero. That there is no first order perturbation effect is analogous to our previous classical argument of there being no oriented averaged dipole moment if one does not allow the molecule's rotation to be altered. Second order perturbation, in fact, allows for this:

$$E_{JM}^{(2)} = \sum_{(J'M')\neq(JM)} \frac{|\langle JM^{\circ}|\hat{\mathcal{H}}'|J'M'^{\circ}\rangle|^2}{\overset{\circ}{E}_{JM}-\overset{\circ}{E}_{J'M'}} . \tag{3.12}$$

For our particular problem,

$$\langle JM|\mu_z|J'M'\rangle = \mu\left(\frac{(J+1)^2 - M^2}{(2J+1)(2J+3)}\right)^{\frac{1}{2}} \delta_{J',J+1}\,\delta_{M',M}$$

$$+ \mu\left(\frac{(J-1)^2 - M^2}{(2J-1)(2J+1)}\right)^{\frac{1}{2}} \delta_{J',J-1}\,\delta_{M',M} . \tag{3.13}$$

Thus only states of identical M and J differing by ±1 contribute to the second order energy of a particular $|JM\rangle$. From (3.5), (3.8), (3.12), and (3.13),

$$E_{JM}^{(2)} = \frac{\mu^2 \mathcal{E}^2}{B} \left[\frac{J(J+1)-3M^2}{2J(J+1)(2J-1)(2J+3)}\right] \text{ for } J \neq 0$$

$$= \frac{\mu^2 \mathcal{E}^2}{B} \left(-\frac{1}{6}\right) \qquad \text{for } J = 0$$

$$= \frac{\mu^2 \mathcal{E}^2}{B} f_2(J,M). \tag{3.14}$$

"μ" is, once again, the dipole moment that would be observed in the molecule-fixed frame. Values for $f_2(J,M)$ for J up to 4 are given in Table 3.1. The functional dependence of Equation (3.14) on μ, $\mathcal{E}$ and B is similar to that in the classical expression of Equation (3.2), and the sign of the Stark energy is dependent upon the relative magnitudes of J and M. Those J,M states for which $f_2(J,M)$ is positive are referred to as "positive Stark states", with a corresponding definition for negative states. Also note that as the only occurrence of M in $f_2(J,M)$ is with a quadratic term, the Stark term does not remove the degeneracy between states that differ only in the sign of M. As an example of the magnitude of this second order perturbation term, for OCS, with $\mu = 0.709$ D and B = 6.09 GHz, $E_{1,0}^0 = 8.06 \times 10^{-17}$ erg, while $E_{1,0}^2 = 1.40 \times 10^{-30}$ erg x $\mathcal{E}^2$(kV/cm).

The approximation made with second order perturbation theory breaks down at higher field strengths, so that higher order corrections may be necessary.[13] The next correction via perturbation theory is the fourth order term:

$$E^{(4)} = \frac{\mu^4 \mathcal{E}^4}{B^3} f_4(J,M) \tag{3.15}$$

where the functional form of $f_4(J,M)$ can be found in the literature[13,14] and values for it for some lower J's are presented in Table 3.1.

Table 3.1

Second and Fourth Order Perturbation Terms
for the Stark Effect on Linear Polar Molecules

(J,M)	$f_2(J,M)$	$f_4(J,M)$
(0,0)	-1/6	
(1,0)	1/10	-1.04×10^{-2}
(1,1)	-1/20	3.39×10^{-4}
(2,0)	1/42	2.29×10^{-4}
(2,1)	1/84	-3.32×10^{-4}
(2,2)	-1/42	4.05×10^{-5}
(3,0)	1/90	1.13×10^{-5}
(3,1)	1/120	-7.03×10^{-6}
(3,2)	0	-3.51×10^{-5}
(3,3)	-1/72	8.52×10^{-6}
(4,0)	6.49×10^{-3}	1.82×10^{-6}
(4,1)	5.52×10^{-3}	-1.46×10^{-7}
(4,2)	2.60×10^{-3}	-4.45×10^{-6}
(4,3)	-2.27×10^{-3}	-6.25×10^{-6}
(4,4)	-9.09×10^{-3}	2.49×10^{-6}

The exact eigenstates and energies for $\hat{\mathcal{H}}$ can be found by a variational calculation using the $|JM\rangle$ functions as a basis. The energies are derivable by diagonalizing the Hamiltonian matrix $\underset{\approx}{\mathcal{H}}$, with elements

$$\mathcal{H}_{ij} = \langle J_i M_i | \; B\hat{\underset{\sim}{J}}^2 - \varepsilon\hat{\mu}_z | J_j M_j \rangle. \tag{3.16}$$

The $B\hat{\underset{\sim}{J}}^2$ contributes only diagonal elements, while the second term, as shown in Equation (3.13), contributes only between elements of identical M's and J's differing by ±1. Thus, the new eigenstates are still characterized by an M, while different J states are mixed somewhat. Energies calculated in this manner for $J \leq 2$ are illustrated graphically in Figure 3.2 and compared to energies evaluated by second order perturbation theory. It is presented with reduced variables $\varepsilon \equiv E/B$ and $\lambda \equiv E\mu/B$. For a sufficiently large λ any rotational state will become a negative Stark state.

As the potential energy of a linear polar molecule is dependent upon the strength of the field it is in, if the molecule is in an inhomogeneous field region, i.e., where the field strength changes with location, then a force $\underset{\sim}{F}$ will be exerted on the molecule via

$$\underset{\sim}{F} = -\underset{\sim}{\nabla} E(r) \tag{3.17}$$

In particular, assuming that second order perturbation theory is sufficient to describe the Stark effect, from (3.14), the force on a molecule in the state $|J,M\rangle$ is

$$\begin{aligned} \underset{\sim}{F}_{JM} &= -\frac{\mu^2}{B} f_2(J,M) \; \underset{\sim}{\nabla} E^2(r) \\ &= -\frac{2\mu^2}{B} f_2(J,M) \; E\underset{\sim}{\nabla} E(r) \end{aligned} \tag{3.18}$$

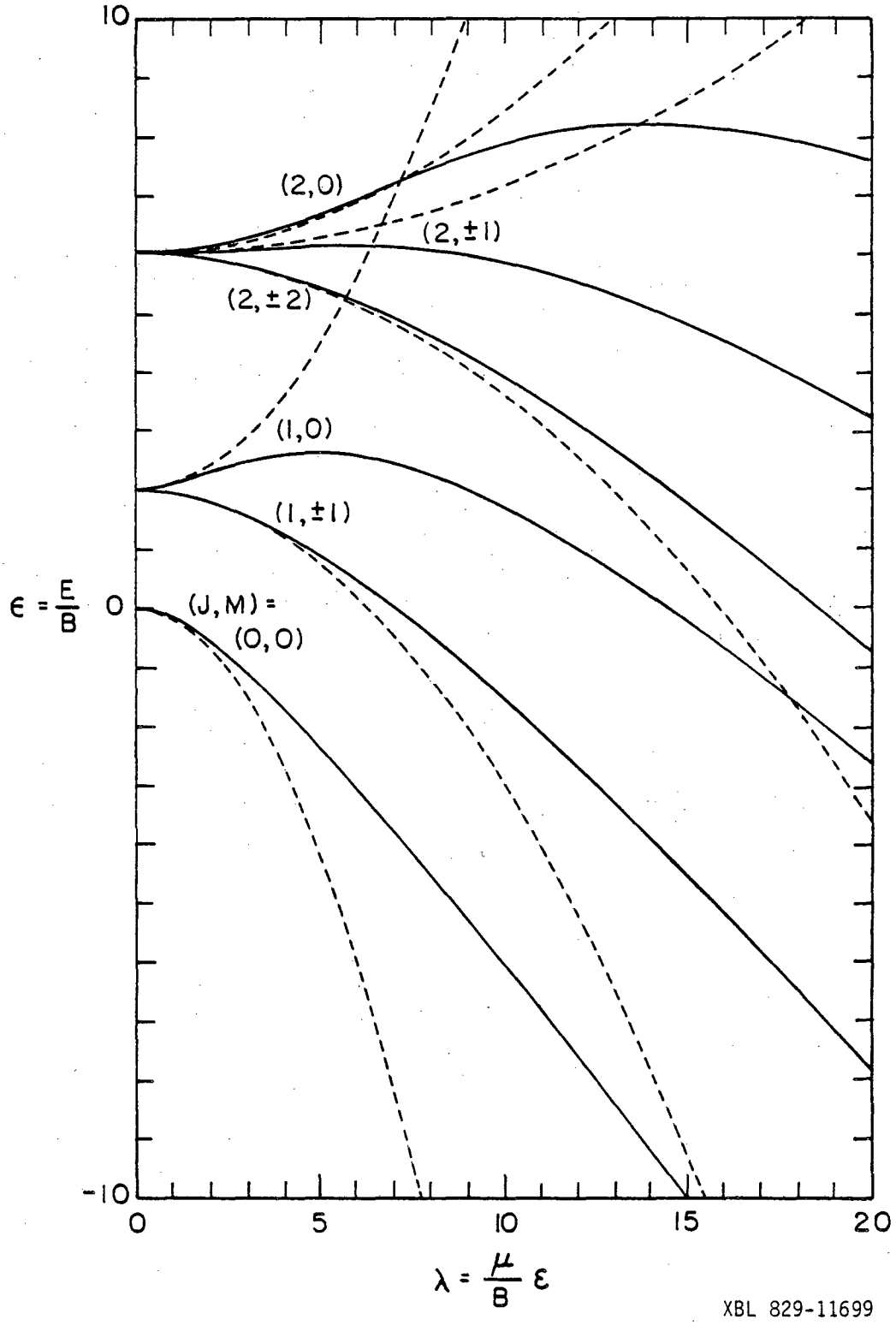

XBL 829-11699

Figure 3.2. Stark energy of a linear rotor for $J \leq 2$ (— from variation calculation; - - - from second order perturbation theory. For OCS, $\lambda/E \approx 0.06$ (kV/cm)$^{-1}$. For $Cl^{35}F$, $\lambda/E \cong 0.03$ (kV/cm)$^{-1}$.)

where $\mathcal{E}(\underset{\sim}{r})$ is the magnitude of the field $\underset{\sim}{\mathcal{E}}(\underset{\sim}{r})$ at $\underset{\sim}{r}$. The particular field relevant to us is the quadrupolar field. Ideally, its cross section consists of four hyperboloid electrodes equally spaced at a distance a_0 from a chosen origin, with static electric potentials of $\pm V_0/2$ applied as indicated in Figure 3.3a. This arrangement produces a potential field

$$\Phi = xy \frac{V_0}{a_0^2} \tag{3.19}$$

and a corresponding electric field

$$\underset{\sim}{\mathcal{E}} = -\underset{\sim}{\nabla}\Phi = -\frac{V_0}{a_0^2}(x\hat{\underset{\sim}{j}} + y\hat{\underset{\sim}{i}}). \tag{3.20}$$

For this field, the Stark energy, via Equation (3.14), becomes

$$E = \frac{\mu^2 f_2(J,M)}{B} \frac{V_0^2}{a_0^4}(x^2 + y^2), \tag{3.21}$$

and a force, by Equation (3.18),

$$\begin{aligned} \underset{\sim}{F} &= -\frac{2\mu^2 f_2(J,M)}{B} \frac{V_0^2}{a_0^4}(x\hat{\underset{\sim}{i}} + y\hat{\underset{\sim}{j}}) \\ &= -k\,\underset{\sim}{r}, \end{aligned} \tag{3.22}$$

where $\underset{\sim}{r} \equiv x\hat{\underset{\sim}{i}} + y\underset{\sim}{j}$ is the position vector from the origin. This force is linearly dependent upon the distance the molecule is from the origin, while the sign of k is dependent upon the relative values of J and M through $f_2(J,M)$. Force equations of different functional form can be found similarly for other field arrangements (e.g., see Ref. 14 for dipole fields).

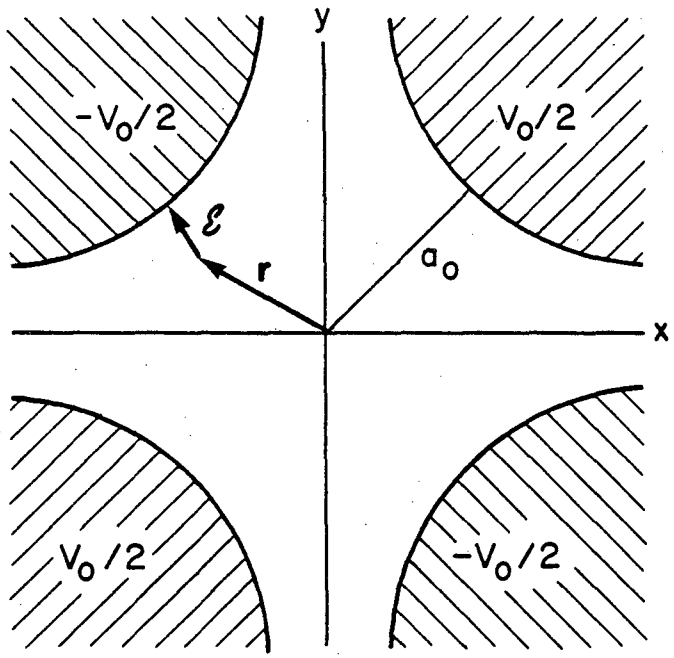

a) Cross section of an ideal quadrupole field.

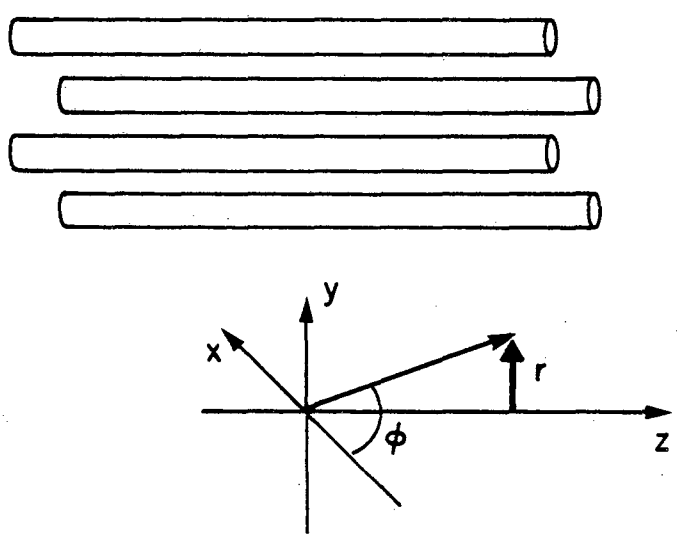

b) Quadrupole rods and cylindrical coordinate reference.

XBL 829-11548

Figure 3.3. Quadrupole field.

In our MBER spectrometer, the quadrupolar field of the previous paragraph is approximated with four parallel circular rods, as in Figure 3.3b. Because of the radial symmetry of the force expression, it is most convenient to treat the trajectory analysis of molecules traveling through the field in cylindrical coordinates. For spatial variables we will use "r" as the distance from the quadrupole axis, "z" as the longitudinal distance along the axis and "ϕ" as the azimuthal coordinate. "v" and "s" will be, respectively, the radial and longitudinal speeds, $\dot{r}$ and $\dot{z}$. Typically, a molecule enters the quadrupole field ($z = z_0$) with a radial position r_0 and a radial speed v_0, where $v_0 << s$, the initial longitudinal speed. We will use the convention that $r(t) < 0$ implies that the molecule has crossed the axis an odd number of times since entering the field region, and that $v(t) < 0$ implies that the molecule is traveling in the opposite direction radially from when it entered the field. Because the only force is radial, the trajectory is independent of ϕ, and ϕ does not change. Furthermore, "s" remains constant while the molecule is within the field. Solving the radial equation of motion from Equation (3.22),

$$m \frac{d^2 r}{dt^2} = -kr, \tag{3.23}$$

gives for $k > 0$ (positive Stark states),

$$r(t) = r_0 \cos(\rho t) + \frac{v_0}{\rho} \sin(\rho t) \tag{3.24}$$

$$v(t) = -\rho r_0 \sin(\rho t) + v_0 \cos(\rho t); \tag{3.25}$$

for $k < 0$ (negative Stark states)

$$r(t) = r_0 \cosh(\rho t) + v_0/\rho \sinh(\rho t) \tag{3.26}$$

$$v(t) = \rho r_0 \sinh(\rho t) + v_0/\rho \cosh(\rho t) \tag{3.27}$$

and for k = 0 (no field, or J = 3, m = ±2)

$$r(t) = r_0 + v_0 t \tag{3.28}$$

$$v(t) = v_0, \tag{3.29}$$

where "m" is the mass of the molecule, and

$$\rho \equiv \frac{|k|}{m} . \tag{3.30}$$

As "s" is a constant of motion, the time variable above can be replaced with the longitudinal variable z via

$$t = z/s. \tag{3.31}$$

Of particular importance in the equations above are (3.24) and (3.25), which indicate that for $k > 0$ or positive Stark states, it is possible for a molecule to enter the field with a diverging velocity, and yet leave the field region with a trajectory converging toward the axis (Fig. 1.2). All negative Stark states will be defocused.

Because of the linear nature of Equations (3.24) - (3.29) it is convenient in trajectory analysis to treat r(z) and v(z) as the two components of a vector $\underset{\sim}{R}(z)$, and the effect of a field region as a linear matrix operator $\underset{\approx}{A}(z)$.[6] If a molecule enters a field region at z_1 with radial conditions $r(z_1) = r_1$ and $v(z_1) = v_1$, then at an arbitrary $z > z_1$ within the same field

$$\underset{\sim}{R}(z) = \begin{pmatrix} r(z) \\ v(z) \end{pmatrix} = \begin{pmatrix} a_1(z-z_1) & a_2(z-z_1) \\ a_3(z-z_1) & a_4(z-z_1) \end{pmatrix} \begin{pmatrix} r_1 \\ v_1 \end{pmatrix}$$

$$= \underset{\approx}{A}(z-z_1)\ \underset{\sim}{R}_1, \tag{3.32}$$

where, from Equations (3.24) - (2.21), for $k > 0$

$$a_1 = a_4 = \cos((z-z_1)\frac{\rho}{s})$$

$$a_2 = \frac{1}{\rho}\sin((z-z_1)\frac{\rho}{s})$$

and

$$a_3 = -\rho\sin((z-z_1)\frac{\rho}{s}), \tag{3.33}$$

for $k < 0$

$$a_1 = a_4 = \cosh((z-z_1)\frac{\rho}{s})$$

$$a_2 = \frac{1}{\rho}\sinh((z-z_1)\frac{\rho}{s})$$

and

$$a_3 = \rho\sinh((z-z_1)\frac{\rho}{s}), \tag{3.34}$$

and for $k = 0$

$$a_1 = a_4 = 1,$$

$$a_2 = (z-z_1)/s$$

and

$$a_3 = 0. \tag{3.35}$$

The value of this form will be seen in a later section.

2. The Initial Molecule Distribution

We now have developed the mechanics required to predict the trajectory of an individual molecule with a given s, r_0, v_0, J and M through the MBER spectrometer via second order perturbation theory. However, the observable in refocusing experiments is dependent upon the ensemble distribution of these parameters, which is to be discussed here. Some of the properties of effusive molecular beams will first be reviewed, with emphasis on their velocity distributions expressed in cylindrical coordinates. Supersonic beams will then be discussed in terms of their general properties and velocity distribution, followed by a non-standard look at rotational distributions. In the succeeding section, the theory presented here will be brought together in explaining our numerical method.

We will let $f(\underset{\sim}{v})d\underset{\sim}{v}$ be the probability of finding a molecule with a vector velocity between $\underset{\sim}{v}$ and $\underset{\sim}{v} + d\underset{\sim}{v}$ within an enclosed volume. In a system at equilibrium and assuming no relativistic effects this is expressed by the Maxwell-Boltzmann distribution, given, in Cartesian coordinates, as

$$f(\underset{\sim}{v})d\underset{\sim}{v} = N_s\, e^{-v_x^2/\sigma_s^2}\, e^{-v_y^2/\sigma_s^2}\, e^{-v_z^2/\sigma_s^2}\, dv_x dv_y dv_z \tag{3.36}$$

where $$\sigma_s^2 \equiv 2kT_s/m \tag{3.37}$$

with k the Boltzmann constant, T_s the temperature of the ensemble, m the mass of a molecule, and N_s a normalization constant, which, itself, is a function only of σ_s. As free space is isotropic, it is in a sense more natural to express this distribution in spherical coordinates. Using the variable transformation suggested by Figure 3.4a,

$$f(\underset{\sim}{v})d\underset{\sim}{v} = N_s\, e^{-c^2/\sigma_s^2}\, c^2 \sin\theta\, dc d\theta d\phi, \tag{3.38}$$

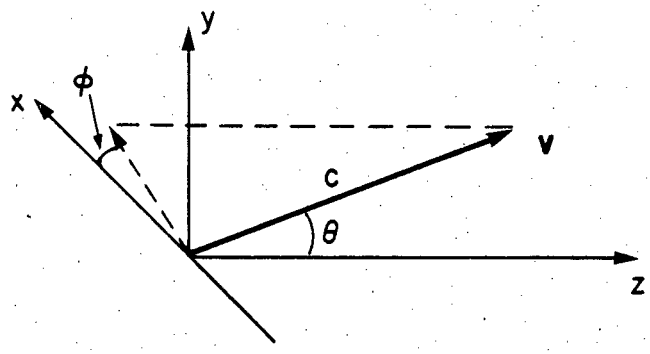

$$c^2 = v_x^2 + v_y^2 + v_z^2$$
$$\cos\theta = v_z/c$$
$$\tan\phi = v_y/v_x$$
$$d\mathbf{v} = dv_x dv_y dv_z = c^2 \sin\theta dc d\theta d\phi$$

a) Spherical velocity coordinates.

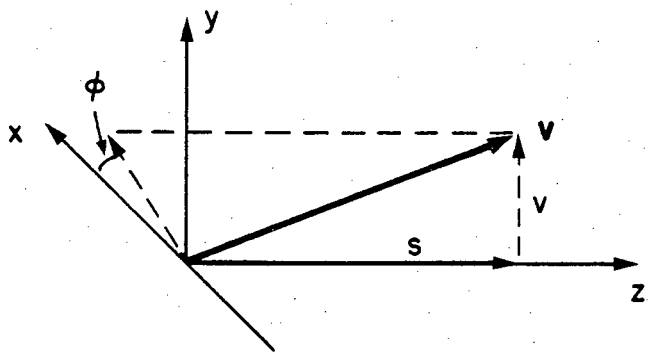

$$s = c \cdot \cos\theta \qquad s = v_z$$
$$v = c \cdot \sin\theta \qquad v^2 = v_x^2 + v_y^2$$
$$c^2 = s^2 + v^2 \qquad \tan\phi = v_y/v_x$$
$$d\mathbf{v} = v\,ds\,dv\,d\phi$$

b) Cylindrical velocity coordinates.

XBL 829-11547

Figure 3.4. Velocity coordinate systems.

where c is the velocity magnitude or speed variable. The part of Equation (3.38) following the exponential function arises from the Jacobian for spherical coordinates. An orifice is now introduced to this volume with the properties that its diameter, D, is considerably smaller than the mean free path, λ, of the molecules within the volume and that the edges of this orifice are very thin compared to λ. Thus, molecules will leave the source region on their chance hitting of the orifice, and they will act independently of each other within the volume and while leaving it. As faster moving molecules will strike the orifice plane with greater frequency, the velocity distribution outside the source will be weighted by an extra factor of c. Secondly, if we pick the orifice to be on the z axis, as in Figure 3.4a, molecules traveling at different angles θ relative to the z axis will "see" different size effective apertures weighted by $\cos\theta$. Thus, the flux distribution measurable outside the volume, in spherical coordinates, will be

$$\begin{aligned} F(\underset{\sim}{v})d\underset{\sim}{v} &\propto c\cos\theta\, f(\underset{\sim}{v})d\underset{\sim}{v} \\ &\propto e^{-c^2/\sigma_s^2}\, c^3 \cos\theta \sin\theta\, dc d\theta d\phi, \end{aligned} \tag{3.39}$$

where flux, $F(\underset{\sim}{v})d\underset{\sim}{v}$, has units of molecules per unit time per unit area, i.e., one counts the number of molecules with a particular velocity $\underset{\sim}{v}$ passing through a normal plane in a time interval.

Returning to the real world of our experiments, molecules are counted by first being ionized by an electron bombardment device, the efficiency of which is proportional to the time the molecule spends within the ionization region. If the ionizer is along the z axis (Fig. 3.4a), this time is inversely proportional to $c\cos\theta$, the speed of the molecule relative to the z axis, so that the detected intensity

of the velocity distribution is reduced by this factor:

$$I(\underset{\sim}{v})d\underset{\sim}{v} \propto F(\underset{\sim}{v})d\underset{\sim}{v}/c\ \cos\theta$$

$$\propto f(\underset{\sim}{v})d\underset{\sim}{v}, \tag{3.40}$$

by Equation (3.39). Thus, the measured intensity, in units of molecules per unit time, is proportional to the velocity distribution within the effusive source. As an aside, the number density of a beam, $N(\underset{\sim}{v})d\underset{\sim}{v}$, is a measure of the number of molecules instantaneously within a unit volume along the beam path with a velocity of $\underset{\sim}{v}$. Though molecules with a greater speed escape from the source with a greater frequency (i.e., have a greater flux) proportional to c because they travel faster, the distance separating molecules of similar speed is also greater by a factor of c. Thus the number density is reduced by this factor of c with respect to the flux, and thus is also proportional to $f(\underset{\sim}{v})d\underset{\sim}{v}$. For this reason, electron bombardment ionizers are often referred to as number density measurers.

As indicated in the previous section MBER trajectories are best described in cylindrical coordinates as the fields are axially symmetric. Using the coordinate transformation indicated in Figure 3.4b, and from Equation (3.39) and (3.40), we get

$$F(\underset{\sim}{v})d\underset{\sim}{v} \propto e^{-v^2/\sigma_s^2}\, e^{-s^2/\sigma_s^2}\ vs\ dvdsd\phi \tag{3.41}$$

and

$$I(\underset{\sim}{v})d\underset{\sim}{v} \propto e^{-v^2/\sigma_s^2}\, e^{-s^2/\sigma_s^2}\ v\ dvdsd\phi, \tag{3.42}$$

where the measured intensity and flux differ by a factor of s, the component of a molecule's velocity parallel to the z-axis. Given the measurable velocity distribution, several properties of the beam can be

evaluated. As an example, the intensity I of an effusive beam measured by a detector on the z axis at a distance L from the source and with an orifice radius R, is

$$I_e = \eta \frac{\int_0^\infty ds\, e^{-s^2/\sigma^2} \int_0^{sR/L} dvv\, e^{-v^2/\sigma^2} \int_0^{2\pi} d\phi}{\int_0^\infty ds\, e^{-s^2/\sigma^2} \int_0^\infty dvv\, e^{-v^2/\sigma^2} \int_0^{2\pi} d\phi}$$

$$= \eta\left(1 - \frac{L}{(L^2+R^2)^{\frac{1}{2}}}\right)$$

$$= \eta(1 - \cos\theta_D) \tag{3.43}$$

where η is the total number of molecules leaving the source per unit time, and θ_D the detector acceptance angle, $\tan^{-1}(R/L)$. Note that the integration limits for s include no negative values as only forward moving molecules can be measured. Table 3.2 gives some useful integrals for the evaluation of some effusive beam statistical properties in cylindrical coordinates, and some results are listed in Table 3.3.

If the condition that made for an effusive source is reversed, namely, that the ratio of the source molecules' mean free path to the source orifice diameter (λ/D_s, commonly referred to as the Knudsen number, Kn) is significantly less than 1, then many collisions will occur between the molecules as they leave through the orifice. If, in addition, the central part of the escaping beam is isolated by a "skimmer" from the stagnant pressure outside the source before a "shock wave" causes nonadiabatic expansion to ensue, a supersonic molecular beam will have been formed.[15] There are two major effects of the adiabatic expansion on the escaping molecules' velocity distribution. The random relative motion of the molecules, both translational and rotational,

Table 3.2

Useful Integrals

$$\int_0^\infty e^{-s^2/\sigma^2}\, ds = \frac{\sqrt{\pi}}{2}\,\sigma$$

$$\int_0^\infty v^{2n}\, e^{-v^2/\sigma^2}\, dv = \frac{1.3.5\ldots(2n-1)}{2^{n+1}}\,\sqrt{\pi}\,\sigma^{2n+1}$$

$$\int_0^\infty v^{2n+1}\, e^{-v^2/\sigma^2}\, dv = \frac{n!}{2}\,\sigma^{2n+2}$$

$$\int_0^w v\, e^{-v^2/\sigma^2}\, dv = \frac{\sigma^2}{2}\,(1 - e^{-w^2/\sigma^2})$$

$$\int_0^\infty e^{-(s-s_0)^2/\sigma^2}\, ds = \sigma \int_{-s_0/\sigma}^\infty e^{-t^2}\, dt = \frac{\sigma\sqrt{\pi}}{2}\,(1+\mathrm{erf}(s_0/\sigma))^*$$

$$\sigma\sqrt{\pi} \quad \text{for} \quad s_0/\sigma > 2^\dagger$$

$$\int_0^\infty s\, e^{-(s-s_0)^2/\sigma^2}\, ds = \sigma \int_{-s_0/\sigma}^\infty (\sigma t + s_0)\, e^{-t^2}\, dt$$

$$= \frac{s_0\sigma\sqrt{\pi}}{2}\,(1+\mathrm{erf}(s_0/\sigma)) + \frac{\sigma^2}{2}\, e^{-s_0^2/\sigma^2}$$

$$s_0\sigma\sqrt{\pi} \quad \text{for} \quad s_0/\sigma > 2^\dagger$$

$$^*\ \mathrm{erf}(x) \equiv \frac{2}{\sqrt{\pi}} \int_0^x e^{-y^2}\, dy$$

† Approximations good to within 0.1% for $s_0/\sigma = 2$, to with 10^{-3}% for $s_0/\sigma > 3$.

Table 3.3

Effusive and Supersonic Beam Characteristics

$f(s) \propto$	$v\, e^{-s^2/\sigma_e^2}\, e^{-v^2/\sigma_e^2}\, dvdsd\phi$	$v\, e^{-(s-s_0)^2/\sigma_b^2}\, e^{-v^2/\sigma_b^2}\, dvdsd\phi$
Normalization	$(\frac{\sigma_e^2}{2})(\frac{\sqrt{\pi}}{2}\sigma_e)(2\pi)$	$(\frac{\sigma_b^2}{2})(\sqrt{\pi}\,\sigma_b)(2\pi)$
	$= \frac{\pi^{3/2}}{2}\sigma_e^3$	$= \pi^{3/2}\sigma_b^3$
$\langle s\rangle =$	$\sigma_e/\sqrt{\pi}$	s_o
$\langle s^2\rangle =$	$\sigma_e^2/2$	$s_0^2 + \frac{1}{2}\sigma_b^2$
$\langle v\rangle =$	$\frac{\sqrt{\pi}}{2}\sigma_e$	$\frac{\sqrt{\pi}}{2}\sigma_b$
$\langle s^2 + v^2\rangle =$	$3/2\ \sigma_e^2$	$s_0^2 + 3/2\ \sigma_b^2$
$s_{mp} =$	0	s_0
$v_{mp} =$	$\sigma_e/\sqrt{2}$	$\sigma_b/\sqrt{2}$
Axis intensity for acceptance angle θ	$N(1-\cos\theta)$	$N(1-\cos\theta\ e^{-\sin^2\theta\ s_0^2/\sigma_b^2})$

tend to "relax" to a lower characteristic temperature T_b, as the collision process tends to distribute the initial random energy of the source molecules more evenly to the molecules within the orifice and during the expansion that continues after the orifice. Thus the beam distribution is now characterized by a lower temperature and the velocity distribution is now centered about a nonzero velocity $s_0\hat{\underset{\sim}{k}}$ which is representative of the conservation of energy after the random energy has reduced. For an ideal molecular beam source of a pure gas, the final beam temperature is given by[16]

$$T_b = T_s(1 + (\frac{\gamma-1}{2})\ M^2)^{-1} \tag{3.44}$$

where T_s is the source temperature, γ is the specific heat ratio C_v/C_p, the ratio of the gas molar heat capacity at constant volume to that at constant pressure, and M is the beam's Mach number. This is in turn given by[18]

$$M = F(\gamma)(\frac{\lambda}{\varepsilon D_s})^{-(\gamma-1)/\gamma}$$

where $F(\gamma)$ is calculated by Anderson and Fenn[16], ε is an empirically determined collision parameter and λ the mean free path of the gas molecules within the source. We have used a simplified version that is correct for Ar:

$$M = 1.17(\lambda/D_s)^{-(\gamma-1)/\gamma} \tag{3.45}$$

The expression for the mean free path of a gas molecule is

$$\lambda = kT_s/\sqrt{2}\pi R^2 P_s \tag{3.46}$$

where P_s is the source pressure and R the effective collision radius of

the gaseous molecule. As an example, for a pure linear molecule gas,

$$\gamma = 7/5 \quad \text{and}$$

$$T_b = T_s(1+\beta^2\ T_s^{-4/7})^{-1} \tag{3.47}$$

with

$$\beta(°K^{2/7}) = 10.19(R(\mathring{A})^2\ D_s(.1\ \text{mm})\ P_s(\text{atm}))^{2/7} \tag{3.48}$$

For P_s = 1 atm, D_s = 0.1 mm and R = 3 Å, T_b = 20 K with a Mach number M = 8.4 for a source temperature of 300 K, and T_b = 37.2 K, M = 7.5 for T_s = 450 K. The flow speed s_0 can be roughly calculated via

$$\frac{1}{2}\ ms_0^2 = C_p(T_s - T_b), \tag{3.49}$$

where m is the molecule mass, reflecting the energy going into the flow velocity from the relaxation of the random translation and rotational energy and from the pressure-volume expansion work. C_p is roughly 5/2 k for monatomic gases and 7/2 k for linear molecules.

The flux distribution for a supersonic beam then should be of the form

$$F_s(\underset{\sim}{v})d\underset{\sim}{v} \propto c\ e^{-(\underset{\sim}{v}-s_0\hat{\underset{\sim}{k}})^2/\sigma_b^2}\ d\underset{\sim}{v}, \tag{3.50}$$

where

$$\sigma_b^2 \equiv 2kT_b/m \tag{3.51}$$

in analogy to Equation (3.37). The leading coefficient of c again reflects the selectivity of faster molecules within the source for escaping. In spherical coordinates[16]

$$F_s(\underset{\sim}{v})d\underset{\sim}{v} \propto c^3 \; e^{-(c-s_0)^2/\sigma_b^2} \cos\theta \, \sin\theta \; dc d\theta d\phi \tag{3.52}$$

is the commonly used distribution, which differs slightly from (3.50) in the value of the exponent function. It is noted here that the escape rate from the source should actually be dependent upon an individual molecule's speed before it undergoes expansion, c', and that the c^2 contribution from Jacobian in (3.52), should similarly reflect the speed distribution before the expansion. This model distribution then implies that the measured molecule speed c is proportional to c'. If the ratio s_0/σ_b is sufficiently large, $F_s(\underset{\sim}{v})$ is effected very little by the form of its nonexponential factors, so the questions suggested here do not remain important. The signal intensity of the supersonic beam, expressed in cylindrical coordinates from Equation (3.50) becomes

$$I(\underset{\sim}{v})d\underset{\sim}{v} \propto v \; e^{-v^2/\sigma_b^2} \; e^{-(s-s_0)^2/\sigma^2} \; dv ds d\phi. \tag{3.53}$$

Statistical properties for this distribution are compared to those for an effusive beam in Table 3.3. As indicated in the integrals of Table 3.2, a standard approximation used in evaluating integrals for this distribution is

$$\begin{aligned} \int_0^\infty s^n \; e^{-(s-s_0)^2/\sigma^2} \; ds &= \int_{-s_0}^\infty (s+s_0)^n \; e^{-s^2/\sigma^2} \; ds \\ &\approx \int_{-\infty}^\infty (s+s_0)^n \; e^{-s^2/\sigma^2} \; ds, \end{aligned} \tag{3.54}$$

which is quite good for $s_0/\sigma_b \sim M > 2$. Most of our work involves $M > 5$. Of note is the intensity of molecules detected by an orifice with angle acceptance θ_D, evaluated similarly as (3.43),

$$I_s = \frac{\eta}{\sqrt{\pi}\sigma_b} \int_0^\infty ds\ e^{-(s-s_0)^2/\sigma^2} (1-e^{-R^2 s^2/L^2\sigma_b^2}),$$

$$= \frac{\eta}{\sqrt{\pi}\sigma_b} \int_0^\infty ds\ e^{-(s-s_0)^2/\sigma^2} - \exp[\frac{-s_0^2}{\sigma^2}(1-a^2)] \int_0^\infty ds\ \exp[-(s/a-s_0 a)^2/\sigma_b^2]$$

$$(\text{with } a^2 \equiv (1+R^2/L^2)^{-1})$$

$$= \eta(1 - \cos\theta_D\ e^{-s^2/\sigma_b^2 \sin^2\theta_D}) \tag{3.55}$$

Taking the ratio of the supersonic to effusive beam intensities for identical flux η from the sources at the limit of small θ_D gives

$$I_s/I_e \approx 2\frac{s_o^2}{\sigma_b^2} + 1 \approx \gamma M^2 + 1. \tag{3.56}$$

This intensity enhancement is among the fringe benefits of working with supersonic molecular beams.

When a mixture of gases is expanded together, the resulting beam properties tend to be mole fraction weighted averages of the properties the pure gas beams would have.[16] In particular, if a small amount of a heavier gas is "seeded" into a carrying beam, the expansion will bring all the molecules to about the same flow velocity, s_0, which may be considerably greater than could have been obtained by the heavy gas alone. The beam temperature, T_b, of the mixture can be estimated by Equations (3.44-3.46) using mole fraction weighted values for C_p, C_v, and πR^2. To calculate s_0, rather than using a direct analog of Equation (3.49), we will use the velocity distribution properties previously calculated, and the mean of the square of the velocities in (3.49), i.e.,

$$\frac{1}{2} m\langle c^2\rangle = \frac{1}{2} m \langle s^2 + v^2\rangle = C_p(T_s - T_b). \tag{3.57}$$

For a binary mixture of gases A and B with mole fractions X_A and X_B, masses m_A and m_B, and heat capacities C_A and C_B, (3.57) becomes

$$X_A \langle\frac{1}{2} m_A c_A^2\rangle + X_B \langle\frac{1}{2} m_B c_B^2\rangle$$

$$= (X_A C_A + X_B C_B)(T_s - T_b) \tag{3.58}$$

From Table 3.3,

$$\langle c_A^2\rangle = s_0^2 + \frac{3}{2}\sigma_A^2$$

and

$$\langle c_B^2\rangle = s_0^2 + \frac{3}{2}\sigma_B^2 \tag{3.59}$$

where

$$\sigma_A^2 \equiv 2kT_b/m_A$$

and

$$\sigma_B^2 \equiv 2kT_b/m_B \tag{3.60}$$

and we have assumed that both of the beam components will relax to the same T_b and s_0. Combining these results,

$$s_0^2 = \frac{2(X_A C_A + X_B C_B)(T_s - T_b) - 3kT_b}{X_A m_A + X_B m_B} . \tag{3.61}$$

In fact it is observed that a heavier seeded component travels with a flow velocity slightly lower than that of the lighter carrier. This "slip" phenomenon indicates that the initial energy of the seed is not fully accommodated during the adiabatic expansion. Another result of this expansion is that heavier particles tend to be focused along the axis of the beam roughly by the ratio of their mass to that of the carrier.[16,17]

Of the remaining degrees of energetic freedom in a gas ensemble, the electronic and vibrational energy channels are irrelevant in our considerations because the typical operating temperatures of our source leaves virtually all molecules in their ground electronic and vibrational states, and this does not change in expansion. The rotational energy, as previously indicated, is strongly effected by the expansion. For a closed system at equilibrium, the rotational distribution for linear molecules follows the standard Boltzmann distribution (assuming the rigid rotor harmonic oscillator approximation)

$$R(J,M) = \frac{e^{-BJ(J+1)/kT_R}}{Q_R(T_R)} , \tag{3.62}$$

where J and M are the rotational quantum numbers, B the molecule's rotational constant, T_R the characteristic rotational temperature, and Q_R the rotational partition function, expressed via

$$Q_R(T_R) = \sum_{J=0}^{\infty} \sum_{M=-J}^{J} e^{-BJ(J+1)/kT_R}$$

$$= \sum_{J=0}^{\infty} (2J+1)\, e^{-BJ(J+1)/kT_R} \tag{3.63}$$

and is roughly equal to kT_R/B for sufficiently great values of this ratio. For both a closed container and an effusive source T_R has the same value as T_s, the source "translation" temperature, as the various energetic degrees of freedom are at mutual equilibrium. In an adiabatic molecular beam expansion, experiments[3,18] have indicated that as the translational temperature of the beam relaxes, T_R also relaxes toward T_b. In principle, rotation to translation energy transfer in collisions is

quite facile, so that in the expansion process the initial rotational energy is largely dumped into the flow velocity s_0.

Most previously made measurements characterizing beam rotational distributions indicate the ensemble properties as T_R and T_b. A question remains, however, if the "microscopic" properties of a beam molecule's individual velocity and rotational state are truly independent beyond being characterized by similar distribution temperatures, i.e., does specifying a molecules velocity give one more information about its most probable rotational state than just specifying T_R. One such correlation argument would suggest that a given molecule with a velocity that varies significantly from s_0 had undergone fewer than the average number of "cooling" collisions during the expansion, and thus the molecule's rotational state would be also correspondingly warmer. Less intuitively appealing perhaps, one may argue that the molecules in a beam have individually about the same total energy. Then a higher translational energy, based on the velocity difference from s_0, would correspond to a lower rotational energy. Because Stark focusing trajectories are velocity dependent this question may be addressed experimentally here. We have chosen to leave a Boltzmann type distribution for the rotational states within each velocity group, but based on a T_R that is dependent both upon the beam translational temperature T_B and the velocity of that group:

$$T_R^{\alpha}(s,v) = \max \frac{T_B}{1+\frac{1}{2}\alpha} \{1 + \alpha(\frac{v^2+(s-s_0)^2}{\sigma_b^2} -1)\}, \ \varepsilon T_B \tag{3.64}$$

where α is a parameter >-2 which determines the type of rotation to velocity correlation, and εT_B is a lower limit placed for rotational temperatures, as nonpositive rotational temperatures are not physically

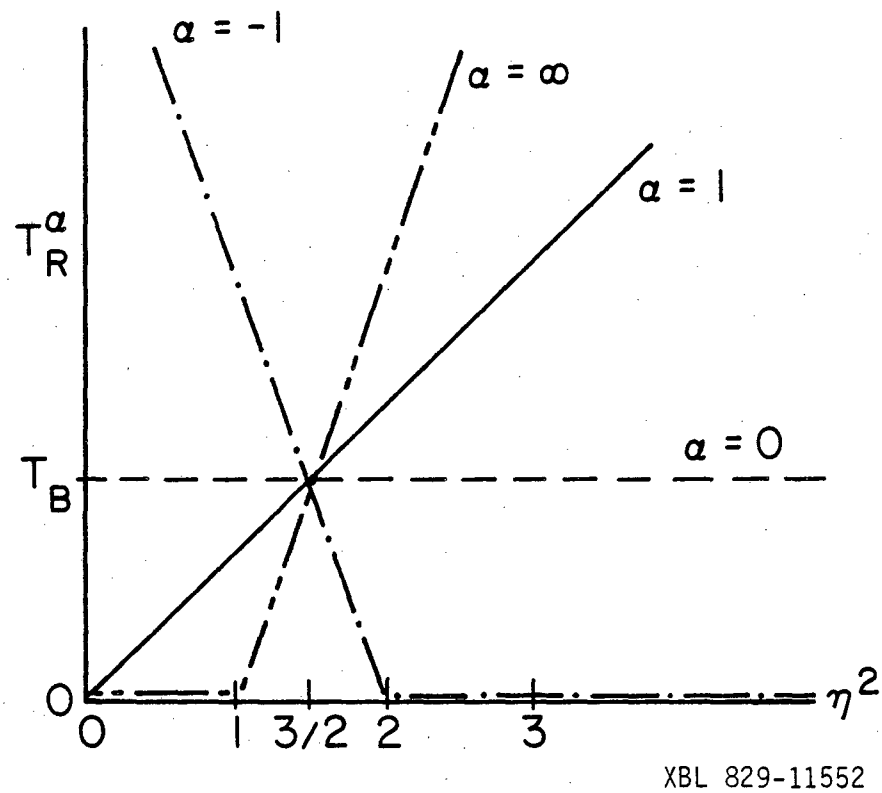

Figure 3.5. Rotational temperature (T_R^α) as a function of $\eta^2 \left(\equiv \frac{(S-S_0)^2+V^2}{\sigma^2} \right)$ for various values of α. (See Equ. (3.64)).

acceptable to this system. This form was devised to have the property that $T_R(s,v) = T_B$ for v and s picked such that

$$\eta^2 \equiv \frac{v^2+(s-s_0)^2}{\sigma_b^2} = \frac{v^2+(s-s_0)^2}{\sigma_b^2} = \frac{3}{2} . \tag{3.65}$$

For $\alpha = 0$, T_R is independent of s and v. For $\alpha = +1$,

$$T_R^{+1}(s,v) = \max\{\frac{2}{3} T_B\eta^2, \varepsilon T_B\}. \tag{3.66}$$

As η^2 becomes smaller, T_R^{+1} reduces. Thus, molecules that travel closer to $s_0\hat{\underset{\sim}{k}}$ are rotationally colder. For α less than 0, Equation (3.64) predicts a negative correlation, where T_R increases with a reduction of η^2. Figure 3.5 indicates graphically the functional form of $T_R^{\alpha}(\eta)$. Other properties of this proposed distribution function will be discussed later.

3. <u>The Numerical Methodology</u>

The quantity desired is the fraction F of a supersonic beam of a polar linear molecule refocused into the detector orifice through our MBER spectrometer as a function of the voltages applied to the A and B fields. For simplicity, the relevant molecular parameters consisting of its mass, m, dipole moment, μ, and rotational constant, B_R will be collectively labeled as X, and the geometric parameters of the spectrometer including the locations of the spectrometer elements z_i (see Fig. 3.6a), the stop-wire and detector orifice diameters, R_s and R_c, and the A and B field interior radius a_0 will be collectively labeled Y. The other relevant parameters include the A and B field voltages, V_A and V_B, and the beam properties s_0, σ_b, T_b, and α, defined in Equation (3.64). Using the distribution of Equation (3.53),

$$F = \frac{\int_0^\infty f(s) e^{-(s-s_0)^2/\sigma^2} ds}{\int_0^\infty e^{-(s-s_0)^2/\sigma^2} ds} \tag{3.67}$$

where f(s) is the fraction of all molecules focused with a given longitudinal speed s. The remaining variables discussed previously are omitted for clarity. Continuing,

$$f(s) = \frac{\int_0^\infty g(s,v^o) v^o e^{-v^{o2}/\sigma^2} dv^o}{\int_0^\infty v^o e^{-v^{o2}/\sigma^2} dv^o}, \tag{3.68}$$

where $g(s,v^o)$ is the fraction of molecules refocused with a given s and v^o, the molecule's initial radial velocity. Recall that in the refocusing process a molecule's radial velocity v will change while its longitudinal velocity s will not. The radial velocity distribution given in Equation (3.53) reflects that distribution leaving the source before any field effects. Again continuing,

$$g(s,v^o) = \sum_{J=0}^{\infty} \sum_{M=-J}^{J} \frac{h(s,v^o,J,M)}{Q_R(T_R)} e^{-J(J+1)B/kT_R(s,v^o)}$$

$$= \sum_{J=0}^{\infty} \sum_{M=-J}^{J} h(s,v^o,J,M)\ R(J,M,s,v^o) \tag{3.69}$$

where $h(s,v^o,J,M)$ is the fraction of molecules refocused with a given s,v^o, J and M, and $R(J,M,s,v^o)$ is defined by Equations (3.62) and (3.64).

To evaluate the function $h(s,v^o,J,M)$ we now return to the second order perturbation Stark focusing process and the formalism introduced

in Equations (3.32) - (3.35). A molecule is detectable if its trajectory possesses the following criteria: (a) it gets by the stopwire at z_4 (see Fig. 3.6a), (b) it remains within the effective focusing fields between z_2 and z_3 for the A field and z_5 and z_6 for the B field, (c) it passes through the detector orifice at z_7, and (d) it does not enter the detector so steeply that it would collide with the ionizer. Using the vector-linear matrix operator of Equation (3.32), we define $\underset{\sim}{R}_i$ via

$$\underset{\sim}{R}_i \equiv \begin{pmatrix} r(z_i) \\ v(z_i) \end{pmatrix} \equiv \begin{pmatrix} r_i \\ v_i \end{pmatrix} \tag{3.70}$$

where z_i are the positions indicated in Figure 6a. For between each z_i and z_{i+1} we can define a matrix $\underset{\approx}{A}_i$ via Equations (3.33)-(3.35) which, aside from the general molecular properties, are dependent upon the field conditions and rotational state for $\underset{\approx}{A}_2$ and $\underset{\approx}{A}_5$, and just dependent on the region lengths for the remaining matrices. Then, by (3.32),

$$\underset{\sim}{R}_{i+1} = \underset{\approx}{A}_i(z_{i+1} - z_i)\underset{\sim}{R}_i. \tag{3.71}$$

For initial conditions, we let z_1 be the source point.

$$v_1 \equiv v(z_1) = v^o, \tag{3.72}$$

as v^o has already been defined as a molecule's initial radial velocity. For the purpose of this calculation we assume a point source so that all molecules begin on the axis with $r(z_1) = 0$, which turns out to be only a small approximation. Because of the linear property of (3.71) and these initial conditions, $r(z)$ and $v(z)$ are proportional to v^o for a given molecule for all z within the spectrometer to z_8, and we can define new variables

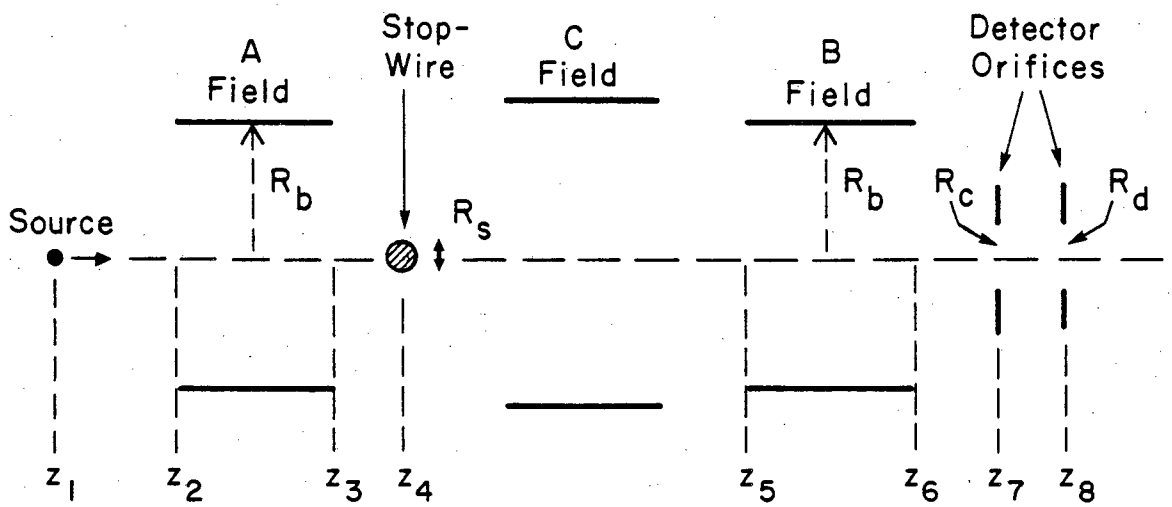

a) Spectrometer geometric parameters for refocusing.

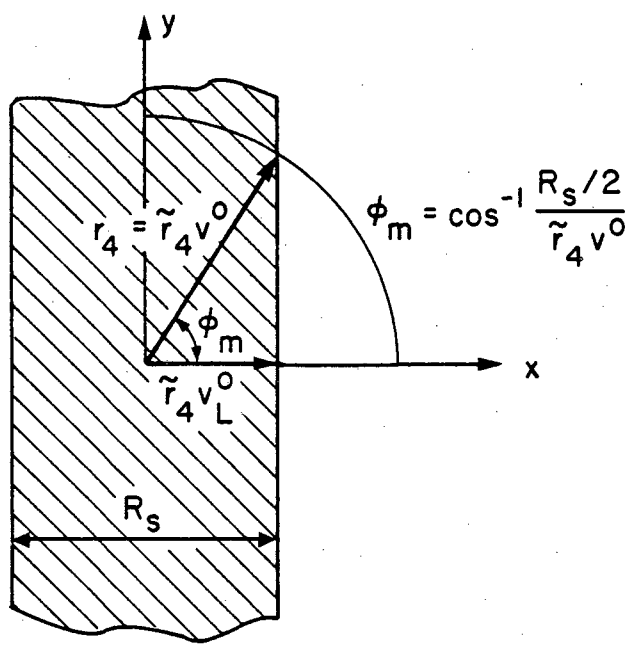

b) Stopwire cross section.

XBL 829-11549

Figure 3.6

$$\tilde{r}(z,V_A,V_B,s,J,M,X,Y) = r(z,V_A,V_B,s,J,M,X,Y)/v^o \quad \text{and}$$

$$\tilde{v}(z,V_A,V_B,s,J,M,X,Y) = v(z,V_A,V_B,s,J,M,X,Y)/v^o \tag{3.73}$$

where $\tilde{v}$ is dimensionless, and $\tilde{r}$ has units of time, and all of the relevant parameters have been included as a reminder that the trajectory is still also dependent upon molecular properties and the field parameters. Thus, it is sufficient to find $\tilde{r}(z)$ and $\tilde{v}(z)$ alone to know the trajectories for all initial radial velocities v^o. Furthermore, for a given s and ϕ, given a particular v_ℓ^o for which the trajectory can get by the stopwire at z_4, then any other trajectory with $v^o > v_\ell^o$ can get by as well. Similarly, if there exists a v_h^o for which the trajectory r(z) remains close enough to the axis to meet the focusing criteria (b)-(d), then these criteria will be met by all trajectories with $v^o < v_h^o$.

It now remains to find those particular values $v_L^o(V_A,V_B,s,\phi,J,M,X,Y)$ and $v_H^o(V_A,V_B,s,\phi,J,M,X,Y)$ such that all trajectories with

$$v_L^o < v^o < v_H^o \tag{3.74}$$

are focusable, and the remaining trajectories are not. The lower limit condition is determined only by criterion (a), the stopwire. If the stopwire were radially symmetric in our coordinate system with diameter R_s, then a trajectory would pass if

$$r_4 = \tilde{r}_4 v_0 > \frac{R_s}{2} \tag{3.75}$$

so that

$$v_L^o = \frac{R_s}{2\tilde{r}_4} \tag{3.76}$$

However, there is a ϕ dependence from the stopwire we use. As can be inferred from Figure 6b, for a given $v^o > v_L^o$, in the quadrant $0 < \phi < \frac{\pi}{2}$ there exists a $\phi_m(v^o)$ such that the stopwire blocks the beam for $\phi_m < \phi < \frac{\pi}{2}$. As the figure indicates,

$$\phi_m(v^o) = \cos^{-1} \frac{R_s/2}{r_e} = \cos^{-1} \frac{v_L^o}{v^o} \quad . \tag{3.77}$$

To find v_H^o, one seeks the strictest constraint of (b), (c), and (d). For (c) and (d) we simply require that

$$r_7 < \frac{R_c}{2} \quad \text{and} \quad r_8 < \frac{R_d}{2} \ ,$$

so that

$$V_{H_c}^o = \frac{R_c}{2\tilde{r}_7} \quad \text{and} \quad V_{H_d}^o = \frac{R_d}{2\tilde{r}_8} \quad . \tag{3.78}$$

For constraint (b), we choose a radius R_b for the quadrupole fields for which a focusable molecule will no longer be allowed to return into the field region. The physical reasons for doing this include collisions with the field pieces, the spherical aberrations of the fields due to not having hyperboloid electrodes and the increasing effect of higher order defocusing Stark terms at the greater field strengths existing here. If a trajectory does not change its direction within the A (B) field, then its maximum radial position is attained at either $z_2(z_5)$ or $z_3(z_6)$. If it does change direction, remembering that this is independent of v^o, the maximum radial position from Equation (3.24) becomes

$$r_A^{max} = [(r_2)^2 + (v_2/\rho)^2]^{\frac{1}{2}}$$

or

$$\tilde{r}_A^{max} = [(\tilde{r}_2)^2 + (\tilde{v}_2/\rho)^2]^{\frac{1}{2}}, \tag{3.79}$$

with similar equations for the B field, changing the index "2" to "5". Then

$$v^o_{H_A} = \max\left\{\frac{R_b}{\tilde{r}_2}, \frac{R_b}{\tilde{r}_3}, \frac{R_b}{\tilde{r}^{max}_A}\right\},$$

and

$$v^o_{H_B} = \max\left\{\frac{R_b}{\tilde{r}_5}, \frac{R_b}{\tilde{r}_6}, \frac{R_b}{\tilde{r}^{max}_B}\right\} \tag{3.80}$$

and finally the actual upper limit for v^o is

$$v^o_H = \min\{v^o_{H_A}, v^o_{H_B}, v^o_{H_c}, v^o_{H_d}\}. \tag{3.81}$$

Returning to our integral distribution function h,

$$h(s,v^o,J,M) = \frac{4\int_o^{\cos^{-1}(v^o_L/v^o)} k(s,v^o,J,M)\,d\phi}{\int_o^{2\pi} d\phi} \tag{3.82}$$

where

$$k(s,v^o,J,M) = 1 \text{ for } v^o_L(s,J,M) < v^o < v^o_H(s,J,M)$$

and $$= 0 \text{ otherwise.} \tag{3.83}$$

Now, reassembling the integral,

$$h(s,v^o,J,M) = \frac{4}{2\pi}\cos^{-1}\frac{v^o_L}{v^o}\; k(s,v^o,J,M), \tag{3.84}$$

$$g(s,v^o) = \frac{2}{\pi}\sum_{J=0}\sum_{M=-J}^{J}\cos^{-1}\frac{v^o_L}{v^o}\; k(s,v^o,J,M)R(J,M,s,v^o), \tag{3.85}$$

$$f(s) = \frac{2}{\pi}\int_0^\infty dv^o v^o\ e^{-v^{o2}/\sigma^2}\ \frac{\sum_J\sum_M \cos^{-1}\left(\frac{v_L^o}{v^o}\right) k(s,v^oJ,M)R(J,M,s,v^o)}{\int_0^\infty v^o\ e^{-v^{o2}/\sigma^2}dv^o}$$

$$= \frac{4}{\pi\sigma^2}\sum_{J=0}\sum_{M=-J}^{J}\int_{v_L^o(s)}^{v_H^o(s)} dv^o \cos^{-1}\frac{v_L^o}{v^o}\ R(J,M,s,v^o)v^o\ e^{-v^{o2}/\sigma^2}, \qquad (3.86)$$

and finally

$$F = \frac{4}{\pi^{3/2}\sigma^3}\int_0^\infty ds\ e^{-(s-s_0)^2/\sigma^2}\sum_J\sum_M\int_{v_i^o}^{v_H^o} dv^o v^o\ e^{-v^{o2}/\sigma^2}\ \cos^{-1}\left(\frac{v_L^o}{v^o}\right)R(J,M) \qquad (3.87)$$

In our calculations and experiments, to remove the factor of total source flux in the measurements of refocusing, we measure F relative to the straight through signal of a beam without a stopwire present, given analytically in Equation (3.55), with $R = R_c/2$ and $L = z_7 - z_1$, so that the percent refocused signal becomes

$$P = \frac{F}{F_0} \times 100 = \frac{F\eta}{I_s}\ . \qquad (3.88)$$

To conclude our analysis of trajectories in our MBER apparatus, we must also see the effect of state transitions within the C field. This is simulated numerically quite simply by instantaneously changing the J and/or M quantum descriptors of our trajectories between the A and B fields, i.e., between z_3 and z_5. For example, if we were to assume a 75% transition between (J,M) = (1,0) and (1,±1), recalling that rotational states are doubly degenerate for $M \neq 0$, we calculate the values for v_H^o for trajectories with a given s with M = 0(±1) in the A field and M = ±1(0) in the B field thereby deriving the function $k(s,v^o,J^*,M^*)$ to use weighted by 0.75 in Equation (3.85) while subtracting $k(s,v^o,J=1,$

$M = 0) \times 0.75$ and $k(s,v^o,J=1, \quad M = 1) \times 0.75$. Results of these calculations are given in the following section. A listing of the computer program "ABFIELD" which does this trajectory analysis is presented in this chapter's appendix.

As a check for the validity of using second order perturbation theory in our analysis, we have also determined trajectories using variational theory to calculate the energies and forces in the focusing fields. The Hamiltonian matrix of Equation (3.16) can be expressed in a block tridiagonal form, with each block having a unique value of the quantum number M. The eigenvalues of these matrices can be solved for by the conversion of the matrix secular equation into a continued fraction form,[9] for which numerical methods exist.[19,20] A program to generate a table of these energies as a function of field strength is given in the appendix. There are several reasons why we have not done all of our trajectory analysis with these variational energies. First, the trajectories cannot be treated analytically as we have done with the second order perturbation calculations. The linear relationship of trajectories $r(z)$ to v^o is not preserved here. Finally, it is not necessary that the range of focusable v^o values is even "connected" in a topological sense. Ideally Monte Carlo type calculations should be used here. We have instead sought values $v_L^{o'}$ and $v_H^{o'}$ from variational calculations close to those of v_L^o and v_H^o from second order perturbation theory to check if under certain field conditions there is a major error in our preferred method. These results will also be presented later.

B. Experimental and Numerical Results

The experimental method used for our refocusing experiments has been

described in the previous chapter. In the first two sets of experiments described here neither static nor radiofrequency voltages were applied to the C field. Aside from the geometric parameters of the spectrometer, given in Table 2.1, the relevant experimental parameters include the gas mixture, the source pressure and temperature and the source nozzle diameter, which determine the initial beam energy distribution, and the A and B field voltages, which determine individual trajectories. The numerical simulations use the same geometric parameters, and have assumed a stopwire diameter of 0.119 cm and a detector orifice diameter of 0.15 cm, consistent with most of the experiments. The effective A and B field radius used, outside of which simulated trajectories are considered unfocusable, has been the inner radius of the quadrupole rods, 0.3175 cm, and the effective ionizer diameter used was 0.4 cm. The initial beam conditions have been inputted several ways, such as inputting the beam mixture, source temperature (T_s) pressure (P_s) and nozzle diameter (D_s), and using Equations (3.44), (3.51) and (3.61) to determine the beam temperature (T_b) and from that the velocity distribution parameters s^o and σ, or directly inputting T_b, or finally, directly inputting s^o and σ. In addition we input a value for the rotational distribution parameter α (see Eq. (3.64)). In the first part of this section the basic experimental and numeric refocusing curves as functions of the A and B field voltages for several linear polar molecules are described and compared. Following that the experimental dependence of the refocusing curves of OCS and ClF on the source conditions will be shown and compared with numerical results from various initial conditions. The third section will discuss the effect of A and B field voltages on the transition spectrum for OCS, again both from a theoretical and experimental point of view.

1. Refocusing as a Function of the A and B Field Voltages

Figure 3.8 gives the refocusing "spectrum" for OCS in a 5% mixture with Ar at source conditions of 1 atmosphere, 22°C and a 100 μ nozzle, in the range of 0-30 kV for both the A and B fields. It has been found that such spectra are quite sensitive to the background pressure within the spectrometer chamber. While the data of Figure 3.7 were taken with a spectrometer pressure on the order of 5×10^{-7} torr, Figure 3.8 depicts data collected with the background pressure about an order of magnitude greater. The enhanced magnitude of the refocusing stems from the larger source nozzle diameter (200 μ) used (the effects of which will be discussed further in the next section), but the general pattern was typical of higher background pressure work. In these and in all the following refocus data to be presented the refocused signal is given as a percentage compared to the signal measured from a beam with the stopwire removed from its path and the A and B fields off. The lensing effect of the quadrupole fields becomes more obvious seeing refocused signals of greater than 100%. In fact, when refocusing scans are made with the stopwire out of the beam path the observed spectra are approximately just these observed superimposed on a flat beam background signal, so that refocused signal comes primarily from molecules with initial trajectories not coincident with the detector orifice. A refocus spectrum of ClF (3% in Ar, $P_s = 1$ atmosphere, $T_s = 22°C$, $D_s = 100$ μ) is given in Figure 3.9. The enhanced refocusing relative to that of OCS and the general change in the form of the spectrum is characteristic of ClF and should ultimately be attributed to the differences in the dipole moments, rotational constants and molecular moments. No refocusing was evident to us in beams of HCl, and HF refocused up to about 30%, and only at the highest A and B settings.

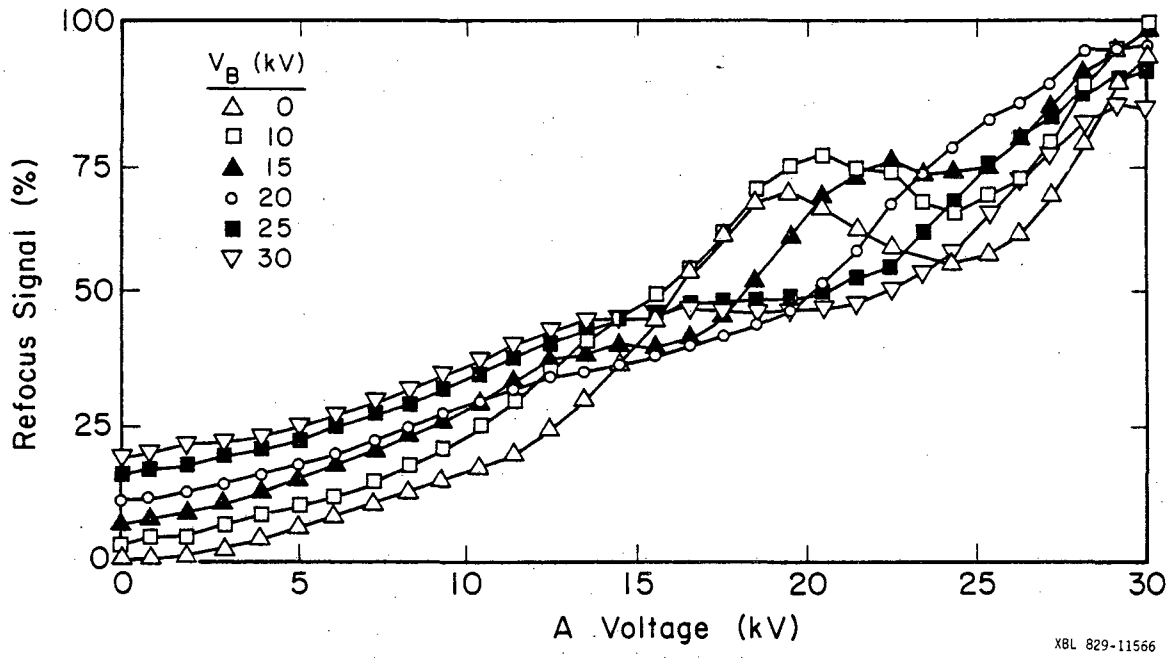

Figure 3.7. Refocusing spectrum of OCS (5% in Ar P_s = 1 atm, T_s = 295 K). Individual lines for different B field voltages (kV).

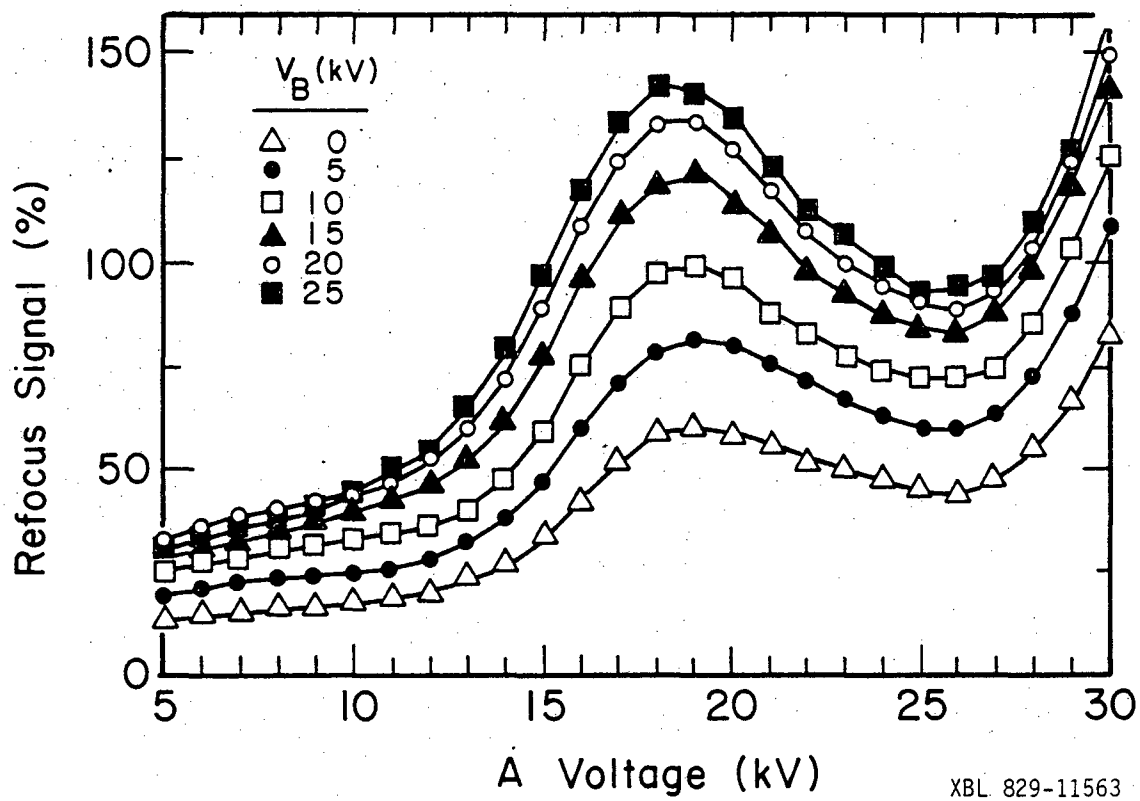

Figure 3.8. Refocusing spectrum of OCS (10% in Ar, P_s = 1 atm, T_s = 300 K, D_s = 200 μ; high background pressure).

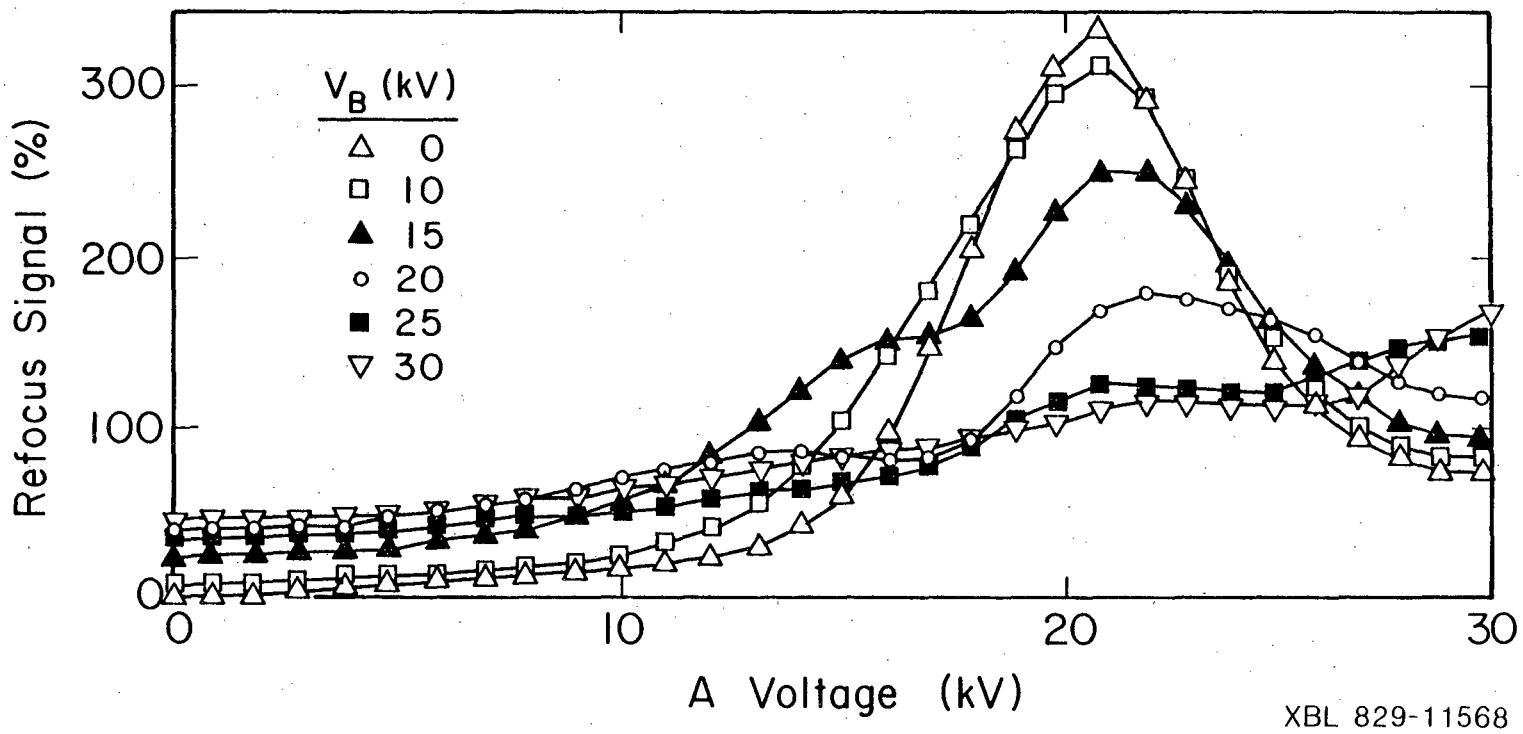

Figure 3.9. Refocusing spectrum of ClF (3% in Ar, P_s = 1 atm, T_s = 295 K, D_s = 100 μ).

Figure 3.10 represents a computer simulation for the refocusing of OCS (10% in Ar, T_s = 20°C, P_s = 1 atm, D_s = 100 μ) calculated by the program ABFIELD, described in the theoretical section and appendix. A beam temperature of 3.08 K was calculated using effective diameters of 3.5 and 2.9 Å for OCS and Ar, respectively, and heat capacities of 2.5 k and 1.5 k. This in turn leads to s_o = 54466 cm/sec and σ = 2920 cm/sec (Mach number = 17.2). For the rotational distribution $\alpha = 0$, so that the rotational temperature is fixed at 3.08 K. Before attempting to compare Figure 3.10 to Figure 3.8, we will discuss in detail the contributions to the simulated refocusing pattern, the knowledge of which is attainable from the computer output. Before this, two more points should be made. First, each curve for a given B voltage (V_B) is a summation of properly weighted curves over the Gaussian "s" distribution centered at s_0. Sharp corners, such as near the maximum of the V_B = 25 kV curve, are due to the choice of how many such "s" curves are included. Secondly, as shown in the previous section, using second order perturbation theory for linear molecules experiencing a Stark effect, given a longitudinal speed s and rotational state (J,M), there exist upper and lower initial transverse velocity limits v_L^o and v_H^o where v_L^o is determined by the stopwire condition and v_H^o by either the detector, ionizer, or A or B field geometric constants. Such a group of molecules is partially focusable only if $v_H^o(s) > v_L^o(s)$. How much this group contributes to the refocusing curves depends both on the magnitude of the difference between these limits and on the number of molecules in the (J,M) state with longitudinal speeds near s.

For Figure 3.11 we will use the V_B = 15 kV curve as representative of curves for V_B = 15 kV. In this paragraph, furthermore, we will discuss molecules traveling at the mean longitudinal speed, s_o. Temporarily

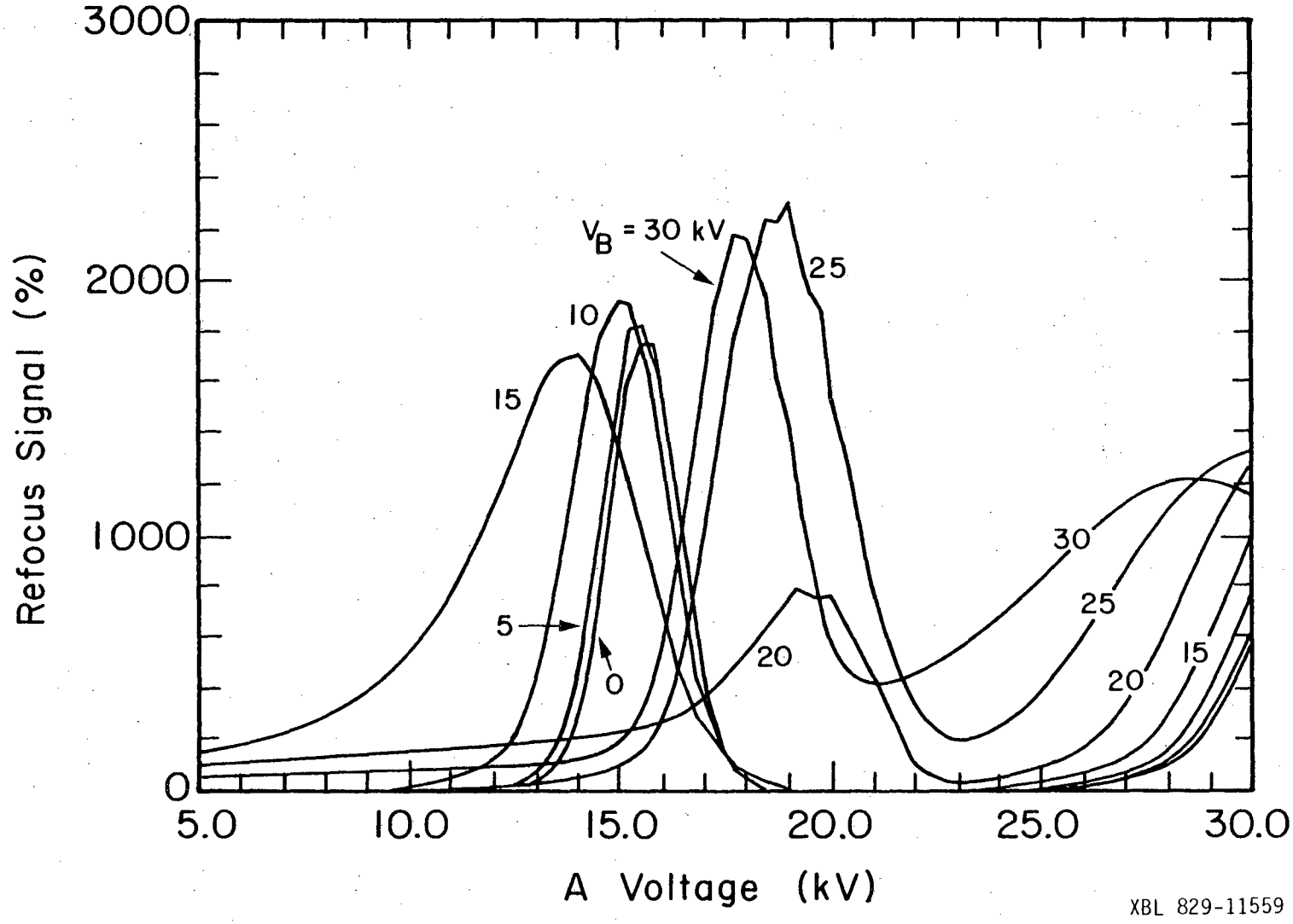

Figure 3.10. Simulated refocusing spectrum of OCS (10% in Ar, T_s = 293 K, T_b = 3.1 K).

considering only the most focusable rotational state (1,0), at V_A = 5 kV there exists $[v_L^o, v_H^o]$ limits of [82,226], where v_H^o is restricted by the detector orifice, and, as $v_H^o > v_L^o$, there is a contribution to the refocused signal. At V_B = 0, 5 or 10 and for V_A = 5, v_L^o remains the same, as the B field does not affect trajectories up to the stopwire, but v_H^o is reduced as the B field pulls only those molecules with a lower initial v^o toward the axis. In those cases, $v_H^o < v_L^o$, and no (1,0) refocusing occurs. Returning to V_B = 15, as V_A increases from 5 to 7 kV, $[v_L^o, v_H^o]$ changes to [88,284], with v_L^o and v_H^o increasing as (1,0) molecules are pulled closer to the axis, but v_H^o increasing substantially faster. Because of the linearity of the radial displacement of molecules from the axis with respect to their initial transverse velocities, all molecules of a given s and (J,M) will cross the axis at the same position along the spectrometer. The increase in v_H^o here affects this crossing point, which was initially far beyond the detector orifice, and approaches it as the A field increases. At V_A = 8, $[v_L^o, v_H^o]$ = [92,335], where v_H^o is now determined by the B field restriction, as the detector determined $v_{H_c}^o$ has exceeded what is passable by the B field. Between V_A = 12 and 13 the (1,0) states are focused directly at the detector orifice and v_H^o would be infinite if there were no other geometric restrictions aside from the orifice. At V_A = 12, v_H^o(562) is still constrained by the B field, while at V_A = 13, v_H^o(-675) is restricted by the A field. The negative sign for v_H^o indicates that the trajectories have crossed the beam axis once before the detector orifice. At V_A = 1.4, $[v_L^o, v_H^o]$ = [139, -725] and the largest fraction of (1,0) molecules are passable for an integral value of V_A. Note that this position is determined both by the crossing point criterion (i.e., that the trajectories are crossing

Table 3.4

Lower (v_L) and Upper (v_H) Transverse Velocity Limits, Total Percent Refocusing (Relative to a Straight Through Beam) and $(1,0) \leftrightarrow (1,1)$ Transition Signal (Relative to Straight Through Beam, Positive for "flop out") for OCS Calculated with Second Order Perturbation Theory, as a Function of A field Voltage (V_A). V_B = 15 kV, Longitudinal Velocity (s) = 54466 cm/sec. Units in cm/sec.

V_A(kV)	$v_L(1,0)$	$v_H(1,0)$[a]	$v_H(1,0)^*$	$v_L(1,1)$	$v_H(1,1)$	$v_H(1,1)^*$	Total Refocusing(%)	Transition(%)
5	82	226	30	74	25	168	136	10
6	85	250	32	73	24	162	175	62
7	88	284	35	72	23	155	240	140
8	92	335[B]	38	71	23	147	356	269
9	96	370[B]	43	69	22	140	443	369
10	102	416[B]	50	68	21	132	574	510
11	109	477[B]	59	66	20	124	778	724
12	117	562[B]	74	64	19	116	1109	1066
13	127	-675[A]	99	62	18	108	1641	1605
14	139	-725[A]	151	60	17	101	1875	1844
15	154	-624	314	58	16	94	1272	1058
16	173	-442	825[A]	56	15	87	483	-1865
17	198	-346	-285	54	14	80	181	+ 91
18	231	-287	-150	52	13	74	40	30
19	276	-248	-104	50	12	69	0	- 8
20	344	-221	- 81	48	12	63	0	- 6
21	449	-202	- 67	46	11	58	0	- 4
22	638	-188	- 58	43	10	54	1	- 3
23	1067	-179	- 52	41	9	50	4	- 2
24	2932	-172	- 48	39	9	46	8	- 1
25	-4676	-169	- 46	38	8	42	28	- 1
26	-1367	-168	- 44	36	8	39	37	0
27	- 832	-169	- 43	33	7	36	76	0
28	- 615	-172	- 43	32	6	33	171	0
29	- 501	-179	- 43	30	6	30	450	0
30	- 432	-189	- 45	29	6	28	1385	0

[a]Unless otherwise indicated, v_H is determined by the detector orifice constraint. 'A' or 'B' indicate the bound is created by the focusing field geometrical constraint.

near the detector) and the field geometry constraints, as v_H^o is still limited by the A field. At $V_A = 15, v_H^o$ is again detector orifice limited as the crossing point recedes from the detector with increasing V_A. By $V_A = 16$ the crossing point is within the B field and at $V_A = 18$ it is in the C field region, with $[v_L^o, v_H^o] = [231, -287]$. v_H^o continues to decrease with V_A increasing and at $V_A = 19$ there is no refocus signal from (1,0). Between $V_A = 24$ and 25 the crossing point reaches the stopwire, so even if v_H^o were not small, v_L^o has become quite large. For $V_A = 25$, $[v_L^o, v_H^o] = [4676, -169]$. With a further increase in V_A, v_L^o again reduces and v_H^o begins to increase as an impending second crossing point approaches from beyond the detector. For $V_B = 15$, $V_A = 30$, $[v_L^o, v_H^o] = [432, -189]$, so no more refocusing from (1,0) occurs on this curve. In Table 3.4 the values for $[v_L^o, v_H^o]$ as just described are listed for $V_B = 15$, s = 54466 cm/sec and (J,M) = (1,0). Also listed are results for the (1,1) state which, as expected, never refocuses, being a negative Stark state. In fact, the only other state to make a contribution to this refocusing curve is the (2,0) state, which starts making a contribution at $V_A = 21$, after the (1,0) state is no longer focusing into the detector. By $V_A = 30$, the v_H^o for (2,0) has become limited by the A field geometry, as its crossing point nears the detector orifice.

For the $V_B = 20$ curve, at $V_A = 5$, $[v_L^o, v_H^o] = [82, -181]$ for the (1,0) state, indicating that the trajectories have already crossed before the detector orifice. Increasing V_A to 21, $[v_L^o, v_H^o] = [449, -778]$, with the detector geometry still the acting constraint on v_H^o. Apparently, as opposed to the $V_B = 15$ trajectories, these do not experience as great a radial displacement in the B field until higher values of V_A, and the increase of v_H^o forebodes the approach of the second crossing point to the

detector. However, at $V_A = 22$, the B field constraint begins reducing v_H^o, while v_L^o is rapidly increasing as the first (1,0) crossing point approaches the stopwire. Thus, maximum refocusing for (1,0) occurs at $V_A = 21$, drops to 0 by $V_A = 23$, and becomes nonzero again near $V_A = 30$, where $[v_L^o, v_H^o] = [+432, 488]$, from the first crossing now receding from the stopwire and the second (1,0) crossing near the detector orifice. Meanwhile, (2,0) begins focusing at $V_A = 16$, accounting for 13% of the refocused signal at $V_A = 22$, 100% at $V_A = 24$ to 29, and 96% at $V_A = 30$. For $V_B = 25$, $V_A = 5$ to 10 there is no contribution from (1,0), as its first crossing point is already within the B field and the trajectories have swung far from their mark when they reach the detector. The maximum attained near $V_A = 19$ from (1,0) occurs as its second crossing point passes through the orifice, and then soon drops as it again becomes detuned and the stopwire increases its effectiveness. The (2,0) state is already focusing at $V_A = 5$ slightly, and its refocusing gradually increases to $V_A = 30$. At $V_A = 27$ the (2, ±1) states begin to focus and at $V_A = 29$ the (3,0) also starts making a contribution. The $V_B = 30$ curve description is similar to that for $V_B = 25$. Thus, looking once more at Figure 3.10, the refocusing maxima for $12 < V_A < 20$ are due to (1,0) states, with the maxima for $V_B \gtrsim 20$ from (1,0) trajectories that have crossed the beam axis once far upstream from the detector, and the refocusing for $V_A > 22$ is primarily from (2,0) trajectories. Finally, as a reminder, Figure 3.10 is summed from contributions over the s distribution. For $s < s_0$, the A and B fields will have longer times to act on the traveling dipole, so that for a given V_B, the refocusing maximum will be shifted toward a lower V_A. The reverse is true for $s > s_0$. Thus the curves observed in Figure 3.10 are wider than what would have

been obtained for only $s = s_0$, and the maxima may be slightly shifted.

As described in the end of the theoretical section, we have also done trajectory calculations using variational theory to analyze the focusing in the A and B field regions. Figure 3.11 represents the refocusing curves for the same conditions as in Figure 3.11, with v_H^o now found using individual trajectory integrations through variationally calculated force fields, while v_L^o is still determined by second order perturbation (as the electric fields encountered near the beam's axis remain low and probably well characterized by this simpler method). Also, fewer "s" points were included to expedite the calculation, causing the greater roughness of Figure 3.11. The greatest changes occur in the magnitude of the refocusing maxima for $V_B \neq 20$ kV. A detailed analysis of the calculations indicates that, as expected, (1,0) trajectories are not as well focused in strong field regions as compared to the perturbation calculations. The A and B geometric constraints, as well as the detector orifice, restrict v_H^o significantly more in the variational calculation. It was shown in the previous paragraph that the $V_B = 20$ curve in the perturbative treatment was made from trajectories with primarily small radial displacements in the field regions. Thus the $V_B = 20$ refocusing curve was not effected as greatly when changing to the variational method. The $V_B > 20$ kV (1,0) maxima are most effected as, having been formed from trajectories that oscillated more than once across the beam axis, their dipoles have experienced larger radial positions in the focusing fields and the change to variation becomes more significant. The (2,0) parts of the curves do not change significantly. The locations of the curve maxima have not changed much either. Though the variational method is probably the more realistic one, its greater difficulty and the

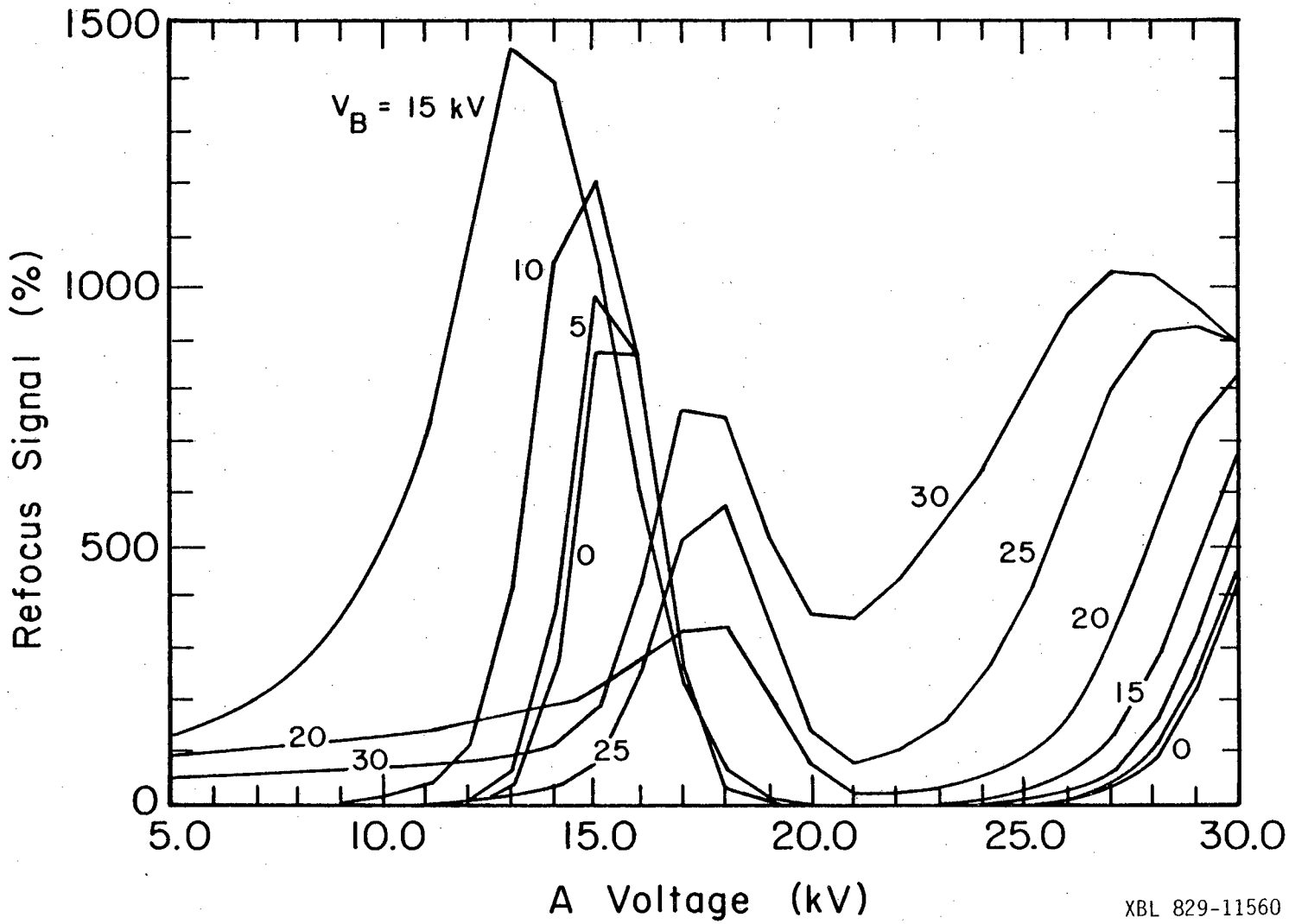

Figure 3.11. Same as Fig. 3.10, using variational theory for trajectories.

recentness of our development of it has constrained us to the use of the perturbative method for the remaining work shown here. In general, it should be remembered that the perturbation treatment over-predicts focusing by up to a factor of two at lower V_B, and somewhat more at greater B voltages.

A simulation of the refocusing for ClF using the perturbative treatment is given in Figure 3.12. The two major qualitative differences between Figures 3.10 and 3.12 stem primarily from the difference of rotational constants between OCS (6081MHz) and ClF^{35} (15484 MHz), as their dipole moments (0.709 and 0.888 D) and masses (60 and 54 amu) do not differ greatly. With the ratio μ/B roughly half as great for ClF, and referring to Figure 3.2, one would expect ClF to focus at roughly twice the voltages of OCS. Given that ClF is lighter, which enhances its focusability, the peak location in Figure 3.12 is rationalized. The enhanced amount of refocusing reflects the greater $J = 1$ population in the ClF beam, again due to its greater rotational constant and a beam temperature on the order of 3 K, as had the OCS simulated beam. The value of this simulation is further reduced by the unaccounted for presence of nuclear quadrupole coupling in ClF. Though discussed in more detail in the following chapter, briefly, with the presence of this coupling and a Cl nuclear spin of 3/2, the molecular states of ClF cannot really be described adequately using a (J,M) basis set. In fact, there are several states for ClF which in the strong field limit can be assigned, for instance, $J = 1$, $M_J = 0$, and each experiences somewhat different focusing effects in intermediate fields. Though a simulation including these effects is possible (Chapter IV will discuss the calculation of molecule state energy as a function of field strength for molecules like ClF),

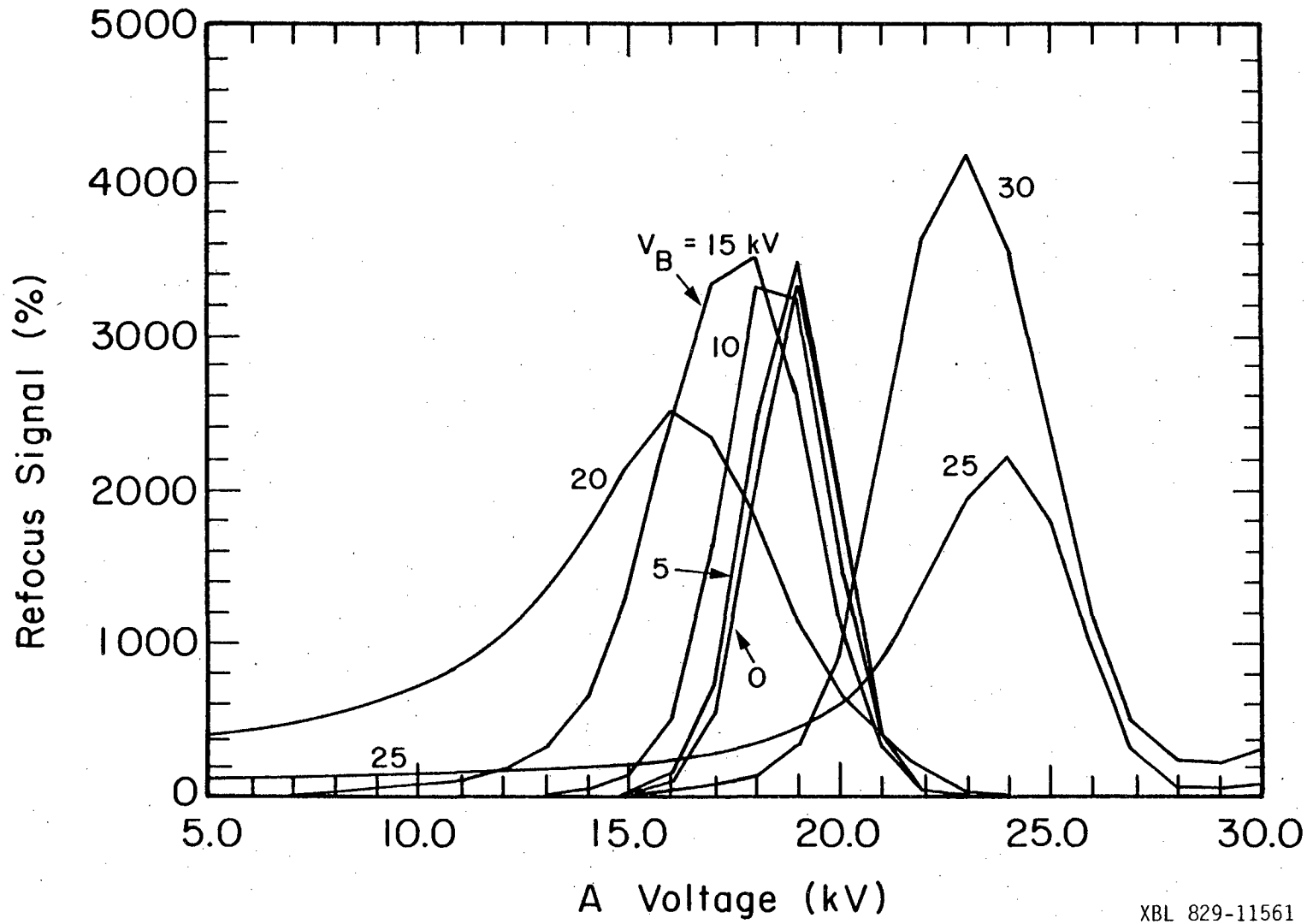

Figure 3.12. Simulated refocusing spectrum of ClF (3% in Ar, T_s = 293 K, T_b = 2.8 K (P_s = 1 atm, D_s = 100 μ)).

we have not done one at this time. Thus, Figure 3.12 is at most of only qualitative interest. Simulations were also done for HCl and HF, each showing refocusing only at greater V_A and V_B. HF refocuses better primarily because of its lower mass. Each have rotational constants an order of magnitude greater than that of ClF, explaining their requirement of high voltage focusing fields.

In comparing the experimental and theoretical refocusing results it is significantly simpler to note their differences rather than their similarities. Looking at Figures 3.7 and 3.10 (or 3.11), one notes that OCS at best refocused about 100%, an order of magnitude less than that predicted. Next, for each value of V_B, the experimental refocusing curves generally increase with V_A, with some peak structure superimposed. A similar effect is evident at low V_A as a function of V_B. There is nothing in our existing model that can account for this. An experiment was done using, in place of a stopwire, a target which allowed only those molecules to pass its central obstacle (of about the same diameter as a stopwire) that were within ca. ¼ cm of the beam axis. This was to test whether this phenomenon was due to voltage enhanced scattering toward the aperture axis, with the hope that the target would remove scattered molecules with unusually large radial displacements. The results when done under conditions as in Figure 3.8, were similar to that figure and lead to no better an understanding of what is happening here. The local maxima of the V_B = 0, 10 and 15 kV curves in Figure 3.7 are at greater V_A than in Figure 3.10, and shift toward greater V_A with increasing V_B, again as opposed to Figure 3.10. Surprisingly, the ClF spectrum of Figure 3.9 has more similarities with its counterpart in Figure 3.12, particularly if one recalls that using variational theory for the Stark

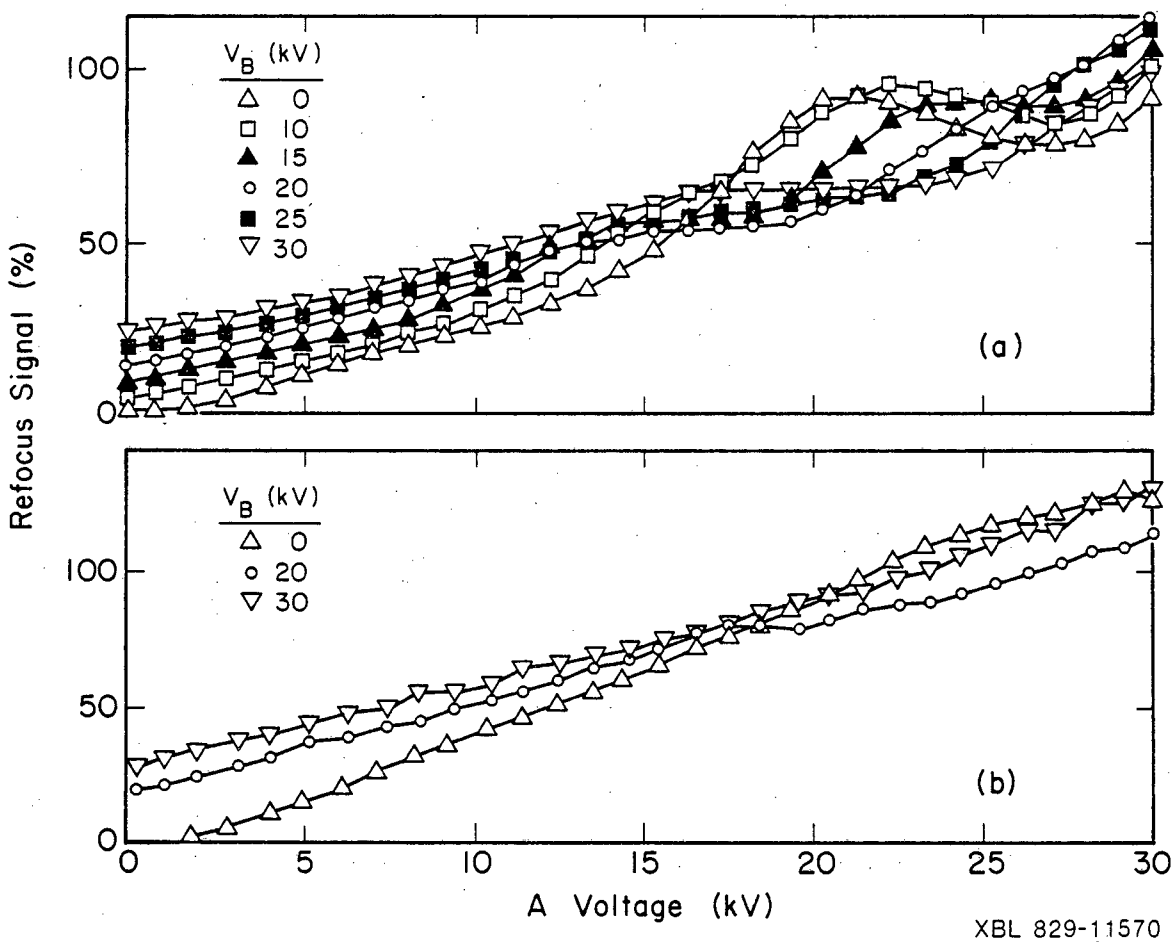

Figure 3.13. Refocusing spectra of OCS (5% in Ar, P_s = 1 atm). a) T_s = 75 C; b) T_s = 155 C.

effect would probably greatly reduce the V_B = 25 and 30 simulated curves, as happened with the OCS calculations. The ClF experimental spectra do not show the general increase of refocusing with V_A and V_B nearly as strongly as was evident in Figure 3.7 (and Fig. 3.8). These problems will be addressed again later.

As for similarities, Figure 3.7 does show bimodal behavior in the V_B = 0, 10 and 15 curves. The reduced refocusing maxima for $V_B \gtrsim 20$ kV compared to the lower values of V_B particularly predicted in Figure 3.11 is reflected here. In going from OCS to ClF, the predicted shift of refocusing maxima toward greater V_A is seen, and the ClF enhanced refocusing of up to 300%, as seen in Figure 3.9, also matches the theory qualitatively. Theoretical simulations of the OCS refocus spectrum with no stopwire, as with the experiment, gave results of the stopwired signal plus the 100% beam signal, [though somewhat larger enhancement for V_A and V_B > 20 kV]. The HF and HCl refocusing results were also qualitatively matched, with HCl not being seen to refocus and HF only slightly, at the highest voltages, though again the theory overpredicted the magnitude.

2. Refocusing as a Function of Source Conditions

Refocusing spectra of OCS (5% in Ar, P_s = 1 atm, D_s = 100 μ) are given in Figure 3.13 for T_s = 75°C and 155°C, to be compared with Figure 3.7. As can be seen, the three general trends with increasing T_s observed are 1) the total amount of refocusing increases slightly, 2) the location of the curves' maxima for V_B = 0, 10 and 15 has shifted to greater V_A, and 3) the various V_B curves become less distinct. Figure 3.14 portrays a ClF spectrum (3% in Ar, P_s = 1 atm, D_s = 100 μ) at T_s = 165°C. Comparing this with Figure 3.9, one sees that the refocusing

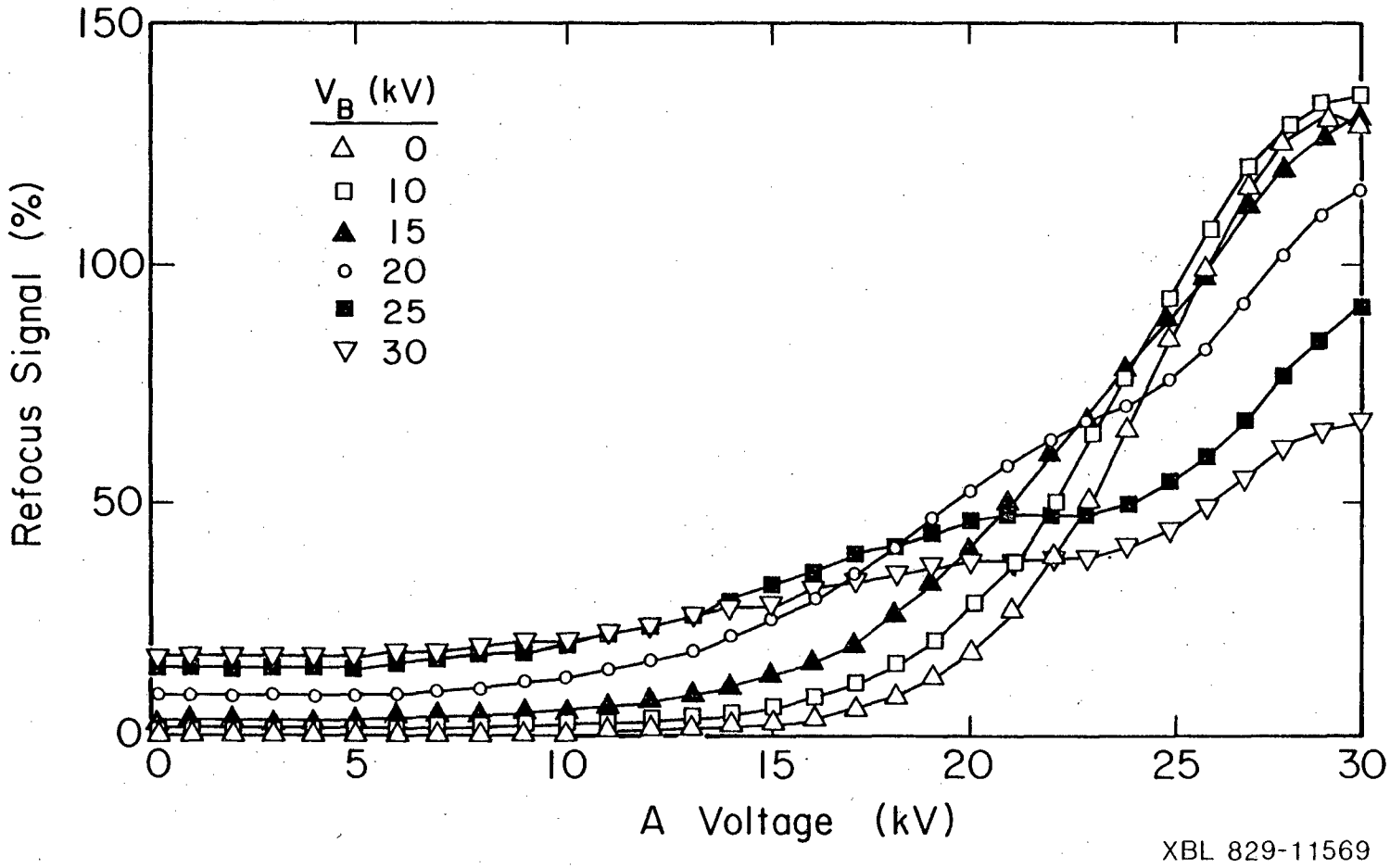

Figure 3.14. Refocusing spectrum of ClF (3% in Ar, P_s = 1 atm, D_s = 100 μ, T_s = 165 C).

maxima have shifted significantly and, in fact, appear to occur at $V_A > 30$ kV for $V_B > 0$ kV. On the other hand, the percent refocusing has decreased.

In Figure 3.15 we have plotted refocusing results for OCS as a function of the source pressure at T_s = 23, 75 and 155°C. At each temperature the A and B fields were fixed at the voltages that gave maximum refocusing for P_s = 1 atm. The signal intensity for a straight through beam changes with the source pressure, so each point on this plot was found by measuring both the stopwired, refocused signal and the "straight through" signal and taking their ratio. Direct comparison of the absolute refocusing at different T_s is difficult to interpret as different focusing voltages were used. However, the three curves do show maxima, and these maxima move to greater P_s with greater T_s. ClF refocusing versus P_s curves are given in Figure 3.16 at T_s = 22 and 165°C, and show a similar trend. Another set of refocusing versus P_s curves for OCS (12% in Ar) is given in Figure 3.17, where all were taken at $T_s \sim 115$°C, but with varying source nozzle diameters (D_s) of 100, 200, and 400 μ.[21] The trends observed in Figures 3.15-3.17 and other similar work on OCS refocusing can be qualitatively summarized thusly: at a fixed T_s and D_s, the refocusing curves go through a maximum as a function of P_s. In our range of studies from T_s = 20°C to 175°C, these maxima were at $P_s < 2$ atm. The maxima shift to greater P_s with either an increase in T_s or decrease in D_s. Generally the amount of refocusing at the maxima is greatest for large D_s values.

In other related work in our laboratory,[22] refocusing of OCS in 50% mixtures with He, N_2 and Ar were studied at T_s values from 22 to 140°C. With each carrier, the required focusing voltages for maximum signal

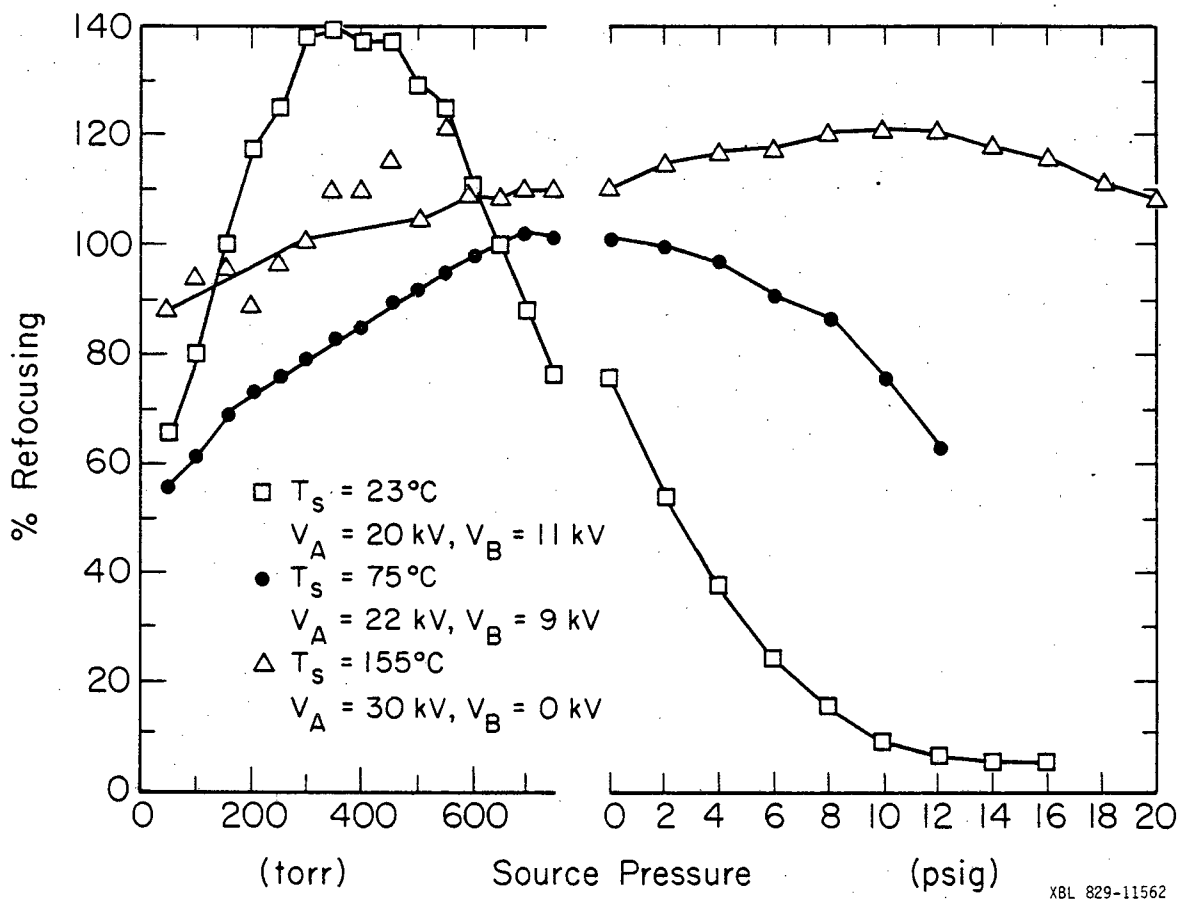

Figure 3.15. Refocusing signal as a function of source pressure for OCS (5% in Ar, D_s = 100 μ), at various T_s.

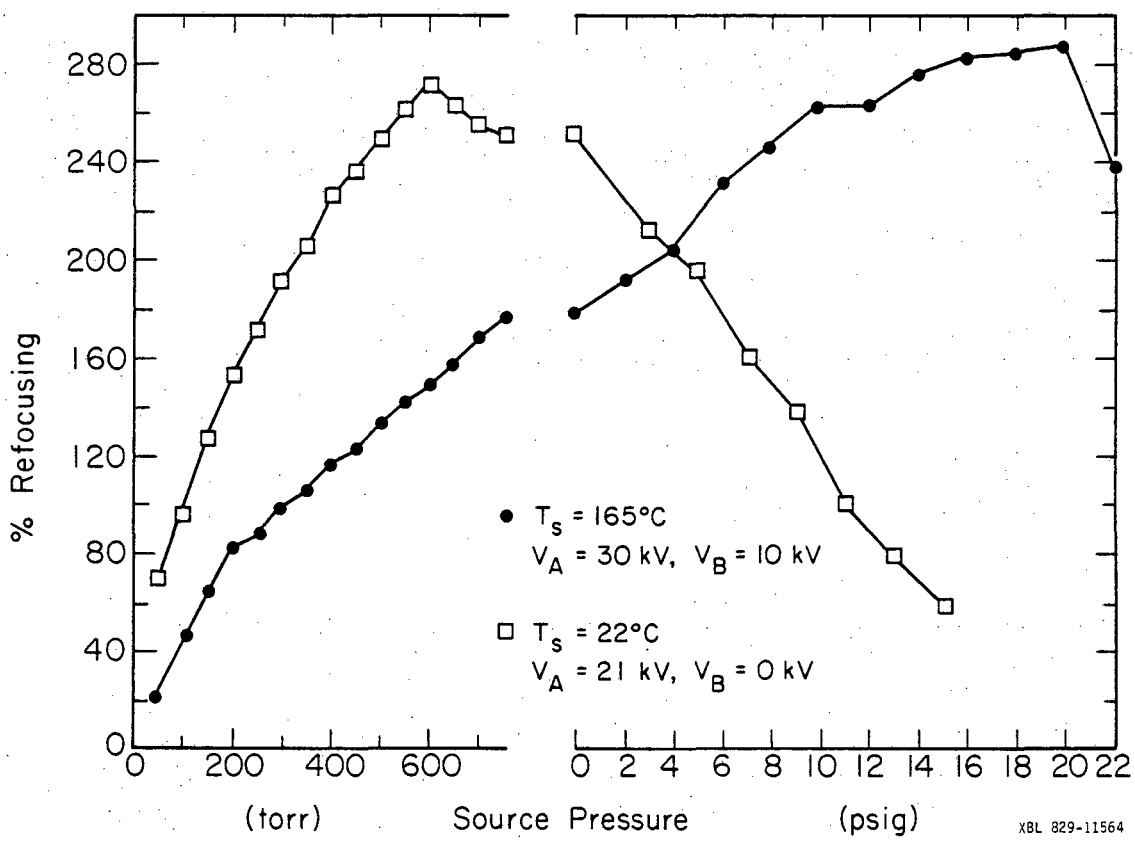

Figure 3.16. Refocusing signal as a function of source pressure for ClF (3% in Ar, D_s = 100 μ), at various T_s.

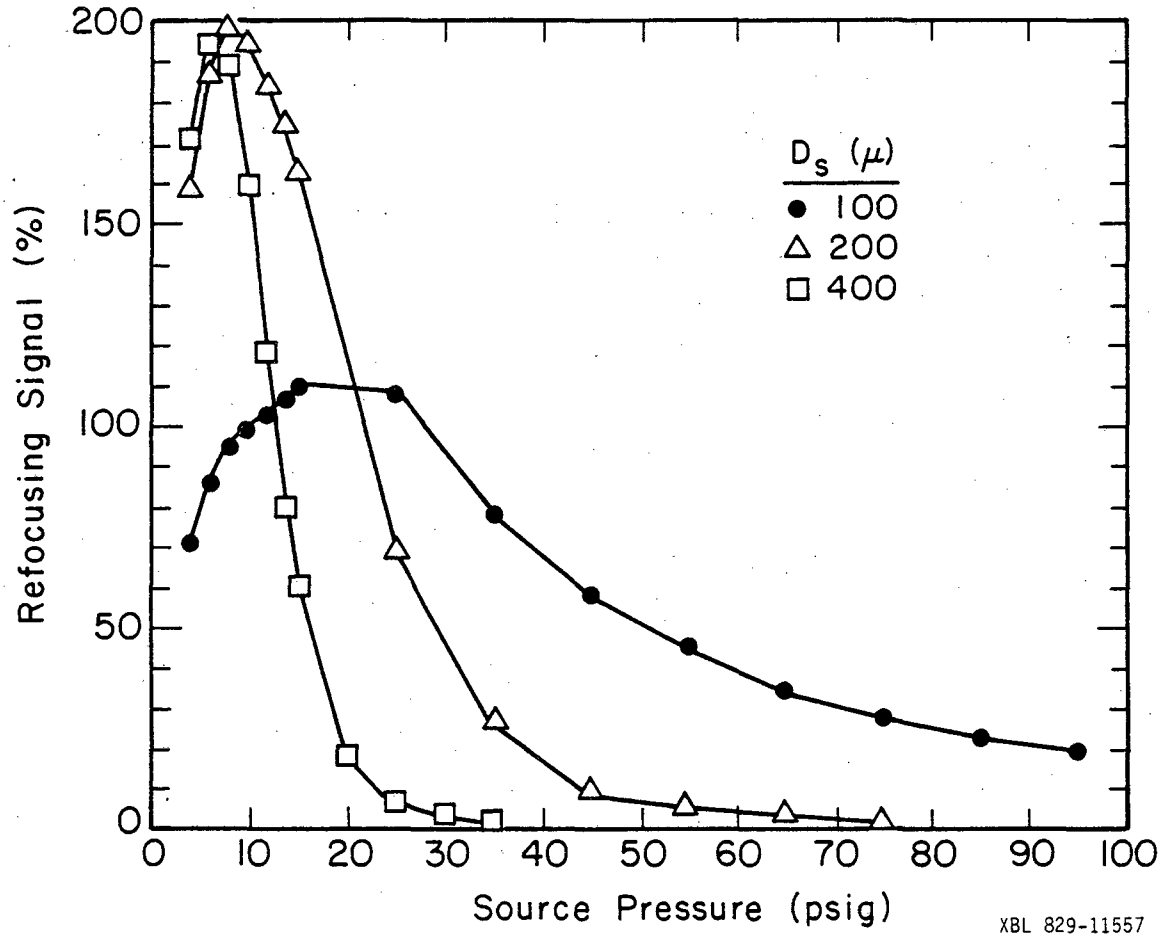

Figure 3.17. Refocusing signal as a function of source pressure for OCS (10% in Ar, T_s = 115 C) at various D_s.

increased with T_s and the refocusing intensity increased as well. In comparing the different carriers, the focusing voltages required for maximum intensity increase from Ar to N_2 to He. Time of flight analysis of 10% OCS in Ar beam was performed at a variety of source pressures, temperatures and nozzle diameters.[21] Using measured speed ratios (s_0/σ_b) and Equation (3.44), for T_s = 2.95 K and a D_s = 100 μ, we found beam temperatures of 4.3, 2.5, and 0.7 K for P_s = 1, 1.7 and 3 atm. At T_s = 390 K, T_b = 5.0, 4.0, and 3.8 K at P_s = 0.78, 1 and 1.7 atm, and at T_s = 446 K, T_b = 7.3, 4.1, 3.1, and 3.0 K at P_s = 0.65, 1, 1.7, and 2.3 atm.

The effect of changing T_s in the numerical simulations is demonstrated in Figure 3.18, where 50% OCS in Ar is refocused with source temperatures of 295, 353, and 413 K. Respective beam temperatures of 4.1, 5.6, and 7.3 K were calculated in the manner described previously, assuming D_s = 100 μ and P_s = 1 atm. Several trends ensue with the increase of T_s, including 1) for a given $V_B \neq 20$ kV, the maximum refocusing point shifts to a higher V_A, 2) the V_B = 20 kV curve shifts from peaking in the vicinity of the $V_B > 20$ kV curves toward the $V_B < 20$ kV curves, 3) the V_B = 15 kV curve increases in magnitude relative to the other curves, 4) the refocusing peaks widen slightly, and 5) the absolute amount of refocusing decreases. To better understand these kinds of trends, a series of calculations were performed in which the velocity distribution parameters s_0 and σ and a fixed rotational temperature T_R were directly inputted and varied independently. Varying s_0 alone one finds that the location of the focusing maxima for both the (1,0) and (2,0) peaks increase almost proportionally with s_0. The amplitudes of the (1,0) maxima are not greatly effected, while that of the second peaks decrease by

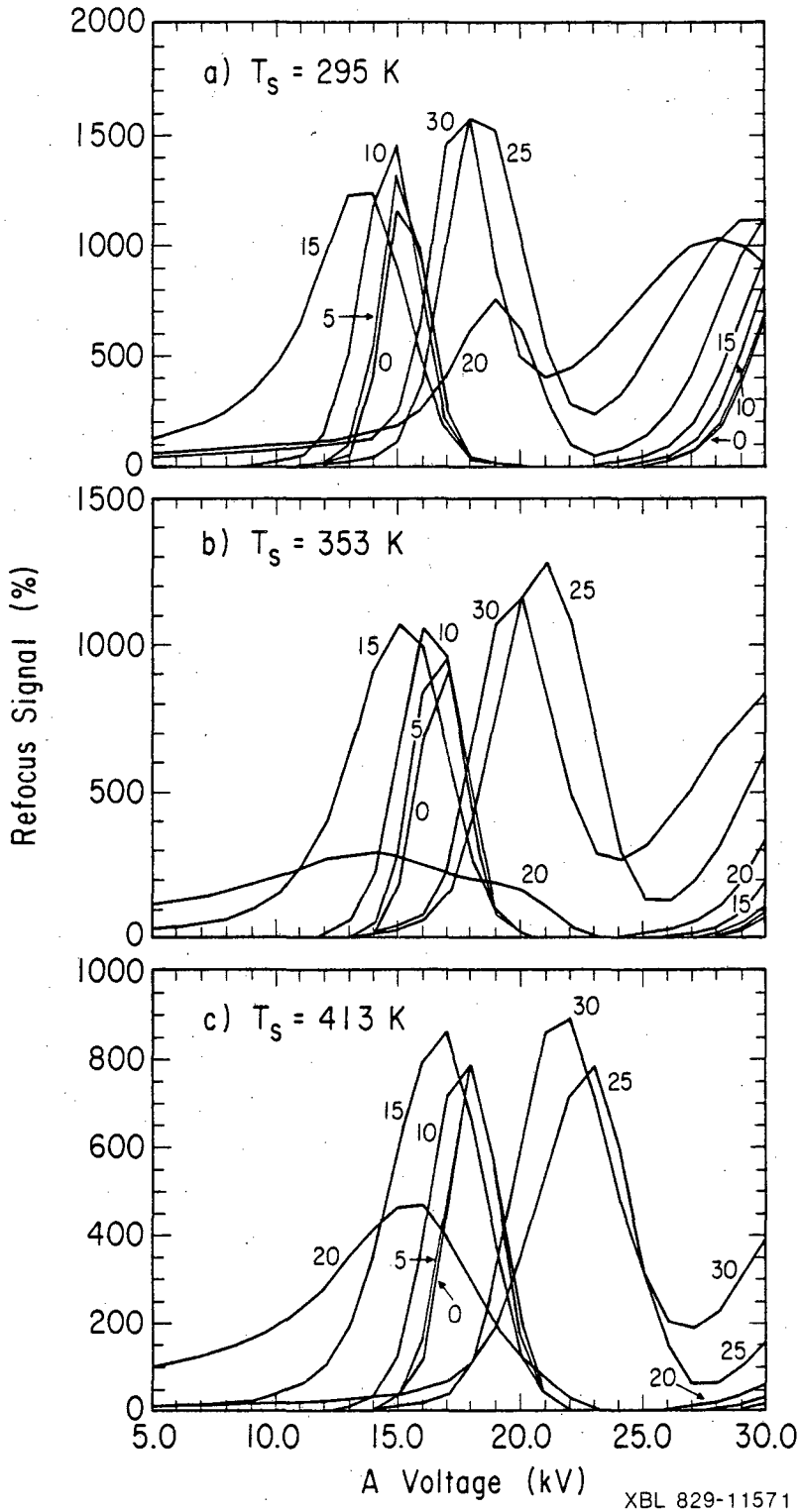

Figure 3.18. Simulated refocusing spectra of OCS (50% in Ar, P_s = 1 atm, D_s = 100 μ). a) T_s = 295 K; b) T_s = 353 K; c) T_s = 413 K.

roughly a factor of $\frac{1}{s_0^2}$. Effects (2) and (3) above are also solely dependent upon s_0, where increasing s_0 shifts the V_A maxima for individual V_B curves down, to the left, and then up from the V_B = 30 toward the V_B = 0 kV maxima. Varying σ had no effect on either the location of the maxima or on the refocusing percentage of the (2,0) peaks. There was a weak inverse dependence of the amplitude of the (1,0) peaks with σ, and increasing σ broadened the refocusing patterns. The amplitudesof the refocusing maxima were most strongly affected by varying T_R, where the amplitudes changed as $\frac{1}{T_R}$ for $T_R > 1$ K. Returning to the derivation of the distribution parameters from source conditions, simulations of 50% OCS in He and N_2 have been done. As expected, when compared with the similar calculations with an Ar carrier, the refocusing spectra show the evidence of increasing s_0 and decreasing T_R as one goes from Ar to N_2 to He.

To rationalize the experimentally observed refocusing maximum as a function of source pressure, we were left to conclude that we were observing dramatic changes in the beam's effective rotational temperature, as the calculations indicated that only T_R could have such dramatic effects on peak amplitude. Inputting directly T_s and T_b into our perturbative program gave the refocusing results in Table 3.5, for T_s = 20°C, and with V_A and V_B fixed at 15 and 11 kV, respectively, to coincide with a sizeable refocusing point from Figure 3.9. Here, T_R is set equal to $T_b(\alpha = 0)$. As can be seen, a refocusing maximum occurs near T_R = 0.8 K. Using Equation(3.62)to determine the value for T_R which maximizes the $J = 1$ population for OCS gives T_R = 0.682 K, which should be close to the rotational temperature for optimum (1,0) signal. On the left-most columns of Table 3.6 are calculated values for T_b for the typical pressures

Table 3.5

Calculated Refocusing as a Function of Inputted Rotational Temperature (OCS(10%/Ar), T_s = 20°C, V_A = 15 kV, V_B = 11 kV, α = 0)

T_R(K)	% Refocusing
2.0	2700
1.5	3180
1.0	3710
0.9	3770
0.8	3800
0.7	3770
0.682	3760
0.6	3640
0.5	3350
0.4	2800
0.3	1920
0.2	754
0.15	264
0.1	29
0.05	0.04

Table 3.6

Calculated Refocusing (%) as a Function of Source Pressure (P_s) for Various Values of α. Corresponding Calculated Beam Temperatures (T_b) and Fraction of Molecules in (J,M) = (1,0) for $\alpha = 0$ (R_{10}) also given. V_A = 15 kV, V_B = 11 kV, T_s = 293 K, OCS(10% in Ar)

P_s(atm)	T_b(K)	$R_{10}(T_R=T_b)$	α						
			-1	0	0.5	0.8	0.9	1.0	2.0
0.13(100 t)	14.5	0.019	120	360	710	1330	1790	930	220
0.26	8.6	0.031	230	640	1190	1990	2340	1450	350
0.39	6.3	0.042	340	920	1640	2520	2720	1880	460
0.53	5.0	0.51	480	1220	2100	2990	3040	2250	570
0.66	4.2	0.059	590	1430	2370	3170	3080	2320	670
0.79	3.7	0.066	690	1620	2610	3300	3100	2350	750
1.0	3.1	0.076	840	1910	2920	3430	3090	2370	870
1.2	2.7	0.84	960	2140	3160	3490	3060	2360	960
1.4	2.4	0.091	1080	2390	3360	3520	3020	2350	1030
1.6	2.1	0.100	1180	2570	3520	3530	2980	2330	1100
1.8	2.0	0.104	1280	2740	3640	3500	2930	2300	1130
2.0	1.8	0.111	1360	2880	3720	3440	2860	2240	1140

at which our experiments were run with OCS (10% in Ar) at T_s = 293 K, as derived from Equations (3,44) - (3.46). The calculated T_b do not go to low enough values to show the refocusing maximum of Table 3.5, though the T_s = 23°C experiment curve of Figure 3.15 evinces such a maximum at P_s ~ 300-400 t (0.39-0.53 atm). Thus, at this point, the model is probably either "greatly" overestimating the beam temperature T_b, or it is wrong to equate the beam translational temperature to its rotational temperature T_R. The time of flight analysis indicated that the former possibility is not correct, and, in fact, that beam temperatures are probably being overestimated. On the other hand, simply to set T_R to a value less than T_b counters the experimental results of other groups. Thus we were led to the α-type distribution of Equation (3.64), which allowed us to alter systematically rotational distributions of the core, and therefore the focusing part of the beam (with initial transverse velocities < 1000 cm/sec) toward lower effective rotational temperatures, while leaving the beam as a whole with a temperature comparable to T_b. In Table 3.6, calculated refocusing amplitudes with V_A = 15 kV, V_B = 11 kV, and T_s = 20 °C are given at various inputted pressures for α from -1 to 2. Of those shown, only for α = 0.8, 0.9, and 1.0 are there pressure dependent maxima. We have not ascertained if a particular α would have this maximum coincide with the experimental results. One notes that though the relative refocusing increase on the low pressure side of the maximum is similar to that seen experimentally in the T_s = 23°C curve of Figure 3.15, the higher pressure side does not have as fast an intensity dropoff. To the extent shown in Table 3.7 for T_s = 150°C, there is somewhat better qualitative agreement between the α = +1 calculations and the T_s = 155°C curve of Figure 3.15.

Table 3.7

Calculated Refocusing versus P_s. V_A = 15 kV, V_B = 11 kV, T_s = 423 K, OCS(10% in Ar)

P_s(atm)	T_b(K)	α 0	α +1
0.26	15.6	380	1250
0.53	9.0	690	1770
0.79	6.6	950	2050
1.0	5.5	1120	2170
1.2	4.8	1270	2240
1.4	4.2	1420	2290
1.6	3.8	1540	2312
1.8	3.5	1660	2322
2.0	3.2	1770	2323
2.2	3.0	1890	2318

3. Transition Signal Intensity as a Function of the A and B Field Voltages

The process that occurs in resonance spectroscopy was briefly described in Chapter I and will be discussed in full detail in the following chapter. Here we will restrict the discussion to transitions for OCS, as OCS can be accurately described with the (J,M) basis set. Furthermore, we will treat transitions phenomenologically, saying that with the C field at a frequency near resonance between two states (J,M) and (J',M'), some fraction of (J,M) molecules will become (J',M'), and the same fraction of (J',M') will become (J,M). Specifically, we will consider the (1,0) to (1,1) transition, where (1,1) represents actually both the $J = 1$, $M = 1$ and $M = -1$ states, which are degenerate in a Stark field. In discussing trajectories, we will let (1,0) refer to molecules which remain in that state throughout the spectrometer path, and $(1,0)^*$ to molecules initially in the (1,0) state, but becoming (1,1) in the C field, and thereby having (1,1) focusing properties within the B field. Similarly, $(1,1)^*$ will refer to molecules initially in the (1,1) state, but changed to the positive Stark state (1,0) in the C field. The theoretical simulations presented here give the calculated <u>difference</u> between the refocused intensity with no transitions occurring and with transitions occurring within the C field. Thus, a "flop out" signal due solely the loss of once focusable (1,0) trajectories to now no longer focusing $(1,0)^*$ trajectories is represented as a positive signal. The choice for the fraction of molecules in a state undergoing a transition has been set to 1.0. Smaller values would just reduce the scale of the simulations following.

Figure 3.19 represents the signal for the $(1,0) \leftrightarrow (1,1)$ transition calculated perturbatively as a function of the A and B field voltages,

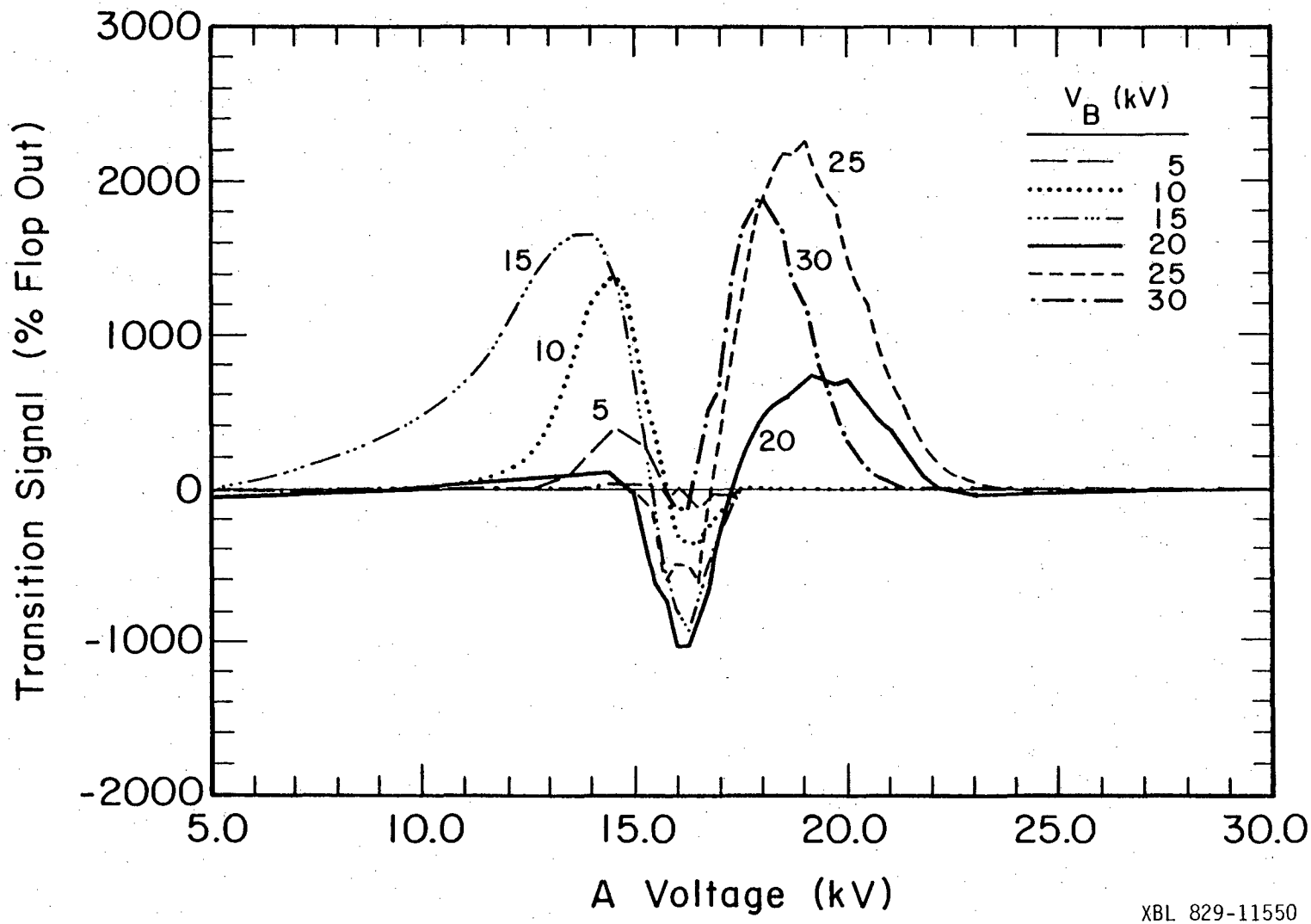

XBL 829-11550

Figure 3.19. Simulated transition signal for the (1,0) ↔ (1,±1) transition for OCS (10% in Ar, P_s = 1 atm, T_s = 293 K) as a function of A and B field voltage. Assumes 100% interconversion in C field.

with the same initial beam conditions that gave the refocusing spectrum of Figure 3.10. Once again, this result will be discussed in detail. There is no signal along the V_B = 0 kV curve as the trajectories of the (1,0) and $(1,0)^*$ states are the same (as are the (1,1) and $(1,1)^*$ states). With no trajectory changes, there is no difference in the signal with the transition off and on. As previously done in this chapter, we will use the V_B = 15 kV curve to typify the process for $V_B \lesssim 15$ kV. There we described the transverse velocity limits $[v_L^o, v_H^o]$ for the focusing (1,0) state, and indicated that the (1,1) molecules never refocus. Here, therefore, we will restrict our attention to the $(1,0)^*$ and $(1,1)^*$ trajectories, and their contribution to the transition process. For V_A from 5 to 13 kV, the $(1,0)^*$ velocity limits change from [82,30] to [127, 99]. As, for this range, $v_H^o < v_L^o$, $(1,0)^*$ do not refocus. As (1,0) states do refocus, there is a positive contribution to the refocusing signal. At V_A = 14 kV there is the largest positive transition signal. As noted before, the refocusing signal of (1,0) now begins decreasing as its trajectories' axis crossing points move upstream away from the detector. However, the $(1,0)^*$, with a large enough V_A to counter the defocusing of V_B = 15, also cross the beam axis, and as V_A increases, the crossing point of $(1,0)^*$ "rapidly" approaches the detector orifice. At V_A = 14 kV, for $(1,0)^*$, $[v_L^o, v_H^o]$ = [139,151], so that some of $(1,0)^*$ is focusing, i.e., not all of the molecules initially in (1,0) miss the detector when changed to (1,1). At V_A = 16 kV, $[v_L^o, v_H^o]$ = [173,825] for $(1,0)^*$, while for (1,0), v_H^o = -442. (Note that (1,0) and $(1,0)^*$ will always have the same v_L^o, as they are identical states up to the stopwire.) Thus, the computer predicts that at these focusing conditions the $(1,0)^*$ trajectories focus better than the (1,0) states. In a sense, the (1,0)

states are "overfocused" and swing wide of the detector, while the $(1,0)^*$ molecules enter the B field with transverse velocities directed toward the beam axis, and the field serves only to slow them down but not to deflect them off axis again. The transition signal becomes large, but negative. The v_H^o for $(1,0)^*$ at this voltage, as an aside, has been limited by the A field geometry. Further increasing V_A causes a quick decrease in v_H^o for $(1,0)^*$ as its crossing point enters the B field. Once a $(1,0)^*$ actually crosses within the B region, its radial velocity is accelerated away from the axis, so the $(1,0)^*$ focusing characteristics are quite "sharp" in terms of the acceptable V_A range. At V_A = 17 kV, the transition signal is positive again, and for $V_A \gtrsim 18$ kV, the $(1,0)^*$ molecules do not refocus at all. Meanwhile, back at V_A = 5 kV, $[v_L^o, v_H^o]$ = [74,168] for $(1,1)^*$. That is, while (1,1) was totally defocusing, $(1,1)^*$ is slightly focusable as the B field "pulls" the newly formed (1,0) states toward the axis. There are no dramatic changes as V_A increases for $(1,1)^*$. The larger V_A, the further the $(1,1)^*$ states are defocused before they enter the B field, the fewer the number of molecules the B field can refocus. The contribution of $(1,1)^*$ to the transition signal is negative and small, and only noticeable when the (1,0) state is no longer focusing, thus causing a slight negative transition signal. These results for the V_B = 15 kV curve are tabulated in Table 3.4.

As indicated before, the refocusing maxima for V_B > 15 kV occurred at those V_A where the (1,0) trajectories crossed the axis at the detector after crossing once before, and so were shifted to higher values of V_A. The $(1,0)^*$ axis crossing, however, is determined mostly by the magnitude of V_A and shows only little V_B dependence. Thus, for V_B = 20 kV, V_A = 16 kV, $[v_L^o, v_H^o]$ = [173,826] for $(1,0)^*$, and [173, -354] for (1,0),

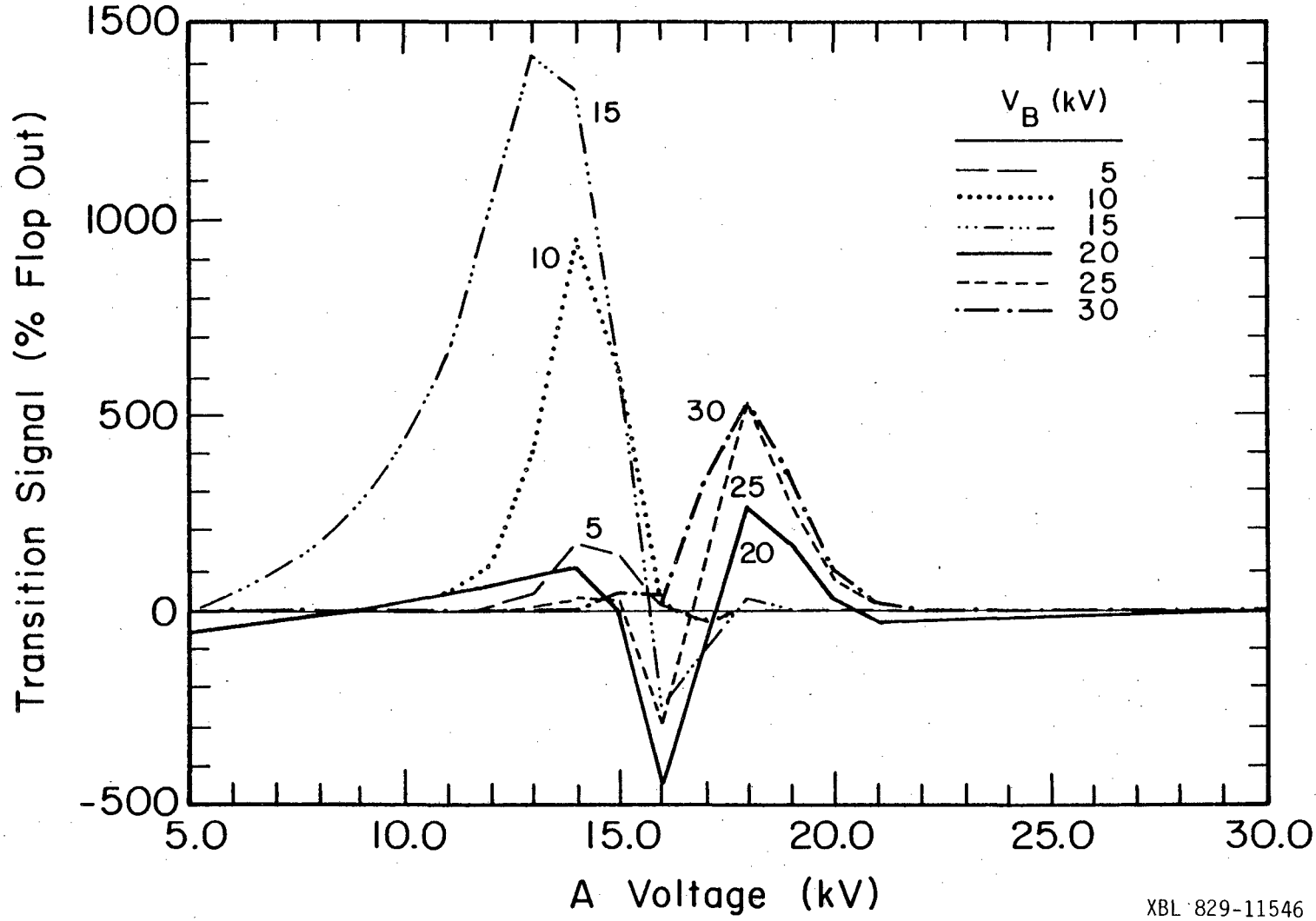

Figure 3.20. Same as Fig. 3.19, using variational theory for trajectories.

so a large negative transition signal is predicted. As the (1,0) state never focuses as well for $V_B = 20$ as for $V_B = 15$ kV, the positive signal at $V_A > 16$ kV is less for $V_B = 20$ than it was for $V_B = 15$ and $V_A < 16$ kV. The $(1,1)^*$ trajectories make more of a contribution at all V_A, so small negative transition signals are anticipated at $V_A < 10$, before the (1,0) state starts growing, and for $V_A > 22$, when the stopwire has begun effectively blocking (1,0). The situation at $V_B = 25$ and 30 kV is similar, except that as (1,0) can be better focused, the positive transition peak is larger, and that the $(1,0)^*$ and $(1,1)^*$ trajectories do not focus as well. Finally, comparing Figures 3.19 and 3.10, note that there are no $(1,0) \leftrightarrow (1,1)$ transition peaks predicted associated with the refocusing maxima at $V_A > 25$ kV, as that refocusing was due primarily to (2,0) states.

Figure 3.20 gives the variational calculation result to parallel Figure 3.19. The qualitative differences are the same as these between Figures 3.10 and 3.11, and negative transition signals are still predicted. In Figure 3.21 are the transition curves calculated for the $(2,0) \leftrightarrow (2,1)$ resonance. Though (2,1) is a positive Stark state as is (2,0), it does not focus as well and a transition, in principle, should be observable. The $(2,1) \leftrightarrow (2,2)$ transition cannot be seen significantly for V_A and $V_B \lesssim 30$ kV as (2,1) is not focusing well yet. The effect of increasing the source temperature to 150°C is seen in Figure 3.22 (the concentration of OCS has also been reduced here), essentially shifting the transition pattern to greater V_A.

Experimental OCS transition curves as a function of A and B field voltages are given in Figures 3.23 and 3.24, at beam conditions corresponding to the experimental refocusing spectra in Figures 3.8 and

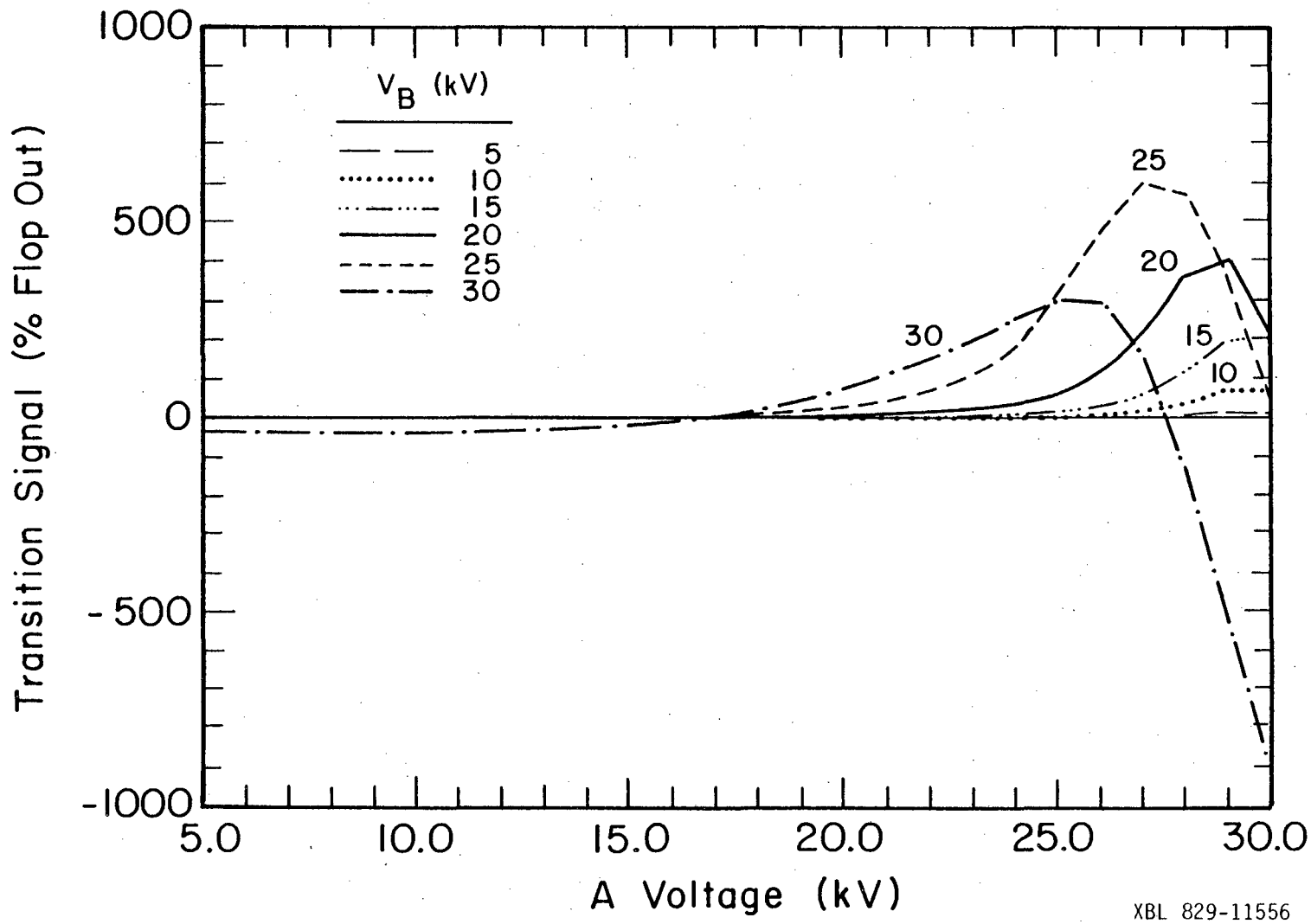

Figure 3.21. Simulated transition signal for the (2,0) ↔ (2,±1) transition of OCS (same conditions as Fig. 3.19).

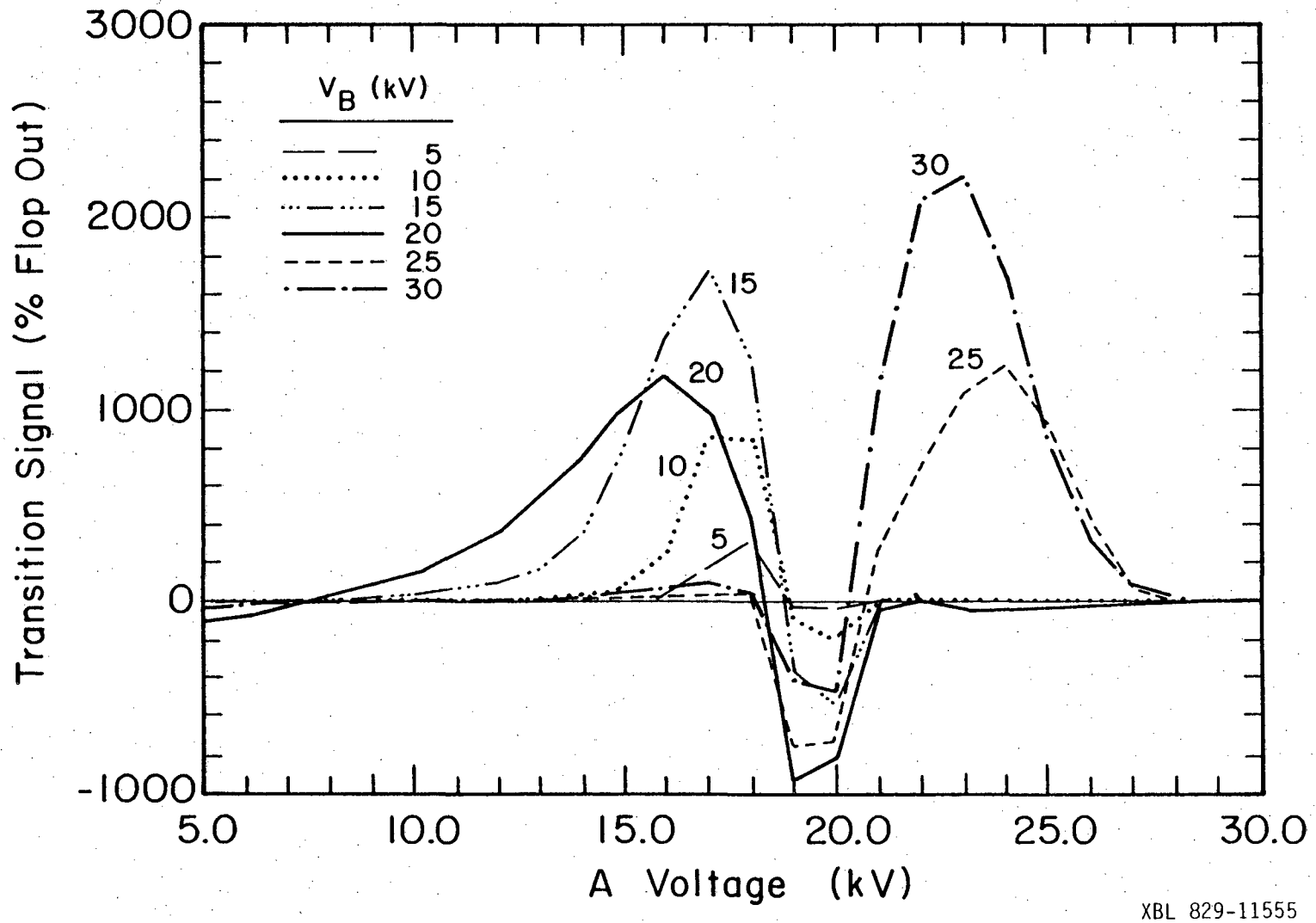

XBL 829-11555

Figure 3.22. Simulated transition signal for the (1,0) ↔ (1,±1) transition for OCS (same conditions as Fig. 3.19, except T_s = 423 K).

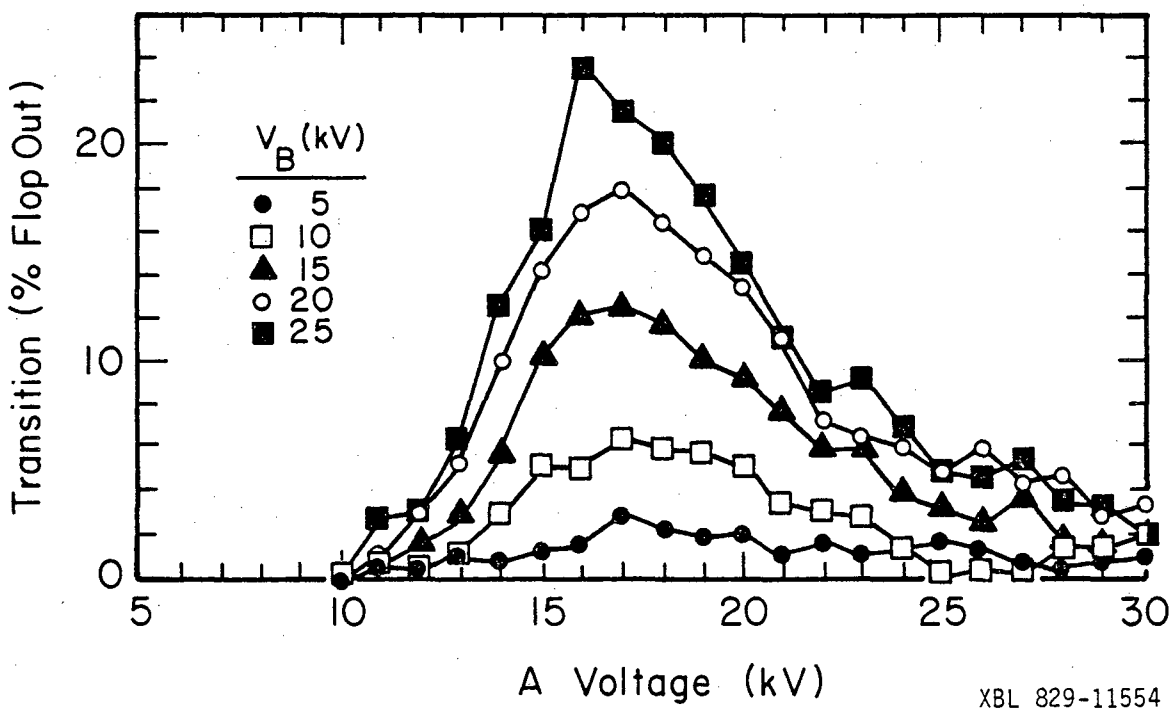

Figure 3.23. Experimental transition signal for the (1,0) ↔ (1,±1) transition for OCS (10% in Ar, P_s = 1 atm, T_s = 300 K, D_s = 200 μ) V_{DC} = 310 V, V_{RF} = 15 V, ν_{RF} = 307 kHz, as a function of A and B field voltage.

3.13b. In Figure 3.23, the C field dc voltage was 310.0 V with an rf voltage of 15 V at 307 kHz and a source temperature of 300 K (D_s = 200 μ, P_s = 1 atm). This transition pattern was found to be independent of the dc voltage with the appropriate radiofrequency. Figure 3.24 arises from T_s = 150°C, P_s = 2 atm, D_s = 100 μ, and C field conditions V_{DC} = 1043 V, V_{RF} = 8 V and ν_{RF} = 3478.5 kHz. Additional detail is supplied for the V_B = 25 kV curve. The negative transition signal seen in this figure has not been previously reported for typical MBER flop out type experiments. We have also observed such a "flop-in" signal for room temperature beams.[25] Finally, we note here that we have observed refocusing effects of up to ca. 10% by changing the buffer field or C field dc voltages for given settings of the A and B fields. We have no explanation for this phenomenon aside from the possible occurrence of "nonadiabatic" transitions after the A field which are reduced by these transversely homogeneous fields.

C. Discussion

1. Refocusing Spectra

We do not have a good understanding of the mismatch we have observed between the experimental and theoretical refocusing plots for OCS (cf. e.g., Figures 3.7 and 3.10). We found no way experimentally to reduce the underlying monotonic increase of refocus signal with the A and B field voltages, with such attempted methods as changing source conditions, changing the background scattering and stopwire configuration within the spectrometer chamber, and altering the detector orifice diameter. For V_A < 10 kV, the refocusing curves in Figure 3.7 increase as V_A^n with n = 1.456 ± 0.002. Theoretically, we could find no combination of inputted

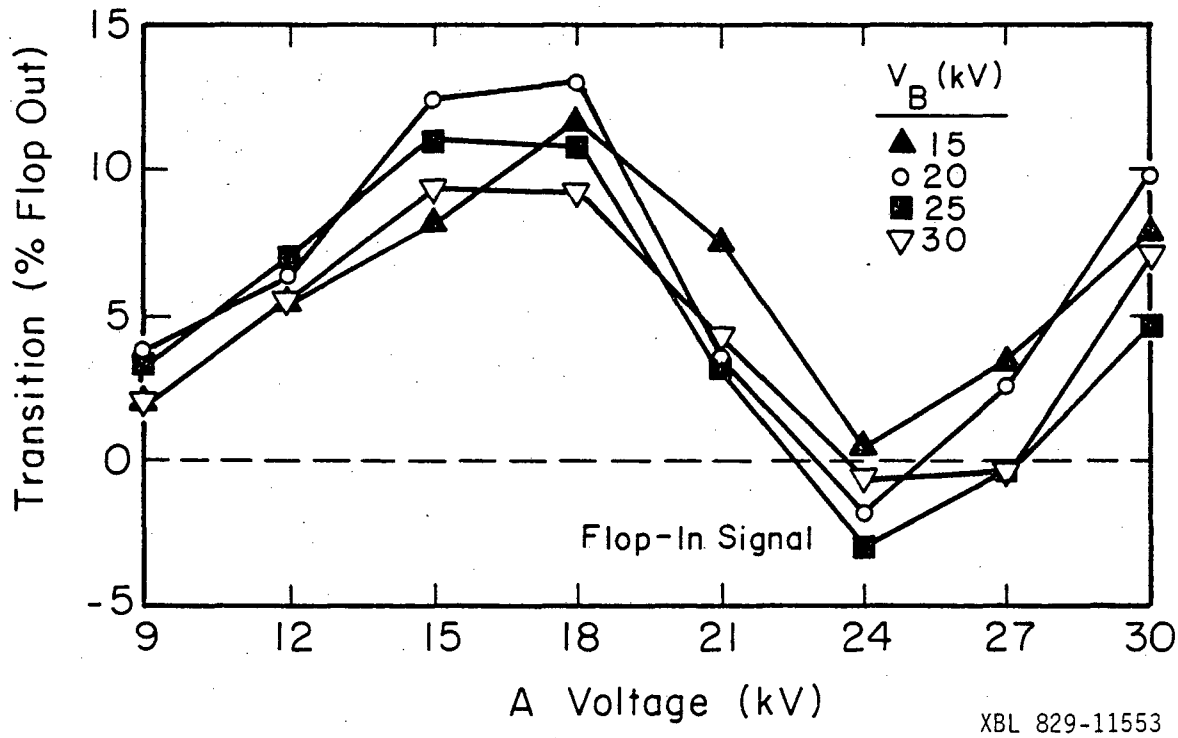

Figure 3.24. Experimental signal for the (1,0) ↔ (1,±1) transition of OCS (3% in Ar, P_s = 2 atm, T_s = 427 K, D_s = 100 μ), V_{DC} = 1043 V, V_{RF} = 8 V, ν_{RF} = 3478.5 kHz.

parameters to duplicate this behavior. The fact that ClF refocusing essentially does not follow this behavior does not help our understanding. The experimental lack of the predicted refocusing intensity is also not understood. It does not seem unreasonable to have refocusing on the order of 1000%, as even our variational calculations predict. There are three possible explanations that occur to us presently. First is the possible inadequacy of our initial theoretical velocity and rotation distribution. Time of flight studies, however, indicate that the beam does have the expected translational properties. The rotational distribution will be discussed in the following section. For now it will just be said that other experimental evidence suggests that using a Maxwell-Boltzmann rotational distribution with the rotational temperature equated to the beam temperature underestimates the $J = 1$ population, so this does not aid in the explaining of this intensity discrepancy. The second possibility is suggested by the previously reported effect of C field dc voltage on refocusing, indicating that nonadiabatic transitions may be occurring after the A field, which is not included in our simulation. Dipolar molecules traveling suddenly from a high to low electric field region may experience Fourier components in the field change resonant to transitions, and the molecules once (1,0) become no longer focusable. As will be shown in the appendix to Chapter IV, however, this effect is expected to be minimal. Finally there is the possibility of some kind of scattering in the experiment that either depletes the refocused signal or enhances the straight through beam signal that is used for normalization. If the problem is experimental and if it could be remedied to give the predicted refocusing, the signal-to-noise in MBER experiments would, in turn, be greatly improved. In any case, as long as the match

between our experimental and theoretical results is so inconsistent, the use of this method in conjunction with the resonance theory of the following chapter to predict velocity convoluted resonance spectra remains questionable.

The better quality of the refocusing spectra of Toennies, et al.[3] is not surprising, given that their focusing fields are of lengths 194[3a] and 169 cm[3b] and that they are working with alkali halides, with almost an order of magnitude greater dipole moments than the linear molecules we have been studying. They indicate in their numeric simulations of the refocusing for CsF in Reference 3b that using only second order perturbation theory for the Stark effect can cause error, and therefore add a fourth order term and use Monte Carlo techniques for careful fitting of their experimental results. We question their exclusion of multiple crossing trajectories in their analysis, as both our work and that of English and Gallagher[5] indicate their contribution to calculated intensities. As Toennies, et al. normalize the amplitudes of their simulations to their experimental results, it is not clear if they find a difference between the predicted and observed absolute intensities. As Wicke[2] suggested, both Toennies and we find a longitudinal velocity selection with given focusing field voltages.

We find the flop-in resonance signal of Figure 3.24 an interesting phenomenon. As such an occurrence is predicted in the simulations, we cautiously suggest that our observed flop-in signal arises from the enhanced focusing of $(1,0)^*$ trajectories over that of the (1,0) trajectories not undergoing transitions to the "defocusing" (1,1) state. Why we did not observe this at lower source temperatures earlier is not understood.[25] Continued experimental investigation of this may suggest different applications of MBER work.

2. Molecular Beam Energy Distribution

There have been a significant number of studies concerning the internal molecular energy relaxation that occurs in an adiabatic expansion. In general it has been found that vibrational relaxation occurs to some extent, but rotational relaxation is much more complete. To state this in a more quantitative manner it has been loosely assumed that the vibrational and rotational state distributions are still "statistical" following the expansion and can be characterized with Boltzmann distribution functions and corresponding "temperatures" T_{vib} and T_{rot}, where T_{rot} is generally found to be on the order of T_b, the beam translational temperature, and T_{vib} less than the source temperature T_s, but still significantly greater than T_b. The questions we wish to address here are how much rotational relaxation occurs and is the rotational distribution really statistical in the expanded beam.

In the Xe seeded CsF, electric quadrupole selector work of Borkenhagen, Malthen, and Toennies[3d] their focusing spectrum for a T_s = 800 K, P_s = 780 t beam was best fit numerically assuming a rotational temperature T_R = 6 K, as compared to a measured translational temperature, by time of flight analysis, of $7.5\ ^{+2.0}_{-1.5}$ K. This, they suggested, infers that rotational relaxation occurs on the order of one collision during the expansion process, and that this, in turn, is rationalized by the strong potential energy anisotropy that these polar molecules can experience in collisions where the relative velocities are only on the order of 2500 cm/sec. In fact, the initial radial velocities of their focusable molecules will be an order of magnitude smaller, lending more support to the effectiveness of collisions for rotational cooling. Using laser induced fluorescence (LIF) and time of flight (TOF)

techniques, Bergmann, et al.[23] studied the dependence of the velocity distribution of Na_2 in a molecular beam as a function of its quantum state. In general they found that a greater internal energy state tended to have a wider velocity distribution, suggesting to them that assuming a uniform T_b for all quantum states is probably a bad approximation. Of particular interest to us is their finding a lower speed ratio (s_0/σ) for $v = 3$, $J = 43$ than for $v = 3$, $J = 13$, indicating that the rotational state alone is somehow correlated to that state's velocity distribution. Bennewitz and Buess[24] used MBER to study the vibrational relaxation of CsF and LiF with several different seeds. Among their results, they noted in work with CsF in Ar different values of T_{vib} along the centerline and boundary of their jet, indicating relaxation as a function of transverse velocity. Furthermore, they found less vibrational relaxation of molecules with longitudinal speeds 1.19 s_0 and 0.86 s_0, than at s_0, where s_0 was their beam's flow velocity. Both of these results are explained by relating the number of collisions a single molecule experiences in the expansion with its final velocity relative to the beam flow velocity. Those molecules traveling significantly faster, slower or in a different direction from the beam flow had fewer "cooling" collisions, and so their T_{vib} was correspondingly greater. On the other hand, in the work of McClelland, et al.[18] using LIF to study seeded I_2 beams, they found vibrational and rotational distributions which were of Boltzmann form. The distributions they found, however, represented molecules from the full cross section of their beam, unlike the MBER work just previously mentioned which sampled particular velocity groups. Finally, we mention the work of Kukolich, et al.[4] where a microwave resonance cavity was used in conjunction with a quadrupole and

single wire focusing fields to study the population in the J = 0,1 and 2 states of OCS from a supersonic source. They found quite strong evidence of a non-Boltzmann rotational distribution, but assign rotational temperatures T_J to each state as a function of the source pressure < 150 t, in general finding $T_0 < T_1 < T_2$. Their comparison of these temperatures loses some meaning, however. As Bennewitz[24] pointed out, and our results concur, different focusing fields result in the sampling of different parts of the initial velocity distribution, so that Kukolich's various T_J are in some sense not from the same beam for different values of J.

Aside from the work of Kukolich there has been little work done investigating the nonstatistical rotational distribution in a molecular beam. The argument that Bennewitz gives concerning the effect of expansion collisions on vibrational cooling and the resulting correlation of T_{vib} to different velocity groups within a beam we feel should hold at least as strongly for the beam's rotational distribution. Furthermore, as it is inherent in an MBER setup to be working at focusing voltages that best collect molecules with longitudinal velocities near the most probable value of s_0, and that only low initial radial velocities v^o are focusable, one is apt to observe a rotational distribution significantly "colder" than a rotational temperature that might characterize the beam as a whole. In Figures 3.15-3.17 we demonstrated a peaking of OCS refocusing strength as a function of source pressure, P_s, under various conditions. We believe the maxima correspond to those conditions which have maximized the J = 1 population in the central part of the beam. Using Equation (3.62) and the rotational constant for OCS (0.291 K), this corresponds to a local rotational temperature of 0.682 K. On the other hand, both TOF measurements and the use of the beam temperature calculation

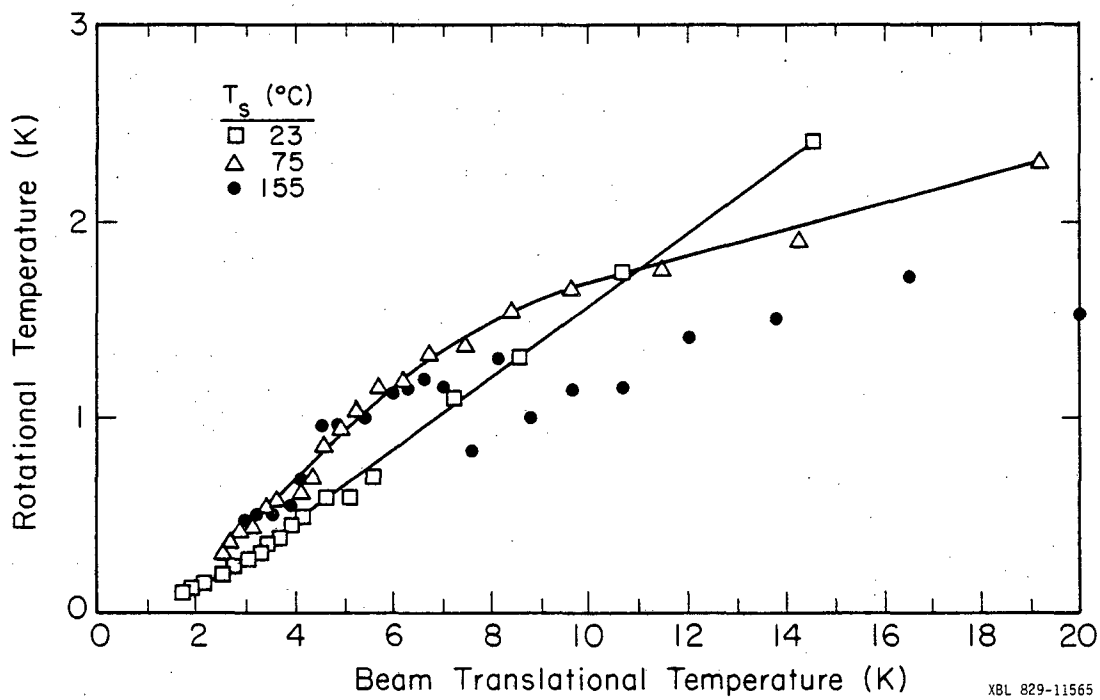

Figure 3.25. Calculated rotational temperature versus calculated beam temperature (see text for method) for OCS (3% in Ar, D_s = 100 μ, various source pressures).

methods of Anderson and Fenn[16] indicate significantly greater beam translational temperatures at these conditions. The drop in refocusing at higher values of P_s corresponds to the depopulating of the $J = 1$ states as most of the core molecules relax to $J = 0$. An obvious way of treating the results of Figure 3.15 is to assume that the refocusing intensities vary directly as the $J = 1$ population. Using Equation (3.62) and further assuming that the maximum refocusing points are at $T_R = 0.68$ K, a rotational temperature can be assigned to each data point. Meanwhile one can use Equations (3.44) - (3.46) to estimate beam translational temperatures from the values of P_s and T_s. A plot of calculated T_R vs T_b for source temperatures of 23, 75, and 150°C is given in Figure 3.25. The curve for $T_s = 23°C$ is quite linear for $T_b > 2.5$ K, with a slope of 0.20. The rate of T_R decrease with T_b clearly has to reduce at low T_b. There would be little physical meaning and no mechanism is apparent for there to be a population inversion which is required for negative values of T_b. The $T_s = 75°C$ curve seems to have two linear components of slopes 0.07 for $T_b > 8$ K and 0.25 for $T_b < 8$ K. The data for $T_s = 155°C$ are too scattered for a curve to be drawn. Admittedly this analysis suffers from a complaint similar to that expressed of Kukolich's results. Working with beams of different flow velocities, the fraction of velocity groups focused varies with s_0.Even in our trajectory simulations, as shown in Table 3.5, we predict maximum refocusing at a fixed V_A and V_B at $T_R \sim 0.8$ K. However, the linearity of the $T_s = 23°C$ curve in Figure 3.25 and the general phenomenon of loss of refocusing at higher pressures, we feel, is compelling evidence of the center beam enhanced relaxation.

The rotation distribution introduced in Equation (3.64) was an attempt to put a systematic dependence of the rotational distribution on a molecule group's velocity distribution. Its form was based on a

correlation of the rotational energy to the translational energy in a frame moving at the beam's flow velocity $s_0\hat{\underset{\sim}{k}}$. The parameter α allowed a linear flexibility for this correlation. In the refocusing simulations for $|\alpha| \leq 1$ the effect of varying α was similar to that of simply changing the rotational temperature of the entire beam. Again, this reflects that primarily the center part of the molecular beam is involved in focusing. There is not enough flexibility in Equation (3.64), however, to mimic well the experiment effects seen in Figures 3.15-3.17, as can be seen in the results of Table 3.6. Values of α near 0.9 do predict refocusing maxima as a function of P_s with $T_s = 20°C$, but this refocusing does not drop off nearly fast enough at higher values of P_s. An example of another interesting property of this rotational distribution form is shown in Table 3.8. The distribution of Equation (3.64) was integrated over the beam velocity variables s and v with $\alpha = +1$ and $T_b = 1.0$ K for OCS, yielding theoretical fractional populations for each J state for the full beam. From these values of N_J/N, and using Equation (3.62) as a definition of T_R (assuming the partition function Q is fixed), rotational temperatures for each J state are estimated using two different methods indicated in the table. Apparently, this distribution predicts that T_R increases with J. This parallels the experimental observations of Kukolich, et al.[4]

In conclusion, we have experimentally obtained Stark refocusing spectra of OCS and ClF as functions of the A and B fields and the source gas composition, pressure, temperature, and nozzle diameter. Computer simulations were attempted to better understand the molecular beam dynamics in an MBER apparatus. For unknown reasons, though some general

Table 3.8

Fractional Rotational State Populations and Rotational Temperatures for $\alpha=1$, $T_b = 1.0$ K (OCS)

J	N_J/N	$T_{R_J}^{(1)}$ (K)	$T_{R_J}^{(2)}$ (K)
0	0.262	-	-
1	0.347	0.36	0.72
2	0.217	0.67	1.19
3	0.104	0.95	1.64
4	4.38×10^{-2}	1.22	2.09
5	1.69×10^{-2}	1.47	2.53
6	6.13×10^{-3}	1.72	2.97
7	2.14×10^{-3}	1.96	3.42
8	7.20×10^{-4}	2.20	3.86

(1) Calculated via

$$T_{R_J} = \frac{BJ(J+1)}{+k\ln(\frac{(2J+1)}{QN_J/N})}$$

(2) Calcuated via

$$T_{R_J} = \frac{2BJ}{k\ln(\frac{N_{J-1}}{2J-1} \cdot \frac{2J+1}{N_J})}$$

properties were numerically reproduced, many qualitative features of the experimental work were not. Among the more interesting aspects of this work was the observation of a "flop-in" signal for OCS at higher source temperatures. More importantly, there is strong evidence given that the rotational energy distribution sampled by the focusing fields is significantly colder than the beam's translational temperature and the suggestion that this points toward a nonstatistical rotational distribution.

It would be beneficial both for better understanding the apparatus and for result analysis to find the cause for our experimental and theoretical discrepancies. More emphasis in the future should be placed on doing variational trajectory calculations. As for the study of the beam energy distribution using MBER, much can be done. Continuing along our experimental lines, the inclusion of a velocity selector in front of the focusing fields, as Toennies, et al. have done, can allow the probing of rotational distributions as a function of molecule velocity. Working with longer fields or more polar molecules would allow the probing of several rotational states. In a different direction, the use of laser induced fluorescence techniques and Doppler tuning could allow the probing of a molecular beam for the coupled velocity-rotation distribution. On the theoretical side, statistical mechanic work is required to develop adequate models for supersonic beams that no longer treat velocity, rotation and vibration independently.

REFERENCES and NOTES for CHAPTER III

1. T. R. Dyke, G. R. Tomasevich, W. Klemperer, and W. E. Falconer, J. Chem. Phys. 57, 2277 (1972).

2. B. G. Wicke, J. Chem. Phys. 63, 1035 (1975).

3a. H. Malthan and J. P. Toennies, Proceedings of the Ninth International Symposium on Rarefied Gas Dynamics, ed. by M. Becker and M. Fiebig (Gottingen, 1974), p.C. 14-1;
b. J. E. Mosch, S. A. Safron, and J. P. Toennies, Chem. Phys. 8, 304 (1975);
c. R. Grice, J. E. Moseh, S. A. Safron, and J. P. Toennies, J. Chem. Phys. 53, 3376 (1970);
d. V. Borkenhagen, H. Malthen, and J. P. Toennies, J. Chem. Phys. 63, 3173 (1975).

4. S. G. Kukolich, D. E. Oates, and J. H. S. Wang, J. Chem. Phys. 61, 4686 (1974).

5. T. C. English and T. F. Gallagher, Jr., Rev. Sci. Inst. 40, 1484 (1969).

6. R. A. Berg, L. Wharton, W. Klemperer, A. Büchler, and J. L. Stauffer, J. Chem. Phys. 43, 2416 (1965); E. W. Kaiser, J. S. Muenter, W. Klemperer, and W. E. Falconer, J. Chem. Phys. 53, 53 (1970).

7. L. Wharton and P. J. Dagdigian, J. Chem. Phys. 57, 1487 (1972); J. Chem. Phys. 57, 710 (1972); J. Chem. Phys. 55, 4980 (1971).

8. H. G. Bennewitz, W. Paul, and C. Schlier, Z. Physik, 141, 6 (1955).

9. P. Kusch and V. Hughes, in Ency. of Physics (Springer-Verlag, Berlin, 1959) 37, 1.

10. N. F. Ramsey, Molecular Beams (Oxford University Press, London, 1956), pp. 287-98.

11. R. G. J. Fraser, Molecular Rays (Cambridge University Press, Cambridge, 1931), pp. 154-60.

12. C. H. Townes and A. L. Schawlow, Microwave Spectroscopy (McGraw-Hill Book Co., New York, 1955).

13. A. C. Legon, D. J. Millen, and S. C. Rogers, J. Mol. Spec. 70, 209 (1978).

14. R. R. Herm and D. R. Herschbach, "Inhomogeneous Electric Deflecting Field for Analysis of Rotational Excitation in Reactive Scattering of Molecular Beams", UCRL-16039 (Lawrence Radiation Laboratory, Berkeley, 1965).

15. A. Kantrowitz and J. Grey, Rev. Sci. Inst. 22, 328 (1951).

16a. J. B. Anderson and J. B. Fenn, Phys. Fluids, 8, 780 (1965);
b. J. B. Anderson, R. P. Andres, and J. B. Fenn, Adv. Chem. Phys. 10, 275 (1966);
c. J. B. Anderson, in Molecular Beams and Low Density Gas Dynamics, ed. by P. O. Wegerer (Dekker, New York, 1974), 4, 1.

17. R. Campargue, from von Karman Inst. fur Fluid Dynamics Lecture Series 8s (Saclay, 1976).

18. G. M. McClelland, K. L. Saenger, J. J. Valentini and D. R. Herschbach, J. Phys. Chem. 83, 947 (1979).

19. D. W. Posener, J. Chem. Phys. 24, 546 (1956).

20. J. D. Swalen and L. Pierce, J. Math. Phys. 2, 736, 740 (1961).

21. Figure 17 and much of the data on refocusing versus pressure studies areextracted from the experimental work of M. Maier in our laboratory. He was also responsible for the time-of-flight measurements made of our beam. Results of this work will be published.

22. Performed by S. Sherrow.

23. K. Bergmann, U. Hefter, and P. Hering, J. Chem. Phys. 65, 488 (1976).

24. H. G. Bennewitz and G. Buess, Chem. Phys. 28, 175 (1978).

25. Subsequent to this writing flop-in signals were seen with a room temperature OCS beam by S. Sherrow. This possibly resulted from the use of a larger detector orifice. As before, it seems largely dependent upon the A field voltage.

APPENDIX

The Computer Programs ABFELDV and ETABLE

The computer program listings for these programs, as well as for programs relevant to Chapters IV and V are reproduced on microfiche and appended to the end of this thesis. In most cases we have tried to document these programs sufficiently enough to allow a clear following of the routines. These programs were run on the CDC 7600 at the Lawrence Berkeley Laboratory. Several of the subroutines referred to in these programs were obtained in object code from the LBL core library. As an example of the method of running a typical job, a standard set of control commands for ABFELDV is listed here.

```
ABRUN,7,200.XXXXXX,LUFTMAN
     (Job card, with account number)

LIBCOPY,JSW,ABFELDV/BR,ABFELDV
     (Calling the program from the PSS library.)

LIBCOPY,JSW,POSE15/BR,POSE15.

LIBCOPY,JSW,DATR/BR,DATR.
     (Calling the necessary data files.)

MATHLIB.
     (Attach the core library.)

FETCHPS,GPACBN7,GPAC,AIDBN,VABN.
     (The graphics routines for the LBL Varian plotter.)

FTN4,I=ABFELDV,B=SUSAN.
     (Compile the FORTRAN program.)

LINK,X,F=SUSAN,F=GPAC,PP=[DATR,,POSE15].
     (Run the program, attaching the required data files.)

GRAPHIC,FILM,FT=VA.
     (Plot the results.)
```

The program ABFELDV calculates the refocusing signal of a polar linear molecule in an MBER experiment as a function of source conditions,

spectrometer geometrical parameters and focusing fields. It uses second order perturbation theory as a first approximation for the limits of the acceptable transverse velocities for a given longitudinal velocity, and then recalculates the upper transverse limit via variational theory. A small change in this program (removal of the CALL SLIMIT2 line in the REFOC2 routine) allows refocusing calculations using only perturbation theory. An example of the data file DATR is appended to this program's listing.

The file POSE15 contains an energy grid for the Stark effect on linear dipoles calculated variationally by program ETABLE. ETABLE calculates the diagonal elements of the Stark interaction matrix by converting this tridiagonal matrix to continued fraction form and solving for its roots. The program uses the method of Posener for rapid convergence, with frequent checking that the roots calculated have not "jumped surfaces", as the convergence is sometimes not well-behaved.

CHAPTER IV

RESONANCE SPECTRA OF LINEAR DIPOLAR MOLECULES

The spectra obtained through MBER can be exceedingly rich in molecular information, due to the high resolution (on the order of 1 kHz ~ 10^{-7} cm^{-1}) inherent to spectroscopy in the radiofrequency and microwave regions. Different spectral peaks observed in MBER have generally two different origins. The primary source of lines is from the existence of different molecular states with corresponding differences in state energies. For a molecule with no net electronic angular momentum and no quadrupole moment associated with any of its nuclei, the most essential terms in the Hamiltonian for MBER are the rotational and Stark energy terms. Quantitative interpretation of the resultant spectra gives direct information on the molecule's rotational constant (and, thus, corresponding geometrical information) and dipole moment. Adding a spin to one or more nuclei the spectrum becomes more complex and correspondingly richer in information, and one can obtain quadrupole coupling and other spin interaction coefficients, further elucidating the molecule's geometry and electronic structure. The second source of spectral structure arises from the time dependence of any transition process, and from the coherent radiation source and narrow molecular velocity distribution inherent in the MBER process. A molecule in a radiation field resonant or nearly resonant to the energy separating two states can be alternately "pumped" up and down between these states via induced adsorption and emission as long as the molecule remains within this field. This effect manifests itself in MBER spectra as an oscillation superimposed on each transition spectral line.

It is the MBER spectrum that is the subject of this chapter. Much of what follows is given fairly detailed attention in the literature. Here it is intended to give an intuitive overview of the quantum mechanics behind the spectral structure. Experimental MBER spectra of OCS and ClF follow, which are in turn followed with attempts at correlating the theory with these results. Some of the general problems in MBER spectra interpretation will be discussed. Aside from relevant computer program listings, in the appendix is a detailed discussion on the time dependent effects in resonant spectroscopy, both in a wide sense and in how it applies to electric resonant work.

A. Theory - Stark and Nuclear Interactions in a Linear Molecule

As mentioned before, this section does not pretend to be a detailed treatise on quantum mechanics. Its purpose is to clarify the salient aspects needed to interpret the complexity of the MBER spectrum. General quantum mechanics texts fill in many of the holes in the discussion that follows.[1] The details of standard microwave spectroscopy are also well explored topics.[2] Here we will be concentrating on the phenomena in radiofrequency spectra, involving transitions within an individual rotational state manifold. Just as an aside, the formalism of irreducible spherical tensors can be quite useful in the analysis of angular momentum operators.[3-5] Though this approach will not be used here, it is advised that an understanding of that method can be a great aid to one's intuition.

In quantum mechanics, the Hamiltonian of a system, or more specifically in our case, of a molecule, contains implicitly all the information about its various states. The kinetic energy and all the

interactions between parts of the molecule or between the molecule and its environment are included in this operator. One can write the Hamiltonian in a quite compact form in terms of simple canonical variables of the individual electrons and nucleons. However, more typically it is written as a collection of terms which separate various interactions and motions into forms which are both easier to deal with in an operative sense and intuitively more tractable in a classical mechanics sense. In this manner one can have terms specifically related to molecular vibration and rotation, and other interactions involving electronic spin and angular momentum, nuclear spin and angular momentum, and external electrostatic and/or magnetic fields.

The Hamiltonian allows one to determine the system's possible stationary states. "Stationary" implies that if the system or molecule can be described as being in such a state, it will remain in that state as long as the Hamiltonian does not change. A function $\phi_a(\underset{\sim}{x}) \equiv |\phi_a>$ which describes such a state must be an eigenfunction of the Hamiltonian operator, with an eigenvalue that corresponds to the states energy:

$$\hat{\mathcal{H}}|\phi_a> = E_a|\phi_a> \tag{4.1}$$

As is true with any other quantum mechanical operator, one can construct a set of all the linear independent eigenstates of $\hat{\mathcal{H}}$, and this set can serve as a "complete basis" for any other function of the same variables. That is, given such a set $\{|\phi_a>\}$ and an arbitrary function $|\alpha_i>$, there exists a set of constant coefficients such that

$$|\alpha_i> = \sum_a A_{ia}|\phi_a> \tag{4.2}$$

This set $\{|\phi_a>\}$ can be constructed to be mutually orthogonal and normalized in an integration sense, and all basis sets to be described here will be assumed to have this property.

In general, when an arbitrary operator $\hat{O}$ acts on an eigenstate of $\hat{\mathcal{H}}$, the result is a function which is no longer an eigenstate of $\hat{\mathcal{H}}$ (i.e., no longer satisfies Eq.(1)). If, however, $\hat{O}$ commutes with $\hat{\mathcal{H}}$, i.e., for an arbitrary function $|\alpha>$,

$$\hat{O}\hat{\mathcal{H}}|\alpha> = \hat{\mathcal{H}}\hat{O}|\alpha>, \tag{4.3}$$

then one can construct a complete set of functions that will be simultaneously eigenfunctions of these two operators. In molecular systems, for example, there exists an operator $\hat{M}_F$ which commutes with $\hat{\mathcal{H}}$, and thus there exists such a set of eigenfunctions. As the eigenvalue of $\hat{\mathcal{H}}$, E, is associated with the classical concept of energy, the eigenvalue of the operator $\hat{M}_F$ (M_F, without a carat) has as a classical counterpart the component of the total nuclear angular momentum of a molecule on some space fixed axis. As they share eigenstates, M_F, as E, is a constant of motion for the molecule as long as there are no changes to the system's energy from its environment.

Another example was given in Chapter III for the rigid rotor, with a Hamiltonian

$$\hat{\mathcal{H}}_{ROT} = B\hat{\underset{\sim}{J}}^2 \tag{4.4}$$

where B is the rotational constant (Eq. (3-4)), and $\hat{\underset{\sim}{J}}$ the operator corresponding to the rotor's orbital angular momentum. The operators $\hat{\mathcal{H}}_{ROT}$, $\hat{\underset{\sim}{J}}$ and a third one, $\hat{M}$, corresponding to the projection of this momentum on a space fixed axis, all mutually commute, and so share a set of

eigenfunctions $\{|\phi_a>\}$, with corresponding eigenvalues $\{E_a, J_a, M_a\}$. As a short hand, we will label an individual eigenstate, when possible, by its eigenvalues aside from energy. For rotational states, then, $|\phi_a>$ can be relabeled $|J_a, M_a>$. For $\hat{\mathcal{H}}_{ROT}$, the values J and M can be referred to as "good quantum numbers" in that they may be used to describe the system's stationary states.

If a new term, $\hat{\mathcal{H}}'$, is added to $\hat{\mathcal{H}}_{ROT}$ to give a new Hamiltonian $\hat{\mathcal{H}}$, and if $\hat{\mathcal{H}}'$ commutes with $\hat{M}$ but <u>not</u> with $\hat{\underset{\sim}{J}}$, then the set of functions $\{|\phi_a>\} = \{|J_a M_a>\}$ can no longer be stationary states for this system. A new set $\{|\alpha_a>\}$ can be constructed that are eigenstates of $\hat{\mathcal{H}}$ and $\hat{M}$, but no longer of $\hat{\underset{\sim}{J}}$, and thus J is no longer a "good quantum number". In classical terms, the rotor's full angular momentum is no longer a constant of the motion. This new set $\{|\alpha_a>\}$ can be expressed as linear combinations of $\{|J_a M_a>\}$ as this latter set is complete. If the magnitude of the effect of $\hat{\mathcal{H}}'$ is much smaller than $\hat{\mathcal{H}}_{ROT}$, then one would find

$$|\alpha_a> = A_{aa}|J_a M_a> + \sum_{a' \neq a} A_{aa'}|J_{a'} M_{a'}> \tag{4.5}$$

where $A_{aa} \sim 1$ and $A_{aa'} << 1$, i.e., that the $|J_a M_a>$'s are <u>almost</u> eigenfunctions of $\hat{\mathcal{H}}$. Then, J is <u>almost</u> a good quantum number. M, in this example, is still good, as $\hat{M}$ commutes with $\hat{\mathcal{H}}$.

1. <u>The Hamiltonian</u>

We will begin here by noting the terms in the normally complete molecular Hamiltonian that will not be included in this analysis. Though MBER is certainly not limited to linear molecules, this study is. The general rotor Hamiltonian for an asymmetric top is not much more complex than that of a linear rotor, and the added complications in the

determination of stationary states are handled with an extension of the method to be described. Microwave and radiofrequency spectroscopy do not usually involve electronic or vibrational transitions. Furthermore, most molecules studied by MBER are without net electronic orbital or spin angular momentum (i.e., having $^1\Sigma$ ground states), so that electronic terms will be excluded from our Hamiltonian and electron coordinates need not be included in the wavefunctions. In our work essentially all molecules are in their vibrational ground state, so that vibrational interaction terms and their associated coordinates also do not concern us. The terms remaining in the full molecular Hamiltonian which will be of consequence in the energetics and state determination are summarized by the equation[6,7]

$$\hat{\mathcal{H}}^{\circ} = \hat{\mathcal{H}}_{ROT} + \hat{\mathcal{H}}_{STARK} + \hat{\mathcal{H}}_{Q} + \hat{\mathcal{H}}_{SR} + \hat{\mathcal{H}}_{SS}. \tag{4.6}$$

The dominant term in this series, $\hat{\mathcal{H}}_{ROT}$, was given in Equation (4). B, the rotational constant of the molecule, is inversely proportional to the rigid rotor's effective moment of inertia:

$$B = h/8\pi I. \tag{4.7}$$

(Most energy expressions will be left in units of Hertz, as these are the conventional units used in microwave and radiofrequency spectroscopy.) The parallel between Equation (4) and the classical expression for rotational energy ($(I\omega)^2/2I$) is obvious.

The second term of (4.6), the Stark term, is due to the interaction of a dipolar rotor with an external electric field $\underset{\sim}{E}$:

$$\hat{\mathcal{H}}_{STARK} = -\hat{\underset{\sim}{\mu}}\cdot\underset{\sim}{E}. \tag{4.8}$$

Much of this term has already been discussed in the previous chapter. The relative magnitude of $\hat{\mathcal{H}}_{STARK}$ compared with the other terms of (4.6) will depend greatly upon the magnitude of the external field. Generally, in our considerations, it will be significantly smaller than $\hat{\mathcal{H}}_{ROT}$. For the purpose of this and the next two sections, the field $\underset{\sim}{E}$ will be constant with respect to time. It will be the time dependent form of the Stark term, however, that will be responsible for the transitions in the latter part of this chapter.

In addition to having a net positive charge, if a nucleus has a spin (I) greater than or equal to one it will also have an electric quadrupole moment. This will interact with the gradient of the field generated by the molecule's electrons, and gives rise to the nuclear electric quadrupole term of $\hat{\mathcal{H}}_0$. Expressed in terms of the nuclear spin operator for a given nucleus $\hat{\underset{\sim}{I}}_i$, the rotation operator $\hat{\underset{\sim}{J}}$, and their associated eigenvalues,

$$\hat{\mathcal{H}}_{Q_i} = eq_i Q_i \frac{3(\hat{\underset{\sim}{I}}_i \cdot \hat{\underset{\sim}{J}})^2 + \frac{3}{2}(\hat{\underset{\sim}{I}}_i \cdot \hat{\underset{\sim}{J}}) - \hat{I}_i^{\,2}\hat{J}^2}{2I_i(2I_i-1)(2J-1)(2J+3)} \,. \tag{4.9}$$

Such a term exists for each nucleus in the molecule with $I_i \geqslant 1$. Here, Q_i is the nuclear quadrupole moment and eq_i, the gradient of the electric field at that nucleus due to charges outside of the nucleus. Though a detailed derivation or intuitive justification of (4.9) will not be given here, it is clear that $\hat{\mathcal{H}}_{Q_i}$ should depend upon the mutual orientations of the nuclear spin with the molecular axis, as the $\hat{\underset{\sim}{I}}_i \cdot \hat{\underset{\sim}{J}}$ terms reflect. The appearance of I_i and J in this expression is allowable as long as they are "good" quantum numbers, which, as will be discussed shortly, is essentially true.

The spin-rotation coupling term in (4.6), $\hat{\mathcal{H}}_{SR}$, is due to the interaction between the nuclear spin magnetic moment of a given nucleus with the magnetic field induced by the charged particles of the molecule rotating with the molecule. This field is therefore parallel to the molecule's angular momentum and the interaction term is given via

$$\hat{\mathcal{H}}_{SR_i} = C_i \, \hat{I}_i \cdot \hat{J}. \tag{4.10}$$

Such a term appears for each nucleus with a spin.

If the molecule has more than one nucleus with a non-zero spin, then their associated magnetic moments will interact, giving rise to the spin-spin term of (4.9),

$$\hat{\mathcal{H}}_{ss} = \frac{S_{ij}}{(2J+3)(2J+1)} \left(3(\hat{\underset{\sim}{I}}_i \cdot \hat{\underset{\sim}{J}})(\hat{\underset{\sim}{I}}_j \cdot \hat{\underset{\sim}{J}}) + 3(\hat{\underset{\sim}{I}}_j \cdot \hat{\underset{\sim}{J}})(\hat{\underset{\sim}{I}}_i \cdot \hat{\underset{\sim}{J}}) - 2(\hat{\underset{\sim}{I}}_i \cdot \hat{\underset{\sim}{I}}_j)\hat{\underset{\sim}{J}}^2\right) \tag{4.11a}$$

This expression is derivable from the classical dipole-dipole interaction expression

$$E_{ss} = \frac{1}{R_{ij}^3} \left(\underset{\sim}{\mu}_i \cdot \underset{\sim}{\mu}_j - 3(\underset{\sim}{\mu}_i \cdot \underset{\sim}{R}_{ij})(\underset{\sim}{\mu}_j \cdot \underset{\sim}{R}_{ij})/R_{ij}^2\right) \tag{4.11b}$$

where $\underset{\sim}{R}_{ij}$ is the vector separating the dipoles $\underset{\sim}{\mu}_i$ and $\underset{\sim}{\mu}_j$. There is also an indirect coupling of the nuclear spins due to the coupling of the nuclei with the electron spins associated with the individual atoms, followed by the effect this has on the electron exchange energy:

$$\hat{\mathcal{H}}'_{ss} = S'_{ij} \, \hat{\underset{\sim}{I}}_1 \cdot \hat{\underset{\sim}{I}}_2. \tag{4.12}$$

Table 1 is a list of observed molecular constants for ClF^{35} and OCS, given here primarily to demonstrate the relative magnitudes of the individual terms in the Hamiltonian expression (4.6). The Stark term is represented by the expression $\mu^2 E^2/B$ for E = 1000 V/cm, from the second order perturbation expression for the Stark effect (Eq. (3-14).

2. Relevant Basis Sets

Given the Hamiltonian $\hat{\mathcal{H}}^\circ$ for a linear molecule, it would be quite difficult if not impossible, to determine directly the stationary states of the molecule which satisfy (4.1). An approach that has significantly more promise is to find a basis set of functions $\{|\phi_a>\}$ that are eigenfunctions of the more significant parts of $\hat{\mathcal{H}}^\circ$, and then determine the linear combinations of these functions $\{|\alpha_a>\}$ that are eigenfunctions for all of $\hat{\mathcal{H}}^\circ$. As $\hat{\mathcal{H}}^\circ$ is made primarily of the operators $\hat{\underset{\sim}{J}}$ and $\hat{\underset{\sim}{I}}_i$, a chosen basis set should consist of eigenfunctions of various combinations of these operators and their projections along some space-fixed direction. Keeping in mind this motivation, and the restrictions concerning the necessity of two operators commuting if they are to share a set of eigenfunctions, we will here derive some likely candidates for basis sets. For the remainder of this chapter we will be considering a system consisting of a linear molecule with at most two nuclei having a nonzero spin, and $eq_1Q_1 >> eq_2Q_2$

Of the types of operators we have considered so far, only the operator $\hat{M}_F$ described previously commutes with the full molecular Hamiltonian, including very small terms left out of Equation (6). Thus, the true eigenstates of the molecule can be only precisely labeled with the eigenvalues E, the molecule's energy, and M_F, the projection of all

Table 4.1

Observed Molecular Constants for OCS and ClF[8]

OCS

$B = 6085.5$ MHz

$\mu = 0.709$ D

$\frac{\mu^2 E^2}{B}$ ($E = 1000$ V/cm) = 10470 kHz.

$C\ell^{35}F$

$B = 15483$ MHz

$\mu = 0.88804$ D

$I_{C\ell^{35}} = 3/2$ $\quad$ $I_F = 1/2$

$eqQ_{C\ell} = -145.872$ MHz $\quad$ $eqQ_F = 0$

$C_{C\ell} = 21.613$ kHz $\quad$ $C_F = -22.56$ kHz

$S = 2.556$ kHz

$S' = 1.074$ kHz

$\frac{\mu^2 E^2}{B}$ ($E = 1000$ V/cm) = 6455.7 kHz

the molecule's nuclei's angular momenta on a space-fixed axis. The operators $\hat{\underset{\sim}{I}}_i$ commute with all the terms we have included in (4.6) for $\hat{\mathcal{H}}_0$, so that I_1 and I_2, representing the magnitudes of the nuclear spins, will also be "good" quantum numbers for us, and, therefore, should remain as appropriate labels for any basis set we may choose. The rotational angular momentum operator, $\hat{J}$, commutes with all of (4.6), with the exception of $\hat{\mathcal{H}}_{STARK}$. Due to the magnitude of $\hat{\mathcal{H}}_{ROT}$ compared to $\hat{\mathcal{H}}_{STARK}$ under most normal electrostatic field conditions, and that $\hat{\mathcal{H}}_{ROT}$ depends solely on the vector operator $\hat{J}$ via Equation (4.4), the quantum number J remains "almost good" for $\hat{\mathcal{H}}^\circ$. Saying this a different way, the actual energies, E_a°, derived from $\hat{\mathcal{H}}^\circ$ with $\hat{\mathcal{H}}_{STARK}$ will be nearly equal to $BJ_a(J_a+1)$ where $\sqrt{J_a(J_a+1)}\hbar$ would be the rotational angular momentum we would assign to the stationary state $|\alpha_a^\circ\rangle$ if the $\hat{\mathcal{H}}_{STARK}$ term were "turned off", i.e., if no external field were present. Thus, even with a field, we can assign a particular J_a with a particular E_a°, and, as E_a° is definitely a good label for some eigenstate $|\alpha_a^\circ\rangle$, we can also assign J_a with that particular eigenstate. The care used here in making the point that J is <u>almost</u> a good quantum number is due to the point that will be made later that it is the small "badness" of J that will allow the transitions observed in MBER.

At this point we have four good labels, excluding the actual energy, to describe the possible eigenstates of $\hat{\mathcal{H}}^\circ$ - namely, M_F, I_1, I_2, and J. However, as it turns out, these are not enough tags to distinguish all the possible linearly independent eigenstates of $\hat{\mathcal{H}}^\circ$. What is needed are labels to indicate the various ways the angular momenta can couple, and the best choice for these extra labels is dependent upon the relative magnitude of the terms in $\hat{\mathcal{H}}^\circ$. We shall try to reach an intuitive feel for what these labels might be.

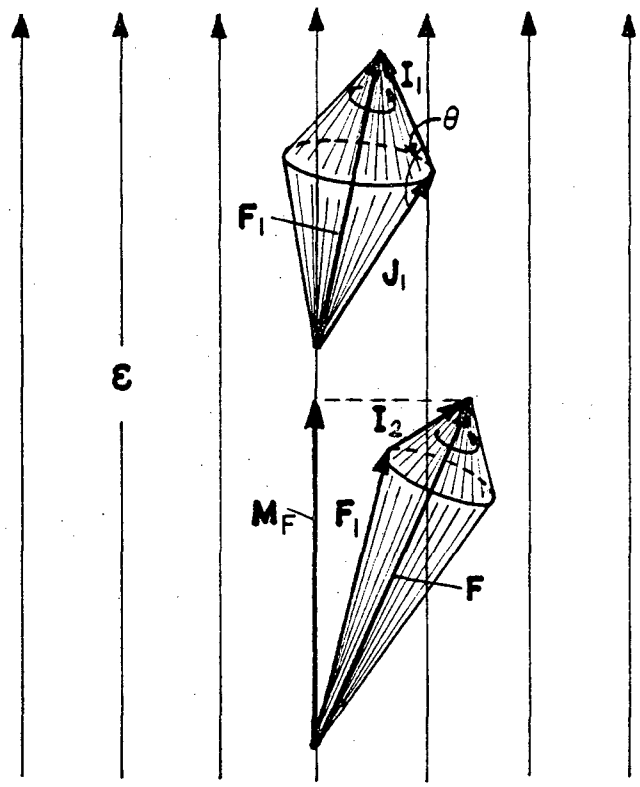

Figure 4.1. Weak field basis angular momentum vectors.

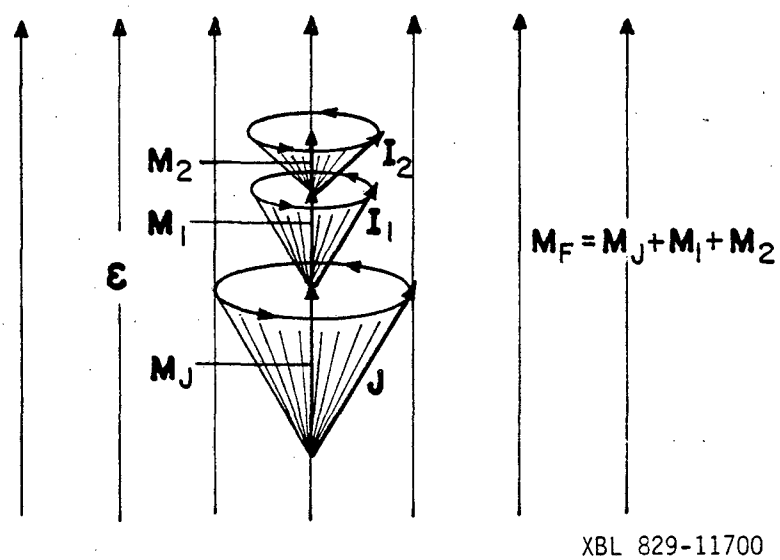

Figure 4.2. Strong field basis angular momentum vectors.

Given a very weak electric field, so that particularly

$$\frac{\mu^2 E^2}{B} << C_2 \text{ or } S_{12},$$

and noting that, in general,

$$C_2 \text{ and } S_{12} << eq_1Q_1$$

(note Table 4.1), then the strongest perturbation to $\hat{\mathcal{H}}_{ROT}$ will be the term $\hat{\mathcal{H}}_{Q_1}$. Noting the form of $\hat{\mathcal{H}}_{Q_1}$ in (4.9), one might expect that in this case, there should be a quantum number associated with the operator "$\hat{\underset{\sim}{I}}_1 \cdot \hat{\underset{\sim}{J}}$", indicative of the mutual orientation of $\underset{\sim}{I}_1$ and $\underset{\sim}{J}$. In a classical sense (see Fig. 4.1), as the energy of the molecule depends so strongly on the angle θ between $\underset{\sim}{I}_1$ and $\underset{\sim}{J}$, that angle should nearly be a constant of motion. Alternatively, if the magnitudes of $\underset{\sim}{I}_1$ and $\underset{\sim}{J}$ are fixed, then so is their vector sum $\underset{\sim}{F}_1$ (as $|\underset{\sim}{F}_1|^2 = |\underset{\sim}{J}|^2 + |\underset{\sim}{I}_1|^2 - 2|\underset{\sim}{J}||\underset{\sim}{I}_1|\cos\theta$). As will be shown in Appendix I, furthermore, $\underset{\sim}{J}$ and $\underset{\sim}{I}_1$ classically precess about F_1, due to the torque they experience from their mutual interaction. Quantum mechanically we will define the operator

$$\hat{\underset{\sim}{F}}_1 = \hat{\underset{\sim}{J}} + \hat{\underset{\sim}{I}}_1, \tag{4.13}$$

with an associated quantum number F_1 indicative of the orientation between $\underset{\sim}{J}$ and $\underset{\sim}{I}_1$. F_1 may have values $|J - I_1|$, $|J - I_1|+1$, ..., $|J + I_1|$. What is left now is how $\underset{\sim}{I}_2$ will couple with the other angular momentum vectors. In a very intuitive sense one might say that (assuming $eq_2Q_2 << S_{12}$, as is the case with $Cl^{35}F$) the magnetic moment of $\underset{\sim}{I}_2$ really interacts only with the magnetic field associated with $\underset{\sim}{F}_1$, as $\underset{\sim}{J}$ and $\underset{\sim}{I}_1$

are precessing about $\underset{\sim}{F}_1$ too quickly for $\underset{\sim}{I}_2$ to couple to either of them individually. So the next operator, representing the total nuclear angular momentum coupled in the order given above, becomes

$$\hat{\underset{\sim}{F}} \equiv \hat{\underset{\sim}{F}}_1 + \hat{\underset{\sim}{I}}_2. \tag{4.14}$$

It will be this total angular momentum coupling to the weak external field that will give rise to the projection operator $\hat{M}_F$, with its associated eigenvalue M_F representing the projection of $\underset{\sim}{F}$ along the direction of the external field $\underset{\sim}{E}$. We now have a sufficient number of labels for the molecule. This "weak field" basis set

$$\{|\phi_a>\}_{wf} \Leftrightarrow \{|JI_1F_1I_2FM_F>\} \tag{4.15}$$

consists of exact eigenfunctions for $\hat{\mathcal{H}}_{ROT} + \hat{\mathcal{H}}_{Q_1}$, which are still pretty good for all of $\hat{\mathcal{H}}_0$ as long as $\underset{\sim}{E}$ is very weak.

In the limit of a strong electric field, where $\hat{\mathcal{H}}_{STARK}$ has a significantly larger effect than $\hat{\mathcal{H}}_{\underset{\sim}{Q}}$ (i.e., $B >> \mu^2E^2/B >> eq_1Q_1$), the rotational angular momentum of the molecule will primarily "couple" to the external field $\underset{\sim}{E}$, as opposed to $\underset{\sim}{I}_1$ as in the weak field case. In classical mechanics, the torque on a dipole by a field is perpendicular to both the dipole and the field directions, and, as a linear molecule's effective dipole moment is parallel to its rotational angular momentum, $\underset{\sim}{J}$, this coupling will result in the angular momentum vector precessing on a conical surface about the external field direction (Fig. 4.2). As a result, the projection of $\underset{\sim}{J}$ on the field direction vector, M_J, will be a constant of motion, and a basis set consisting of stationary states of this system can be eigenfunctions of the associated operator $\hat{M}_J$. The magnetic moments of the nuclei will couple to $\underset{\sim}{E}$ indirectly, for, as $\underset{\sim}{J}$ is

"rapidly" precessing about $\underset{\sim}{E}$, the nuclear dipoles will only experience the electric and magnetic fields due to the projection of $\underset{\sim}{J}$ along $\underset{\sim}{E}$. Thus in this case, $\underset{\sim}{I}_1$ and $\underset{\sim}{I}_2$ will also precess about $\underset{\sim}{E}$, and their projections in this direction, M_1 and M_2, will also nearly be constants of motion, and, correspondingly, nearly good quantum numbers. The projection of the total nuclear angular momentum will just be the sum of the projections due to rotation and nuclear spins,

$$\hat{M}_F = \hat{M}_J + \hat{M}_1 + \hat{M}_2. \tag{4.16}$$

As M_J, M_1 and M_2 are good quantum numbers in this basis, and M_F commutes with all other projection operators, M_F itself is good, and in fact is just the algebraic sum of M_J, M_1 and M_2. The strong field basis set, then, can be represented as

$$\{|\phi_a>\}_{sf} \Leftrightarrow \{|JM_J I_1 M_1 I_2 M_2>\}, \tag{4.17}$$

where the label M_F has been left off because it is redundant. These are good eigenfunctions for $\hat{\mathcal{H}}_{ROT} + \hat{\mathcal{H}}_{STARK}$, as far as J is ever a good quantum number with $\hat{\mathcal{H}}_{STARK}$ present.

Neither of these sets of functions are close to being eigenstates for molecules in electric fields of intermediate strength. For $eq_1Q_1 >> \mu^2E^2/B >> C_2$ or S_{12} or eq_2Q_2, one appropriate basis set may consist of mutual eigenstates of the operators $\hat{\underset{\sim}{J}}$, $\hat{\underset{\sim}{I}}_1$, $\hat{\underset{\sim}{F}}_1 (= \hat{\underset{\sim}{J}} + \hat{\underset{\sim}{I}}_1)$, $\hat{M}_{F_1}$, $\hat{\underset{\sim}{I}}_2$ and $\hat{M}_2$ where $\hat{M}_{F_1}$ is the projection of $\hat{\underset{\sim}{F}}_1$ or $\underset{\sim}{E}$. In this case, the strongest interaction is between $\underset{\sim}{J}$ and $\underset{\sim}{I}_1$, as in the weak field case. F_1 then couples to the electric field, and $\underset{\sim}{I}_2$, as in the strong field basis, indirectly couples to the field. Alternatively, one could choose a basis set characterized by the operators $\underset{\sim}{J}$, $\underset{\sim}{I}_1$, $\underset{\sim}{I}_2$, $\underset{\sim}{I}$ $(=\underset{\sim}{I}_1 + \underset{\sim}{I}_2)$,

$\hat{\underset{\sim}{F}}(=\hat{\underset{\sim}{J}}+\hat{\underset{\sim}{I}})$, and $\hat{M}_F$. However, the actual stationary states of a molecule in a field that does not satisfy the criteria of the weak or strong cases will not, in general, be eigenstates of $\hat{\underset{\sim}{F}}_1$, $\hat{\underset{\sim}{F}}$, $\hat{M}_J$, $\hat{M}_I$, or any of the operators introduced since the third paragraph of this section. The prescribed course here is to choose one basis set, typically one of those described above, determine the effect of operating on each basis function with the full Hamiltonian $\hat{\mathcal{H}}^\circ$, and use the results to determine the actual eigenstates of $\hat{\mathcal{H}}^\circ$.

3. <u>The Numerical Solution of Eigenstates and Energies</u>

The problem to solve is given a complete basis set of functions $\{|\phi_a>\}$ which are not eigenstates of the Hamiltonian $\hat{\mathcal{H}}^\circ$, find a new set of states, $\{|\alpha_b>\}$, which are linear combinations of $\{|\phi_a>\}$, i.e.,

$$|\alpha_b> = \sum_a A_{ba}|\phi_a>, \tag{4.18}$$

such that $\{|\alpha_b>\}$ are eigenstates of $\hat{\mathcal{H}}_0$, i.e.,

$$\hat{\mathcal{H}}^\circ|\alpha_b> = E_b^\circ|\alpha_b>. \tag{4.19}$$

The effect of $\hat{\mathcal{H}}^\circ$ on a particular element of $\{|\phi_a>\}$ is to give a new function which can be expressed as a linear combination of $\{|\phi_a>\}$:

$$\hat{\mathcal{H}}^\circ|\phi_a> = \sum_{a'} H_{aa'}|\phi_{a'}>. \tag{4.20}$$

Due to the orthonormal nature of the basis sets used here one can write

$$H_{aa'} = <\phi_{a'}|\hat{\mathcal{H}}^\circ|\phi_a>. \tag{4.21}$$

This expression defines a "matrix representation" $\underset{\approx}{H}$ of the Hamiltonian

$\hat{\mathcal{H}}^{\circ}$ in the basis $\{|\phi_a>\}$. It will now be stated without further proof (though, from this point in our development the proof is trivial), that there exists a unitary transformation which will diagonalize the Hamiltonian matrix:

$$\underset{\approx}{A}^{-1} \underset{\approx}{H} \underset{\approx}{A} = \underset{\approx}{E}. \tag{4.22}$$

The diagonal elements of $\underset{\approx}{E}$ are in fact the eigenvalues of $\hat{\mathcal{H}}^{\circ}$, and the columns of the transformation matrix $\underset{\approx}{A}$ are those coefficients in (4.18) which connect the old basis set $\{|\phi_a>\}$ to the actual eigenfunctions of $\hat{\mathcal{H}}^{\circ}$. In practice, one determines the matrix $\underset{\approx}{H}$ for a given basis set of functions, solves the secular equation

$$\det(\underset{\approx}{H} - \underset{\approx}{E}_b \underset{\approx}{I}) = 0 \tag{4.23}$$

where $\underset{\approx}{I}$ is the identity matrix, to determine the eigenvalues of the matrix $\underset{\approx}{H}$, and then finds the eigenvectors $\underset{\sim}{A}_b$ expressed in the given basis such that

$$(\underset{\approx}{\mathcal{H}} - E_b \underset{\approx}{I})\underset{\sim}{A}_b = 0. \tag{4.24}$$

The structure of the Hamiltonian matrix $\underset{\approx}{H}$ can be quite simplified by the appropriate choice of basis functions. For example, given a basis set of functions $\{|\phi_a>\}$ that are eigenfunctions of the operator $\hat{\underset{\sim}{M}}_F$, as are all the basis sets described in the previous section, and given that this operator commutes with $\hat{\mathcal{H}}^{\circ}$, and, finally, that all quantum mechanic operators are Hermitian (an important point neglected until now) one can easily show that

$$(M_a - M_b) <\phi_b|\hat{\mathcal{H}}^{\circ}|\phi_a> = 0 \tag{4.25}$$

for $\hat{M}_F|\phi_a> = M_a|\phi_a>$ and $\hat{M}_F|\phi_b> = M_b|\phi_b>$. That is, there can only be matrix elements in $\underset{\approx}{H}^\circ$ connecting states which have the same eigenvalues associated with the operator $\hat{M}_F$. Similarly, $\underset{\approx}{H}^\circ$ is "block diagonal" in regard to the operators $\hat{I}_1$ and $\hat{I}_2$ if $\underset{\approx}{H}^\circ$ is expressed in terms of any of the aforementioned basis sets.

As an example in the evaluation of nonzero elements of $\underset{\approx}{H}$, we will determine the value of the matrix element of $\hat{\underset{\sim}{I}}_1 \cdot \hat{\underset{\sim}{J}}$ using the strong field basis (4.17). That is, we will evaluate

$$H^{SR}_{aa'} = <J^{a'} M_J^{a'} I_1^{a'} M_1^{a'} I_2^{a'} M_2^{a'} | (\hat{\underset{\sim}{I}}_1 \cdot \hat{\underset{\sim}{J}}) | J^a M_J^a I_1^a M_1^a I_2^a M_2^a> \tag{4.26}$$

One can decompose the vector operators into their scalar components, i.e.,

$$\hat{\underset{\sim}{J}} = \hat{J}_x \underset{\sim}{i} + \hat{J}_y \underset{\sim}{j} + \hat{J}_z \underset{\sim}{k}$$

$$\hat{\underset{\sim}{I}}_1 = \hat{I}_{1x} \underset{\sim}{i} + \hat{I}_{1y} \underset{\sim}{j} + \hat{I}_{1z} \underset{\sim}{k} \tag{4.27}$$

If $\underset{\sim}{k}$ is chosen as the direction of the fixed field $\underset{\sim}{E}$, then one can identify the operators $\hat{J}_z$ and $\hat{I}_{1z}$ with $\hat{M}_J$ and $\hat{M}_1$, respectively. It is useful to define the following complex operators

$$\hat{J}_+ \equiv \hat{J}_x + i\hat{J}_y \qquad \hat{J}_- \equiv \hat{J}_x - i\hat{J}_y$$

$$\hat{I}_{1+} = \hat{I}_{1x} + i\hat{I}_{1y} \quad \hat{I}_{1-} \equiv \hat{I}_{1x} - i\hat{I}_{1y} \tag{4.28}$$

The operator of concern can then be reexpressed via

$$(\hat{\underset{\sim}{I}}_1 \cdot \hat{\underset{\sim}{J}}) = \hat{M}_1 \cdot \hat{M}_J + \frac{1}{2}\, \hat{I}_{1+} \cdot \hat{J}_- + \frac{1}{2}\, \hat{I}_{1-} \cdot \hat{J}_+ . \tag{4.29}$$

The use of the strong field basis set becomes advantageous here as it has the property of being made of functions that are direct products

of three sets of functions spanning smaller spaces. In more coherent terms, the function variables associated with the sets of operators $\hat{\underset{\sim}{J}}$ and $\hat{M}_J$, $\hat{\underset{\sim}{I}}_1$ and $\hat{M}_1$, and $\hat{\underset{\sim}{I}}_2$ and $\hat{M}_2$ are different, in contrast to the weak field basis set, where, for example, the operators $\hat{\underset{\sim}{J}}$, $\hat{\underset{\sim}{F}}_1$, $\hat{\underset{\sim}{F}}$ and $\hat{M}_F$ share some variables. Thus, it is appropriate here to discuss the effect of, say, the operator $\hat{J}_+$ on the $|JM_J>$ part of a strong field basis function alone, as it will not have any effect on the remaining part of the function. The effects of the $\hat{\underset{\sim}{J}}$ operators on $|JM_J>$ are listed here, with the proofs relegated to any of numerous standard quantum texts:

$$\hat{J}_\pm|J,M_J> = \hbar[(J\mp M_J)(J\pm M_J+1)]^{\frac{1}{2}}\ |J,M_J\pm 1>$$

$$\hat{M}_J|J,M_J> = \hbar M_J|J,M_J>. \tag{4.30}$$

Similar equations hold for the $\underset{\sim}{I}_1$ family, replacing $\hat{J}_\pm$ with $\hat{I}_{1\pm}$, $\hat{M}_J$ with $\hat{M}_1$, J with I_1 and M_J with M_1. It can be casually observed here that the components of the operator $\hat{\underset{\sim}{I}}_1\cdot\hat{\underset{\sim}{J}}$ will not "connect" basis functions of differing I_1, J, I_2 or M_2. Indeed the operators associated with these eigenvalues commute with $\hat{\underset{\sim}{I}}_1\cdot\hat{\underset{\sim}{J}}$, so that this is just another manifestation of (4.25). The full evaluation of (4.26) can now be easily done by the use of (4.29), (4.30) and the orthonormality of our basis set:

$$\begin{aligned} H^{SR}_{aa'} = \hbar^2\Big\{ & M^a_1 M^a_J\ \delta_{m^a_1,m^{a'}_1}\ \delta_{m^a_J,m^{a'}_J} \\ & + \tfrac{1}{2}[(I^a+M^a_1)(I^a-M^a_1+1)(J^a-M^a_J)(J^a+M^a_J+1)]^{\frac{1}{2}}\ \delta_{m^a_1-1,m_1{}^{a'}}\ \delta_{m^a_J+1,m^{a'}_J} \\ & + \tfrac{1}{2}[(I^a-M^a_1)(I^a+M^a_1+1)(J^a+M^a_J)(J^a-M^a_J+1)]^{\frac{1}{2}}\ \delta_{m^a_1+1,m^{a'}_1}\ \delta_{m^a_J-1,m_J{}^{a'}}\Big\} \\ & \times \delta_{J^a,J^{a'}}\ \delta_{I^a_1,I^{a'}_1}\ \delta_{I^a_2,I_2{}^{a'}}\ \delta_{m^a_2,m^{a'}_2}. \end{aligned} \tag{4.31}$$

Thus $\hat{\underset{\sim}{I}}_1 \cdot \hat{\underset{\sim}{J}}$ "connects" states of the strong field basis that satisfy the conditions that

$$\Delta M_J = -\Delta M_1 = 0, \pm 1 \tag{4.32}$$

and that no other quantum numbers differ. Given (4.32) and that $\Delta M_2 = 0$, it is clear that

$$\Delta M_J + \Delta M_1 + \Delta M_2 = \Delta M_F = 0 \tag{4.33}$$

for H^{SR}_{aa}, to be nonzero, reinforcing the notion of (4.25). Table 4.2 is a summary of the connections made by the various terms of $\hat{\mathcal{H}}^{\circ}$ between the strong field basis set functions.

It is in part because of the relative ease demonstrated above in the evaluation of Hamiltonian matrix elements, that the calculations done in this work will involve solely the use of the strong field basis set (4.17). The second reason is due to the commuting of the operator $\hat{M}_J$ of this basis with $\hat{\mathcal{H}}_{STARK}$, which will give significant advantages when dealing with transitions and time dependent fields, as will be seen. The chief disadvantage is that typically spectroscopy between states is studied in weak field conditions, where the weak field basis is more nearly correct. The "better" the basis set one uses to set up the Hamiltonian matrix $\underset{\approx}{H}$, the more nearly diagonal it already is, and, therefore, the easier it is to extract its eigenvalues. Using a strong field basis for the weak field case results with a harder job for the computer, but a significantly easier job for the programmer.

In the second appendix to this chapter is a listing for the computer program "W vs E" which calculates state energies for a given linear molecule by the method previously described, as a function of the electric

Table 4.2

Operator Connections Made Between the Strong Field Basis Set Eigenfunction Labels

	J	M_J	I_1	M_1	I_2	M_2	M_F
$\hat{\mu}_z$	±1	0	0	0	0	0	0
$\hat{\mu}_x$	±1	±1 or ∓1	0	0	0	0	±1 or ∓1
$\hat{\underset{\sim}{J}}$	0	0	0	0	0	0	0
$\hat{\underset{\sim}{I}}_i$	0	0	0	0	0	0	0
$\hat{\underset{\sim}{I}}_1 \cdot \hat{\underset{\sim}{J}}$	0	0, ±1	0	0, ∓1	0	0	0
$(\hat{\underset{\sim}{I}}_1 \cdot \hat{\underset{\sim}{J}})^2$	0	0, ±1, ±2	0	0, ∓1, ∓2	0		0
$(\hat{\underset{\sim}{I}}_1 \cdot \hat{\underset{\sim}{J}})(\hat{\underset{\sim}{I}}_2 \cdot \hat{\underset{\sim}{J}})$	0	0 +1 -1 ±2	0	0, ±1 0, -1 0, +1 ∓1	0	0, ∓1 -1, 0 +1, 0 ∓1	0
$(\hat{\underset{\sim}{I}}_1 \cdot \hat{\underset{\sim}{I}}_2)$	0	0	0	0, ±1	0	0, ∓1	0

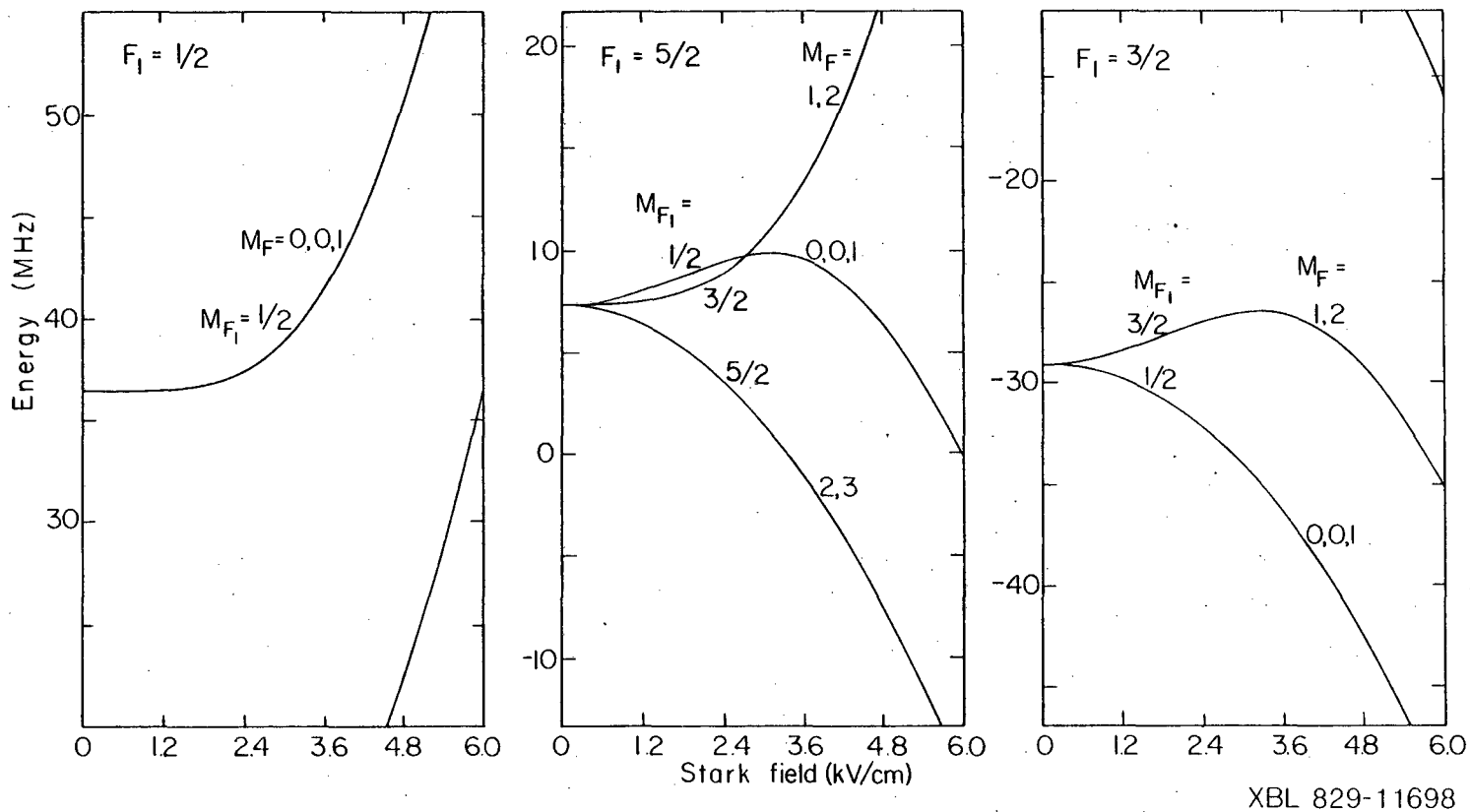

Figure 4.3. J=1 energy levels for $Cl^{35}F$ as a function of external electric field (V/cm). Energies in kHz relative to BJ(J+1) for ClF. (Calculated from spectral constants of Ref. 8.)

field strength. This program uses the strong field basis approach, with one further change which allows the use of a minicomputer for this work. The Hamiltonian matrix is made block diagonal with respect to the operator $\hat{\underset{\sim}{J}}$, leaving significantly smaller matrices of unique values of J to be diagonalized. The Stark term of the full Hamiltonian of Equation (4.6) is accounted for with a second and fourth order perturbation approximation that includes the energetic effects on the individual states within the J' manifold of interest from states with $J = J' \pm 1$ and $J' \pm 2$. The perturbation terms are added directly to the diagonal elements of this Hamiltonian matrix. Comparing results of this type of calculation to more complete calculations which do not prediagonalize with respect to J shows sufficient accuracy throughout the field strength regions of interest to us. Figure 4.3 depicts the energies of the states of $Cl^{35}F$ as a function of field strength up to $E = 6000$ v/cm, while Table 4.3 and 4.4 presents energies and states at a few specific field strengths. In both of these, the characters of the states are given by labeling them with quantum numbers from the different types of basis set descriptions given before. The method used for this labeling and a discussion of the energy trends will be left to later. As an aside, it is the changing character of these curves of Figure 4.3 that was alluded to in Chapter III when it was said that ClF refocusing calculations could not be done just with the consideration of the Stark effect. For a molecule like $O^{16}C^{12}S^{32}$ which has no nuclear spins, the full Hamiltonian only has the rotational and Stark terms. To the extent discussed in Chapter III, the basis set $|JM_J\rangle$ is rather good at the field strengths transitions will be looked for, and the perturbative results from that chapter are sufficient.

Table 4.3

The Strong Field Basis Set for $C\ell^{35}F$, $J = 1$

State ID#	J	I_1	I_2	M_J	M_1	M_2	M_F
1	1	3/2	1/2	0	1/2	-1/2	0
2	1	3/2	1/2	0	-1/2	1/2	0
3	1	3/2	1/2	1	-1/2	-1/2	0
4	1	3/2	1/2	1	-3/2	1/2	0
5	1	3/2	1/2	-1	3/2	-1/2	0
6	1	3/2	1/2	-1	1/2	1/2	0
7	1	3/2	1/2	0	3/2	-1/2	1
8	1	3/2	1/2	0	1/2	1/2	1
9	1	3/2	1/2	1	1/2	-1/2	1
10	1	3/2	1/2	1	-1/2	1/2	1
11	1	3/2	1/2	-1	3/2	1/2	1
12	1	3/2	1/2	0	3/2	1/2	2
13	1	3/2	1/2	1	3/2	-1/2	2
14	1	3/2	1/2	1	1/2	1/2	2
15	1	3/2	1/2	1	3/2	1/2	3

Table 4.4

Calculated Energies and Eigenstates for $Cl^{35}F$, J=1, for E_{DC} = a) 10 V/cm and b) 500 V/cm

a) E_{DC} = 10 V/cm

Energy (kHz)[1]	S.F. State Contribution (%)[2]						Label[3]
	1	2	3	4	5	6	$M_F = 0$
-29202	3	3	27	20	20	27	$F_1 = 3/2$, F = 2,1
-29187	3	3	27	20	20	27	
7316	30	30	15	5	5	15	$F_1 = 5/2$, F = 3,2
7340	30	30	15	5	5	15	
36400	17	17	8	25	25	8	$F_1 = 1/2$, F = 1,0
36419	17	17	8	25	25	8	
	7	8	9	10	11		$M_F = 1$
-29202	15	5	10	40	30		$F_1 = 3/2$, F = 2
-29187	45	2	30	13	10		$F_1 = 3/2$, F = 1
7316	13	40	20	20	7		$F_1 = 5/2$, F = 3
7340	27	20	40	10	3		$F_1 = 5/2$, F = 2
36419	0	33	0	17	50		$F_1 = 1/2$, F = 1
	12	13	14				$M_F = 2$
-29202	60	0	40				$F_1 = 3/2$, F = 2
7316	33	17	50				$F_1 = 5/2$, F = 3
7340	7	83	10				$F_1 = 5/2$, F = 2
	15						$M_F = 3$
7316	100						$F_1 = 5/2$, F = 3

[1] Energies given relative to the pure rotor energy of 30.963 GHz.

[2] % strong field basis contributions use state labels given in Table 4.3.

[3] Labels in (a) from weak field basis, and in (b) from the intermediate field basis. $M_F = 0$ states are formed by 50-50 contributions from the functions indicated.

Table 4.4 (continued)

b) E_{DC} =500 V/cm

Energy (kHz)[1]	S.F. State Contribution (%)[2]						Label[3]
	1	2	3	4	5	6	$M_F = 0$
-29331	3	3	27	20	20	27	$F_1 = 3/2$, $M_{F_1} = \pm 1/2$
-29316	3	3	27	20	20	27	
7444	30	30	15	5	5	15	$F_1 = 5/2$, $M_{F_1} = \pm 1/2$
7467	30	30	15	5	5	15	
36402	17	17	8	25	25	8	$F_1 = 1/2$, $M_{F_1} = \pm 1/2$
36420	17	17	8	25	25	8	
	7	8	9	10	11		$M_F = 1$
-29328	0	7	0	53	40		$F_1 = 3/2$, $M_{F_1} = 1/2$
-29063	59	0	41	0	0		$F_1 = 3/2$, $M_{F_1} = 3/2$
7364	40	1	58	0	0		$F_1 = 5/2$, $M_{F_1} = 3/2$
7453	1	59	1	30	10		$F_1 = 5/2$, $M_{F_1} = 1/2$
36420	0	34	0	16	50		$F_1 = 1/2$, $M_{F_1} = 1/2$
	12	13	14				$M_F = 2$
-29074	59	0	41				$F_1 = 3/2$, $M_{F_1} = 3/2$
7174	0	100	0				$F_1 = 5/2$, $M_{F_1} = 5/2$
7355	41	0	59				$F_1 = 5/2$, $M_{F_1} = 3/2$
		15					
7155		100					$F_1 = 5/2$, $M_{F_1} = 5/2$

4. Transitions

As previously stated, if a molecule is in a particular eigenstate, it will remain there until there is a change to its Hamiltonian (barring spontaneous decay, which is briefly described in the appendix). State transitions, therefore, involve the addition of a time dependent perturbation to the molecule's Hamiltonian,

$$\hat{\mathcal{H}} = \hat{\mathcal{H}}^{\circ} + \hat{\mathcal{H}}'(t). \tag{4.34}$$

For transitions caused by electromagnetic radiation the principle term of this perturbation is simply a time dependent Stark energy term,

$$\hat{\mathcal{H}}'(t) = -\hat{\underset{\sim}{\mu}}\cdot\underset{\sim}{E}_{RF}\cos\omega t, \tag{4.35}$$

where $\hat{\mu}$ is the dipole operator previously described, $\underset{\sim}{E}_{RF}$ the maximum electric field associated with the oscillating radiation fields and the angular frequency of this radiation. The classical and quantum mechanical effects of this term are described in detail in Appendix A. In essence, one calculates the eigenstates $|\phi_j(t)\rangle$ of our new $\hat{\mathcal{H}}$ using as a basis set the eigenstates of $\hat{\mathcal{H}}^{\circ}$, $|\alpha_i\rangle$. The new states of interest are those formed by two states of the old $\hat{\mathcal{H}}_0$ basis that differed in energy by $\sim\hbar\omega$. If we refer to these states as $|\alpha_1\rangle$ and $|\alpha_2\rangle$ and assume that before our radiation is turned on our system is described totally by $|\alpha_1\rangle$, after being in the field for a time τ our system will be described via

$$|\phi(\tau)\rangle = a_1(\tau)|\alpha_1\rangle + a_2(\tau)|\alpha_2\rangle. \tag{4.36}$$

At time $t = 0$, $a_1(t) = 1$ and $a_2(t) = 0$. At time τ, $a_2(\tau)$ may be nonzero, and if the radiation is now turned off, the quantity $|a_2(\tau)|^2$ represents

the probability of a transition from $|\alpha_1\rangle$ to $|\alpha_2\rangle$:

$$P_{12}(\omega,\tau) = |a_2(\tau)|^2 \tag{4.37}$$

Taking the results from the appendix for a two level system,

$$P_{12}(\omega,t) = \frac{(2\omega_1)^2}{(2\omega_1)^2+(\omega_0-\omega)^2} \sin^2\{\tfrac{t}{2}((2\omega_1)^2 + (\omega_0 - \omega)^2)^{\frac{1}{2}}\} \tag{4.38}$$

where

$$\omega_0 \equiv |E_{\alpha_1}(\mathcal{E}_{DC}) - E_{\alpha_2}(\mathcal{E}_{DC})|/\hbar \tag{4.39}$$

is the resonant frequency dependent on the initial energies of the states $|\alpha_1\rangle$ and $|\alpha_2\rangle$, which will in turn be dependent upon the DC field strength from the static Stark term, and

$$\omega_1 \equiv |\langle\alpha_2| - \underset{\sim}{\mu} \cdot \underset{\sim}{\mathcal{E}}_{RF} |\alpha_1\rangle|/\hbar \equiv H_{12}/\hbar \tag{4.40}$$

is the "coupling" constant that depends on how the states $|\alpha_1\rangle$ and $|\alpha_2\rangle$ mix in the presence of a field. "t" here is the time duration of the interaction field.

With Equation (4.38) at hand, the problem of calculating the probability of a transition is now reduced to the evaluation of ω_1 or H_{12} in Equation (4.40). Values of ω restricted to the radio frequency realm, which is the frequency range of interest to us, correspond energetically to transitions between states of the same J, i.e., $J_1 = J_2$. However, as will be seen below, the value of the matrix element

$$\langle J_2 M_{J_2} | \underset{\sim}{\mu} | J_1 M_{J_1} \rangle$$

is nonzero only for $\Delta J = J_2 - J_1 = \pm 1$. Thus, to find H_{12} of Equation (4.40) to be nonzero requires that, if $|\alpha_1\rangle$ and $|\alpha_2\rangle$ are expressed in a $|J,M_J\rangle$ basis, they must contain terms of different J. The mechanics of the problem are thus to express $|\alpha_1\rangle$ and $|\alpha_2\rangle$ as linear combinations of the complete strong field basis $|a_i\rangle \equiv |J_i M_{J_i} I_{1_i} M_{1_i} I_{2_i} M_{2_i}\rangle$, but, unlike the method described at the end of the last section, the diagonalization process cannot use a block diagonal approximation for J, for we need to know precisely how the J states mix. Once we can express the states in the strong field basis, i.e., know the values of A_{ij} for, as in Equation (4.2),

$$|\alpha_i\rangle = \sum_i A_{ij} |a_i\rangle, \tag{4.41}$$

we can then evaluate H_{12} via

$$\langle\alpha_2|-\underset{\sim}{\mu}\cdot\underset{\sim}{E}_{RF}|\alpha_1\rangle = \sum_i \sum_{k'} A_{i1} A^*_{k2} \langle a_k|-\underset{\sim}{\mu}\cdot\underset{\sim}{E}_{RF}|a_i\rangle . \tag{4.42}$$

As will be seen, the choice of the strong field basis makes the evaluation of the matrix elements on the right of Equation (4.42) particularly simple.

As an example we will solve for H_{12} for molecules like OCS which have no nuclear spin. Then the stationary Hamiltonian is

$$\hat{\mathcal{H}}_0 = \hat{\mathcal{H}}_{ROT} + \hat{\mathcal{H}}_{STARK} \tag{4.43}$$

and we use as our basis set $|a_i\rangle = |J_i M_{Ji}\rangle$, which is diagonal for $\hat{\mathcal{H}}_{ROT}$ but not $\hat{\mathcal{H}}_{STARK}$. In order to find exactly the eigenstates $|\alpha_j\rangle$, and hence the coefficients A_{ij}, one would need to diagonalize the entire $\langle J_i M_{Ji}|\hat{\mathcal{H}}_0|J_k M_{Jk}\rangle$ matrix. This, however, would be quite formidable,

given the large number of possible values of J. The actual eigenstates $|\alpha_j>$ end up being predominantly associated with a particular $|J_i M_{Ji}>$, with contributions from other states rapidly decreasing as the value of J from those other states differs more from J_i. As long as the Stark perturbation is significantly less than the pure rotational energy it is a quite good approximation to allow only the mixing of one J_i state with states of $J_k = J_i \pm 1$. In fact, first order perturbation theory allows precisely this, so we shall use its mechanics, as opposed to matrix diagonalization, to find our A_{ij}. Given an initial basis set $|a_i^{(0)}>$ with energies $E_i^{(0)}$ and a Hamiltonian perturbation $\hat{\mathcal{H}}_s$, the first order perturbation eigenstates are given via

$$|a_j^{(1)}> = |a_j^{(0)}> + \sum_{i \neq j} \frac{<a_i^{(0)}|\hat{\mathcal{H}}_s|a_j^{(0)}>}{E_j^o - E_i^o} |a_i^{(0)}>. \tag{4.44}$$

We identify $|a_j^{(0)}>$ to $|J_j M_{Ji}>$, $|a_j^{(1)}>$ to $|\alpha_j>$ and $\hat{\mathcal{H}}_s$ to $\hat{\mathcal{H}}_{STARK}$. Much of the mechanics of this problem was worked on in Chapter III in Equations (3.10)-(3.13). Briefly, we have

$$\hat{\mathcal{H}}_s = -\hat{\underset{\sim}{\mu}} \cdot \underset{\sim}{E}_{DC} = -\hat{\mu}_z E_{DC} \quad \text{and} \tag{4.45}$$

$$E_i^o = BJ_i(J_i + 1),$$

and combining Equation (4.44) here with Equation (3.3-3.13), we get

$$\begin{aligned} |\alpha_j> &\approx |J\ M^{(1)}> \\ &= N_{JM}\{|JM^{(0)}> - \frac{\mu E_{DC}}{2B} \frac{J^2 - M^2}{J^2(2J-1)(2J+1)}^{\frac{1}{2}} |J-1, M^{(0)}> . \\ &+ \frac{\mu E_{DC}}{2B} \frac{(J+1)^2 - M^2}{(J+1)^2(2J+1)(2J+3)}^{\frac{1}{2}} |J+1, M^{(0)}>\} . \end{aligned} \tag{4.46}$$

where we have dropped the "j" subscripts for simplicity from J_j and M_j "N_{JM}" is a normalization constant approximately equal to 1 as $\mu E_{DC}/2B$ is typically quite small. "μ", as before, is the dipole moment of the molecule in a frame rotating with the molecule. The energy of this state is given by the second order perturbation result of Equation (3.3-3.14). Comparing Equation (4.46) to (4.41) one notes that we have now solved for the A_{ij}. We also note that each $|\alpha_j\rangle$ has a unique quantum number M, i.e., "M" is still a good quantum number in our new basis.

Knowing $|\alpha_j\rangle$ now, we consider the effect of the time perturbation. We will assume here that the radiation vector E_{RF} of Equation (4.35) is in the x direction, perpendicular to the direction of E_{DC}, so that

$$-\hat{\mu}\cdot E_{RF} = -\hat{\mu}_x E_{RF}. \tag{4.47}$$

The matrix elements for μ_x in the $|J,M\rangle$ basis are given by

$$\langle JM|\mu_x|J+1,M\pm1\rangle = \mp \frac{\mu}{2}\left(\frac{(J\pm M+2)(J\pm M+1)}{(2J+1)(2J+3)}\right)^{\frac{1}{2}} . \tag{4.48}$$

Thus, μ_x connects the strong field states $|a_i\rangle$ and $|a_j\rangle$ only if $J_j - J_i = \pm1$ and $M_j - M_i = \pm1$. As our eigenstates $|\alpha_j\rangle$ from Equation (4.46) consist of strong field basis states with only a particular value of M, Equation (4.48) also indicates that "perpendicular" transitions between $|\alpha\rangle$ states can only occur if $M = \pm1$ between those states. Combining Equations (4.42), (4.46), and (4.48), we can now evaluate H_{12}:

$$\begin{aligned} H_{12} &= \langle J,M^{(1)}| - \hat{\mu}_x E_{RF}|J,M\pm1^{(1)}\rangle \\ &= \frac{\mu^2 E_{DC} E_{RF}}{4B} f^{\pm}(J,M) \end{aligned} \tag{4.49}$$

where,

$$f^{\pm}(J,M) = \frac{[(J\pm M+1)(J\pm M)(J^2-M^2)]^{\frac{1}{2}} - [(J\mp M-1)(J\mp M)(J^2-(M\pm 1)^2)]^{\frac{1}{2}}}{J(2J+1)(2J-1)}$$

$$+ \frac{[(J+M+1)(J+M)((J+1)^2-M^2)]^{\frac{1}{2}} - [(J\pm M+2)(J\pm M+1)((J+1)^2-(M\pm 1)^2)]^{\frac{1}{2}}}{(J+1)(2J+1)(2J+3)} \tag{4.50}$$

Appendix I attempts to give some intuitive sense for the leading factor of Equation (4.49). Values for $f^{\pm}(J,M)$ for $J \leqslant 5$ are given in Table 4.5 If we consider $\underset{\sim}{E}_{RF}$ parallel to $\underset{\sim}{E}_{DC}$, H_{12} looks quite similar to the second order perturbation energy:

$$H_{12} = \frac{\mu^2 E_{DC} E_{RF}}{2B} f_2(J,M) \tag{4.51}$$

where $f_2(J,M)$ was defined in Equation (3.14). However, with $\underset{\sim}{E}_{RF}$ parallel to $\underset{\sim}{E}_{DC}$ there is only coupling between $|\alpha_i\rangle$ states of the same M. Since we are already restricting ourselves to $\Delta J = 0$ transitions in radio-frequency spectroscopy, for molecules like OCS, $\Delta J = 0$, $\Delta M = 0$ implies no change in the state at all.

For the more general case of molecules with nuclear spin, as ClF, the idea is the same but the method slightly different. As with OCS, when determining the stationary states $|\alpha_i\rangle$ of $\hat{\mathcal{H}}^{\circ}$ from Equation (4.6) we need to find the contributions from different J states in the strong field basis $|a_i\rangle = |JM_J I_1 M_1 I_2 M_{2_i}\rangle$ from the Stark DC term. The program "TWOSPIN" in Appendix II includes only the contributions as far as $J_j = J_i \pm 1$ in the calculation of $|\alpha_j\rangle$, just as we limited ourselves in the evaluation of the $|\alpha\rangle$ for OCS. This program, then, differs from "W.vs E" by diagonalizing a matrix connecting the basis elements of J-1, J, and J+1 to find the states $|\alpha\rangle$ associated with J, and therefore does not need to have the Stark perturbative results added along the

Table 4.5

Change of Second Order Energy Coefficient and Transition Probability Factor for a Linear Rotating Dipole

J	M	M+1	$\Delta f_2^+(J,M)$ [1]	$f^+(J,M)$ [2]
1	0	1	0.30	0.4243
2	0	1	0.0238	0.05832
2	1	1	0.0714	0.1429
3	0	1	5.56×10^{-3}	1.925×10^{-2}
3	1	2	1.67×10^{-2}	5.270×10^{-2}
3	2	3	2.78×10^{-2}	6.804×10^{-2}
4	0	1	1.95×10^{-3}	8.712×10^{-3}
4	1	2	5.84×10^{-3}	2.479×10^{-2}
4	2	3	9.74×10^{-3}	3.644×10^{-2}
4	3	4	1.36×10^{-2}	3.857×10^{-2}
5	0	1	8.55×10^{-4}	4.681×10^{-3}
5	1	2	2.56×10^{-3}	1.357×10^{-2}
5	2	3	4.27×10^{-3}	2.094×10^{-2}
5	3	4	5.98×10^{-3}	2.538×10^{-2}
5	4	5	7.69×10^{-3}	2.433×10^{-2}

[1] $\Delta f_2^+(J,M) \equiv f_2(J,M+1) - f_2(J,M)$ where $f_2(J,M)$ is defined by Equation (3.14).

[2] $f^+(J,M)$ is defined by Equation (4.50). As note it can be shown that $f^-(J,M) = f^+(J,M-1)$.

diagonal. The selection rules for $\hat{\underset{\sim}{\mu}}\cdot\underset{\sim}{E}_{DC}$ in the strong field basis were indicated in Table 4.2. Diagonalizing this Hamiltonian matrix now gives the coefficients A_{ij} of Equation (4.41) in the matrix that performs the diagonalizing transformation, as shown in Equation (4.22), i.e., we now know the eigenstates of H_0 as

$$|\alpha_j\rangle = \sum_i A_{ij} \; |JM_J I_1 M_1 I_2 M_2{}_i\rangle. \tag{4.52}$$

Again, given the A_{ij}, H_{12} can be evaluated via Equation (4.42). The matrix elements for $\langle a_k|-\hat{\underset{\sim}{\mu}}\cdot\underset{\sim}{E}_{RF}|a_i\rangle$ are the same for this strong field basis as they were for the $|JM\rangle$ basis, with M_J substituted in for M in the equations for $\hat{\mu}_x$ and $\hat{\mu}_z$, (4.48) and (3.13). Besides having perpendicular, $\Delta M_J = \pm 1$, transitions as with OCS, parallel $\Delta M_J = 0$ transitions are now also allowed, as there now may be several different stationary states of $\hat{\mathcal{H}}_0$ with the same J and M_J. Recall that in the weak field limit M_J is not a "good" quantum number if the molecule has nuclear spin, so that a single $|\alpha_j\rangle$ state may have contributions from strong basis states of different M_J, again making H_{12} evaluation slightly more complex. Table 4.6 presents some of the J = 1 eigenfunctions derived for ClF including the J = 0 and J = 2 contributions and all the J = 1 eigenvalues, while Table 4.7 gives values for ω_0 and H_{12} connecting these states for both the parallel and perpendicular transitions.

The transition line shapes as a function of the radiating frequency are given for simple two level systems by Equation (4.38) and are described qualitatively in Appendix I. The two level approximation works as long as neither of the two $|\alpha_j\rangle$ states of interest which have a resonant frequency of ω_0 (Eq. (4.39)) are resonant to any other states at a frequency within a few factors of ω_1 (Eq. (4.40)) from ω_0.

Table 4.6

a) $J=1$, $M_F = 2$ and 3 Eigenstates for ClF, $\mathcal{E}_{DC} = 1052$ V/cm in the Strong Field Basis[1]

M_F	State#
3	$\|1\rangle = 1.0000\|1,1,3/2,1/2\rangle + 0.0034\|2,1,3/2,1/2\rangle$
2	$\|2\rangle = 0.0066\|0,0,3/2,1/2\rangle - 0.7558\|1,0,3/2,1/2\rangle - 0.0003\|1,1,3/2,-1/2\rangle$
	$+ 0.6548\|1,1,1/2,1/2\rangle - 0.0030\|2,0,3/2,1/2\rangle + 0.0022\|2,1,1/2,1/2\rangle$
	$\|3\rangle = 0.0001\|0,0,3/2,1/2\rangle - 0.0065\|1,0,3/2,1/2\rangle - 0.9999\|1,1,3/2,-1/2\rangle$
	$- 0.0080\|1,1,1/2,1/2\rangle - 0.0034\|2,1,3/2,-1/2\rangle$
	$\|4\rangle = 0.0057\|0,0,3/2,1/2\rangle - 0.6547\|1,0,3/2,1/2\rangle + 0.0103\|1,1,3/2,-1/2\rangle$
	$- 0.7558\|1,1,1/2,1/2\rangle - 0.0026\|2,0,3/2,1/2\rangle - 0.0026\|2,1,1/2,1/2\rangle$

b) Eigenvalues for $J=1$, ClF, $\mathcal{E}_{DC} = 1052$ V/cm

State#	M_F	Energy[2]	State#	M_F	Energy
1	3	6601.80	9	1	36451.10
2	2	-28659.50	10	0	-29778.92
3	2	6621.13	11	0	-29764.31
4	2	7493.69	12	0	7859.95
5	1	-29775.52	13	0	7882.94
6	1	-28647.56	14	0	36432.69
7	1	7504.32	15	0	36451.39
8	1	7868.20			

[1] Basis states are in the form $|J, M_J, M_1, M_2\rangle$. $I_1 = 3/2$ and $I_2 = 1/2$ throughout.

[2] Energies relative to $BJ(J+1) = 30966.$ MHz.

Table 4.7

Transition Frequencies (ω_0) and Connecting Dipole Matrix Elements (H_{12}) for ClF, J = 1, E_{DC} = 1052 V/cm

$\Delta M_F = 0$			$\Delta M_F = \pm 1$		
ω_0 [1]	I,K [2]	H_{12}/E_{RF} [3]	ω_0 [1]	I,K [2]	H_{12}/E_{RF} [3]
1128.0	5,6	-0.01	14.7	8,13	0.01
872.6*	3,4	-0.02	8.2	8,12	-0.01
363.9*	7,8	-0.02	29830.0*	3,9	0.01
35280.6	2,3	-0.02	1247.1	3,8	-0.02
37279.8*	5,7	0.04	36163.8*	2,7	-0.03
28946.8	7,9	-0.06	65080.2*	6,14	0.13
36515.8	6,8	-0.07	65099.0*	6,15	0.13
			65110.6*	2,9	0.19
			37269.6*	7,11	0.21
			37283.2*	7,10	0.25
			37269.2*	4,5	0.33
			378.6*	7,13	-0.35
			66226.9*	5,15	-0.35
			355.6*	7,12	0.35
			66215.4*	9,11	-0.35
			66230.0*	9,10	0.35
			66208.2*	5,14	0.35
			374.5*	4,8	0.50
66215.7*	11,15	-0.61	28583.2*	8,15	-0.62
66226.6*	5,9	0.61	28568.2*	9,13	-0.64
66211.6*	10,14	-0.61	28591.2*	9,12	-0.64
			1131.4	6,10	-0.65
			1116.8	6,11	-0.65
			28564.5*	8,14	0.67
			37647.1*	8,10	0.70
37643.7	5,8	0.76	37658.4	5,13	0.70
37624.3	11,12	0.76	37635.5	5,12	0.71
37661.9	10,13	-0.76	37632.5	8,11	-0.71

(continued)

Table 4.7 (continued)

$\Delta M_F = 0$			$\Delta M_F = \pm 1$		
ω_0 [1]	I,K [2]	H_{12}/E_{RF} [3]	ω_0 [1]	I,K [2]	H_{12}/E_{RF} [3]
			36507.5	6,12	0.77
			36530.5	6,13	-0.78
			28928.4	7,14	-0.91
			1116.0	2,5	0.92
			883.2	3,7	0.94
			891.9*	1,4	-0.94
28582.9*	8,9	-1.86	28947.1	7,15	-0.95
28549.8*	13,14	-1.86	35261.3	1,2	-1.09
28591.4*	12,15	1.86	35268.7	3,6	-1.09
36151.9*	6,7	2.02	36537.7	2,8	-1.09
36153.2*	2,4	-2.02	28957.4	4,9	1.31

[1] Transition frequency (kHz).

[2] Interacting states' labels (see Fig. 4.3 and Table 4.6).

[3] Dipole matrix element (kHz/(Volt(RF) cm^{-1})).

* Transitions observable by Stark focusing (the focusable states are #4, 7, 9, 14, and 15).

Qualitatively the predicted line shape is a Lorentzian envelope about a sinusoidal beating. This beating would be evident in other forms of spectroscopy as well if they had the resolution on the order of ω_1, which most do not.

There are other aspects of the transition spectra due to the molecular beam part of the MBER. Collisional perturbations and Doppler effects play essentially no role in determining the lineshapes. In fact, it is in part the narrow velocity distribution inherent with molecular beams that allows the observation of Rabi beating. Increasing the time molecules spend within the resonance region would permit the use of lower rf voltages, reducing ω_1 of Equation (4.38) and thereby narrowing the linewidth. However, it is difficult to reduce a beam's speed below the flow velocities we are using without simultaneously broadening the velocity distribution. Increasing the length of the resonant region would introduce a different source of inhomogeneities.

Ultimately there are three conditions to be met for a transition to be observable in our MBER apparatus. First, trivially, the resonance frequency ω_0 must be attainable. Again, the value of ω_0 is dependent upon the C field static voltage, typically on the order of 0-1000 V/cm. Secondly, as elaborated upon in this section, there must be a sufficiently large dipole matrix element connecting the two states, related to the frequency ω_1, which is dependent both on the static and rf voltages within the C field. This ω_1 contains the radiative dipolar selection rules for the transition. Finally, for the transition to be detected, the initial state must be focusable by the A field while the final state is either defocused or much less focusable by the B field. This is the Stark selection rule for MBER spectroscopy. As the A and

B fields are of strengths on the order of 10^4 V/cm, the behavior of the initial and final states needs to be known here, as well as at the field strength in the transition region, to predict the presence of a flop-out or flop-in signal.

B. Experimental and Numerical Results

1. OCS Data

The experimental method for taking MBER spectra has been described in detail in Chapter II. The spectra shown in this and in the following section were taken with a 100 μ diameter source nozzle, a 0.032" diameter stopwire barrier and a 0.06" diameter detector orifice. The C field was set for the parallel-perpendicular mode. A typical OCS resonance spectrum is given in Figure 4.4. As indicated in the caption, this spectrum corresponds to a dc voltage of 1043.4 V applied to the C field and rf voltages of 10 V (measured peak to peak) through the frequency range. The A and B fields were set to their first refocusing maximum (see Chapter III), with $V_A \approx 20$ kV and $V_B \approx 11$ kV. This OCS spectrum is seen as an oscillatory pattern beating at about 5 kHz and enclosed by an envelope with a 40 kHz FWHM centered at 3479 kHz. The general shape is in qualitative agreement with that predicted by theory for a single resonance transition, though, as will be seen later, it cannot be matched quantitatively to Rabi's formula (Eq. (4.38)). The beating nodes do not generally return to the baseline due to velocity averaging effects. The remaining spectra of this section were taken to examine the effects of varying the parameters relevant to Rabi's formula on the OCS $J = 1$, $M = 0 \leftrightarrow \pm 1$ line shapes.

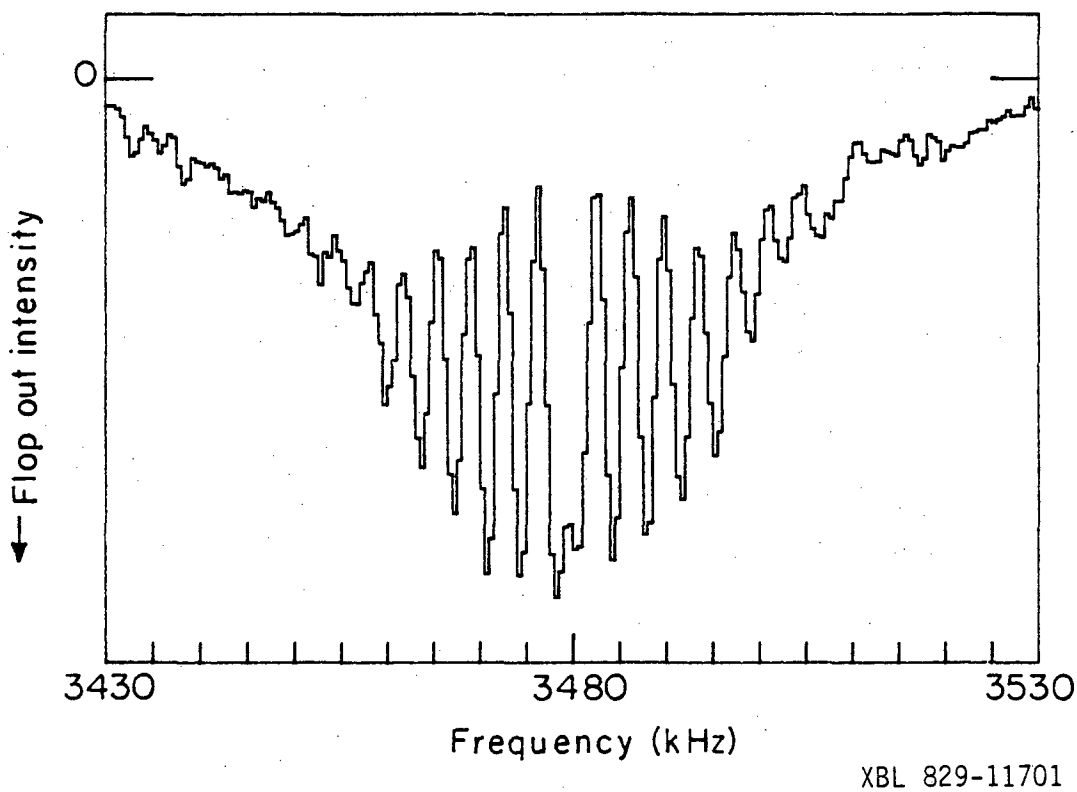

Figure 4.4. OCS resonance spectrum for the J=1, M=0 ↔ ±1 transition. (V_{DC} = 1043.4 V, V_{RF} = 10 V peak to peak. Beam 5% OCS in Ar, P_s = 1.2 atm, T_s = 23°C.)

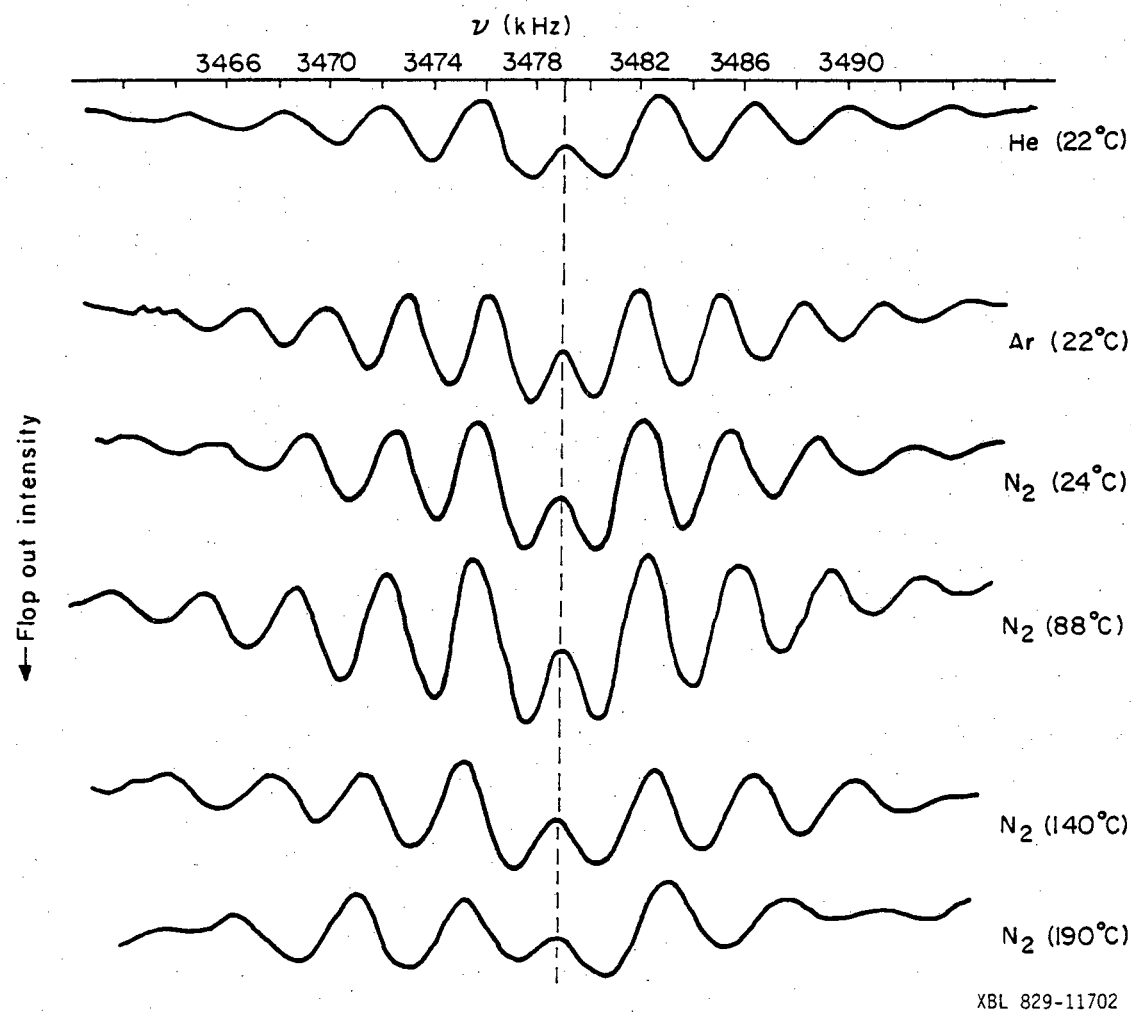

Figure 4.5. OCS resonance spectra for various carrier gases and source temperatures. (V_{DC} = 1043.4 V, V_{RF} = 11 V. Beam 50% OCS in indicated gas, P_s = 1.7 atm. A and B fields adjusted for best signal. Spectra taken by S. A. Sherrow.)

Two methods were used to vary τ, the time period that the molecules experience the radiation field: changing the source temperature and changing the molecular beam composition. These affect the mean beam velocity. Figure 4.5 gives some representative results for OCS seeded in Ar, He and N_2 carriers and some temperature variation. In general one notes that aside from heat capacity effects, the larger the mean mass of a particle within the beam, the lower the resultant mean speed, s_0, will be via energy conservation, and, thus, the longer τ will be. Increasing τ in Eq. (4.38) would lead to a decrease in the separation of the nodes as a function of ω. As an example, the ratio of the separations between the first and second nodes to the sight of ν_0 for the He and Ar spectra in Figure 4.5 is ca. 1.3. Meanwhile, the inverse ratio of the square roots of the average masses of these beams is 1.25. A decrease in the source temperature also decreases the beam velocity and thereby decreases the nodal separations. The ratio of the first and second node separations for T_s = 413 and 297 K (with a N_2 carrier) from Figure 4.5 is 1.17, while the ratio of the square roots of their temperature is 1.18.

The effects of varying just the dc voltage of the Stark field involve changing the resonant frequency and the line shape. As OCS has no nuclear spins, the resonant frequency for the J = 1 transition can be accurately predicted via the second order perturbation equation for energy levels given by Equation (3.14). Using established spectroscopic values for the rotational constant and dipole moment of OCS and our measured central frequencies for the transition as a function of the applied dc voltage to the C field flats (V_{DC}), one can calculate the effective spacing between the C field flats, r_c, as

Table 4.8

OCS (1,0) ↔ (1,1) Resonance Frequencies as a Function of Applied DC Voltage to the C Field

V_{DC}(V)	ν_0 (kHz)	ν_0/V_{DC}^2	ν_0/V_{DC}^2(calc)*
1043.6	3480.70	3.1959×10^{-3}	3.1958×10^{-3}
911.4	2655.35	3.1967×10^{-3}	3.1965×10^{-3}
723.6	1673.95	3.1970×10^{-3}	3.1974×10^{-3}
620.3	1230.15	3.1971×10^{-3}	3.1978×10^{-3}
311.3	310.05	3.1992×10^{-3}	3.1986×10^{-3}

* From best fit of $\frac{\nu_0}{V_{DC}^2} = A + B\,V_{DC}^2$, with

$A = 3.1989(4) \times 10^{-3}$ and $B = -2.9(6) \times 10^{-12}$. ("A" implies a C field spacing of 0.9908 cm.)

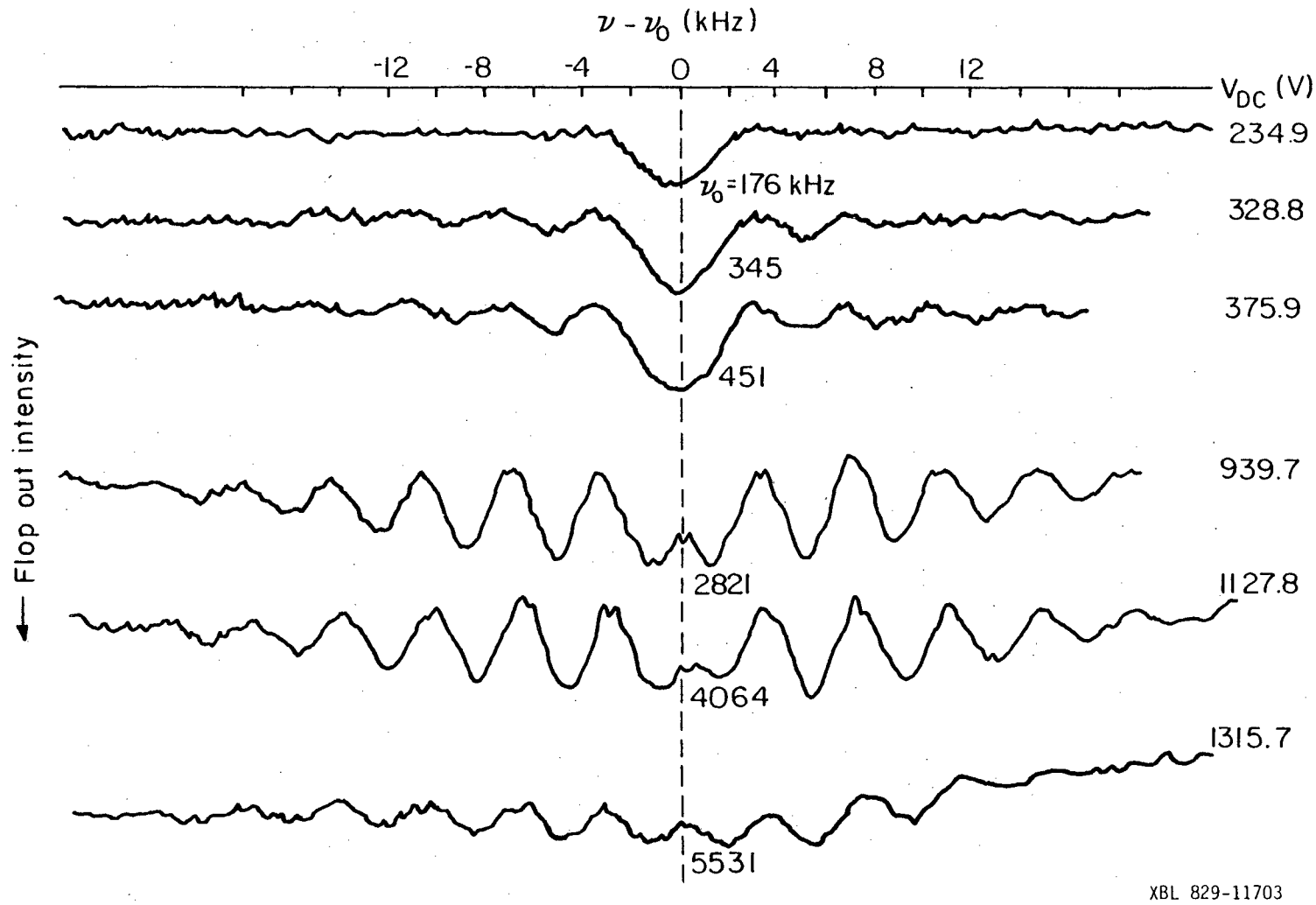

Figure 4.6. OCS resonance spectra at various Stark field voltages (V_{RF} = 10 V, P_s = 1 atm, T_s = 23°C. Frequencies measured relative to the center of the resonance pattern, ν_0).

$$\mathcal{E}_{DC} = V_{DC}/r_c, \tag{4.53}$$

by linearly fitting the frequencies versus V_{DC}^2. In Table 4.8 data from such a series of experiments are presented with the resulting best fit allowing for a fourth order perturbation term as well (Eq. 3.15). This allowed the determination of a 0.9908 cm separation in the C field. The line shape effect of varying V_{DC} is indicated in Figure 4.6. The center resonance frequencies, ν_0, at various V_{DC}'s have been aligned to allow a comparison of the beating patterns. As the voltage is increased the shape evolves from a single peak of width 6 kHz, to a symmetric oscillation about ν_0. Further increasing V_{DC} increases the relative amplitude of the "secondary" peaks to that of ν_0 and creates some asymmetry in the pattern, until at high V_{DC} the spectrum becomes too distorted to assign accurately a value for the center frequency. The baseline itself becomes skewed. However, the nodal separations do not appear to be very sensitive to V_{DC}.

Changing the rf voltage amplitude while holding V_{DC} constant does not alter ν_0, but does vary the line shape in a manner similar to that mentioned above. Figure 4.7 shows this effect for OCS with V_{DC} = 428 V. For the given V_{RF} range one observes the spectrum evolving again from a single maximum to a beating pattern with the secondary structure growing with V_{RF} while the nodal spacing remains insensitive to the rf power. Asymmetry also develops. This is seen again in Figure 4.8 where V_{DC} = 1043 V. As V_{RF} increases the distortion increases; the baseline of the peaks shifts, and the node positions shift as well. The flop out intensity at ν_0 = 3478.8 kHz as a function of V_{RF} (V_{DC} fixed at 1043 V) is plotted in Figure 4.9. As qualitatively predicted by Rabi's formula,

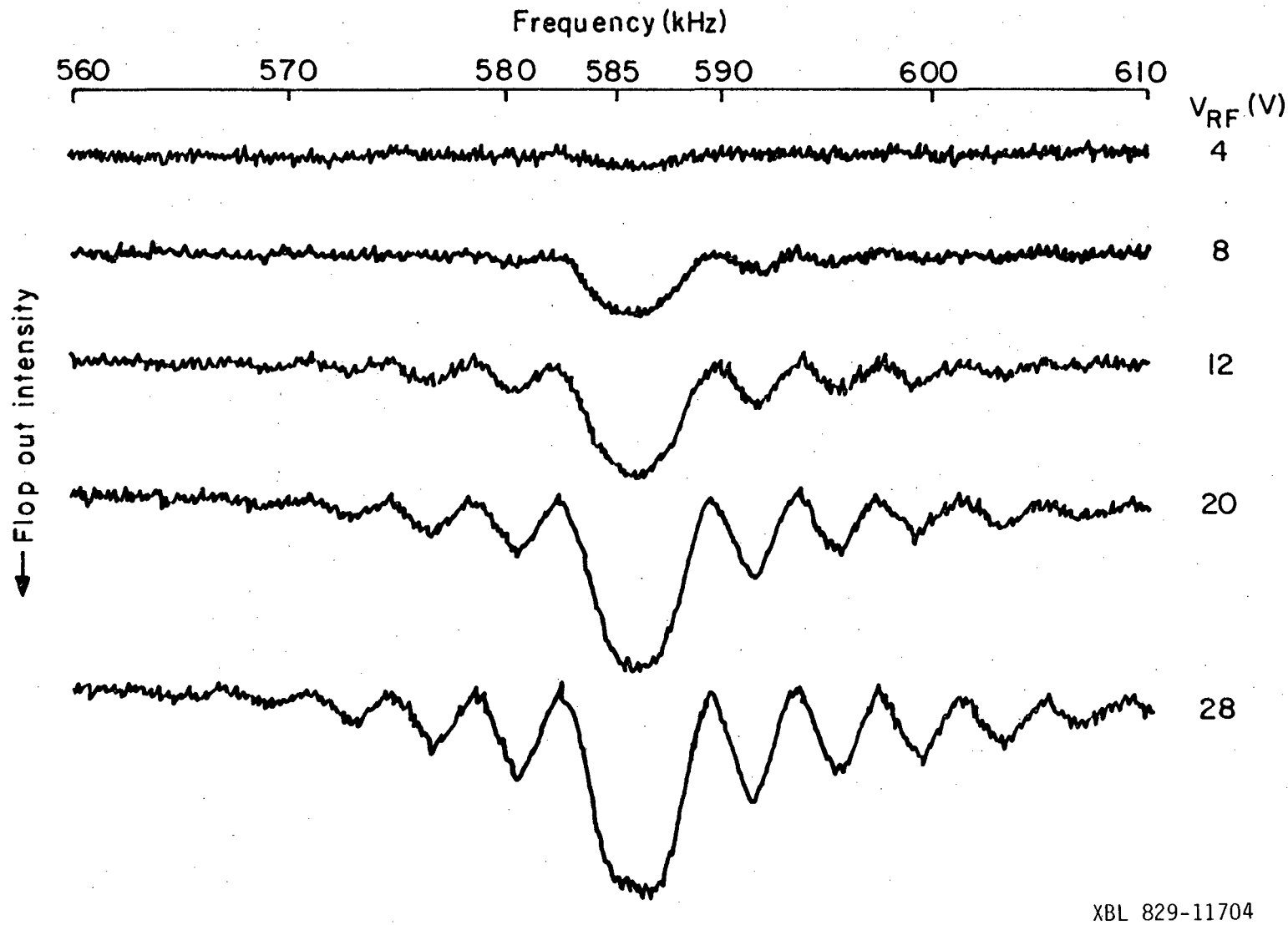

Figure 4.7. OCS resonance spectra at various RF voltages (V_{DC} = 428 V, P_s = 1 atm, T_s = 23°C).

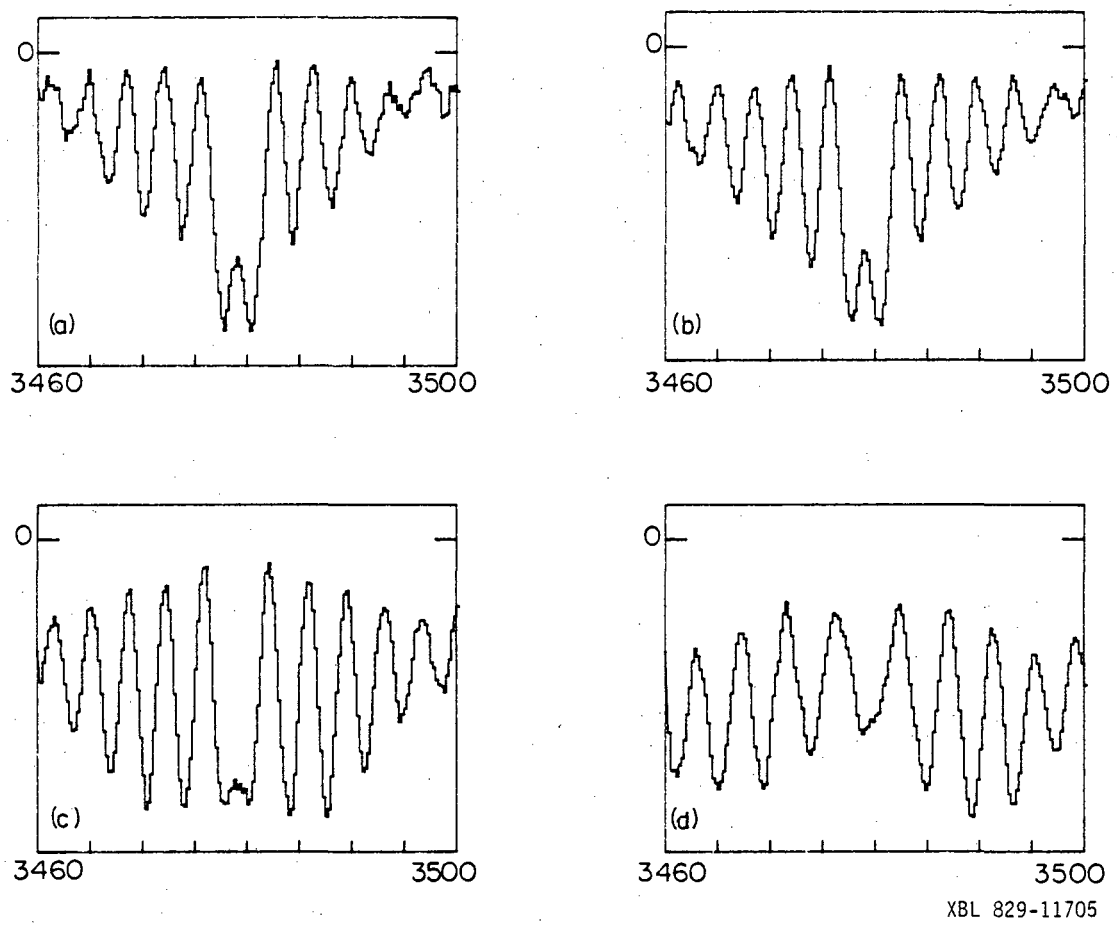

Figure 4.8. OCS resonance spectra at various RF voltages (V_{DC} = 1043 V, P_s = 1.2 atm, T_s = 23°C). V_{RD} = (a) 3V; (b) 5 V; (c) 10 V; (d) 20 V.

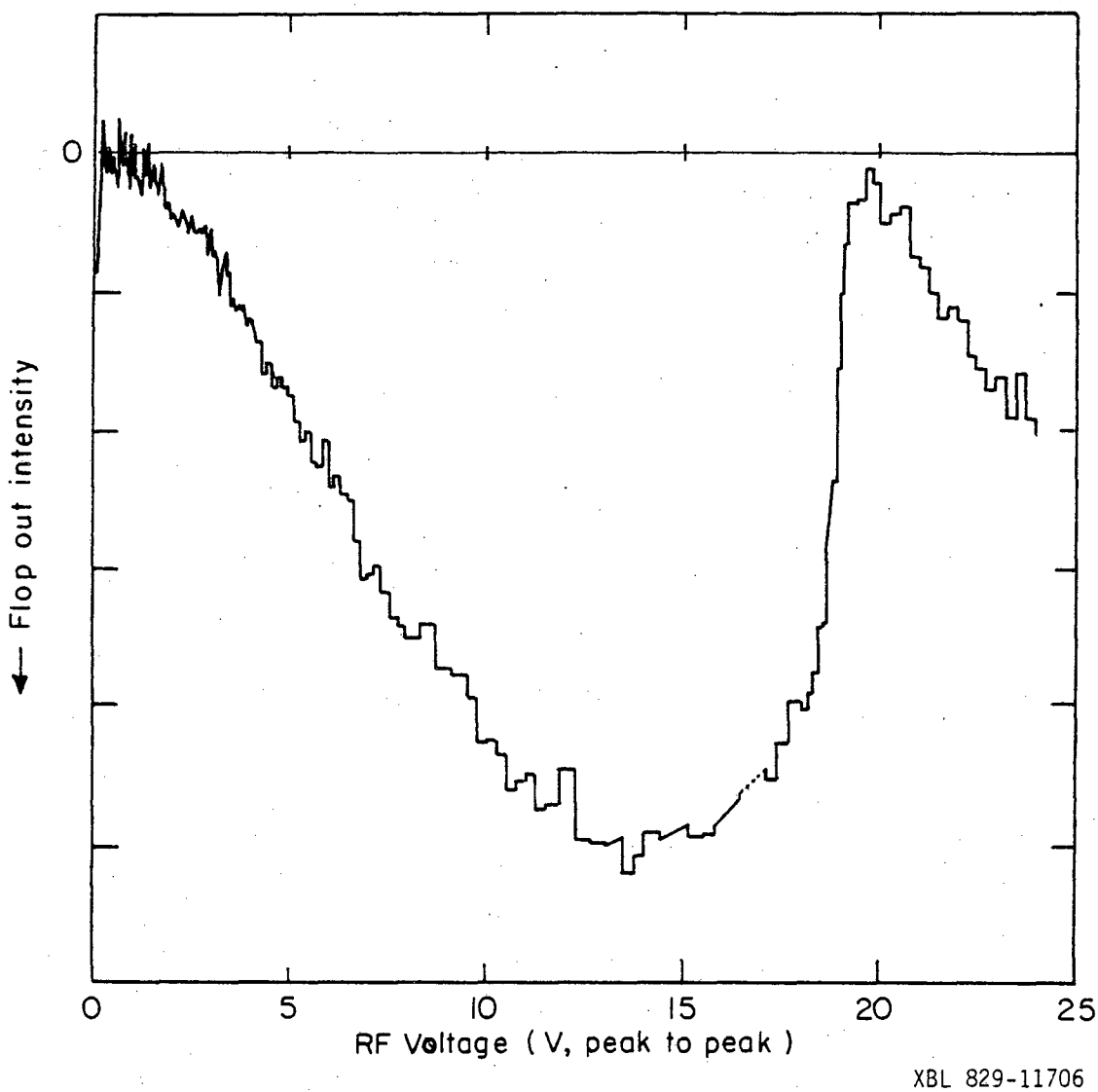

Figure 4.9. OCS transition strength as a function of RF voltage (V_{DC} = 1043 V, ν = 3478.8 kHz, P_s = 1.2 atm, T_s = 23°C).

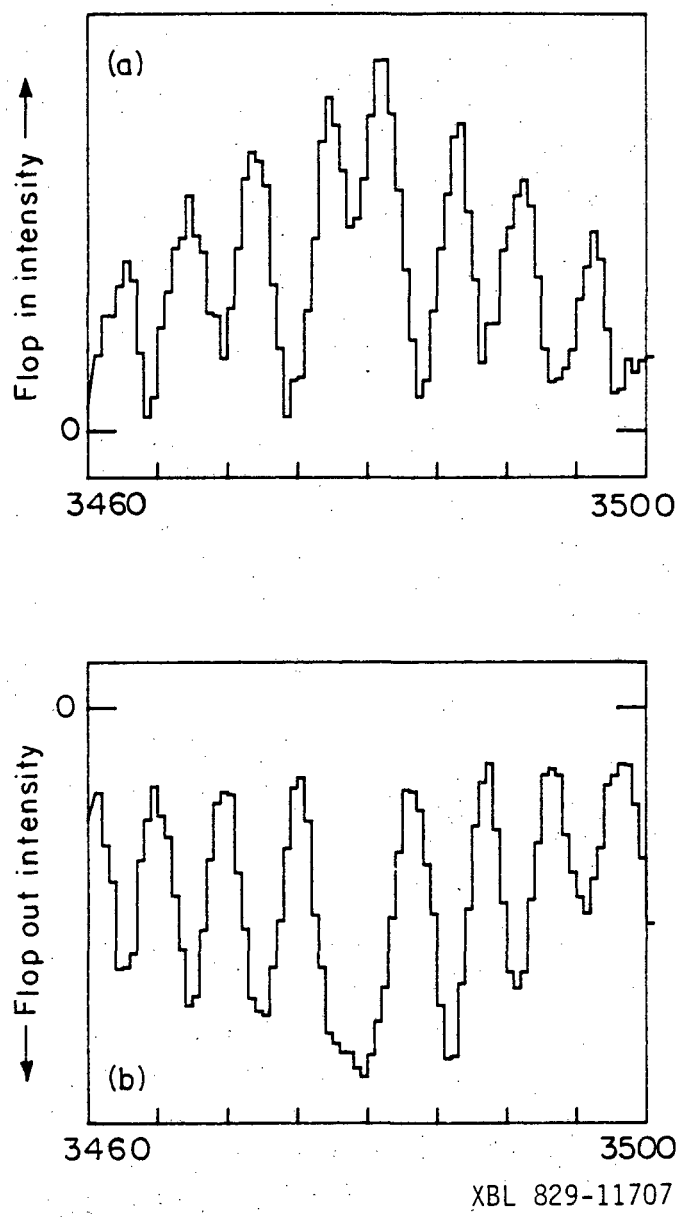

Figure 4.10. OCS resonance spectra (a) Flop in: V_A = 25 kV, V_B = 25 kV; (b) Flop out: V_A = 18 kV, V_B = 25 kV. (V_{DC} = 1043 V, V_{RF} = 8 V, P_s = 2 atm, T_s = 147°C, 5% in Ar).

it does show an oscillation, though its form is distorted from a pure sinusoidal shape.

As an example of other observed results for OCS spectra, Figure 4.10 compares a flop in spectrum to a flop out one. As discussed in Chapter III, this phenomenon is predicted to occur and be particularly dependent upon the A field focusing voltage. Recently this has been found to also be sensitive to the detector aperture diameter. Attempting to cause an OCS J = 1 transition with the C field in parallel only mode (see Chapter II) gave a resonance signal about one third as strong as when using the parallel-perpendicular mode. As this transition is supposed to require an rf excitation perpendicular to the dc Stark field, there is an indication of some rf field line distortion in the parallel mode. Finally, no J = 2 transitions for OCS were observable from our apparatus. In those experiments, the A and B fields were tuned to maximum voltages to enhance the J = 2 refocus signal, but to no avail.

2. <u>ClF Data</u>

As indicated in Section IVA the ClF J = 1 resonance spectrum can have many peaks due to the additional eigenstates present corresponding to the coupling of the Cl and F nuclear spins to the molecule's rotation. (See Tables 4.4, 6 and 7.) Figure 4.11 and Table 4.9 indicate the resonance regions we observed with the Stark field at 1043 V. The rough assignment (with intermediate field basis labels) of the transitions in Table 4.9 was made by the use of Table 4.7 and Figure 4.3. Other expected peaks indicated by Table 4.7 were sought but not found.

The effect of varying the Stark dc voltage can be seen for the $F_1 = 1/2 \rightarrow 3/2$ resonances in Figure 4.12. As with the OCS spectra, these spectra shift to different frequency regions with V_{DC}, but not in as

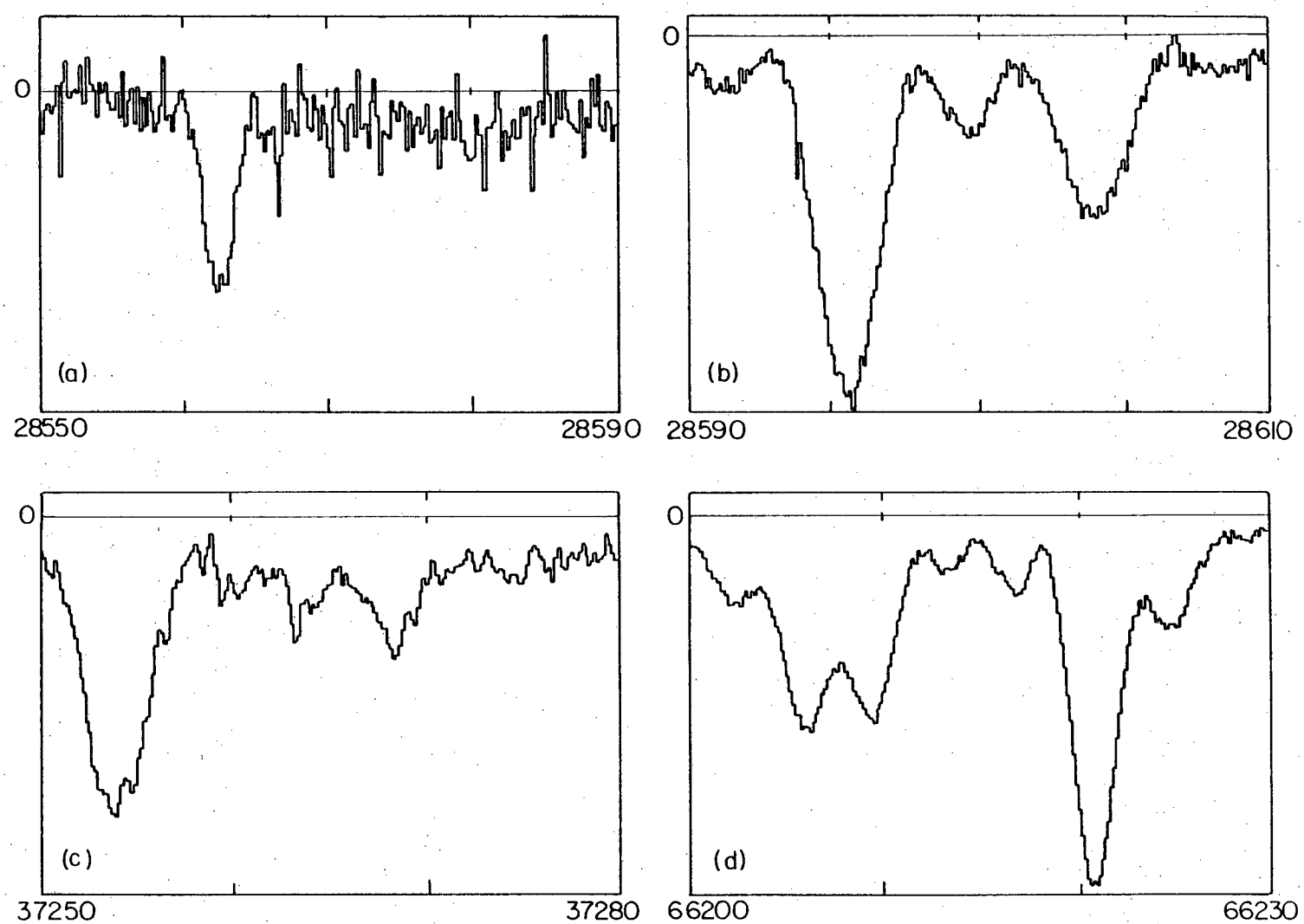

XBL 829-11697

Figure 4.11. ClF resonance spectra for J=1 transitions (V_{DC} = 1043 V, 30% in Ar, P_s = 1 atm, T_s = 23°C. See Table 4.9.)

Table 4.9

Observed ClF Resonance Flop Out Peaks. $\mathcal{E}_{DC} = 1054$ V/cm, Low Resolution (see Fig. 4.10. Units in kHz.)

28562.0	$F_1 = 1/2 \rightarrow 5/2$
28595.7	$M_{F_1} = 1/2 \rightarrow 1/2$
28599.7	
28604.1	$M_F = 0,1 \rightarrow 0,1$
37253.9	$F_1 = 5/2 \rightarrow 3/2$
37268.3	$M_{F_1} = 3/2 \rightarrow 1/2$
37263.2	$M_F = 1 \rightarrow 0,1$
66221.0	$F_1 = 1/2 \rightarrow 3/2$
66206.3	
66209.6	$M_{F_1} = 1/2 \rightarrow 1/2$
66216.8	
66213.5	$M_F = 0,1 \rightarrow 0,1$
66224.6	

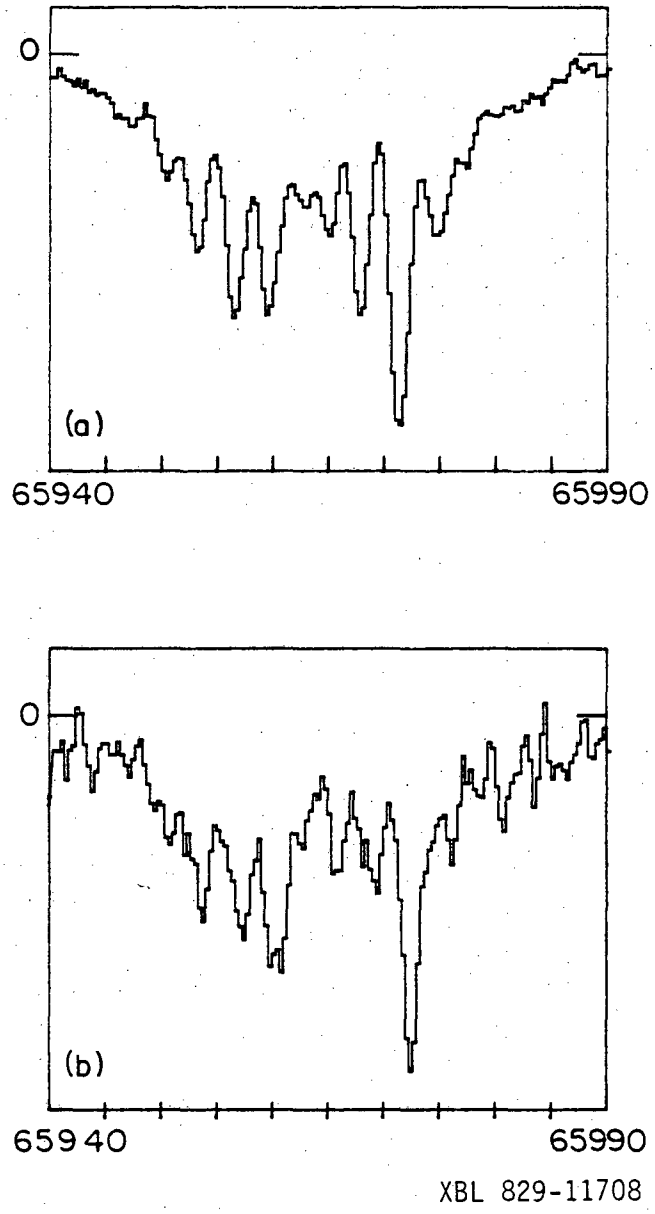

Figure 4.12. ClF resonance spectra J=1, $F_1 = 1/2 \leftrightarrow 3/2$ at V_{DC} = (a) 247.5 V; (b) 808.0 V (V_{RF} = 1.6 V, P_s = 1.2 atm, T_s = 23°C, V_A = 24 kV, V_B = 17 kV).

easily a calculable manner. Though the spectral pattern is more complex, in this example the change in V_{DC} maintains the peaks' relative spacing and amplitude. Figure 4.13, which demonstrates the spectrum change for $F_1 = 1/2 \rightarrow 5/2$ with V_{DC}, shows at first glance a significantly more complex series of change. This was probably at least partially due to the greater rf amplitude available at these frequency ranges. On closer inspection, however, one finds that though relative amplitudes are changing, with the appropriate choice of a reference frequency for each of the spectra in Figure 4.13, there is a good deal of consistency in the peaks' relative spacing. This is further indicated numerically in Table 4.10.

The effect of varying V_{RF} with V_{DC} fixed at 1043.4 V for the $F_1 = 1/2 \rightarrow 3/2$ transition, as illustrated in Figure 4.14, is not very dramatic. This may again be largely due to the limited range of rf power available to us near frequencies of 66 MHz. The effect of the $F_1 = 1/2 \rightarrow 5/2$ transition as V_{RF} is varied from 20 to 60 V (peak to peak) is quite spectacular, as indicated in Figure 4.15 (V_{DC} = 808 V). Relative peak positions do not change much, but amplitudes tend to change quite a bit. There also appear to be significant "flop in" peaks which are also V_{RF} dependent. It is also of interest to compare (a) and (b) of Figure 4.15 with (a) and (b) of Figure 4.14, noting the qualitative match of spectral patterns, though centered at different frequencies, between spectra taken at both different V_{DC} and V_{RF}. Figure 4.16 maps the ClF $F_1 = 1/2 \rightarrow 5/2$ transition strengths at ν = 28784.0, 28788.2 and 28792.4 kHz with V_{DC} fixed at 808 V as a function of V_{RF}. One notices both flop-out and flop-in at a single frequency depending upon V_{RF}.

Table 4.10

Relative Peak Locations for the J=1, $F_1 = 1/2 \leftrightarrow 5/2$ Transitions of ClF at Various Stark Voltages. (Units in kHz. Reference Frequencies are Indicated in Figure 4.13 by Tic Marks at the Top of the Plots.)

V_{DC}(V) /	247.5	465.3	808.0	1043.4
	-33.0	-	-36.3	-37.3
	-29.0	-	-29.2	-30.0
	-26.4	-26.0	-24.6	-24.0
	-21.7	-22.4	-18.6	-18.7
	-17.7	-18.0	-17.6	-
	-12.4	-12.4	-12.6	-12.4
	- 8.7	- 8.7	- 9.2	- 8.8
	- 5.0	- 5.4	- 4.6	- 3.8
	0.0	0.0	0.0	0.0
	-	5.3	3.7	2.8
	7.0	9.6	7.7	7.2
	14.6	15.0	11.7	11.0
	19.0	18.6	17.7	-
Reference Frequency	29064.7	28990.7	28788.0	28596.0

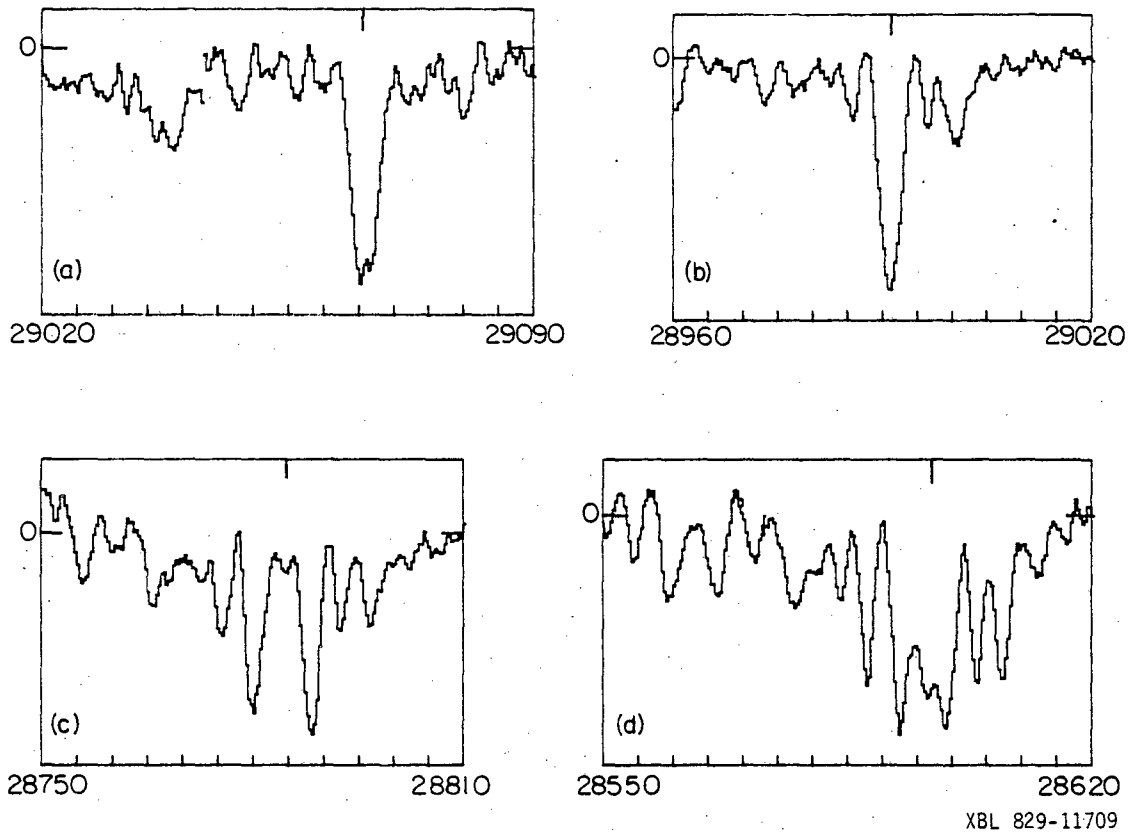

Figure 4.13. ClF resonance spectra J=1, $F_1 = 1/2 \leftrightarrow 5/2$ at V_{DC} = (a) 247.5; (b) 465.3; (c) 808.0; and (d) 1043.4 V. (V_{RF} = 60 V, P_s = 1.4 atm, T_s = 23°C). See also Table 4.10.

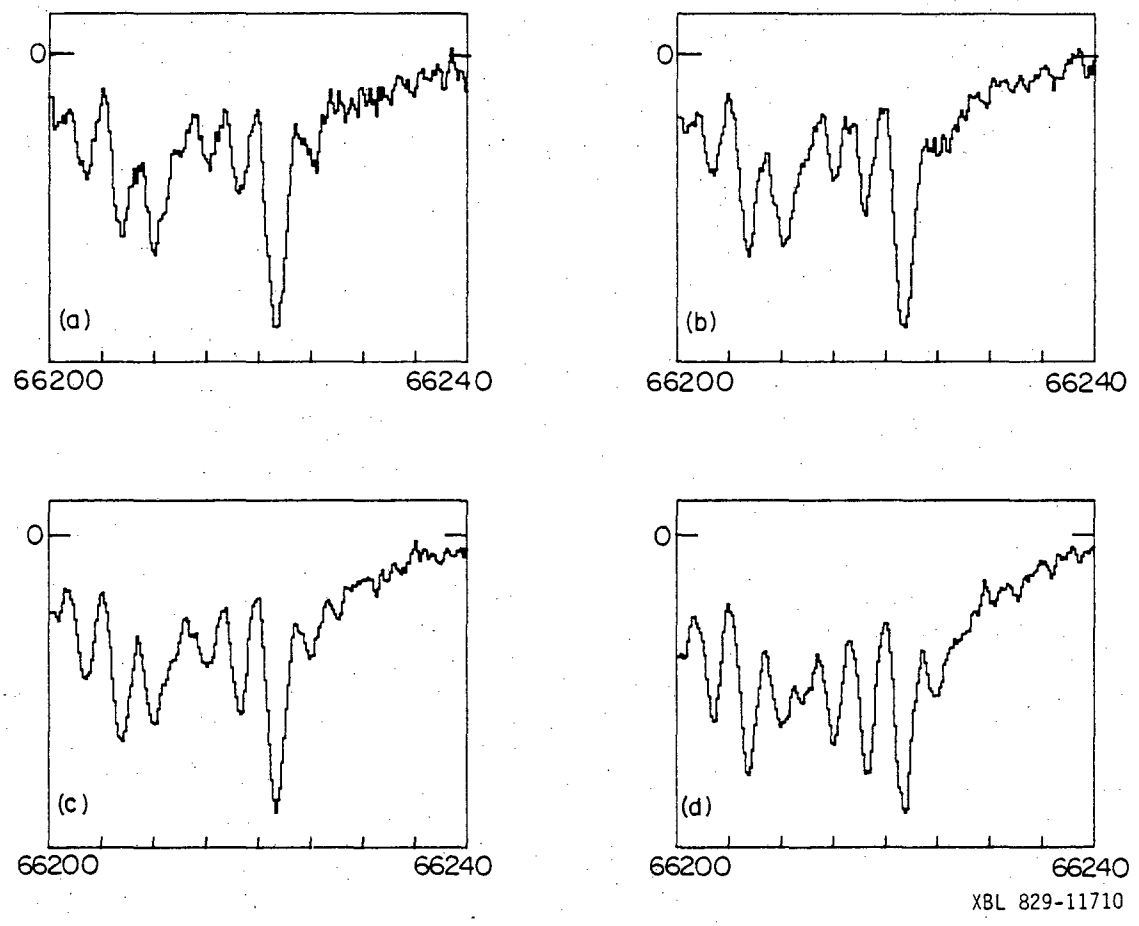

Figure 4.14. ClF resonance spectra J=1, $F_1 = 1/2 \leftrightarrow 3/2$ at V_{RF} = (a) 0.8; (b) 1.0; (c) 1.3; and (d) 1.6 V. (V_{DC} = 1043 V, P_s = 1 atm, T_s = 23°C).

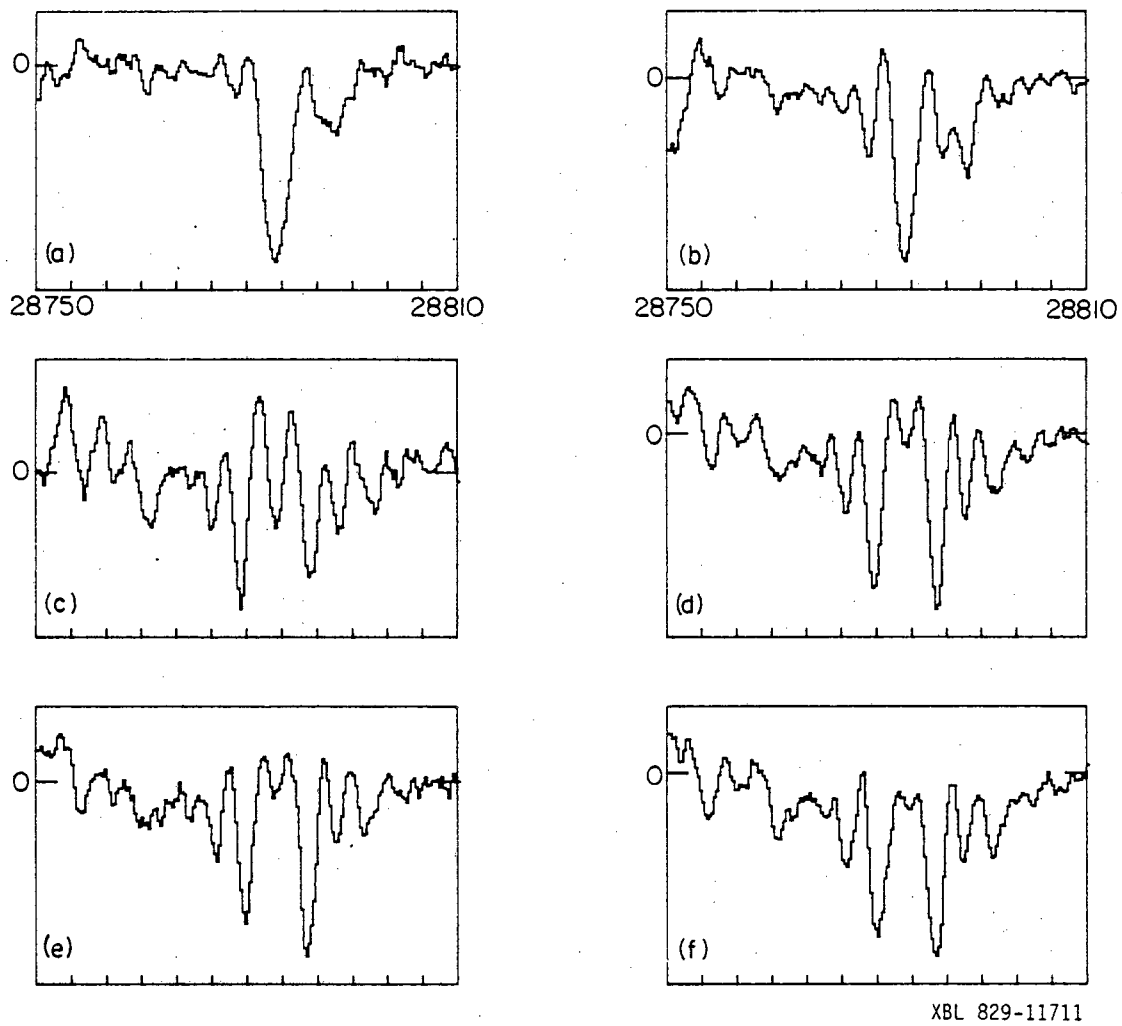

Figure 4.15. ClF resonance spectra J=1, $F_1 = 1/2 \leftrightarrow 5/2$ at V_{RF} = (a) 20; (b) 30; (c) 35; (d) 40; (e) 50; and (f) 60 V. (V_{DC} = 808 V, P_s = 1 atm, T_s = 23°C).

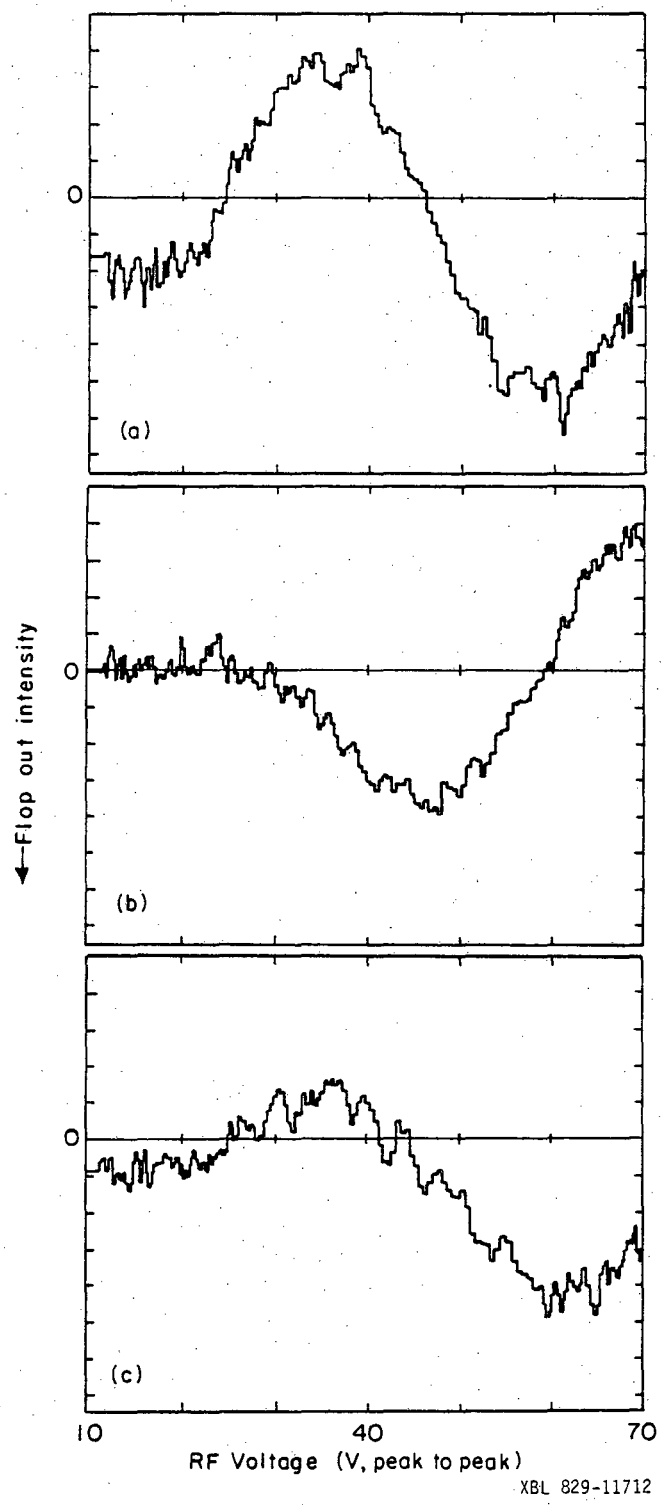

Figure 4.16. ClF transition strength (J=1, F_1 = 1/2 ↔ 5/2) as a function of RF voltage. ν = (a) 28784.0; (b) 28788.2; and (c) 28792.4 kHz. (V_{DC} = 808 V, P_s = 1 atm, T_s = 165°C).

3. Calculation Results

One of the motivations for our detailed work with OCS was to test for the fitting of Rabi's formula,

$$P_{12}(\omega) = \frac{(2\omega_1)^2}{(2\omega_1)^2+(\omega_0-\omega)^2} \sin^2\{\tfrac{t}{2}((2\omega_1)^2 + (\omega_0-\omega)^2)^{\frac{1}{2}}\}, \qquad (4.38)$$

with an experimental spectrum which had no ambiguity of line assignments from multiple closely lying levels. With such a fit and an empirical evaluation of ω_1, it was felt that one would thereby be able to calibrate the rf field strength actually present between the C field flats. From a given spectrum, five different ways occurred to us to evaluate ω_1. First, with the knowledge of the approximate rf and dc voltages in the C field and knowing the spectroscopic parameters of the transition, a theoretical calculation for ω_1 is possible. From Equations 4-38, 40, 49 and 50,

$$\omega_1^{(1)} = \sqrt{2}\ (\tfrac{1}{2}E_{RF})(E_{DC})(\frac{\mu^2}{4B\hbar})f^+(J,M). \qquad (4.54)$$

The leading radical factor arises from Equation A71 in Appendix I due to the degeneracy of the J = 1, M = ±1 states both of which couple to J = 1, M = 0. E_{RF}, the applied rf voltage, is halved, as in a sense only 50% of that radiation is polarized properly for transitions. (This is also elaborated upon in the Appendix.) $f^+(1,0)$ can be taken from Table 4.5. The second method simply notes that the envelope for the beating in Rabi's formula as a function of ω is a Lorentzian, which, from Equation (4.38), has a half width at half maximum of $2\omega_1$. A third approach involves the nodes in the spectral pattern. Assuming that the HWHM, ω_H, of the spectrum is at $2\omega_1$, if there are n nodes between ω_0 and ω_H, then, from Equation (4.38),

$$\frac{t}{2}((2\omega_1)^2 - \omega_H{}^2)^{\frac{1}{2}} - \frac{t}{2}(2\omega_1) \approx n\pi$$

or

$$\omega_1^{(3)} \approx \frac{n\pi}{(\sqrt{2}-1)t} . \tag{4.55}$$

In a given spectrum, n can be counted and t can be evaluated by a knowledge of the length of the resonance region and the mean velocity of the molecules, thereby allowing a reestimation of ω_1. The fourth way uses data like that shown in Figure 4.9. If the transition intensity is measured as a function of ω_1 with ω set at resonance, then from Equation (4.38),

$$I \propto \sin^2(t\omega_1). \tag{4.56}$$

From Equation (4.54), ω_1 is directly proportional to E_{RF}. If one assumes that the first node for $E_{RF} > 0$, E_{RF}^n , occurs when $\omega_1 t = \pi$, i.e., $\omega_1^n = \pi/t$, then measuring E_{RF}^n and calculating ω_1^n allows a determination of ω_1 for an arbitrary rf field:

$$\omega_1^4 = \frac{\omega_1^n}{E_{RF}^n} E_{RF}. \tag{4.57}$$

Finally, one can attempt a best least squares fit of Equation (4.38) to an actual spectrum. The calculation can be improved for velocity spread effects by using the focusing simulation methods of Chapter III to determine the population contribution to the transition signal from different velocity groups.

These methods were all attempted on a single OCS spectrum - that shown in Figure 4.8b. Given that the applied dc field was 1052 V/cm and

that the rf strength inputted to the C field was 5 V/cm, $\omega_1^{(1)}$ = 52.4×10^3 sec^{-1} or 8.34 kHz. (Note that ω_1 has natural units of radians/sec. Conversion to units of frequency involves division by 2π.) The measured HWHM for Figure 4.8(b) is 12 kHz, giving $\omega_1^{(2)} = 38 \times 10^3$ sec^{-1}. Using Equation (4.55), setting $t \approx 15$ cm $\div$ 5.5×10^4 cm/sec, and setting n to approximately 2.5 gives as an estimate $\omega_1^{(3)} = 70 \times 10^3$ sec^{-1}. From Figure 4.9, $\mathcal{E}_{RF}^n \approx 20$ V/cm, and, with $\omega_1^n = \pi/t = 11.5 \times 10^3$ sec^{-1}, then, for $\mathcal{E}_{RF} = 5$ V/cm, Equation 4.57 gives $\omega_1^{(4)} \approx 2.9 \times 10^3$ sec^{-1}. Given that the node spacing and Lorentzian shape methods predict such different values for ω_1, it is not surprising that the computer fit for the spectrum was quite poor. The least squares analysis allowed for the optimization of two parameters: ω_1 and an overall normalization factor. It found a value for ω_1 similar to that of the HWHM method. No further numerical analysis of the OCS transition line shapes has as of yet been attempted.

The energies and eigenstates for $Cl^{35}F$ as a function of electric field strength have been calculated from previously reported spectroscopic constants[8] and were presented in Figure 4.3 and Tables 4.4, 6 and 7 for J = 1. Though in principle there are 24 different J = 1 states, each state with $M_F > 0$ has a corresponding degenerate state with $M_F' = -M_F$. Furthermore, the splitting between states due to the spin of the fluorine nucleus is not resolvable in Figure 4.3, thus leaving only six apparently different curves. The M_F labeling in Figure 4.3 and Table 4.4 is an easily obtained result from the calculation as the Hamiltonian matrix is block diagonalized in M_F. F_1 is the primary label at very weak fields due to the strength of the Cl^{35} quadrupole coupling. At the moderate field strengths, at which our spectroscopy is performed, M_{F_1} becomes a

meaningful label. Their assignments to the lines of Figure 4.3 are made to be consistent with the lines' respective M_F values. At the high field limit, eight states are seen to be Stark focusable (i.e., their energies increase with field strength) corresponding to a strong field basis set label of $M_J = 0$, while the remaining sixteen states show $M_J = \pm 1$ character. The identities for our observed ClF transitions were indicated in Table 4.9. As a result of the poor fitting of Rabi's formula to OCS spectra, the uncertainty as to which peaks correspond to the central resonance frequencies in our ClF spectra, and the lack of clear identification of the specific transitions we are observing (compare Tables 4.9 and 4.7), no direct attempt has been made to fit our ClF spectra with a computer simulation which would have included the Rabi oscillations. Table 4.7 predicts values for ω_1 on the order 30-60 kHz for the $F_1 = 1/2 \rightarrow 5/2$ transitions (where V_{RF} was as large as 60 V) and up to 1 kHz for the $1/2 \rightarrow 3/2$ transitions (where V_{RF} was limited to 1.5 V). The only other item of a quantitative nature to note is that in the data depicted previously, the spectra of Figures 4.13(a) and (b) correspond to $V_{RF}V_{DC}$ products of approximately 15000 and 28000 V^2, respectively, while those for Figures 4.15(a) and (b) have $V_{RF}V_{DC}$ values of 16000 and 24000 V^2. That these pairs of spectra have similar qualitative features corresponds correctly to the notion that the line shapes are determined by the Rabi parameter ω_1 which is in turn directly proportional to E_{RF} and E_{DC}.

C. Discussion

This section must obviously focus on the mismatch between our experimental and predicted results. Among those aspects of our OCS spectra that we do not understand is the spectrum distortion we observed, particularly

at large values of V_{RF} and V_{DC}. As indicated in the previous section, we could not find a single value for ω_1 in an apparently undistorted spectrum, indicating that Rabi's formula is not consistent with our observations. The regularity of the nodal spacing as a function of τ, as indicated in Section B1, is also not consistent with Rabi's formula unless ω_1 is quite small compared to $1/\tau$, which is probably not the case here. We expected that our evaluation of $\omega_1^{(1)}$ would overestimate the true value of ω_1 as we could not predict the rf power loss in the resonance field region. However, the mismatch of $\omega_1^{(2)}$ and $\omega_1^{(3)}$ is not rationalizable within the context of the theoretical model posed here. As for the ClF spectra, we do not understand why we have not found lines corresponding to the $F_1 = 5/2 \rightarrow 3/2$, $M_{F_1} = 3/2 \rightarrow 3/2$ or $F_1 = 1/2 \rightarrow 3/2$, $M_{F_1} = 1/2 \rightarrow 3/2$ transitions. Both of these, particularly the former, are predicted to be observable by our calculations. (Refer to Table 4.7.) The values of ω_1 we have calculated do not appear obviously consistent with the spectral features. Finally, the appearance of both flop-in and flop-out features in a single ClF spectrum is not consistent with our analysis. As indicated in our model in Chapter III, whether the transition signal appears as an increase or decrease over the background (no transition) signal depends solely on the A and B field focusing conditions for OCS. All of the possible transitions observed in a single ClF spectrum of, say, from Figure 4.15 or 16 occur from one of the focusing $F_1 = 1/2$, $M_{F_1} = 1/2$ states, which, noted in Figure 4.3, all should experience similar electrostatic forces, to one of the defocusing $F_1 = 5/2$, $M_{F_1} = 1/2$ states, which also behave in a field nearly identically. Thus, as with OCS, this spectral region should evince either flop-in or flop-out character, but not both.

As support for the resonance theory here it should be indicated that Rabi's formula has been fit well to MBER spectra of the nuclear-spinless HCN system[9] as well as to the LiBr systems.[10] We are not really in a position now to evaluate critically our theoretical treatment beyond what has been stated in the Appendix. Here are mentioned a few possible experimental artifacts. As indicated in Appendix I, there are several possible sources for line shifting from the true ω_0 value predicted for a transition. Our calibration of the C field spacing presented in Section B1 did not include these, so that our predicted spacing of the flats may not be accurate. However, this uncertainty alone does not account for the difficulties of the preceding paragraph. The dc homogeneity of our field was verified by reparalleling the plates between a set of spectra, with no apparent change observed in our results. There is a good deal of uncertainty on the nature of the rf field, however. We were surprized to find that the perpendicular ($\Delta M = \pm 1$) OCS transition maintained 30% of its signal strength when performed in our parallel-only radiation node, indicating the presence of many stray rf field lines in our C field region. In our parallel-perpendicular mode we do not know the relative field strength of the different rf components as of yet. The amount of rf power absorbed by the C field circuitry as a function of rf frequency is also unknown to us. Finally, the only explanation we currently have for the flop-in flop-out problem of the previous paragraph is to assume the existence of a large amount of rf field strength inhomogeneity between the C field flats, which would result with different molecule velocity groups possibly experiencing very different transition probabilities.

The complexity of our ClF spectra indicates that spectral fitting procedures which do not include Rabi beating features are probably not adequate in determining very detailed spectral constants. Given that Rabi splitting features can appear easily up to 20 kHz away from the central resonance frequency, and that ω_0 itself may not appear as a local spectral maximum creates doubt as to the validity of the values of C_{Cl}, C_F, S, and S' in Table 4.1. Short of doing a full spectrum simulation, our work shown in Figure 4.16 suggests an alternate approach. If one assumes a certain spectral feature corresponds to a central resonance frequency, ω_0, one can then plot the intensity of that feature as a function of E_{RF}. The nodal spacing observed, as indicated by Equation (4.38) and (4.49), will depend on τ, which is fixed for a given spectrum, and $\alpha_1 \equiv 2\omega_1/E_{RF}$, which, for a given E_{DC}, is characteristic of a particular transition. A nearby spectral feature at a frequency δ away from ω_0 can be similarly treated experimentally. If this feature is due to the same transition, then this E_{RF} spectrum should fit to

$$I(E_{RF}) \propto L(E_{RF}) \sin^2\{\tfrac{\tau}{2}(\delta^2 + \alpha_1^2 E_{RF}^2)^{\frac{1}{2}}\}. \tag{4.58}$$

$L(E_{RF})$ is the Lorentzian factor and does not introduce nodes to $I(E_{RF})$. Thus, if such a fitting produces the same α_1, it is due to a transition between the same states as ω_0.

In conclusion, MBER spectra of OCS and ClF taken on our apparatus under various C field conditions have been presented here. A detailed theory has also been presented to predict the MBER line shapes. Though several qualitative features are common to the theory and experiments, there are several major discrepancies that we have not been able to

explain. Much future work of both a theoretical and experimental nature is suggested here. The quantum analysis offered in Appendix I for the transition process in NMR kinds of experiments may not be as simply applicable to MBER transitions as we have suggested. The uncertainties extant with our C field can only be reduced with a broader data base and direct comparisons with other apparatuses. Finally, significantly more work should be done in the fitting of complex experimental MBER spectra in conjunction with Rabi's formula. Though the overall problem is quite complicated, enough of the underlying theory is understood now to make such a study almost tractable.

REFERENCES to CHAPTER IV

1. C. Cohen-Tannoudji, B. Diu, and F. Laloë, Quantum Mechanics (John Wiley & Sons and Hermann, Paris, 1977).

2. C. H. Townes and A. L. Schawlow, Microwave Spectroscopy (McGraw-Hill, New York, 1955).

3. A. R. Edmonds, Angular Momentum in Quantum Mechanics (Princeton University Press, Princeton, 1957).

4. M. E. Rose, Elementary Theory of Angular Momentum (John Wiley & Sons, New York, 1957).

5. B. L. Silver, Irreducible Tensor Methods: An Introduction for Chemists (Academic Press, New York, 1976).

6. V. Hughes and L. Grabner, Phys. Rev. 79, 829 (1950).

7. N. F. Ramsey, Molecular Beams (Oxford University Press, London, 1956).

8. R. E. Davis and J. S. Muenter, J. Chem. Phys. 57, 2836 (1972).

9. T. R. Dyke, G. R. Tomasevich, and W. Klemperer, J. Chem. Phys. 57, 2277 (1972).

10. R. C. Hilborn, T. F. Gallagher, Jr., and N. F. Ramsey, J. Chem. Phys. 56, 855 (1972).

APPENDIX I

RABI'S FORMULA: TRANSITIONS IN A TWO-LEVEL SYSTEM

Both classical and quantum mechanical derivations of Rabi's formula for transition probability as a function of excitation frequency and duration (Eq. 4.38) have been presented in several sources.[1-6] As the manifestations of this expression, i.e., Rabi beating, are so blatant in MBER spectroscopy, a somewhat detailed derivation will be presented here with the particular purpose of aiding the reader's intuition concerning the resonance transition process. The classical phenomenon will be discussed in terms of magnetic dipoles interacting with static and oscillatory magnetic fields, as the Rabi effect can be described somewhat more easily in this context than in that of the Stark interaction. The classical parallels to the Stark effect will be drawn later. A quantum mechanical derivation for the transition probabilities in a general two level system will then be presented, and this, in turn, will be connected to the Stark transitions in MBER.

1. Classical View of Magnetic Resonance and Rabi's Formula

The Dipole System and Interaction with a Field. We will be considering a system of identical particles each spinning with the same angular momentum magnitude. Though no net charge is present, each particle does consist of a distribution of charges, so that a magnetic dipole moment of magnitude "μ" is generated for each particle in a direction parallel to that particle's spin:

$$\underset{\sim}{\mu}^i = \gamma\hbar\underset{\sim}{S}^i, \tag{A.1}$$

where γ is the particle's gyromagnetic constant. In this system the dipoles, as the particles will be referred to henceforth, are sufficiently separated that mutual interactions can be neglected. In the absence of an external field, space is isotropic, and all orientations of a dipole have the same potential energy, which we shall arbitrarily set to zero. Thus, in this ensemble of dipoles each will be pointing in a random direction. This gives a zero net "magnetization" M for the system, where

$$\underset{\sim}{M} \equiv \sum_i \underset{\sim}{\mu}^i. \tag{A.2}$$

The energy, E^i, of a magnetic dipole in the presence of any external magnetic field $\underset{\sim}{H}$ is

$$E^i = -\underset{\sim}{\mu}^i \cdot \underset{\sim}{H}. \tag{A.3}$$

As different orientations of the ith dipole now correspond to different energies, there will be a torque $\underset{\sim}{\tau}^i$ such that

$$\underset{\sim}{\tau}^i = \hbar \frac{d}{dt} \underset{\sim}{S}^i = \underset{\sim}{\mu}^i \times \underset{\sim}{H} \tag{A.4}$$

Equations (A.3) and (A.4) supply all the dynamic information concerning the interaction by any type of magnetic field on our system of dipoles. For instance, the equation of motion of the dipole $\underset{\sim}{\mu}^i$ is obtainable from (A.4) and (A.1) via

$$\frac{d}{dt} \underset{\sim}{\mu}^i = \underset{\sim}{\mu}^i \times \gamma \underset{\sim}{H}, \tag{A.5}$$

and for the entire magnetization of the system,

$$\frac{d}{dt} \underset{\sim}{M} = \underset{\sim}{M} \times \gamma \underset{\sim}{H}. \tag{A.6}$$

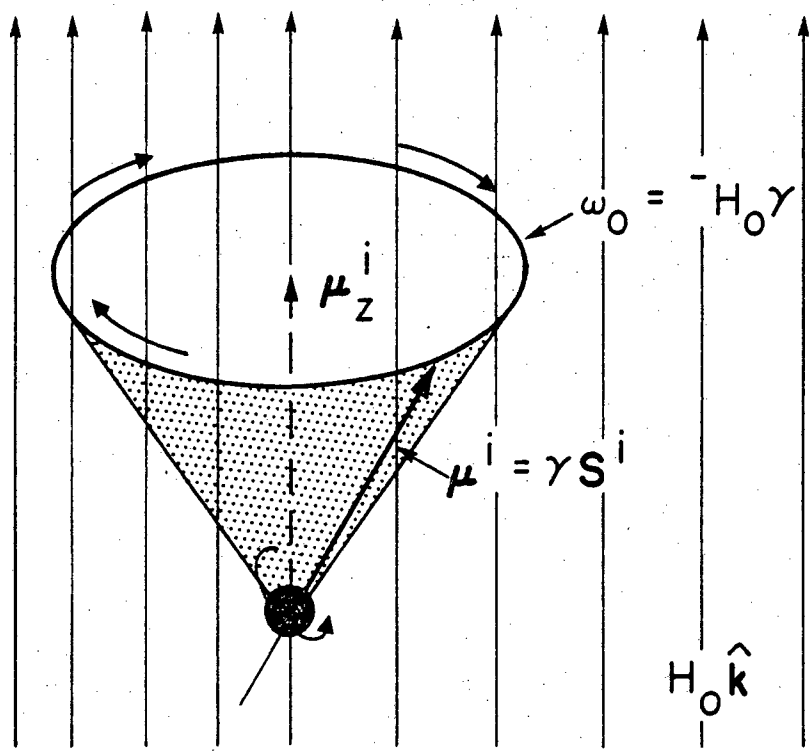

XBL 829-11407

Figure A.1. Precession of a magnetic dipole ($\underset{\sim}{\mu}$) in a magnetic field $\underset{\sim}{H}$ ($=H_0\underset{\sim}{\hat{k}}$).

Let $\underset{\sim}{H}$ be the static field $H_0\hat{\underset{\sim}{k}}$. Then, by (A.3) and (A.4),

$$E^i = -\mu_z^i H_0 = -\hbar\gamma S_z^i H_0 = -\hbar\omega_0 S_z^i, \tag{A.7}$$

where S_z^i is the projection of $\underset{\sim}{S}^i$ in the $\hat{k}$ direction, and ω_0, the "Larmor frequency", is defined by

$$\omega_0 \equiv \gamma H_0. \tag{A.8}$$

Rewriting (A.5),

$$\frac{d}{dt}\underset{\sim}{\mu}_i = -\omega_0\hat{k} \times \underset{\sim}{\mu}_i. \tag{A.9}$$

$\underset{\sim}{\mu}^i$, as a function of time, maintains its magnitude μ (as $\underset{\sim}{\mu}_i$ is perpendicular to $\frac{d}{dt}\underset{\sim}{\mu}_i$, then $\underset{\sim}{\mu}_i \cdot \frac{d}{dt}\underset{\sim}{\mu}_i = \frac{1}{2}\frac{d}{dt}|\underset{\sim}{\mu}_i|^2 = 0$) and precesses about $\hat{k}$ with a constant angle at a frequency $-\omega_0$ (see Fig. A.1). A similar description is true for the motion of the magnetization vector $\underset{\sim}{M}$. As mentioned before, a random system of dipoles has no net magnetization. Thus, from the above, introducing a magnetic field alone cannot induce a nonzero value for $\underset{\sim}{M}$. We will assume that some method exists to have an initial value for $\underset{\sim}{M}$, e.g., in the random system of dipoles described before there exists a way to remove some dipoles pointing downward leaving a net upward nonzero magnetization. Then, when $\underset{\sim}{H}$ is turned on, the magnitude of this magnetization will be preserved. (In actual NMR, an initial magnetization is obtained by the interaction of the individual dipoles with the surrounding temperature bath, once different orientations of the dipoles correspond to different energies.)

<u>Rotating Frame and Adiabatic Processes</u>. Unraveling the motion of a dipole of the system's magnetization in more complicated magnetic fields

is greatly aided by the use of a rotating coordinate system or frame. Say that the axes of a coordinate system x',y',z' with direction vectors $\hat{\underset{\sim}{i}}'$, $\hat{\underset{\sim}{j}}'$, and $\hat{\underset{\sim}{k}}'$, are rotating at a frequency $\underset{\sim}{\Omega}$ relative to the fixed world. Then,

$$\frac{d}{dt}\hat{\underset{\sim}{i}}' = \underset{\sim}{\Omega} \times \hat{\underset{\sim}{i}}', \frac{d}{dt}\hat{\underset{\sim}{j}}' = \underset{\sim}{\Omega} \times \hat{\underset{\sim}{j}}', \text{ etc.} \tag{A.10}$$

Let $\underset{\sim}{F}(t)$ be an arbitrary vector function of time defined in the x',y',z' coordinate system. Then the time derivative of $\underset{\sim}{F}(t)$ as seen in the fixed world, $d\underset{\sim}{F}(t)/dt$, will have contributions from both the change in $\underset{\sim}{F}(t)$ within the rotating system,

$$\frac{\delta \underset{\sim}{F}(t)}{\delta t} = \hat{\underset{\sim}{i}}' \frac{dF_{x'}}{dt} + \hat{\underset{\sim}{j}}' \frac{dF_{y'}}{dt} + \hat{\underset{\sim}{k}}' \frac{dF_{z'}}{dt} \tag{A.11}$$

and from the rotation of $\underset{\sim}{F}(t)$ relative to inertial coordinates:

$$\frac{d\underset{\sim}{F}}{dt} = \frac{\delta \underset{\sim}{F}}{\delta t} + \underset{\sim}{\Omega} \times \underset{\sim}{F}. \tag{A.12}$$

As a specific example, consider measuring a dipole moment $\underset{\sim}{\mu}^i$ in the static magnetic field $H_0\hat{\underset{\sim}{k}}$, within a frame rotating at $\underset{\sim}{\Omega}$ relative to the inertial frame. The derivative in Equation (A.9) is for an inertial frame, so, combining (A.9) and (A.12), we obtain

$$\frac{d\underset{\sim}{\mu}^i}{dt} = -\omega_0\hat{\underset{\sim}{k}} \times \underset{\sim}{\mu}^i = \frac{\delta \underset{\sim}{\mu}^i}{\delta t} + \underset{\sim}{\Omega} \times \underset{\sim}{\mu}^i,$$

or, with rearrangement,

$$\frac{\delta \underset{\sim}{\mu}^i}{\delta t} = (-\underset{\sim}{\Omega}-\omega_0\hat{\underset{\sim}{k}}) \times \underset{\sim}{\mu}^i. \tag{A.13}$$

If $\underset{\sim}{\Omega} = 0$, our frame x',y',z' is really stationary, and one observes $\underset{\sim}{\mu}^i$

Figure A.2. Dipole in a magnetic field.

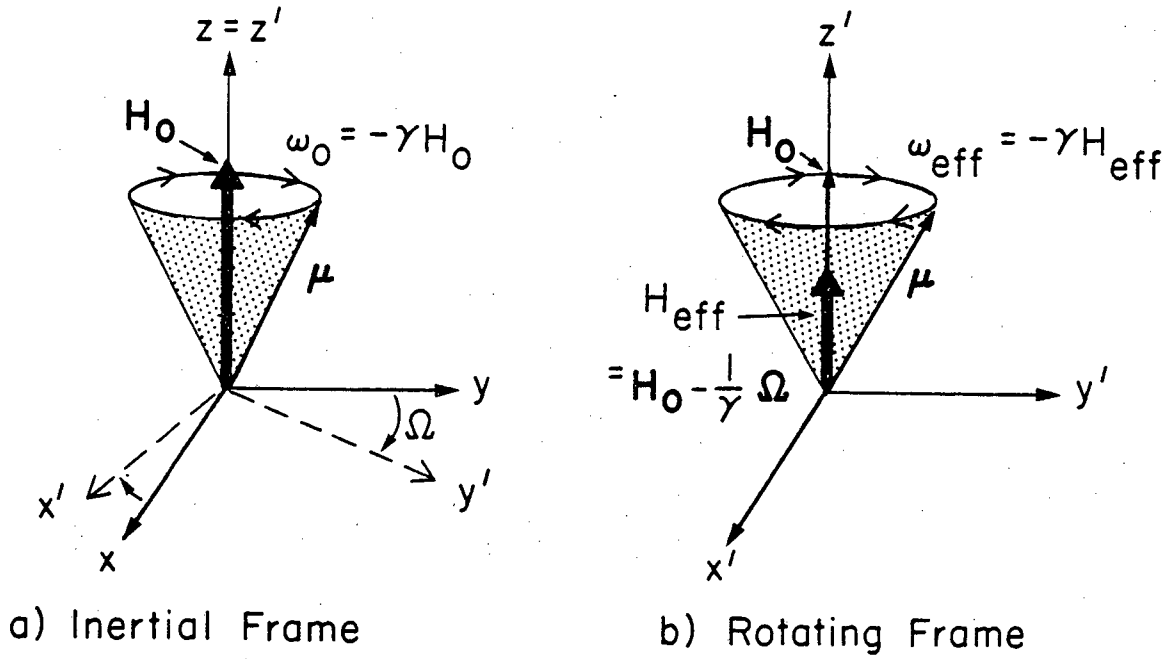

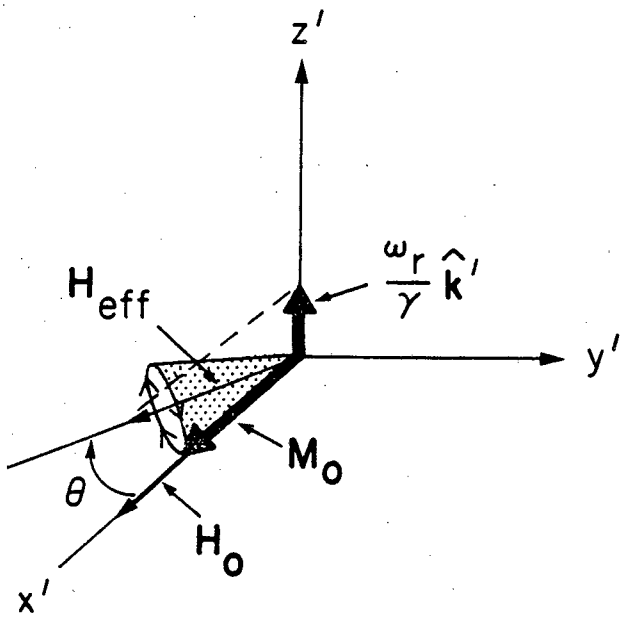

XBL 829-11404

Figure A.3. Dipole in a slowly rotating magnetic field. (Rotating frame reference with the fixed axis along the rotation axis z' and the field along x'.)

precessing at frequency $-\omega_0$. Now begin rotating the coordinate system from which we are viewing. We will confine $\underset{\sim}{\Omega}$ to be parallel to $\hat{\underset{\sim}{k}}$, i.e., $\underset{\sim}{\Omega} = \Omega\hat{\underset{\sim}{k}}$, so that

$$\frac{\delta \underset{\sim}{\mu}^i}{\delta t} = =(\Omega + \omega_0)\hat{\underset{\sim}{k}} \times \underset{\sim}{\mu}^i. \tag{A.14}$$

From our frame one would then observe $\underset{\sim}{\mu}^i$ precessing at a frequency $-(\omega_0 + \Omega)$, different from that in the inertial frame. In fact, one would believe that $\underset{\sim}{\mu}^i$ was precessing at a different frequency because it was experiencing an effective magnetic field

$$\underset{\sim}{H}_{eff} = (\frac{\omega_0}{\gamma} + \frac{\Omega}{\gamma})\ \hat{\underset{\sim}{k}} = (H_0 + \frac{\Omega}{\gamma})\hat{\underset{\sim}{k}} \tag{A.15}$$

rather than $H_0\hat{\underset{\sim}{k}}$ alone. If we had conveniently chosen $\underset{\sim}{\Omega} = -\underset{\sim}{\omega}_0$, then $\underset{\sim}{H}_{eff}$ would be zero, and, from (A.13) $\delta\underset{\sim}{\mu}^i/\delta t$ would also be zero. That is, if one were rotating with the dipole at its frequency, it would <u>appear</u> stationary.

As another use of the rotating frame method, consider a field $\underset{\sim}{H}_0$ that is almost static, except that it is "slowly" changing its direction. We are interested in its effect on a net magnetization $\underset{\sim}{M}$. "Slowly" means that if $\underset{\sim}{H}_0$ is rotating at an angular frequency $\underset{\sim}{\omega}_r$, then $\omega_r << \omega_0$, i.e., that $\underset{\sim}{H}_0$ is changing direction at an angular velocity much less than the Larmor angular velocity of the magnetization vector. Let $\underset{\sim}{H}_0$ start along the x axis in the inertial system and continue to rotate about $\hat{\underset{\sim}{k}}$. We now choose a coordinate system rotating about $\hat{k}$ at frequency ω_r, so that $\underset{\sim}{H}_0$ appears fixed in the x' direction. (Refer to Fig. A.3.) By Equation (A.13),

$$\frac{\delta \underset{\sim}{M}}{\delta t} = -(\omega_r\hat{\underset{\sim}{k}}' + \omega_0\hat{\underset{\sim}{i}}') \times \underset{\sim}{M}. \tag{A.16}$$

Instead of precessing about $H_0\hat{\underset{\sim}{i}}'$, $\underset{\sim}{M}$ precesses about the effective magnetic field

$$\underset{\sim}{H}_{eff} = H_0\hat{\underset{\sim}{i}}' + \frac{\omega_r}{\gamma}\hat{\underset{\sim}{k}} \tag{A.17}$$

which is at an angle $\theta = \tan^{-1} \omega_r/\gamma H_0$ to $\underset{\sim}{H}_0$. If $\omega_r << \gamma H_0$, though, θ will be very small, so that $\underset{\sim}{M}$ will remain at nearly a constant angle with respect to $H_0\hat{\underset{\sim}{i}}'$. In the inertial frame this means that the projection of $\underset{\sim}{M}$ onto $\underset{\sim}{H}_0$ will remain essentially constant as $\underset{\sim}{H}_0$ changes direction. If $\underset{\sim}{M}$ were initially parallel to $\underset{\sim}{H}_0$, it essentially remains so. A process such as this, where $\underset{\sim}{H}_0$ changes slowly enough so that $\underset{\sim}{M}$ can follow it is known as an "adiabatic" change.

<u>Addition of an Alternating Field</u>. Typically, in an experiment, when one adds an alternating magnetic (or, in the case of MBER, electric) field to a system, it is in the linearly polarized form

$$\underset{\sim}{H}_1(t) = \hat{i}H_x \cos(\omega t). \tag{A.18}$$

For reasons that will become apparent, it is convenient to mathematically decompose this to right and left circularly polarized waves

$$\begin{aligned}\underset{\sim}{H}_x(t) &= \underset{\sim}{H}_R(t) + \underset{\sim}{H}_L(t) = \\ &= \frac{H_x}{2}(\hat{i}\cos\omega t + \hat{j}\sin\omega t) + \frac{H_x}{2}(\hat{i}\cos\omega t - \hat{j}\sin\omega t),\end{aligned} \tag{A.19}$$

corresponding to magnetic fields rotating about the $\hat{k}$ direction at frequencies ω and $-\omega$, respectively. If, in an experiment, one has a static magnetic field $\underset{\sim}{H}_0$ along $\hat{\underset{\sim}{k}}$ so that dipoles are precessing at a frequency $-\omega_0 = -\gamma H_0$ about $\hat{\underset{\sim}{k}}$, intuition may suggest that a magnetic field

rotating at a frequency near $-\omega_0$ will have a greater effect on these dipoles than one rotating near $+\omega_0$. For this reason, we will temporarily ignore the $\underset{\sim}{H}_R(t)$ part of (A.19), and take as our full magnetic field

$$\underset{\sim}{H}(t) = \underset{\sim}{H}_0 + \underset{\sim}{H}_1(t) = H_0\hat{\underset{\sim}{k}} + H_1(\hat{i}\cos\omega t - \hat{j}\sin\omega t), \tag{A.20}$$

where typically $H_1 << H_0$. From (A.5) we then have the equation of motion of an individual dipole:

$$\frac{d\underset{\sim}{\mu}}{dt} = \underset{\sim}{\mu} \times \gamma[\underset{\sim}{H}_0 + \underset{\sim}{H}_1(t)]$$

$$= -(\hat{\underset{\sim}{k}}\omega_0 + \hat{\underset{\sim}{i}}\omega_1 \cos\omega t - \hat{\underset{\sim}{j}}\omega_1 \sin\omega t) \times \underset{\sim}{\mu} \tag{A.21}$$

where

$$\omega_1 \equiv \gamma H_1. \tag{A.22}$$

Now we will pick a rotating frame, with a stationary axis, z', coincident with the direction of $\underset{\sim}{H}_0(\hat{k})$ and with an x' axis that follows $\underset{\sim}{H}_1(t)$. As already discussed, $\underset{\sim}{H}_1(t)$ rotates at a frequency $-\omega$ about $\hat{\underset{\sim}{k}}$. Thus, in the context of (A.13), $\underset{\sim}{\Omega} = -\omega\hat{\underset{\sim}{k}}$, and

$$\frac{\delta\underset{\sim}{\mu}}{\delta t} = -[(\omega_0 - \omega)\hat{\underset{\sim}{k}}' + \omega_1\hat{\underset{\sim}{i}}'] \times \underset{\sim}{\mu} \tag{A.23}$$

$$= \underset{\sim}{\mu} \times \gamma\underset{\sim}{H}_{eff} \tag{A.24}$$

where

$$\underset{\sim}{H}_{eff} = (H_0 - \frac{\omega}{\gamma})\hat{\underset{\sim}{k}}' + H_1\underset{\sim}{i}'. \tag{A.25}$$

Picture our $\underset{\sim}{\mu}$ precessing about $\underset{\sim}{H}_0$ in a frame rotating at $-\omega\underset{\sim}{k}$ before the alternating field $\underset{\sim}{H}_1(t)$ is turned on. From this point of view it

appears that $\underset{\sim}{\mu}$ sees an effective field of $(H_0 - \frac{\omega}{\gamma})\hat{\underset{\sim}{k}}$, as it precesses at $-(\omega_0 - \omega)$ about $\hat{\underset{\sim}{k}}$. If we then suddenly turn on the alternating field $\underset{\sim}{H}_1(t)$ in the inertial world, $\underset{\sim}{\mu}$ will instantaneously see $\underset{\sim}{H}_{eff}$ (A.25). This is what $\underset{\sim}{\mu}$ will now precess about <u>in the rotating frame</u>, at a frequency

$$\omega_{eff} = \gamma|\underset{\sim}{H}_{eff}| = \sqrt{(\omega_0 - \omega)^2 + \omega_1^2}. \tag{A.26}$$

Referring to Figure A.4a, which shows a rotating frame where $\omega < \omega_0$, assume $\underset{\sim}{\mu}$ started in its lowest energy direction oriented along the z' axis when $\underset{\sim}{H}_1(t)$ was turned on. $\underset{\sim}{\mu}$ then precesses along a cone about $\underset{\sim}{H}_{eff}$. As long as $\underset{\sim}{H}_1(t)$ is on, energy is being periodically absorbed and returned by $\underset{\sim}{\mu}$ as its orientation with respect to $\underset{\sim}{H}_0$ changes. If $\underset{\sim}{H}_1(t)$ is left on only for a time τ, $\underset{\sim}{\mu}$ will have precessed about the cone an angle of $\phi = \omega_{eff}\,\tau$, with a net change in energy with regard to the static field $\underset{\sim}{H}_0$ alone (unless $\omega_{eff}\tau = 2n\pi$). With $\underset{\sim}{H}_1(t)$ turned off, $\underset{\sim}{\mu}$ will be left at an angle α to $\underset{\sim}{H}_0$ (Fig. A.4b), and will then precess about $\underset{\sim}{H}_0$ maintaining this angle. In Figure A.5, $\omega = \omega_0$. If $\underset{\sim}{\mu}$ starts along the z' axis, it remains motionless until $\underset{\sim}{H}_1(t)$ is turned on. Now $\underset{\sim}{H}_{eff} = H_1\,\hat{\underset{\sim}{i}}'$, and $\underset{\sim}{\mu}$ will precess about the x' axis, normal to the direction of $\underset{\sim}{H}_0$. If $\underset{\sim}{H}_1(t)$ is now turned off at time τ, such that $\phi = \gamma H_1\tau = \pi$ (a so-called π or 180° pulse), $\underset{\sim}{\mu}$ would be left fully inverted from its initial direction. Given a $\pi/2$ pulse instead, $\underset{\sim}{\mu}$ would be left perpendicular to the z' axis, along y'.

In an inertial frame, the motion of $\underset{\sim}{\mu}$ due to $\underset{\sim}{H}(t)$ will be the precession of the preceding paragraph plus the motion of our rotating frame. In the static field $\underset{\sim}{H}_0$, $\underset{\sim}{\mu}$ defined a cone of precession about the z axis, with the angle α between $\underset{\sim}{\mu}$ and $\hat{\underset{\sim}{k}}$ fixed. Now one suddenly turns on an

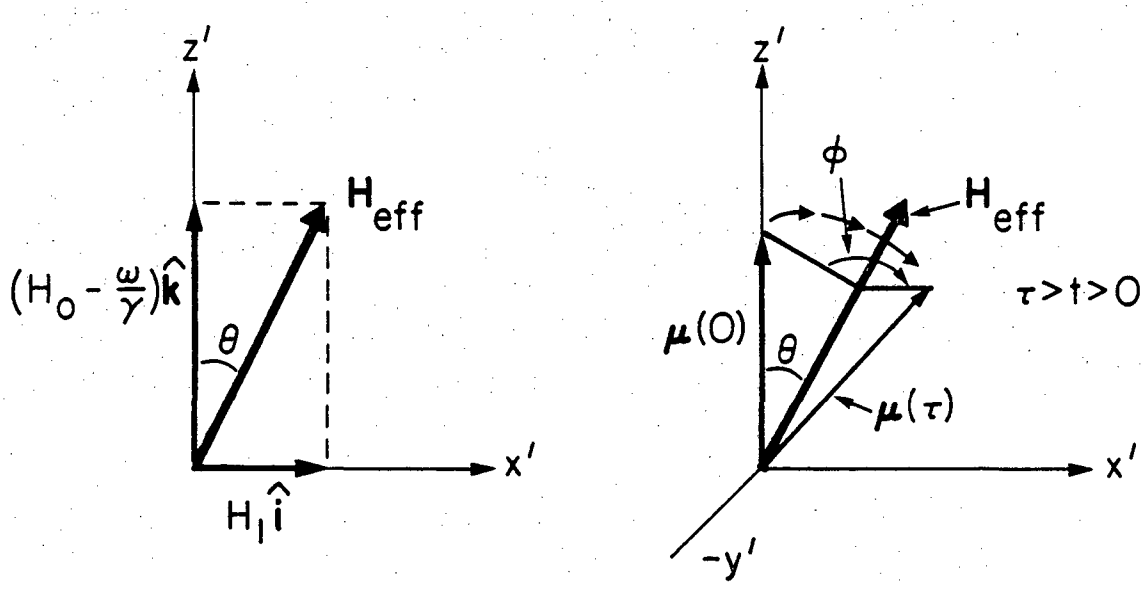

a) Dipole precession in the presence of the alternating field $\mathbf{H}_1$ for time τ.

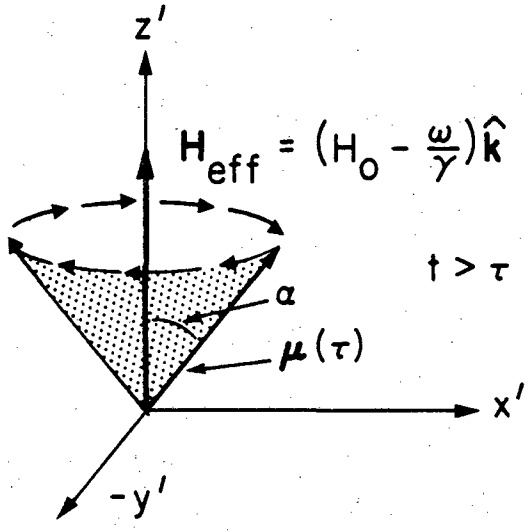

b) Precession after alternating field pulse.

XBL 829-11418

Figure A.4. Precession of a dipole during and after an alternating field pulse ($\underset{\sim}{H}_1(\omega t)$) in the presence of a static field ($H_0\hat{k}$) viewed from a frame rotating at the alternating field frequency (ω).

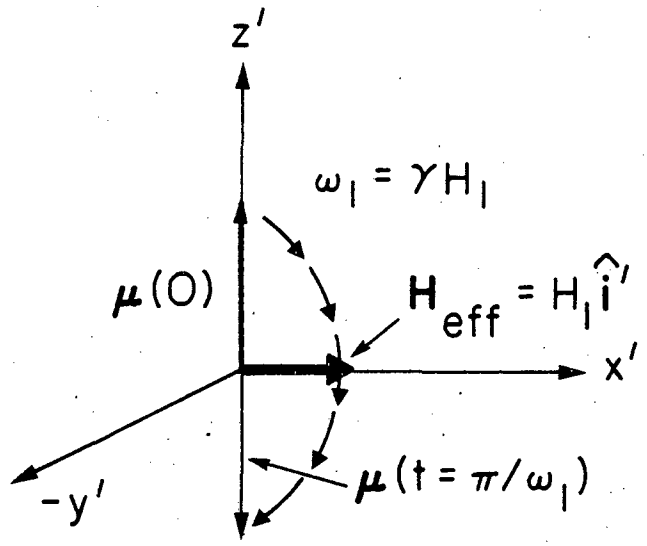

a) π pulse

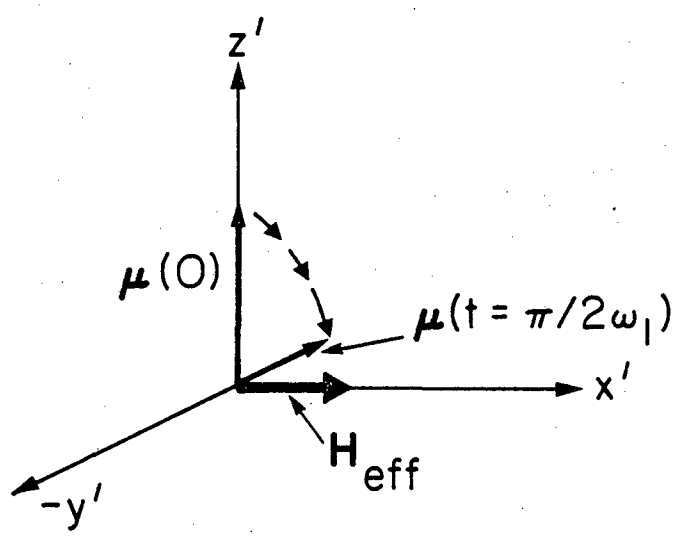

b) $\pi/2$ pulse

XBL 829-11417

Figure A.5. Dipole precession during a resonant ($\omega = \omega_0$) alternating field pulse. Viewed from a frame rotating at ω_0.

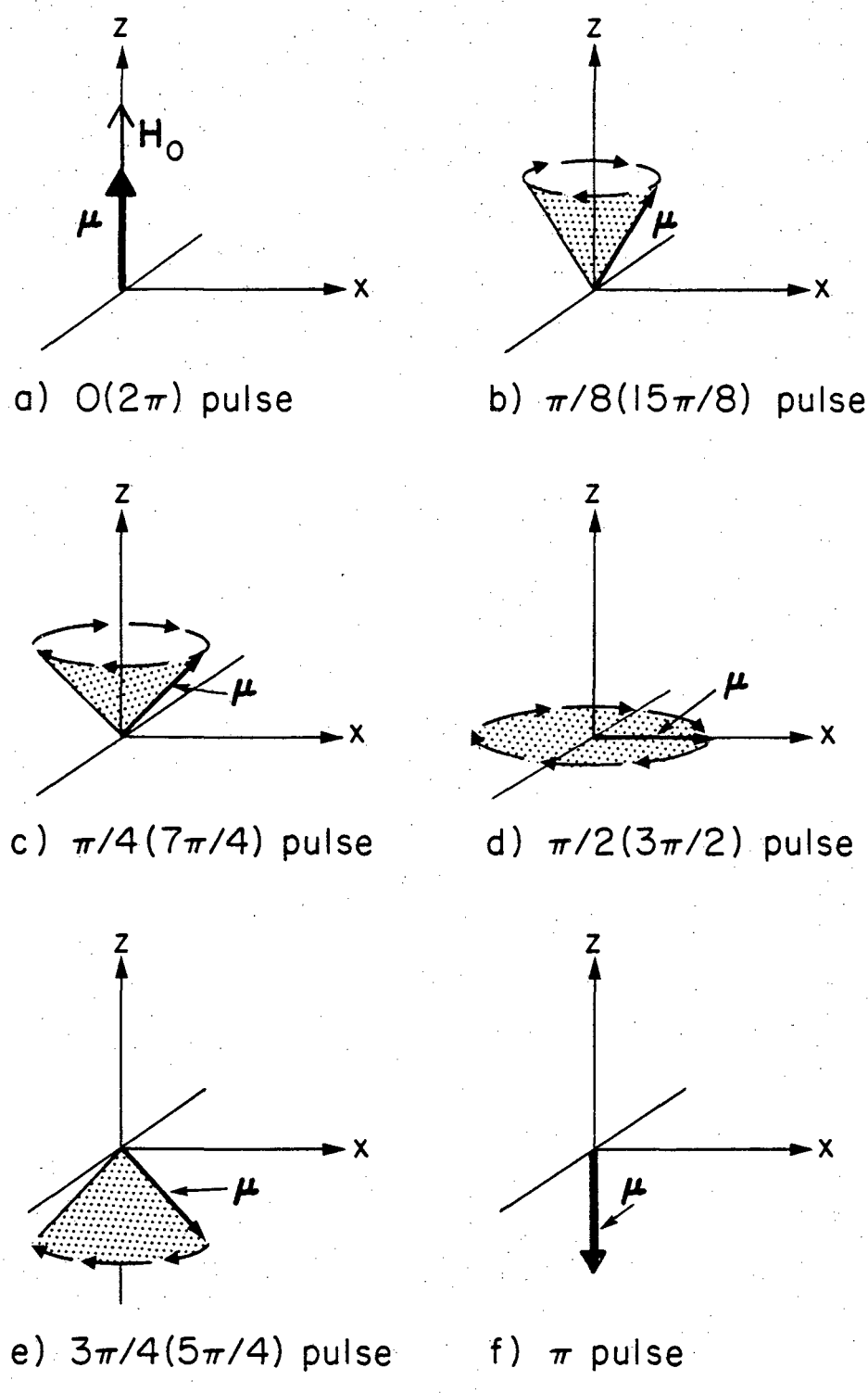

XBL 829-11405

Figure A.6. Dipole precession after a resonant pulse. (Inertial frame).

alternating field, as in (A.20), where $H_1 << H_0$. If the rotating frequency is at resonance, i.e., $\omega = \omega_0 = \gamma H_0$, the dipole sees it as stationary, and slowly precesses about it as it rapidly precesses about $\hat{\underset{\sim}{k}}$. As in Figure A.6, one would see the cone defined by the motion of $\underset{\sim}{\mu}$ gradually open. If $\underset{\sim}{\mu}$ began parallel to $\underset{\sim}{H}_0$, as time progressed the precession cone would open from a line to a disc in the x-y plane ($\alpha = \pi/2$). It would then start closing in the opposite direction and eventually collapse to a line pointing antiparallel $\underset{\sim}{H}_0$. If the resonant alternating field is turned off now (at $\alpha = \pi$), $\underset{\sim}{\mu}$ would be left pointing in the opposite direction from where it began. If the field were left on, the line would again open to a cone, back to the disc, and eventually back to its initial line ($\alpha = 2\pi$). The frequency of this periodic motion is $\omega_1 = \gamma H_1$. Now suppose ω is slightly less than ω_0. Again, $\underset{\sim}{\mu}$ will start to precess about $\underset{\sim}{H}_1$ while it continues its much more rapid precession about $\underset{\sim}{H}_0$. However, $\underset{\sim}{H}_1$ does not "keep up" with the rapid precession of $\underset{\sim}{\mu}$ at ω_0. The cone associated with $\underset{\sim}{\mu}$ will continue to open (i.e., α will increase) until $\underset{\sim}{H}_1$ has slipped totally out of phase with $\underset{\sim}{\mu}$. The torque acting on $\underset{\sim}{\mu}$ will have gradually decreased to zero only to begin to increase in the opposite direction. The cone begins to close, before it has been able to fully invert (i.e., α never gets to π). The further off resonance ω is, the less the cone will open before it will begin to close, as $\underset{\sim}{H}_1$ goes out of phase with $\underset{\sim}{\mu}$ sooner. The frequency for this periodic motion is given by (A.26).

<u>Energy Absorption and Rabi's Formula</u>. Assume once again, that $\underset{\sim}{\mu}$ is parallel to $\underset{\sim}{H}_0$ before the alternating field $\underset{\sim}{H}_1(t)$ is turned on. The energy of this dipole is at a minimum in this direction, given, by (A.3), as

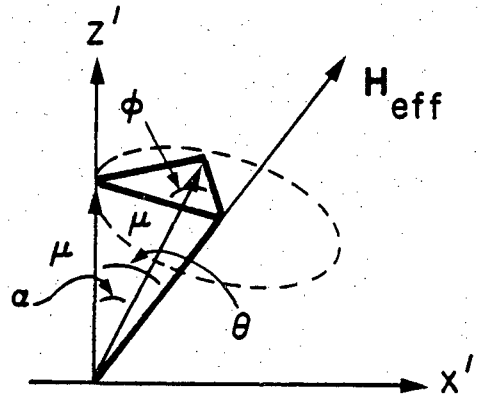

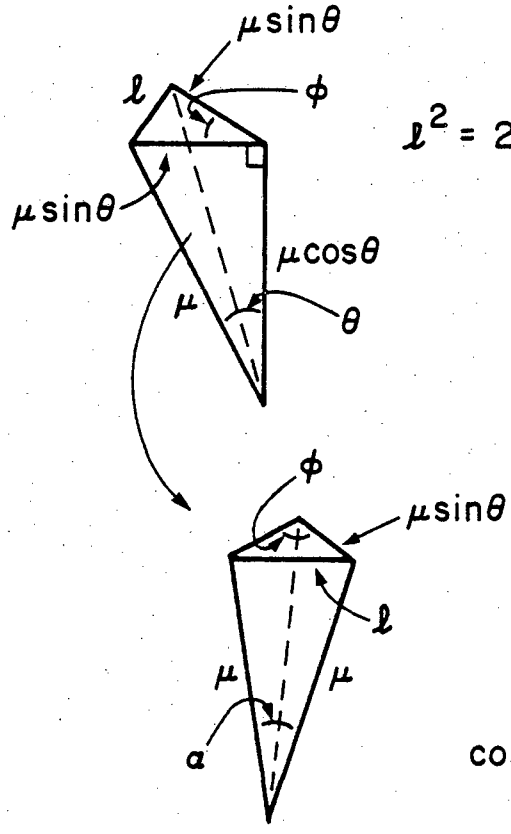

$$\ell^2 = 2\mu^2\sin^2\theta - 2\mu^2\sin^2\theta\cos\phi$$

$$\cos\alpha = \frac{2\mu^2 - \ell^2}{2\mu^2}$$

$$= 1 - \sin^2\theta(1 - \cos\phi)$$

$$= 1 - 2\sin^2\theta\sin^2\phi/2$$

XBL 829-11406

Figure A.7. Geometric determination for "cosα" in the Rabi equation.

$$E(t=0) = -\mu H_0.$$

If $\underset{\sim}{H}_1(t)$ is then turned on for a time τ, $\underset{\sim}{\mu}$ will be left precessing about $\underset{\sim}{H}_0$ at some angle α, with a potential energy

$$E(t=\tau) = -\underset{\sim}{\mu} \cdot \underset{\sim}{H}_0 = -\mu H_0 \cos\alpha. \tag{A.27}$$

The energy absorbed from $\underset{\sim}{H}_1(t)$ is then

$$\Delta E = \mu H_0 (1 - \cos\alpha). \tag{A.28}$$

The value of $\cos\alpha$ as a function of ω_0, ω_1, ω(from (A.23)) and τ can be calculated geometrically. As in Figure A.4, in the rotating frame and in the presence of $\underset{\sim}{H}_1(t)$ $\underset{\sim}{\mu}$ precesses about $\underset{\sim}{H}_{eff}$ at an angle

$$\phi = \omega_{eff}\tau = \sqrt{(\omega_0 - \omega)^2 + \omega_1^2}\,\tau \tag{A.29}$$

if $\underset{\sim}{H}_1(t)$ is left on for time τ. $\underset{\sim}{H}_{eff}$ itself is at an angle θ to $\hat{\underset{\sim}{k}}'$, where

$$\theta = \tan^{-1} \frac{H_1}{H_0 - \frac{\omega}{\gamma}} = \tan^{-1} \frac{\omega_1}{\omega_0 - \omega}. \tag{A.30}$$

A geometric proof is sketched out in Figure A.7, ending with the result

$$\cos\alpha = 1 - 2\sin^2\theta \sin^2\frac{\phi}{2}. \tag{A.31}$$

Keep in mind that the plane of the circle described by the tip of $\underset{\sim}{\mu}$ is perpendicular to H_{eff}. Combining Equations (A.28) - (A.31) gives

$$\Delta E = 2\mu H_0 \frac{\omega_1^2}{\omega_1^2 + (\omega_0 - \omega)^2} \sin^2\left[\left(\omega_1^2 + (\omega_0 - \omega)^2\right)^{\frac{1}{2}} \frac{\tau}{2}\right]. \tag{A.32}$$

A transition of $\underset{\sim}{\mu}$ going from parallel to antiparallel with respect to $\underset{\sim}{H}_0$

corresponds to a "full transition" and the maximum possible energy change

$$\Delta E_{max} = 2\mu H_0. \tag{A.33}$$

The fraction P of a full transition from a pulse of a field like $\underset{\sim}{H}_1(t)$ is then

$$P = \frac{\Delta E}{\Delta E_{max}} = \frac{\omega_1^2}{\omega_1^2+(\omega_0-\omega)^2} \sin^2[(\omega_1^2+(\omega_0-\omega)^2)^{\frac{1}{2}} \frac{\tau}{2}], \tag{A.34}$$

the Rabi formula. In essence, the Rabi formula as a function of ω has an oscillatory factor and a "Lorentzian" factor that serves as an envelope for the oscillation, centered at ω_0.

<u>The Rabi Spectrum</u>. In the type of experiment to be discussed here, an ensemble of particles each with a magnetic dipole moment is given a net magnetization $\underset{\sim}{M}$ that is initially in the direction of a static magnetic field $H_0\hat{\underset{\sim}{k}}$. In a given experiment, an alternating field of the form $\underset{\sim}{H}_1(t) = H_1(\cos\omega t\hat{\underset{\sim}{i}} - \sin\omega t\hat{\underset{\sim}{j}})$ of fixed amplitude H_1 and variable frequency ω is turned on for a fixed time τ. A spectrum here will consist of a plot of the function P of (A.34) as a function of ω, for fixed $\omega_0(=\gamma H_0)$, $\omega_1(=\gamma H_1 << \omega_0)$ and τ. This plot will then be proportional to the amount of energy absorbed by the ensemble from $\underset{\sim}{H}_1(t)$ as a function of ω. In a quantum mechanical sense, as will be described with more detail in the following section, it also corresponds to the probability of a dipole $\underset{\sim}{\mu}$ in the ensemble undergoing a full transition (i.e., from pointing essentially parallel to the static field to pointing antiparallel).

In a first experiment, ω_1 and τ_a are picked so that ϕ(as defined in (A.29)) is equal to π for $\omega_\alpha = \omega_0$. A sample spectrum for this is sketched in Figure A.8. Figure A.9 represents rotating frame views for

Figure A.8. Rabi spectrum for a π pulse of resonance.

Figure A.9. Dipole precessions caused by pulses of various frequencies ω (referred from Fig. A.8), viewed in frames rotating at the resonant frequency, ω_0.

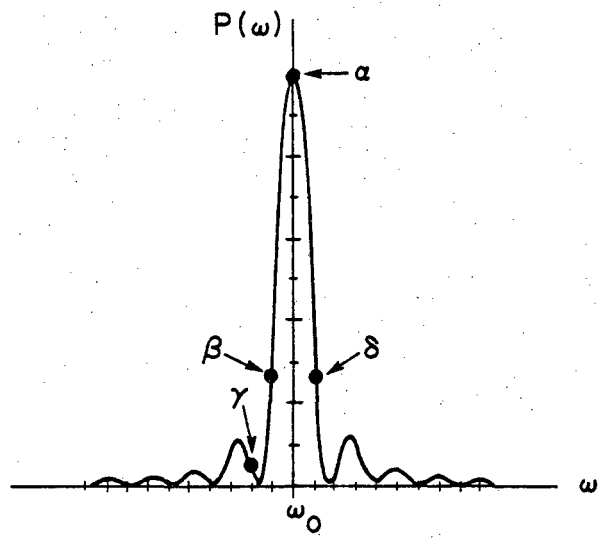

Figure A.8

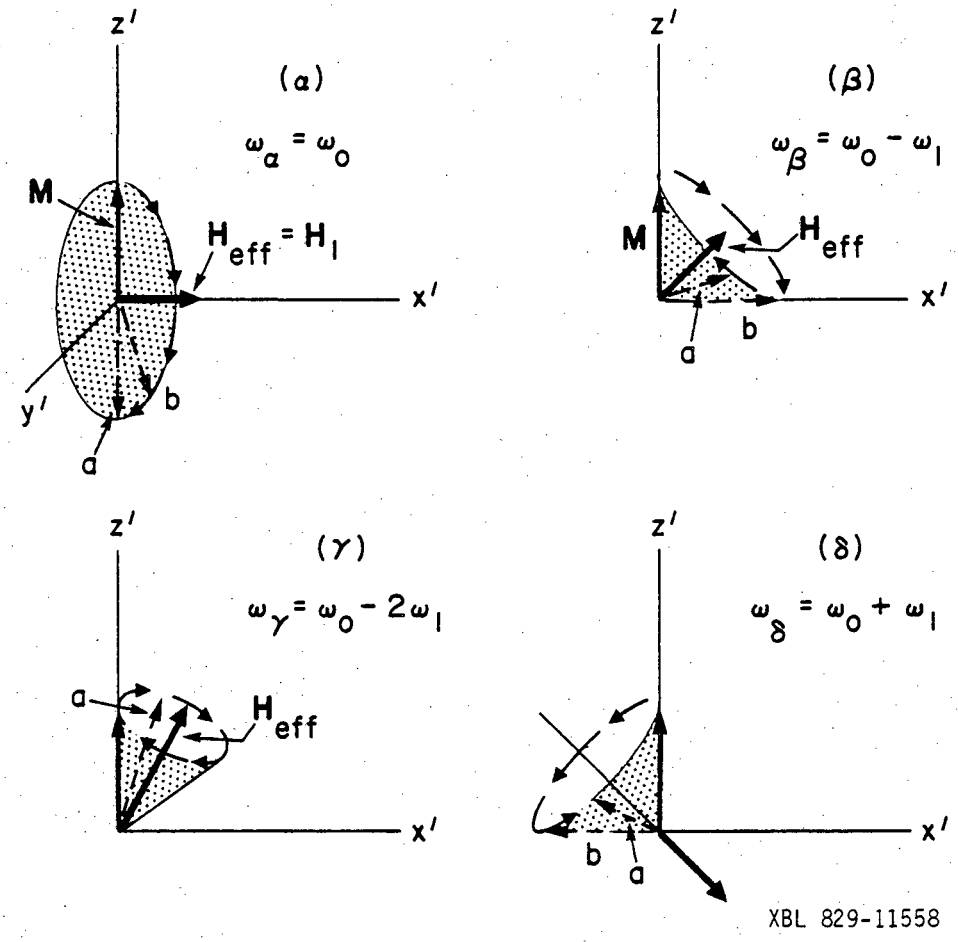

Figure A.9

four different frequencies ω particularly marked in Figure A.8. In case α, ω_α is at the resonance frequency ω_0. By the condition set here for ω_1 and τ, this corresponds to a π pulse as described previously and as indicated at point 'a' in Figure A.9-α. As this involves the total inversion of $\underset{\sim}{M}$, it corresponds to the maximum possible absorbed energy, and is indicated by point 'α' on the spectrum in Figure A.8. In case β, ω is reduced: $\omega_\beta \approx \omega_0 - \omega_1$. In Figure A.9-$\beta$, $\underset{\sim}{H}^\beta_{eff}$ (A.25) has changed direction and lengthened. As a result, the precession rate ω_{eff} for $\underset{\sim}{M}$ has increased, so that $\underset{\sim}{M}$ precesses further around its cone than in case α, to point 'a' in Figure A.9-β. Two effects have reduced the amount of transitions and the absorption of energy here. First, even if τ were changed so that $\underset{\sim}{M}$ were allowed a maximum change in case β (corresponding to point b in Figure A.9-β), this would still not be a full transition, for the physical reasons discussed in the previous section. Secondly, what was a π pulse for case α is greater than a π pulse for β, and the amount of net energy absorbed is further reduced, as indicated by point β in Figure A.8. As ω is further reduced from ω_β, the precession cone of $\underset{\sim}{M}$ in the rotating frame becomes narrower, and $\underset{\sim}{M}$ will wrap further around (as $|\underset{\sim}{H}_{eff}|$ increases), until at a particular ω, $\underset{\sim}{M}$ has experienced a full 2π pulse from τ_a and no net transition has occurred. This point on Figure A.8a corresponds to the first node to the left of ω_0. Illustrated in Fig. A.9-γ, is the case for some $\omega_0 < \omega_0 - 2\omega$. Here $\phi > 2\pi$, and the amount of energy absorbed begins to increase again. For a slightly smaller ω, τ_a will correspond to a 3π pulse, giving the first maximum to the left of ω_0 in Figure A.8a. This pattern continues to the left with a series of nodes and maxima, with the decreasing maxima related to the narrowing of the precession cones. As an example for $\omega > \omega_0$, consider

$\omega_\delta = \omega_0 + \omega_1$ in Figure A.9-δ, and compare it to Figure A.9-β. With H_{eff} pointing in a negative direction with respect to the z axis, M precesses (in the reverse direction) about a cone that is the mirror image with respect to the y'-z' plane of that in case β, resulting in the same net amount of energy absorption as with β. An extension of this should indicate that spectrum 'a' should be symmetric about ω_0.

Simulated spectra for other values of $\omega_1\tau$ are given in Figure A.10. If $\omega_1\tau > \pi$, then at no frequency ω can a π pulse be experienced. When $\omega_1\tau = 2\pi$, a node occurs at $\omega = \omega_0$, and maxima will occur <u>close</u> to those frequencies ω where 3π pulses are being experienced (close, because the Lorentzian envelope will shift these maxima toward ω_0 slightly). As $\omega_1\tau$ is further increased, the two maxima will "approach" ω_0 until they again appear to merge, and there is once again a maximum at ω_0. The second derivative of P at ω_0, from (A.34),

$$\left.\frac{d^2P(\omega)}{d\omega^2}\right|_{\omega=\omega_0} = \frac{2}{\omega_1^2}\sin\frac{\omega_1\tau}{2}\left(\frac{\omega_1\tau}{2}\cos\frac{\omega_1\tau}{2} - \sin\frac{\omega_1\tau}{2}\right), \tag{A.35}$$

changes sign at $\omega_1\tau = 2n\pi$ for n an integer, and when $\omega_1\frac{\tau}{2} = \tan(\omega_1\frac{\tau}{2})$, indicating that a spectrum will have a local maximum at ω_0 for $0 < \omega_1\tau < 2\pi$, $\sim 2.89\pi < \omega_1\tau < 4\pi$, $\sim 4.91\pi < \omega_1\tau < 6\pi$, <u>et al</u>. Nodes, in general, occur at frequencies $\omega_n^{\pm}$ where

$$\omega_n^{\pm} = \omega_0 \pm \frac{2\pi}{\tau}\left[n^2 - \left(\frac{\omega_1\tau}{2\pi}\right)^2\right]^{\frac{1}{2}} \tag{A.36}$$

for n an integer $\geq \frac{\omega_1\tau}{2\pi}$. The magnitude of the pulses corresponding to the nodes in Figure A.10 are indicated. Finally, note that for $\omega_1\tau = (2n+1)\pi$, as n increases, the relative heights of the maxima not at ω_0 increase and the peaks become closer.

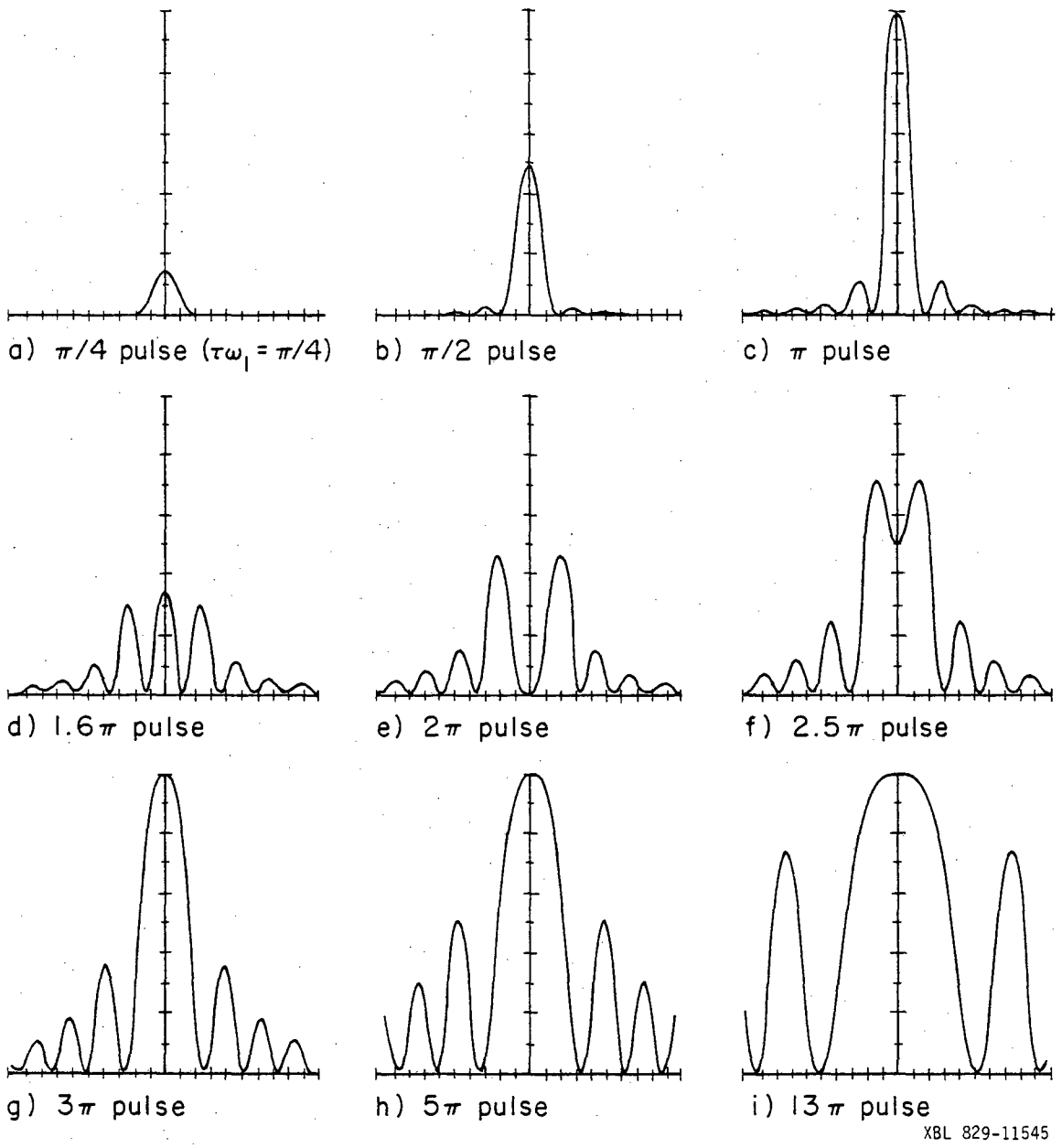

Figure A.10. Rabi spectra at various pulse lengths.

2. A Quantum Mechanic Derivation of Rabi's Formula

We will be considering here a very general two level system interacting with a permanent, time independent Hamiltonian $\hat{\mathcal{H}}^{\circ}$, and, for a finite time, a time dependent perturbation $\hat{\mathcal{H}}'(t)$. Though this description is not specifically for the case of magnetic resonance on spin systems, parallels with the classical description of the previous section will occasionally be made for clarity. The fact that most real systems, particularly in an MBER experiment, have more than two levels will be addressed later.

Before the perturbation $\hat{\mathcal{H}}'(t)$ is turned on, the system can be described by one of two stationary states which are represented by eigenfunctions ($|\alpha\rangle$ and $|\beta\rangle$) of the static Hamiltonian $\hat{\mathcal{H}}^{\circ}$:

$$\hat{\mathcal{H}}^{\circ}|\alpha\rangle = E_{\alpha}|\alpha\rangle$$

$$\hat{\mathcal{H}}^{\circ}|\beta\rangle = E_{\beta}|\beta\rangle, \qquad \text{(A.37)}$$

where E_{α} and E_{β} are the associated eigenvalues (energies) of $|\alpha\rangle$ and $|\beta\rangle$, respectively.

The time dependent perturbation $\hat{\mathcal{H}}'(t)$ will be defined by its effect on $|\alpha\rangle$ and $|\beta\rangle$ by

$$\hat{\mathcal{H}}'(t)|\alpha\rangle = W\, e^{-i\omega t}|\beta\rangle$$

and

$$\hat{\mathcal{H}}'(t)|\beta\rangle = W^{*}\, e^{i\omega t}|\alpha\rangle\ . \qquad \text{(A.38)}$$

This operator is a general quantum mechanical description of an oscillatory (at frequency ω) interaction between two states. It is Hermitian, as it should be. Diagonal terms are not expressed here, but

in what follows, E_α and E_β can be redefined to include them. Finally, note the similarity of the matrix element

$$W\, e^{-i\omega t} = W(\cos\omega t - i\, \sin\omega t)$$

to the classical time dependent interaction $\underset{\sim}{H}_1(t)$ of the last section in Equation (A.20).

Combining (A.37) and (A.38), with $\hat{\mathcal{H}} \equiv \hat{\mathcal{H}}^\circ + \hat{\mathcal{H}}'(t)$, we have

$$\begin{aligned} \hat{\mathcal{H}}(t)\,|\alpha\rangle &= E_\alpha\,|\alpha\rangle + W\, e^{-i\omega t}\,|\beta\rangle \\ \hat{\mathcal{H}}(t)\,|\beta\rangle &= W^*\, e^{+i\omega t}\,|\alpha\rangle + E_\beta\,|\beta\rangle \end{aligned} \tag{A.39}$$

or, in matrix form,

$$\underset{\approx}{\mathcal{H}}(t)\begin{pmatrix} |\alpha\rangle \\ |\beta\rangle \end{pmatrix} = \begin{pmatrix} E_\alpha & We^{-i\omega t} \\ W^* e^{i\omega t} & E_\beta \end{pmatrix}\begin{pmatrix} |\alpha\rangle \\ |\beta\rangle \end{pmatrix} \tag{A.40}$$

Clearly $|\alpha\rangle$ and $|\beta\rangle$ are no longer eigenstates of $\hat{\mathcal{H}}(t)$. A particular eigenstate of $\hat{\mathcal{H}}(t)$, which will be referred to as $|\psi(t)\rangle$, should be time dependent as is $\hat{\mathcal{H}}(t)$. Since $|\alpha\rangle$ and $|\beta\rangle$ form a complete basis set for all possible states, $|\psi(t)\rangle$ can be expressed as a linear combination of them, with time dependent coefficients:

$$|\psi(t)\rangle = a_\alpha(t)\,|\alpha\rangle + a_\beta(t)\,|\beta\rangle. \tag{A.41}$$

We will stop here to give motivation to what follows. Assume that before $\hat{\mathcal{H}}'(t)$ was turned on our system was purely described by the state $|\alpha\rangle$. This can be interpreted in either of two ways. One could say that there is one element in our system which generally has a certain probability of being either in the $|\alpha\rangle$ state or in the $|\beta\rangle$ state, but that before the interaction was turned on it was measured and found to be $|\alpha\rangle$.

On the other hand, one can talk of an ensemble of elements all initially in the $|\alpha\rangle$ state. When $\hat{\mathcal{H}}'(t)$ is turned on, $|\alpha\rangle$ is no longer a stationary state. $|\psi(t)\rangle$ is one now. As time proceeds, $|\psi(t)\rangle$ will consist of varying mixtures of the states $|\alpha\rangle$ and $|\beta\rangle$. When $\hat{\mathcal{H}}'(t)$ is turned off at time τ, $|\alpha\rangle$ and $|\beta\rangle$ again become stationary states. The description of the system is no longer $|\alpha\rangle$, but

$$|\psi(\tau)\rangle = a_\alpha(\tau)|\alpha\rangle + a_\beta(\tau)|\beta\rangle.$$

From elementary quantum mechanics, the probability P of our one element system being measured and found to be in state $|\beta\rangle$, as the fraction of our many element system found to be in $|\beta\rangle$, will be

$$P = a_\beta^*(\tau)a_\beta(\tau) \tag{A.42}$$

In other words, P will be the probability of a transition from $|\alpha\rangle$ to $|\beta\rangle$, and to find P we need to find $a_\beta(t)$.

The time dependent coefficients of (A.41) are found by solving the differential equation

$$i\hbar \frac{d}{dt} |\psi(t)\rangle = \hat{\mathcal{H}}(t)|\psi(t)\rangle. \tag{A.43}$$

Using (A.41) for $|\psi(t)\rangle$ and (A.39),

$$\begin{aligned} i\hbar \frac{d}{dt} a_\alpha(t)|\alpha\rangle + i\hbar \frac{d}{dt} a_\beta(t)|\beta\rangle \\ &= a_\alpha(t)\hat{\mathcal{H}}|\alpha\rangle + a_\beta(t)\hat{\mathcal{H}}|\beta\rangle \\ &= (a_\alpha(t)E_\alpha + a_\beta(t)W^* e^{i\omega t})|\alpha\rangle \\ &+ (a_\alpha(t)W e^{-i\omega t} + a_\beta(t)E_\beta)|\beta\rangle. \end{aligned}$$

As $|\alpha\rangle$ and $|\beta\rangle$ are linearly independent, their coefficients can be collected and set to zero, giving

$$i\hbar \frac{d}{dt} a_\alpha(t) = E_\alpha a_\alpha(t) + W^* e^{i\omega t} a_\beta(t)$$

$$i\hbar \frac{d}{dt} a_\beta(t) = W e^{-i\omega t} a_\alpha(t) + E_\beta a_\beta(t). \tag{A.44}$$

It is convenient here to make a function substitution so that we will be solving a pair of coupled differential equations without time dependent coefficients. The function substitution

$$b_\alpha(t) \equiv e^{i\omega t/2} a_\alpha(t)$$

$$b_\beta(t) \equiv e^{-i\omega t/2} a_\beta(t) \tag{A.45}$$

is related to the use of a rotating frame in the classical example. Making the appropriate substitutions in (A.44) gives

$$i\hbar \frac{d}{dt} b_\alpha(t) = (E_\alpha - \frac{\hbar\omega}{2}) b_\alpha(t) + W^* b_\beta(t)$$

$$i\hbar \frac{d}{dt} b_\beta(t) = (E_\beta + \frac{\hbar\omega}{2}) b_\beta(t) + W b_\alpha(t) \tag{A.46}$$

or, in matrix form,

$$\frac{d}{dt}\begin{pmatrix} b_\alpha(t) \\ b_\beta(t) \end{pmatrix} = \frac{1}{i\hbar}\begin{pmatrix} E_\alpha - \frac{\hbar\omega}{2} & W \\ W^* & E_\beta + \frac{\hbar\omega}{2} \end{pmatrix}\begin{pmatrix} b_\alpha(t) \\ b_\beta(t) \end{pmatrix} \tag{A.47}$$

In general, the solution to a differential equation like the above is

$$\begin{pmatrix} b_\alpha(t) \\ b_\beta(t) \end{pmatrix} = A_+ \underset{\sim}{C}_+ e^{\lambda_+ t} + A_- \underset{\sim}{C}_- e^{\lambda_- t}, \tag{A.48}$$

where λ_+ and λ_- are the eigenvalues of $\underset{\approx}{H}^b$; $\underset{\sim}{C}_+$ and $\underset{\sim}{C}_-$, their corresponding eigenvectors; and A_+ and A_-, constants to be determined by initial conditions. The eigenvalues of $\underset{\approx}{H}^b$, the matrix of Equation (A.47), are

$$\lambda_\pm = \frac{1}{i\hbar}\left(\frac{E_\alpha+E_\beta}{2} \pm \sqrt{\frac{E_\alpha-E_\beta-\omega}{2}^2 + |W|^2}\right)$$

$$\equiv \frac{E_\pm}{i\hbar}, \tag{A.49}$$

with corresponding eigenvectors

$$\underset{\sim}{C}_+ = \begin{pmatrix} \cos(\frac{\theta}{2})\ e^{-i\phi/2} \\ -\sin(\frac{\theta}{2})\ e^{-i\phi/2} \end{pmatrix}$$

and

$$\underset{\sim}{C}_- = \begin{pmatrix} \sin(\frac{\theta}{2})\ e^{i\phi/2} \\ \cos(\frac{\theta}{2})\ e^{i\phi/2} \end{pmatrix}, \tag{A.50}$$

where

$$\theta \equiv \tan^{-1} \frac{2|W|}{(E_\alpha-E_\beta-\hbar\omega)} \tag{A.51}$$

and

$$e^{i\phi} = \frac{W}{|W|} \tag{A.52}$$

Now using Equations (A.48-A.50) and (A.45), we can write the functions $a_\alpha(t)$ and $a_\beta(t)$:

$$a_\alpha(t) = A_+ \cos(\frac{\theta}{2})\ e^{-i\phi/2}\ e^{-it(\frac{E_+}{\hbar} + \omega)}$$

$$+ A_- \sin(\frac{\theta}{2})\ e^{i\phi/2}\ e^{-it(\frac{E_-}{\hbar} + \omega)} \tag{A.53}$$

continued

$$a_\beta(t) = -A_+ \sin(\tfrac{\theta}{2})\, e^{-i\phi/2}\, e^{-it(\frac{E_+}{\hbar} + \omega)}$$
$$+ A_- \cos(\tfrac{\theta}{2})\, e^{i\phi/2}\, e^{-it(\frac{E_-}{\hbar} - \omega)} .$$

To determine A_+ and A_- we use the initial conditions described previously, namely, that at $t = 0$ when the interaction is turned on, our system is totally described by $|\alpha\rangle$, i.e.,

$$a_\alpha(0) = 1 \quad \text{and} \quad a_\beta(0) = 0. \tag{A.54}$$

From (A.53) this gives

$$A_+ = e^{i\phi/2} \cos(\tfrac{\theta}{2})$$
$$A_- = e^{-i\phi/2} \sin(\tfrac{\theta}{2}), \tag{A.55}$$

and

$$a_\alpha(t) = \cos^2(\tfrac{\theta}{2})\, e^{-it(\frac{E_+}{\hbar} + \omega)} + \sin^2(\tfrac{\theta}{2})\, e^{-it(\frac{E_-}{\hbar} + \omega)}$$
$$a_\beta(t) = \sin(\tfrac{\theta}{2})\cos(\tfrac{\theta}{2})\left[-e^{-it(\frac{E_+}{\hbar} - \omega)} + e^{-it(\frac{E_-}{\hbar} - \omega)}\right] . \tag{A.56}$$

Finally, the probability P of a transition from $|\alpha\rangle$ to $|\beta\rangle$ at time τ, by (A.42) and (A.56), is

$$P = |a_\beta(\tau)|^2$$
$$= \sin^2(\tfrac{\theta}{2})\cos^2(\tfrac{\theta}{2})\left(2 - e^{i\tau \frac{E_+ - E_-}{\hbar}} - e^{-i\tau \frac{E_+ - E_-}{\hbar}}\right)$$
$$= \sin^2\theta \, \sin^2 \left\{ \frac{E_+ - E_-}{\hbar} \frac{\tau}{2} \right\}, \tag{A.57}$$

and by substitution with (A.51) and (A.49),

$$P = \frac{|2W|^2}{|2W|^2+(E_\alpha-E_\beta-\hbar\omega)^2} \sin^2\{(|2W|^2 + (E_\alpha-E_\beta-\hbar\omega)^2)^{\frac{1}{2}} \frac{\tau}{2\hbar}\}. \qquad (A.58)$$

If one makes the simple identification of

$$\omega_1 = 2|W|/\hbar \qquad (A.59)$$

and

$$\omega_0 = (E_\alpha-E_\beta)/\hbar, \qquad (A.60)$$

one reobtains the Rabi formula of Equation (A.34).

3. MBER and Rabi's Formula

Classical View of MBER versus Magnetic Resonance. The parallels between an electric resonance experiment and the magnetic resonance experiment described in this appendix are easily noted. Once again we have molecules with angular momentum $\underset{\sim}{J}$, and now an electric dipole moment $\underset{\sim}{\mu}_E$ which, for linear molecules, points along the direction of the interatomic bonds. Note, this is not along the direction of $\underset{\sim}{J}$. The Stark interaction in an electrostatic field $\underset{\sim}{E}$ is

$$E = -\underset{\sim}{\mu}_E \cdot \underset{\sim}{E}, \qquad (A.61)$$

similar to Equation (A.3). In the A field of our apparatus, molecules with particular dipolar (or rotational) orientations are selected so that the beam entering the C field has a net polarization as contrasted to a certain magnetization established in magnetic resonance. In the presence of a static field the beam also experiences an alternating electric field within the C region,

$$\underset{\sim}{E}'(t) = E_{RF} \cos\omega t\, \hat{i}\,, \qquad (A.62)$$

similar to the effect in Equation (A.18), for a period τ equal to the amount of time that an individual molecule remains in that field. Upon leaving the C field, a net change in the beam's polarization is then detected by use of the B field and mass spectrometer.

The problem in a classical description of the Stark effect arises partly from the fact that a linear molecule has no zero field electric dipole moment in the laboratory frame due to its rotation about an axis perpendicular to the molecular axis. As discussed in Chapter III, however, in the presence of an electric field the rotor's motion will be perturbed, causing the creation of a net effective dipole moment $\underset{\sim}{\mu}_{eff}$ in the laboratory frame, and

$$E = -\underset{\sim}{\mu}_{eff} \cdot \underset{\sim}{E}. \tag{A.63}$$

Classically it can be shown that the component of $\underset{\sim}{\mu}_{eff}$ in the direction of $\underset{\sim}{E}$ is

$$\underset{\sim}{\mu}_{eff} \cdot \hat{\underset{\sim}{k}} = \frac{1}{2}\,\mu^2(\underset{\sim}{J})^2\ IE(3\cos^2\theta-1) \tag{A.64}$$

where μ is the molecule's dipole magnitude in a frame rotating with it; 'I', the molecule's moment of inertia; E, the magnitude of the stationary field; and θ, the angle that the molecule's axis of rotation makes with $\hat{\underset{\sim}{k}}$, the direction of $\underset{\sim}{E}$.

In the magnetic resonance picture, $\underset{\sim}{\mu}_m$ was proportional to a particle's angular momentum, $\underset{\sim}{S}$. In addition, the magnitude of $\underset{\sim}{\mu}_m$ in a magnetic field was constant (via Equation (A.4) and its accompanying discussion), so that the magnitude of $\underset{\sim}{S}$ was also fixed. For the Stark effect, the equation of motion is

$$\underset{\sim}{\tau} = \frac{d\underset{\sim}{J}}{dt} = \underset{\sim}{\mu}_{eff} \times \underset{\sim}{E}. \tag{A.65}$$

Comparing to Equation (A.4), a big difference is that $\underset{\sim}{J}$ is not parallel to $\underset{\sim}{\mu}_{eff}$. The arguments following (A.4) are not applicable here. The torque acting on $\underset{\sim}{J}$ is <u>not</u> perpendicular to $\underset{\sim}{J}$, so that the magnitude of $\underset{\sim}{J}$ is <u>not</u> a constant of motion. The previous discussion of a rotating linear dipole in an electrostatic field already characterized the rotor's motion with changes in angular frequency, so that it is no real surprise now to see again that $|\underset{\sim}{J}|$ is not fixed. If $\underset{\sim}{E}$ is static, we have from Equation (A.65)

$$\frac{d\underset{\sim}{J}}{dt} \cdot \underset{\sim}{E} = 0 = \frac{d}{dt}(\underset{\sim}{J} \cdot \underset{\sim}{E}), \tag{A.66}$$

so that the projection of $\underset{\sim}{J}$ onto $\underset{\sim}{E}$, J_z, is a constant of the motion. In a stationary frame $\underset{\sim}{J}$ is roughly confined to a solid cone about the $\hat{\underset{\sim}{k}}$ axis. To come up with a rotating frame to follow the precession of $\underset{\sim}{J}$ is now obviously quite difficult.

<u>Quantum Mechanical View of the Stark Effect</u>. The justification for using Rabi's formula for electric resonance transitions is inherent in the generality of our quantum derivation of the formula. A detailed derivation of the ω_0 and ω_1 coefficients of Equation (A.34) for the Stark effect is presented in Chapter IV. Arguing very heuristically here, in the C field two states are "connected" by the oscillatory field. By Equation (A.63) and (A.61), the energies of these states in the presence of an electrostatic field $\underset{\sim}{E}_{DC}$ will be proportional to $|\underset{\sim}{\mu}_{eff}||\underset{\sim}{E}_{DC}|$, so that the energy difference in Equation (A.59) should generally look like

$$E_\alpha - E_\beta = \frac{\mu^2 E_{DC}^2}{B} f(J_\alpha, M_\alpha, J_\beta, M_\beta) \tag{A.67}$$

where f is a function of the rotational properties of the two states and $B \propto 1/I$ is the rotational constant. In the presence of an oscillatory field $\underset{\sim}{E}_{RF}(t)$, the frequency of the precession between the states (similar to ω_1 in the classical magnetic resonance case, and $|W|$ in the quantum argument) should be proportional to $-\underset{\sim}{\mu}_{eff} \cdot \underset{\sim}{E}_{RF}$, or

$$W = \frac{\mu^2 E_{DC} E_{RF}}{B} f'(J_\alpha, M_\alpha, J_\beta, M_\beta, X), \tag{A.68}$$

where f' is dependent on the states' rotational properties and the relative orientation of $\underset{\sim}{E}_{DC}$ and $\underset{\sim}{E}_{RF}$.

The justification for treating electric resonance transitions in a two level sense is seen in the resultant Rabi formula (A.58). If one initially has a single state $|\alpha_a>$, and if the energies separating all other states $|\alpha_a'>$ from $|\alpha_a>$, $(E_{a'}-E_a)$, are significantly greater than their corresponding connecting matrix elements $W_{aa'}(=<\alpha_{a'}|\hat{\underset{\sim}{\mu}}\cdot\hat{\underset{\sim}{E}}_{RF}|\alpha_a>)$, only those particular states $|\alpha_{a''}>$ where $(E_{a''} - E_a)/\hbar$ is approximately within $|W_{aa''}|/\hbar$ of the exciting frequency W will interact. In general, the ratio of elements $W_{aa'}$ to state energies E_a', from (A.67) and (A.68), is

$$\frac{W}{E} \approx \frac{E_{RF}}{E_{DC}} \equiv \varepsilon. \tag{A.69}$$

In our experiments, ε generally ranges from 0.01 to 0.1. Rabi's formula will break down at ω such that $E_a \pm \hbar\omega$ is within $\varepsilon\hbar\omega$ of more than one other state. With one important exception, this generally does not happen for molecules without nuclear spin, like OCS, but needs to be worried about when nuclear spin couplings can create states of relatively close energies.

The important exception mentioned above is the case of a rotational state $|J,M=0\rangle$ interacting with the states $|J, M= \pm 1\rangle$, as these latter states are degenerate in the Stark effect. This system should be considered as a three-level system. The parallel equation to (A.40) for this system can be shown to be

$$\hat{\mathcal{H}}(t)\begin{pmatrix} |+1\rangle \\ |0\rangle \\ |-1\rangle \end{pmatrix} = \begin{pmatrix} E_1 & W e^{+i\omega t} & 0 \\ W^* e^{-i\omega t} & E_0 & -We^{+i\omega t} \\ 0 & -W^* e^{-i\omega t} & E_1 \end{pmatrix}\begin{pmatrix} |+1\rangle \\ |0\rangle \\ |-1\rangle \end{pmatrix} \tag{A.70}$$

where the inherent symmetry and degeneracy between the states $|+1\rangle$ and $|-1\rangle$ give the simple structure of the matrix $\mathcal{H}$. This system is, in fact, easily transformed to a two level system of a state $\frac{1}{\sqrt{2}}(|+1\rangle + |-1\rangle)$ interacting with $|0\rangle$, and the orthogonal state $\frac{1}{\sqrt{2}}(|+1\rangle - |-1\rangle)$ not interacting at all. The resulting form of Rabi's formula for a transition out of $|0\rangle$ to either $|+\rangle$ or $|-\rangle$ becomes

$$P_{0\to+1} + P_{0\to-1} = \frac{(2\sqrt{2}W)^2}{(2\sqrt{2}W)^2+(E_1-E_0-\hbar\omega)^2} \sin^2\{((2\sqrt{2}W)^2 + (E_1-E_0-\hbar\omega)^2)^{\frac{1}{2}} \frac{\tau}{2}\} , \tag{A.71}$$

where, compared to (A.58), W has been simply replaced by $\sqrt{2}W$, reflecting that $|0\rangle$ has two different states it can turn to, so that the transition rate has increased.

<u>Other Possible Distortions to the MBER Spectrum</u>. There is a question of whether a molecule leaving the A field state-selected, but in regards to a particularly oriented static field $\mathcal{E}_A$, maintains its orientation with regards to the static C field, $\mathcal{E}_{DC}$. If the change in field occurs slowly enough, one can treat the problem in a similar manner as the rotating magnetic field and Equations (A.16). For the process to be "adiabatic"

there it was necessary that the Larmor frequency $_0$ be significantly greater than the frequency of field rotation ω_r. Here, typically,

$$\omega_0 \sim \frac{E_0}{\hbar} \sim \frac{\mu^2 E_A{}^2}{2B} > 10^7 \text{ sec}^{-1}$$

whereas

$$\omega_r \sim \frac{1}{\Delta t} \sim 10^4 \text{ sec}^{-1},$$

where Δt is the transit time while the field rotation is occurring. Thus, it is evident that molecules traveling from the A field to the B field do so largely adiabatically.

The neglect of spontaneous emissions in the transition field or later is justified by the small magnitude of the transition frequencies involved. The Einstein transition rate for spontaneous emission is

$$A_{\alpha\beta} = \frac{4\omega_{\alpha\beta}^3}{3\hbar c^3} \langle\alpha|\hat{\underset{\sim}{\mu}}|\beta\rangle^2, \tag{A.72}$$

where $\omega_{\alpha\beta}$ is the transition frequency. For $\omega_{\alpha\beta}$ on the order of 1 MHz, and $\langle\alpha|\hat{\underset{\sim}{\mu}}|\beta\rangle$ typically on the order of $E_{DC} \times 1$ cm/V-sec, $A_{\alpha\beta} \sim 10^{-37}$ sec^{-1}. As a molecule is only in the experiment for $\sim 10^{-3}$ sec, spontaneous emission is not very likely.

A typical time dependent electric field is of the form of Equation (A.62), and not circularly polarized as was $\underset{\sim}{H}_1(t)$ in (A.20). The treatment for magnetic resonance involved the decomposition of a linearly polarized oscillatory field into two circularly polarized fields, followed by the treatment of only the part rotating with the dipoles. There are two effects to note. The first is that only half of the amplitude of the linearly polarized field is effective in causing the

desired transitions (Eq. (A.19)). The second, more subtle effect is caused by the presence of the circular component rotating in the wrong direction. It can be shown that this will shift the apparent resonant frequency from the true ω_0 to the value, correct to first order in ω_1^2, given by[2]

$$\omega_{res} = \omega_0 + \frac{\omega_1^2}{4\omega_0} . \tag{A.73}$$

For the MBER transition, this corresponds to a shift

$$\Delta = \frac{\omega_{res} - \omega_0}{\omega_0} \sim \varepsilon^2 \tag{A.74}$$

where ε is defined in Equation (A.69). For experiments where $\mathcal{E}_{DC} \sim$ 1000 V/cm and $\mathcal{E}_{RF} \sim 10$ V/cm, this corresponds to an error in ω_0 determination of 0.01%, or about 1 kHz for a typical $\Delta J = 0$ transition.

Rabi's formula applies to systems where all elements are exposed to an oscillatory field for the same time τ. The FWHM of Equation (A.34) for $\omega_1\tau = \pi$ can be shown to be

$$\Delta\omega_{\frac{1}{2}} \approx 1.6\ \pi/\tau. \tag{A.75}$$

The C field is about 15 cm long, a typical velocity is about 5×10^4 cm/sec; hence τ is about 3×10^{-4} sec, giving $\Delta\omega_{\frac{1}{2}} \sim 2.7$ kHz. In a real experiment, molecules are characterized by varying velocities, giving varying values of exposure times τ in the C field. A broad distribution of τ's would wash out the Rabi modulation in a spectrum, leaving just the somewhat broadened Lorentzian envelope. A narrower distribution would give broadened oscillations. These effects are discussed in more

detail in Chapter IV. Doppler broadening is a much smaller effect and will not be considered here.

A final cause for line broadening is inhomogeneities in the static C field. The applied oscillatory field is easily controlled in frequency to much less than 1 kHz. As transition frequencies are proportional to E_{DC}^2, a width of field strengths of $E_{DC}\delta$ will lead to a width of transition intensities of $\sim 2E_{DC}^2\delta$. From diffraction tests, $\delta \sim 10^{-4}$, contributing an additional broadening term of 2 kHz for a transition near 10 MHz.

REFERENCES to APPENDIX I

1. C. Cohen-Tannoudji, B. Diu, and F. Laloe, Quantum Mechanics (John Wiley & Sons and Hermann, Paris, 1977), Chpt. 3 and 4.

2. N. F. Ramsey, Molecular Beams (Oxford University Press, London, 1956).

3. C. P. Slichter, Principles of Magnetic Resonance (Harper & Row, New York, 1963).

4. A. Abragam, The Principles of Nuclear Magnetism (Clarendon Press, Oxford, 1961).

5. C. H. Townes and A. L. Schawlow, Microwave Spectroscopy (McGraw-Hill, New York, 1955).

6. R. T. Schumacher, Introduction to Magnetic Resonance (W. A. Benjamin, Inc., New York, 1970).

APPENDIX II

The Computer Programs W. vs E and TWOSPIN

Program W. vs E is written in BASIC and designed for the use by a PET computer and HP plotter-printer. A listing for this follows. W. vs E calculates the state energies of a linear molecule with nuclear spins as a function of external electric field strength and plots out the resultant adiabatic curves (e.g., Fig. 4.3). It diagonalizes a Hamiltonian matrix expressed in a strong field basis representation and includes the Stark interaction as a second and fourth order perturbation to the diagonal elements (i.e., it maintains J as a good quantum number). Program TWOSPIN is listed on the microfiche appended to this thesis (see the appendix to Chapter III). It calculates transition frequencies and strengths for linear polar molecules with nuclear spins, again using a strong field basis, but not prediagonalizing in the J quantum number. Both of these programs were based on routines developed by the W. Klemperer group at Harvard University.

```
100 Z1=0:Z2=0:Z3=0:Z4=0:Z6=0:Z7=0:Z8=0:Z9=0:Z0=0
110 DIM A(25,25),Q(25,25)
120 DIM M(35,4),MJ(35),N(35),E(25),EM(35)
125 DIM C(25,25),EC(25)
130 REM PROGRAM W.VS.E....CALCULATES AND PLOTS ENERGY
131 REM OF ROTATIONAL STATES AS A FUNCTION OF ELECTRIC
132 REM FIELD STRENGTH ...... HENRY ...7/23/80
135 INPUT"DO YOU WISH TABLES ON SCREEN OR PRINTER ";A$
137 IF A$="PRINTER" THEN 150
140 OPEN 201,3:GOTO 155
150 OPEN 201,4,1
155 OPEN 202,12    :OPEN 203,13
160 PRINT"EXCEPT FOR I, ENTER THE FOLLOWING PARAMETERS ";
161 PRINT"IN UNITS OF KILOHERTZ."
170 FOR I=1TO2:PRINT"I";I;:INPUTI(I):PRINT"QE";I;
175 INPUT QE(I): PRINT"CA";I; : INPUT CA(I) :NEXT
180 READSA(1),JS(1),SA(2),JS(2)
190 REM DATA FOR CL-F
200 REM DATA 2.556,1.074,0,0
205 DATA 0,0,0,0
210 INPUT"DIPOLE MOMENT(DEBYE)";MU:INPUT"ROT. CONSTANT(MHZ.)";BO
220 M9=MU:MU=(.50348*MU)^2/BO/2:MS=MU^2/BO/2
250 PRINT"DO YOU WANT TO RUN FOR ALL POSSIBLE ";
255 INPUT"M-SUB-F'S FOR THE GIVEN J";A$
500 INPUT"MINIMUM FIELD (VOLTS/CM.)";EA:INPUT"MAXIMUM FIELD";EZ
510 INPUT"NUMBER OF FIELD INCREMENTS";EI
520 EB=EA:EY=EZ:EJ=(EY-EB)/EI:EE=EA
540 CMD201:GOSUB 8460:PRINT#201
550 CMD203:GOSUB 8460:PRINT#203
600 INPUT"LOWEST ANTICIPATED ENERGY(KHZ)";ZL
605 INPUT"HIGHEST ENERGY";ZH
1000 REM
1001 REM
1200 REM GETS 'J' AND 'MF'...FINDS ALL STATES WITHIN
1205 REM THAT MANIFOLD
1280 INPUT"J";JJ:J2=2*JJ:IFJJ<0THEN END
1290 FM=JJ+I(1)+I(2)+I(3)+I(4): MI=FM-INT(FM) : MF=MI-1
1300 GOSUB11310
1350 GOSUB9000
1370 IF A$<>"Y" THEN 1400
1380 MF=MF+1 : IF MF>FM THEN 1280
1390 GOTO 1420
1400 INPUT"M-SUB-F";MF:IF MF<0 THEN 1280
1410 IF MF>FM THEN 1480
1420 J=0
1430 FOR JS=0TOJJ:JW=JS
1440 FOR JT=I(1) TO -I(1) STEP -1
1450 MJ(J)=JW:M(J,1)=JT
1460 M(J,2)=MF-JW-JT
```

```
1470 IF ABS(M(J,2)-INT(M(J,2)))=ABS(I(2)-INT(I(2)))THEN 1490
1480 PRINT"BAD M-SUB-F":GOTO 1370
1490 IF ABS(M(J,2))>I(2)THEN J=J-1
1500 J=J+1 : NEXT
1510 IF JW>0 THEN JW=-JW:GOTO 1440
1520 NEXT
1530 CMD 201
1540 NT=J-1:PRINT"J=";JJ,"M-SUB-F=";MF,"# OF STATES=";NT+1
2580 GOSUB 20630
2998 REM
2999 REM
3000 IF EE<=EZ THEN 3010
3004 PRINT#202,"PUUR"
3008 EE=EA : GOTO 1370
3010 E2=EE^2*MU*1000 : E4=MS*1000*EE^4
3020 PRINT#201,"ELECTRIC FIELD="EE" VOLTS/CM  ";
3025 PRINT#201,"(MU^2*E^2/BO/2="E2"KHZ)"LIST8520
3030 GOSUB11100
3100 FORI=0TONT:MJ=ABS(MJ(I))
3110 FOR K=0 TO NT
3120 A(I,K)=C(I,K)
3130 IF I=K THEN A(I,K)=A(I,K)+SK(MJ)
3140 NEXT:NEXT
3200 N=NT: GOSUB 31540
3210 EE=EE+EJ:GOTO 3000
8000 REM
8001 REM
8200 REM ECHOING INPUT
8460 PRINT"NUCL.    I       QE        CA"
8470 FORI=1TO2
8480 PRINT" "I"      "I(I)"    "QE(I)"    "CA(I):NEXT
8485 PRINT"SA="SA(1);"JS="JS(1)
8490 PRINT"DIPOLE MOMENT="M9" DEBYE"
8500 PRINT"ROTATIONAL CONSTANT="BO" MHZ."
8520 PRINT"LOW ELECTRIC FIELD="EA"VOLTS/CM    ";
8525 PRINT"HIGH FIELD="EZ"VOLTS/CM."
8530 RETURN
8998 REM
8999 REM
9000 REM SET UP FOR PLOTTING
9005 D$=STR$(EB):E$=STR$(EY):F$=STR$(ZH):G$=STR$(ZL)
9010 C$=",":PRINT#202,"IP400,500,7500,6500;"
9020 PRINT#202,"SC"D$C$E$C$STR$(ZH-(ZH-ZL)/6)C$F$";"
9030 FOR I=0TO6: H$=STR$(ZL+(ZH-ZL)*I/6)
9040 PRINT#202,"XA"H$C$STR$((EY-EB)/20)C$D$C$E$C$"2;"
9050 NEXT
9060 FOR I=0TO3: H$=STR$(EB+(EY-EB)*I/3)
9070 PRINT#202,"YA"H$C$STR$(1000)C$G$C$F$C$"1;"
9080 NEXT
9090 RETURN
```

```
11098 REM
11099 REM
11100 REM STARK ENERGY TO FOURTH ORDER
11110 SK(0)=E4*11/135-E2/3:IF JJ=0 THEN RETURN
11120 FORJ=0TOJJ
11130 X=((JJ+1)^2-J^2)*(J^2-(JJ+2)^2)/(J2+1)/(J2+5)
11135 X=X/(JJ+1)^2/(J2+3)^3
11140 X1=((JJ-1)^2-J^2)*(JJ^2-J^2)/(J2-3)/(J2+1)/(J2-1)^3/JJ/JJ
11150 X2=((JJ+1)^2-J^2)*(JJ^2-J^2)/(J2-1)/(J2+3)/(J2+1)^2
11155 X2=X2/JJ/JJ/(JJ+1)^2
11160 X3=((JJ+1)^2-J^2)^2/(J2+3)^2/(J2+1)^2/(JJ+1)^3
11170 X4=-(JJ^2-J^2)^2/(J2-1)^2/(J2+1)^2/JJ^3
11175 X=X+X1+X2+X3+X4
11180 SK(J)=X*E4+E2*(JJ*(JJ+1)-3*J^2)/JJ/(JJ+1)/(J2+3)/(J2-1)
11190 NEXT
11200 RETURN
11300 REM SETS COEFFICIENTS FOR SOME TERMS
11310 FORJ=1TO4:CR(J)=0:SS(J)=0:EQ(J)=0:NEXT
11320 IFJJ=0 THEN RETURN
11330 FORJ=1TO4
11340 SS(J)=SA(J)/(J2+3)/(J2-1):CR(J)=CA(J)
11350 IFI(J)>=1 THEN EQ(J)=QE(J)/(J2+3)/(J2-1)/(2*I(J)^2-I(J))/4
11360 NEXT:RETURN
20498 REM
20499 REM
20500 REM GENERATES HAMILTONIAN MATRIX IN ARRAY 'A'
20630 FORI=0TONT
20640 FORK=ITONT
20650 MJ=MJ(I):RO=3*MJ^2-JJ*(JJ+1):IFK=I GOTO21020
20660 FORJ=1TO4:D(J)=M(I,J)-M(K,J):NEXT
20670 DJ=MJ-MJ(K):DA=ABS(DJ)
20680 IFD(1)=0 AND D(2)=0 THENL1=2:GOTO20710
20690 IFD(3)=0 AND D(4)=0 THENL1=1:GOTO20710
20700 X=0:GOTO21070
20710 SS=SS(L1):JS=JS(L1):L2=2*L1:L1=L2-1
20720 D1=D(L1):M1=M(I,L1):I1=I(L1)
20730 D2=D(L2):M2=M(I,L2):I2=I(L2):D3=ABS(D1):D4=D1+D2
20740 Q1=EQ(L1):Q2=EQ(L2):C1=CR(L1):C2=CR(L2)
20750 T1=D1^2+D2^2+DJ^2
20760 IFT1>8 THEN X=0:GOTO21070
20770 IFT1=8 GOTO20970
20780 IFT1=6 GOTO20810
20790 IFT1=2 GOTO20850
20800 PRINT"LEVEL LABLE ERROR"T1:END
20810 IF DA<>2 GOTO20700
20820 IF DJ<0 THENMJ=-MJ:M1=-M1:M2=-M2
20830 X=(JJ-MJ+1)*(JJ+MJ)*(JJ-MJ+2)*(JJ+MJ-1)*(I1-M1)*(I1+M1+1)
20840 X=SQR(X*(I2-M2)*(I2+M2+1))*1.5*SS:GOTO21070
20850 IFDJ>.1 THEN G=(JJ+MJ)*(JJ-MJ+1):GOTO20890
20860 IFDJ<-.1 THEN G=(JJ-MJ)*(JJ+MJ+1):GOTO20910
```

```
20870 IFD1<0 THEN M1=-M1:M2=-M2
20880 X=SQR((I1+M1)*(I1-M1+1)*(I2+M2+1)*(I2-M2))
20885 X=X*(JS-SS*RO)/2: GOTO 21070
20890 IFD1=0 THEN G=SQR(G*(I2+M2+1)*(I2-M2)):GOTO20950
20900 G=SQR(G*(I1+M1+1)*(I1-M1)):GOTO20930
20910 IFD1=0 THEN G=SQR(G*(I2-M2+1)*(I2+M2)):GOTO20950
20920 G=SQR(G*(I1-M1+1)*(I1+M1))
20930 X=SS*G*1.5*M2*(MJ+MJ-DJ)+C1*G/2-Q1*G*1.5
20935 X=X*(1+2*MJ*M1+2*(M1-D1)*(MJ-DJ))
20940 GOTO21070
20950 X=SS*G*1.5*M1*(MJ+MJ-DJ)+C2*G/2-Q2*G*1.5
20955 X=X*(1+2*MJ*M2+2*(M2-D2)*(MJ-DJ))
20960 GOTO21070
20970 IFDJ<0 THEN MJ=-MJ:M1=-M1:M2=-M2
20980 IFD1=0 THEN Q1=Q2:M1=M2:I1=I2
20990 X=(JJ+MJ)*(JJ-MJ+1)*(JJ+MJ-1)*(JJ-MJ+2)*(I1+M1+1)*(I1-M1)
21000 X=-SQR(X*(I1+M1+2)*(I1-M1-1))*Q1*1.5
21010 GOTO21070
21020 X=M(I,1)*M(I,2)*(JS(1)+2*RO*SS(1))+M(I,3)
21025 X=X*M(I,4)*(JS(2)+2*RO*SS(2))
21030 FORJ=1TO4
21040 X=X+CR(J)*MJ*M(I,J)-EQ(J)*RO*(3*M(I,J)^2-I(J)*(I(J)+1))
21050 NEXT
21070 C(I,K)=X : C(K,I)=X
21080 NEXT
21090 NEXT
21100 RETURN
30998 REM
30999 REM
31000 REM FOR W.VS.E,OUTPUTING TO PLOTTER AND PRINTER
31540 IFN=0 THEN E(0)=A(0,0):Q(0,0)=1:GOTO 31580
31570 GOSUB 41750
31575 PRINT#201,"# ITERATIONS="Z9"   TIME="TB$
31580 EM=-1E10:AM=A(0,0):IM=0
31590 FOR K=0TON
31600 FOR I=0TON
31610 IF A(I,I)>=EM AND A(I,I)<AM THEN AM=A(I,I) : IM=I
31620 NEXT
31630 PRINT#201,AM; :A(IM,IM)=AM-.0001 :E(K)=AM
31640 FORI=0TON:Z1=INT(Q(I,IM)^2*100+.5)
31645 PRINT#201,Z1;:NEXT:PRINT#201
31650 EM=AM : AM=1E10
31660 IF EE=EL THEN 31810
31670 REM PLOTTING
31690 PRINT#202,"PAPU"STR$(EE-EJ)C$STR$(EO(K))",PD"
31700 PRINT#202,"PA"STR$(EE)C$STR$(E(K))",PU"
31810 EO(K)=E(K)
31820 NEXT:PRINT#201
31830 RETURN
40998 REM
```

```
40999 REM
41000 REM DIAGONALIZES 'A', LEAVING EIGENVALUES IN 'A',
41010 REM AND EIGENVECTORS AS COLUMNS IN 'Q'
41750 L=.01:PRINT#201
41760 TI$="000000"
41770 FORI1=0TON
41780 FORI2=0TON
41790 Q(I1,I2)=0
41800 NEXT
41810 Q(I1,I1)=1
41820 NEXT
41830 Z9=0
41840 Z1=0:Z2=1
41850 Z0=A(N,N)^2
41860 FORZ4=0TON-1
41870 Z0=Z0+A(Z4,Z4)^2
41880 FORZ8=Z4+1TON
41890 IF ABS(A(Z4,Z8))<ABS(A(Z1,Z2))THEN41910
41900 Z1=Z4:Z2=Z8
41910 NEXT
41920 NEXT
41930 IF ABS(A(Z1,Z2))<LTHEN42280
41940 IF A(Z1,Z1)<>A(Z2,Z2)THEN41970
41950 Z6=.707106781:Z3=SGN(A(Z1,Z2))*Z6
41960 Z7=SGN(Z3):GOTO 42000
41970 Z7=A(Z1,Z1)-A(Z2,Z2)
41980 Z7=2*SGN(Z7)*A(Z1,Z2)/(ABS(Z7)+SQR(Z7*Z7+4*A(Z1,Z2)^2))
41990 Z6=1/SQR(1+Z7*Z7):Z3=Z7*Z6
42000 Z9=Z9+1:PRINTZ9,Z0
42010 FOR Z4=0TON
42020 Z8=Q(Z4,Z1)
42030 Q(Z4,Z1)=Z8*Z6+Q(Z4,Z2)*Z3
42040 Q(Z4,Z2)=Q(Z4,Z2)*Z6-Z8*Z3
42050 NEXT
42060 IF Z1<1THEN 42120
42070 FOR Z4=0TOZ1-1
42080 Z8=A(Z4,Z1)
42090 A(Z4,Z1)=Z8*Z6+Z3*A(Z4,Z2)
42100 A(Z4,Z2)=Z6*A(Z4,Z2)-Z8*Z3
42110 NEXT
42120 IF Z1>Z2-2THEN 42180
42130 FOR Z4=Z1+1TOZ2-1
42140 Z8=A(Z4,Z2)
42150 A(Z4,Z2)=Z6*Z8-Z3*A(Z1,Z4)
42160 A(Z1,Z4)=Z6*A(Z1,Z4)+Z3*Z8
42170 NEXT
42180 IF Z2>N-1THEN 42240
42190 FOR Z4=Z2+1TON
42200 Z8=A(Z1,Z4)
42210 A(Z1,Z4)=Z6*Z8+Z3*A(Z2,Z4)
```

```
42220 A(Z2,Z4)=Z6*A(Z2,Z4)-Z3*Z8
42230 NEXT
42240 Z8=A(Z1,Z1)
42250 A(Z1,Z1)=Z6*Z6*(Z8+Z7*(2*A(Z1,Z2)+Z7*A(Z2,Z2)))
42260 A(Z2,Z2)=Z6*Z6*(A(Z2,Z2)-Z7*(2*A(Z1,Z2)-Z7*Z8))
42270 A(Z1,Z2)=0:GOTO 41840
42280 CMD 201:TB$=TI$:RETURN
60000 END
```

CHAPTER V

THE ARGON-ALKALI HALIDE MOLECULE SYSTEM - AN ELECTROSTATIC MODEL

With the advent of supersonic molecular beams in electric resonance spectroscopy, a variety of small van der Waals molecules have been studied in recent years,[1-3] yielding direct information on their structures and indirect information on the forces involved with bonding. A single, intuitive model to describe and predict simultaneously all of these molecules' geometries and other energetic characteristics has yet to be found. Van der Waals bonds in molecules ranging from Ar_2 to the C_6H_6 - Cl_2 complex have been well described by models with attractive forces derived from nearly classical electrostatic and dispersive terms. These were particularly appealing in their simplicity. However, the bond in molecules such as ArClF has not been so easily described. A Lewis acid-base model involving the "chemical" bonding of the highest occupied molecular orbital of one participant to the lowest unoccupied molecular orbital of the other has been invoked, and found to give a satisfactory view of many molecules at which electrostatic models apparently seem to fail. Electrostatic models in general are criticized[3] for ignoring quantum effects that are felt to be necessary in any bonding description. To better understand the relative merits of these two types of models, other classes of weakly bound molecules need to be studied.

An electrostatic model is used here to predict the energetics and the equilibrium configurations for molecules of the type $Ar\text{-}M^+X^-$, where M^+X^- represents one of twenty alkali halide molecules, with $M^+ = Li^+$, Na^+, K^+, Rb^+, or Cs^+ and $X^- = F^-$, Cl^-, Br^-, or I^-. The alkali and

halide ions individually are closed-shelled, with no low-lying excited electronic states. With this and with the positions of the charge centers in MX (M^+X^-) relatively obvious, the ArMX system would seem particularly well-suited as a test case for an electrostatic bonding model. The calculations presented here are anticipatory of experimental results with which they can be compared.[44]

A. Introduction

Previous experimental studies of the Ar-MX potential systems have been restricted to beam inelastic scattering work. Among these studies is the work of Reed and Wharton[4] on the differential cross section of Ar-LiF scattering; the energy transfer investigation of Loesch and Herschbach[5] on the Ar/CsI system (later studied by Greene, et al.[6]); the vibrational energy transfer in the Ar/KBr^+ system by Crim, et al.[7]; and the ionic dissociative collision study for systems including Ar with CsI, CsBr, RbI and KI of Tully, et al.[8] Though some estimates of the potential energy surface at the new equilibrium configuration of the ArMX complexes have been made, the relatively high energy of these experiments in comparison to the predicted potential wells would suggest a lack of sensitivity to the features of such surfaces.

The basis of the attraction part of our electrostatic calculations is from the model suggested by Rittner[9] for MX systems. Brumer and Karplus[10] have shown that the general form of the Rittner potential can be derived from a quantum mechanical perturbative treatment of the interaction between the closed-shell ions, using the methods of Murrell, et al.[11] The electrostatic model has been used for a variety of systems including MX,[9,10,12-14] $(MX)_2$,[15-17] $(MX)_3$,[18], BX_2[19] (for B = alkaline earth cations) M_2X^+ [20-21] and MX_2^-,[21] and, where data have been available,

has given reasonable results. The electron gas model of Gordon and Kim,[22-23] a nearly *ab initio* technique, has given slightly better agreement on systems for which experimental results are available.

In the section that follows, the terms of the electrostatic theory we have used are described in some detail. The sources of the empirically determined parameters are also given. Finally, the program followed in the derivation of our potential surfaces and geometries is elaborated upon. The following section includes descriptions and tabulations of our results for the ArMX system, as well as derived results for some MX, M_2X^+, MX_2^-, ArM_2^{+2}, and ArX_2^{-2} systems. In the discussion section the model we have used is critically examined. An alternate view of the Lewis acid-base binding model is also suggested. Finally, our results are compared with the scant amount of previous relevant experimental and theoretical data.

B. The Electrostatic Theory

In the theory we have used to describe the ArMX systems, there are three basic terms in the expression for the potential energy. The dominant attractive term is electrostatic in nature, involving the Coulomb interactions between the nuclear point charges and the dipoles induced at all three nuclear centers. Our second term, also attractive in nature, includes the dispersion energy from London forces and is expressed as a pairwise interaction proportional to r^{-6}, where r is an internuclear distance. All the repulsive effects from orbital overlap, including electron exchange energies, electron kinetic energies, and nuclear repulsion, are expressed by semi-empirical exponential pairwise interaction terms. It is these three terms that are described in detail here.

1. Coulombic Interaction

Rittner[9] pointed out that the description of the binding energy and observed dipole moment of alkali halide monomers was significantly improved if one considered contributions in the dipole and energy not only from the separation of two point charges, but also from the polarization of a given ion by the field exerted by the opposing ion (Fig. 1a). The measured dipole moment is reduced while the binding interaction increases. Given the general equation for the vector electric field exerted at point "i" by a charged monopole at j (in a medium of unit dielectric constant),

$$\underset{\sim}{E}_i = -\frac{Q_j}{r_{ij}^2}\,\hat{\underset{\sim}{r}}_{ij}, \tag{5.1}$$

and for the field at point i from a dipole at point j,

$$\underset{\sim}{E}_i = \frac{3\underset{\sim}{\mu}_j\cdot\hat{\underset{\sim}{r}}_{ij}}{r_{ij}^3}\,\hat{\underset{\sim}{r}}_{ij} - \frac{\underset{\sim}{\mu}_j}{r_{ij}^3}, \tag{5.2}$$

one can determine the values of the dipoles induced at each nucleus. Here, Q_j is the charge at nucleus j; $\underset{\sim}{\mu}_j$, the vector dipole moment of j; r_{ij}, the distance between points i and j; and $\hat{\underset{\sim}{r}}_{ij}$, the unit vector from i to j. Ignoring hyperpolarizability and assuming that the polarizability tensor is isotropic, the dipole moment induced at point i by the field $\underset{\sim}{E}_i$ is

$$\underset{\sim}{\mu}_i = \alpha_i\,\underset{\sim}{E}_i, \tag{5.3}$$

where α_i is the polarizability at i. Equations (5.1-5.3) lead to a coupled set of equations to determine the induced dipole moments in the

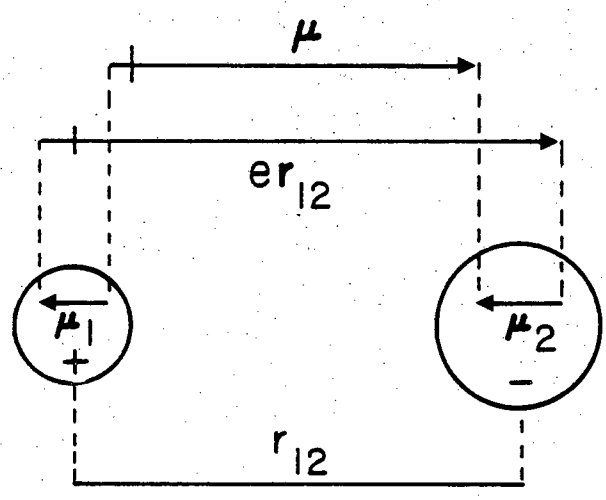

a) The Rittner model for alkali halides.

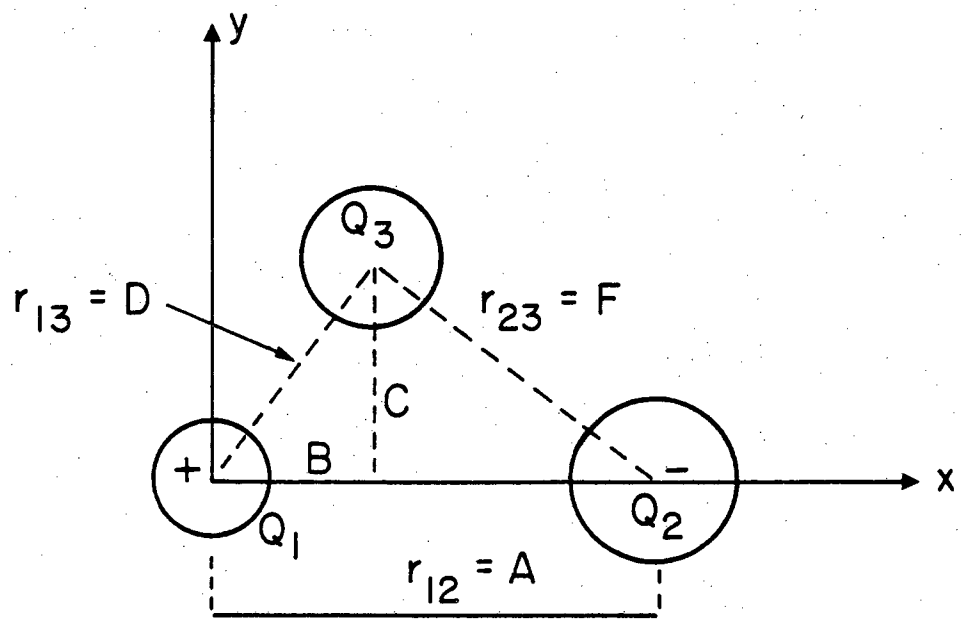

b) Distance parameters for the triatomic Rittner calculation.

XBL 829-11410

Figure 5.1

MX system (see Fig. 1a), namely

$$\frac{\mu_1}{\alpha_1} = E_1 = \frac{e}{r_{12}^{\ 2}} + \frac{2\mu_2}{r_{12}^{\ 3}}$$

$$\frac{\mu_2}{\alpha_2} = E_2 = \frac{e}{r_{12}^{\ 2}} + \frac{2\mu_1}{r_{12}^{\ 3}} \ . \tag{5.4}$$

(The vector notation has been dropped as this system is one dimensional.) From (5.4), the induced dipole moments of M^+ and X^- can be trivially derived and then used in the energy considerations.

This model is easily expanded conceptually for larger systems. As seen in Figure 1b, a system of three particles of arbitrary charges Q_i is parameterized by three distances. In our calculations typically the origin is placed at the nucleus of the alkali cation (particle 1), the halide anion (particle 2) is on the X-axis at a distance $A = r_{12}$ from the alkali, and the third atom is at coordinates (B,C) relative to the cation. As this system is planar, Equations (5.1), (5.2), and (5.3) lead to a coupled linear system of six equations - one for each of two directional components for three induced dipole moments. For the system in Figure 1b, this can be expressed in matrix form via

$$\underset{\approx}{M}\ \underset{\sim}{U} = \underset{\sim}{Q} \tag{5.5}$$

where U is the dipole vector

$$\underset{\sim}{U} = \begin{pmatrix} \mu_{1x} \\ \mu_{2x} \\ \mu_{3x} \\ \mu_{1y} \\ \mu_{2y} \\ \mu_{3y} \end{pmatrix},$$

$\underset{\sim}{Q}$ the charge vector

$$\underset{\sim}{Q} = \begin{pmatrix} \frac{-Q_2}{A^2} - \frac{Q_3 B}{D^3} \\ \frac{Q_1}{A^2} - \frac{Q_3(B-A)}{F^3} \\ \frac{Q_1 B}{D^3} + \frac{Q_2(B-A)}{F^3} \\ \frac{-Q_3 C}{D^3} \\ \frac{-Q_3 C}{F^3} \\ \frac{Q_1 C}{D^3} + \frac{Q_2 C}{F^3} \end{pmatrix}$$

and $\underset{\approx}{M}$ the field interaction matrix

$$\underset{\approx}{M} = \begin{pmatrix} \frac{1}{\alpha_1} & \frac{-2}{A^3} & \frac{C^2-2D^2}{D^5} & 0 & 0 & \frac{-3BC}{D^5} \\ \frac{-2}{A^3} & \frac{1}{\alpha_2} & \frac{C^2-2(B-A)^2}{F^5} & 0 & 0 & \frac{-3(B-A)C}{F^5} \\ \frac{C^2-2B^2}{D^5} & \frac{C^2-2(B-A)^2}{F^5} & \frac{1}{\alpha_3} & \frac{-3BC}{D^5} & \frac{-3(B-A)C}{F^5} & 0 \\ 0 & 0 & \frac{-3BC}{D^5} & \frac{1}{\alpha_1} & \frac{1}{A^3} & \frac{B^2-2C^2}{D^5} \\ 0 & 0 & \frac{-3(B-A)C}{F^5} & \frac{1}{A^3} & \frac{1}{\alpha_2} & \frac{(B-A)^2-2C^2}{F^5} \\ \frac{-3BC}{D^5} & \frac{-3(B-A)C}{F^5} & 0 & \frac{B^2-2C^2}{D^5} & \frac{(B-A)^2-2C^2}{F^5} & \frac{1}{\alpha_3} \end{pmatrix}.$$

The induced dipole moments, $\underset{\sim}{\mu}$, can now be solved for.

Given the point charges, induced dipole moments and the distances between these particles, the electrostatic interaction energy can be calculated. Several terms are involved. The energy of interaction between point charges is given by

$$V_{ij}^{cc} = \frac{Q_i Q_j}{r_{ij}} . \tag{5.6}$$

From the energy of interaction of a dipole $\underset{\sim}{\mu}$ with a field $\underset{\sim}{E}$,

$$V = -\underset{\sim}{E} \cdot \underset{\sim}{\mu},$$

and Equations (1.1) and (1.2), the charge-dipole and dipole-dipole interactions are given by

$$V_{ij}^{cd} = \frac{Q_j}{r_{ij}^{\ 2}} \underset{\sim}{\mu}_i \cdot \hat{\underset{\sim}{r}}_{ij} \tag{5.7}$$

and

$$V_{ij}^{dd} = \frac{1}{r_{ij}^{\ 3}} (\underset{\sim}{\mu}_i \cdot \underset{\sim}{\mu}_j - 3(\underset{\sim}{\mu}_i \cdot \hat{\underset{\sim}{r}}_{ij})(\underset{\sim}{\mu}_j \cdot \hat{\underset{\sim}{r}}_{ij})) \tag{5.8}$$

Finally, there is the potential energy required to separate the charges to induce a dipole,

$$V_j^{ind} = \frac{1}{2} \underset{\sim}{\mu}_j \cdot \underset{\sim}{E}_j = \frac{\mu_j^{\ 2}}{2\alpha_j} . \tag{5.9}$$

O'Konski[24] has shown that the terms (5.6) to (5.9) can be collected and conveniently expressed via

$$V^E = \frac{1}{2} \sum_{i>j} \frac{Q_i Q_j}{r_{ij}} - \frac{Q_i \underset{\sim}{\mu}_j \cdot \hat{\underset{\sim}{r}}_{ij}}{r_{ij}^{\ 4}} \tag{5.10}$$

A semiempirical model such as this can be particularly sensitive to the choice of parameters used. Some discussion relevant to this will be brought up later. For our electrostatic potential, the interatomic distances will be allowed to vary in order to find the potential minimum configuration. The two sets of empirical parameters needed here to determine the induced dipoles and, hence, the energies are thus the charges, q_i, and polarizabilities, α_i. We have used unit charges for the alkalis and halides and have left the rare gas atom neutral. As Rittner indicated, his model is classically correct if the charge at point i is at least $\alpha_j^{1/3}$ from the nucleus j that it is polarizing. Later it will be shown how this is imposed in our model. The effect of outer shell penetration may change the effective charge at a nucleus,[25] but as this model is being used for closed-shell atoms, the electron overlap is minimal. The polarizabilities of the alkali and halide ions are tabulated in several places.[26-29] We have primarily used the gas phase calculated results of Pauling.[26] The polarizability of Ar was taken to be 1.64 $\mathring{A}^3$, as given by Teachout and Pack.[30] These values are listed in Table 5.1.

2. Repulsive Interaction

The repulsive energy term used is based on the exponential Born-Mayer[31] model for MX crystals,

$$V_{ij}^R = B_{ij}\, e^{-a_{ij} r_{ij}}, \tag{5.11}$$

where B_{ij} and a_{ij} are energetic and hardness parameters determined empirically, and r_{ij}, the distance separating the species i and j. The exponential form is an approximation to the effect of the small overlap

Table 5.1

Potential Function Parameters[a]

i	α_i	ρ_{ii}	R_{ii}	n_i
Ar	1.64 $Å^3$	0.256 Å	2.612 Å	5.486
Li^+	0.029	0.020	2.008	1.93
Na^+	0.181	0.074	2.546	3.94
K^+	0.840	0.142	3.110	5.40
Rb^+	1.42	0.161	3.348	5.32
Cs^+	2.44	0.138	3.558	7.49
F^-	1.05	0.486	2.182	3.953
Cl^-	3.69	0.524	2.972	5.486
Br^-	4.81	0.544	3.222	6.218
I^-	7.16	0.550	3.604	7.610

[a] See text for sources.

of the outer electron orbitals of closed-shell species due to the Pauli exclusion principle. The parameters B_{ij} and a_{ij} are dependent on the identities of species i and j. If actual spectroscopic or collision data do not exist between these species, some kind of combining rule is required to derive good values for these parameters from other molecular systems, e.g., to derive the repulsive parameters between species A and B from a knowledge of the A-A and B-B repulsions. A particularly satisfying scheme has been suggested empirically by Gilbert[32] and derived theoretically by Smith.[33] In Smith's distortion model, the energy of interaction between two closed-shell species is determined by locating a plane of interaction between the colliding nuclei which minimizes the repulsive energies of the individual atoms while placing equal forces on either side of the plane. One can express Equations (5.11) in the mathematically equivalent form

$$V_{ij}^{R} = f\rho_{ij}\, e^{(R_{ij}-r_{ij})/\rho_{ij}}, \tag{5.12}$$

where f is a scaling constant with units of force, ρ_{ij} $(= 1/a_{ij})$ is a hardness parameter and R_{ij}, a range parameter, both of the latter with units of distance. Smith and Gilbert then showed that if one knew values for R_{AA}, R_{BB}, ρ_{AA} and ρ_{BB} from experimental data, then the parameters for the A-B interaction can be given via

$$R_{AB} = \frac{1}{2}\,(R_{AA} + R_{BB})$$

and (5.13)

$$\rho_{AB} = \frac{1}{2}\,(\rho_{AA} + \rho_{BB}).$$

Gilbert has given values for R_{ij} and ρ_{ij} for the alkali halides determined from experimental spectral data. He determines values for ρ_{ii} and R_{ii} using first an SCF calculation for Li_2^{2+} to determine $\rho_{Li_2^{2+}}$ and $R_{Li_2^{2+}}$ and then using Equation (5.13) iteratively to determine values for the remaining alkali and halide ions. Smith used collisional information on Ar to find R_{Ar^2} and ρ_{Ar^2}. These, with collision-based data for values of ρ_{ij} and R_{ij} for the alkali halides and $ArCl^-$, can similarly be used to find values for ρ_{ii} and R_{ii}. We have chosen Smith's tabulations, as it gave better internal consistency among the rare gas atoms and alkali and halide ions, and produced better predictions for MX energetics and dipole moments. Table 5.1 includes the values for the ρ_{ii} and R_{ii} used, based on a chosen value of f at 1 eV/Å, so that values for R_{ij} would be of bond length order. Table 5.2 compares experimental values of ρ_{ij} and R_{ij} with those predicted by values in Table 5.1. Agreement is seen to be relatively good, with the exception of ArK^+. This problem will be discussed later.

Our repulsive energy is taken to be pairwise additive, giving the net expression

$$V^R = \sum_{i>j} f\rho_{ij}\, e^{(R_{ij}-r_{ij})/\rho_{ij}} \tag{5.14}$$

Smith predicts that his model works best in the 0.1-10 eV repulsive energy range, and that the greatest inaccuracies would occur between pairs of atoms of most different sizes. His distortion model also predicts dipole induction at the nuclei beyond that previously discussed. In general, we have excluded these inductions from our calculations, but their implications will be discussed later.

Table 5.2

Repulsive Energy Parameters Used for the M^+X^- Systems

	Experimental		Calculated	
	ρ_{ij}(Å)	R_{ij}(Å)	ρ_{ij}(Å)	R_{ij}(Å)
LiF	0.264	2.110	0.253	2.095
NaF	0.278	2.369	0.280	2.364
KF	0.310	2.632	0.311	2.646
RbF	0.326	2.750	0.330	2.765
CsF	0.345	2.878	0.312	2.870
LiCl	0.272	2.484	0.272	2.490
NaCl	0.295	2.750	0.299	2.759
KCl	0.332	3.035	0.333	3.041
RbCl	0.353	3.163	0.349	3.160
CsCl	0.352	3.282	0.331	3.265
LiBr	0.274	2.609	0.282	2.615
NaBr	0.313	2.892	0.309	2.884
Kbr	0.345	3.172	0.343	3.166
RbBr	0.359	3.295	0.359	3.285
CsBr	0.310	3.374	0.341	3.390
LiI	0.280	2.803	0.285	2.806
NaI	0.313	3.071	0.312	3.075
KI	0.349	3.370	0.346	3.357
RbI	0.362	3.479	0.362	3.476
CsI	0.319	3.572	0.344	3.581
Cl^-Ar	0.386	2.750	0.390	2.792
K^+Ar	0.277	2.615	0.199	2.861

3. Dispersive Interaction

Only the pairwise r_{ij}^{-6} term was used to characterize the London forces. Thus, our dispersive energy expression was of the form

$$V^D = -\sum_{i>j} \frac{C_{ij}}{r_{ij}^6} . \tag{5.15}$$

The energy coefficients were determined using the Slater-Kirkwood[34] approximation

$$C_{ij} = \frac{3}{2} \frac{e^2 a_o^{\frac{1}{2}} \alpha_i \alpha_j}{(\alpha_i/n_i)^{\frac{1}{2}} + (\alpha_j/n_j)^{\frac{1}{2}}} \tag{5.16}$$

Where C is the electron charge; a_o, the Bohr radius; α_i, the polarizability of species i; and n_i, the effective number of electrons in the outermost shell of i. In our initial calculations, n_i was set to 8 for all M^+, X^- and Ar, with the exception of Li^+ ($n_i = 2$), indicating the actual number of electrons in the outer-most shell of the atom. This approximation, however, allows for too strong a shielding from underlying electrons. Later calculations used values of n_i for alkalis as calculated by Buckingham.[35] Rare gas n_i's were calculated from the rare gas homonuclear dimer dispersion constants from Starkschall and Gordon.[36] The halide n_i's were set equal to those for the corresponding isoelectronic rare gases. Values for n_i are listed in Table 5.1.

4. Calculation

Using parameters in Table 5.1 one can express the potential energy of the triatomic species ArMX as a function of its interatomic distances:

$$V\ (r_{12}, r_{13}, r_{23}) = V^E + V^R + V^D. \tag{5.18}$$

In our calculations, the values for r_{ij} are determined which minimize Equation (5.18), as well as the corresponding attractive and repulsive energy values and dipole moment. As was previously mentioned, a limit of closest approach between nuclei is required for the Rittner model. In practice, without such a boundary, the calculated induced dipoles become quite large, as the dipole-induced dipole effect becomes greater then the charge-induced dipole effect at a given distance. The Smith distortion model also predicts such a problem and indicates the presence of other forces which would negate a dipole singularity. We have used as a limit for closest approach between species i and j

$$L_{ij} = \frac{3}{4} (\alpha_i^{1/3} + \alpha_j^{1/3}) \tag{5.19}$$

where α_i and α_j are the polarizabilities. A potential minimum has always been found outside these limits.

Similar calculations were also performed for just the alkali halide, MX, determining its ionic dissociation energy, bond length and dipole moment with our parameters. This served as an internal check for our calculations and also allowed a calculation of the binding energy of Ar to the MX molecule. We have defined this binding energy via

$$D(\text{Ar-MX}) = -(V_{eq}(\text{ArMX}) - V_{eq}(\text{MX})), \tag{5.20}$$

i.e., as the negative difference between the minimum energies for ArMX and for the MX molecule alone with Ar at infinity. In general, the MX bond is a bit longer in the ArMX complex; therefore, this definition is not precisely the same as just the energy of the Ar-MX bond. Fixing r_{MX} at its value in the equilibrium configuration of ArMX, we then

calculated potential V(ArMX) for various positions of Ar relative to MX, and from these constructed potential energy contour maps. Finally, again fixing r_{MX} as above, we determined force constants associated with the motion of Ar from its equilibrium position. We have defined these force constants via

$$f_R = \left.\frac{\partial^2 V}{\partial R^2}\right|_{R_e,\theta_e} \tag{5.21}$$

$$f_\theta = \left.\frac{1}{R_e^{\,2}}\,\frac{\partial^2 V}{\partial \theta 2}\right|_{R_e,\theta_e} \tag{5.22}$$

and

$$f_{R\theta} = \left.\frac{1}{R_e}\,\frac{\partial^2 V}{\partial R \partial \theta}\right|_{R_e,\theta_e} \tag{5.23}$$

where R is the distance from Ar to the center of mass of MX; θ, the angle that $\underset{\sim}{R}$ makes with the MX axis; and R_e and θ_e, the equilibrium values of R and θ. The numerical values for these expressions were approximated by second order difference equations.

Further details of the calculation method and a listing of the computer program used are to be found in the appendix of this chapter.

C. Results

To give a sense of the goodness of our potential model and choice of parameters, experimentally determined values[10] for the ion dissociation energies, bond lengths and dipole moments for alkali halides are presented in Tables 5.3 and 5.4, and compared to those determined by our model, therein referred to as variation 0. Results for various other choices

Table 5.3

Derived Binding Energies for MX Systems[a]

	Experimental	Var. 0	Var. 1	Var. 2	Var. 3
LiF	62300	69531	69731	68938	81578
NaF	50500	56293	56680	55441	61715
KF	49000	49395	49892	48049	52961
RbF	45900	47602	48180	46048	
CsF	44700	46558	46917	44862	47711
LiCl	54800	59234	59288	58937	61854
NaCl	44800	48524	48673	47942	48942
KCl	40200	42579	42823	41503	42028
RbCl	39000	40940	41247	39648	
CsCl	37300	40235	40460	38656	37920
LiBr	51800	56268	56297	56026	
NaBr	43100	46328	46422	45823	
KBr	38400	40666	40829	39705	
RbBr	37200	39073	39283	37912	
CsBr	35700	38424	38570	36975	
LiI	48600	52240	52246	52071	
NaI	40600	43506	43539	43061	
KI	35900	38278	38341	37470	
RbI	34700	36762	36854	35773	
CsI	34500	36182	36220	34907	

		Var. 0	Var. 4	Var. 5
LiCl	54800	59234	56147	59194
KCl	40200	42579	42469	42524
CsCl	37300	40235	40373	40284

[a] (Energy in cm^{-1} units. Method variations described in text).

Table 5.4

Derived Bond Distances and Dipoles of MX System[a]

	Experimental	Var. 0	Var. 1	Var. 2	Var. 3
LiF	1.564 (6.32)	1.465 (4.50)	1.459 (4.46)	1.481 (4.64)	1.32
NaF	1.926 (8.16)	1.825 (6.77)	1.811 (6.66)	1.855 (6.99)	1.68
KF	2.171 (8.59)	2.091 (7.43)	2.067 (7.23)	2.155 (7.94)	1.98
RbF	2.270 (8.55)	2.173 (7.14)	2.140 (6.84)	2.257 (7.88)	
CsF	2.345 (7.88)	2.330 (7.12)	2.314 (6.96)	2.406 (7.86)	2.36
LiCl	2.021 (7.13)	1.906 (4.11)	1.905 (4.10)	1.914 (4.19)	1.85
NaCl	2.361 (9.00)	2.270 (7.00)	2.265 (6.96)	2.292 (7.19)	2.21
KCl	2.667(10.27)	2.562 (8.28)	2.550 (8.16)	2.620 (8.75)	2.56
RbCl	2.787(10.51)	2.661 (8.29)	2.644 (8.13)	2.733 (8.97)	
CsCl	2.906(10.39)	2.798 (8.28)	2.787 (8.16)	2.891 (9.22)	2.89
LiBr	2.170 (7.27)	2.041 (4.11)	2.041 (4.10)	2.048 (4.18)	
NaBr	2.502 (9.11)	2.409 (7.15)	2.405 (7.12)	2.429 (7.33)	
KBr	2.821(10.63	2.710 (8.61)	2.702 (8.54)	2.761 (9.06)	
RbBr	2.945(10.8)	2.815 (8.74)	2.803 (8.62)	2.883 (9.37)	
CsBr	3.072(10.8)	2.948 (8.75)	2.941 (8.68)	3.034 (9.61)	
LiI	2.392 (7.43)	2.283 (4.24)	2.283 (4.24)	2.288 (4.29)	
NaI	2.711 (9.24)	2.643 (7.37)	2.642 (7.36)	2.659 (7.52)	
KI	3.048(10.8)	2.953 (9.08)	2.950 (9.05)	2.996 (9.46)	
RbI	3.177(11.4)	3.065 (9.35)	3.060 (9.30)	3.123 (9.89)	
CsI	3.315(11.6)	3.194 (9.42)	3.192 (9.40)	3.274(10.21)	
			Var. 4	Var. 5	
LiCl	2.021 (7.13)	1.906 (4.11)	1.965 (5.62)	1.908 (4.14)	
KCl	2.667(10.27)	2.562 (8.28)	2.557 (8.38)	2.567 (8.35)	
CsCl	2.906(10.39)	2.798 (8.28)	2.793 (8.19)	2.789 (8.14)	

[a] Bond distances in Å (dipole moments) in Debye. Variations described in text.

of parameters are also presented in these tables. Variation 1 uses the actual number of electrons in the atom's or ion's outermost shell (2 or 8) in place of the effective n_i's of Table 5.1, basically increasing the van der Waals energy contribution by 20%. Variant 2 is like 0 with the dispersion contribution to the energy totally surpressed. Variant 3 also suppresses the dispersion term and uses values for ρ_{ii} and R_{ii} from Gilbert. A few calculations were also done using polarizability values from Tessman, et al.[27] (Variation 4) and using variable polarizabilities from Brumer and Karplus (Variation 5), based on Paulings' values, but modulated with r_{MX}.

A direct comparison of the binding energies and dipole moments of variation 0 with the experimental values indicates an average over estimation of the binding energy by ~5% (somewhat greater for lithium halides), underestimation of dipole moments by 20%, and underestimation of bonding lengths by ~5%. This error is consistent in that a prediction of too small a base would reduce the dipole moment further by the increased induced dipole moments at the nuclei (Fig. 5.1a). We suspect this error comes primarily from using values too great for the polarizabilities of the ions, as suggested by de Wijn[13] and Brumer and Karplus.[10] However, as seen in Table 5.4, Variation 5 is not much improved. Though Variation 2 does seem to give values closer to the experimental values for MX, the lack of a dispersion term greatly misrepresents the shape of the potential about MX, as will be seen.

The results of the calculations for the ArMX complexes by Variation 0 are summarized in Tables 5.5 and 5.6. Table 5.5 gives the geometrical values for the equilibrium configurations of the ArMX molecules and the

Table 5.5

ArMX Equilibrium Geometries (Å and degrees), Ar-MX Binding Energies (cm^{-1}), and Dipole Moment Charge from MX(D)

	r_e(Ar-M)	r_e(Ar-X)	∢(Ar-M-X)	D(Ar-MX)	Δμ μ(Ar-MX)-μ(MX)
LiF	2.60	4.07	180°	373	0.63
NaF	2.99	4.82	180°	283	0.50
KF	3.47	4.71	113°	162	0.00
RbF	3.71	3.87	77°	144	-0.19
CsF	3.66	3.80	75°	215	-0.20
LiCl	2.57	4.49	180°	453	0.75
NaCl	2.96	5.24	180°	338	0.59
KCl	3.44	4.53	97°	208	-0.08
RbCl	3.65	4.33	85°	184	-0.15
CsCl	3.63	4.25	82°	253	-0.15
LiBr	2.56	4.61	180°	486	0.80
NaBr	2.95	5.37	180°	358	0.62
KBr	3.42	4.84	104°	220	0.00
RbBr	3.64	4.58	89°	193	-0.12
CsBr	3.62	4.47	85°	261	-0.12
LiI	2.54	4.84	180°	564	0.89
NaI	2.94	5.59	180°	393	0.67
KI	3.40	4.92	101°	246	-0.02
RbI	3.61	4.74	90°	217	-0.11
CsI	3.61	4.64	86°	285	-0.12

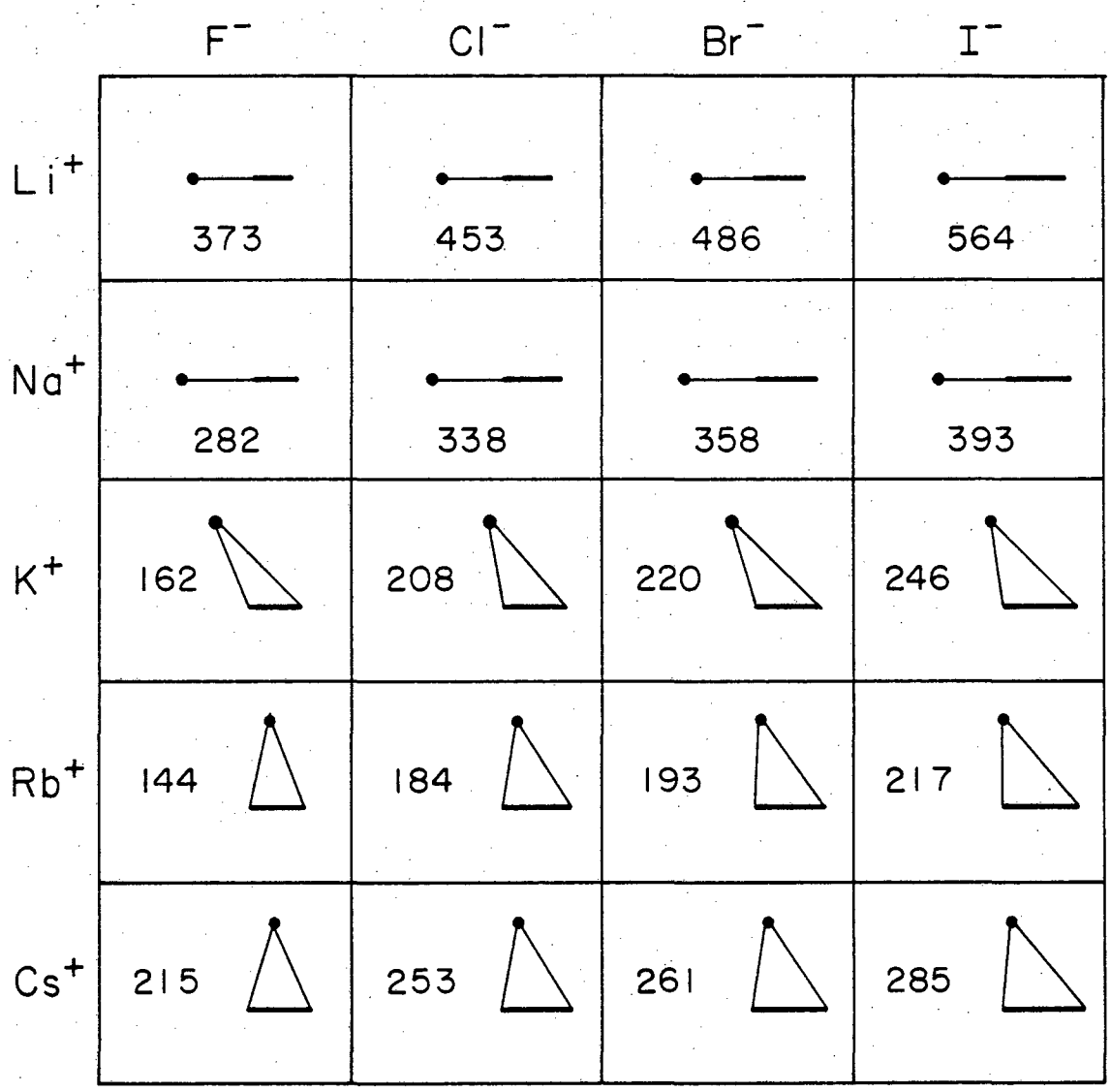

Equilibrium Geometries and Binding Energies (cm^{-1})

Ar MX

Repulsion + Electrostatic + Dispersion

XBL 829-11415

Figure 5.2

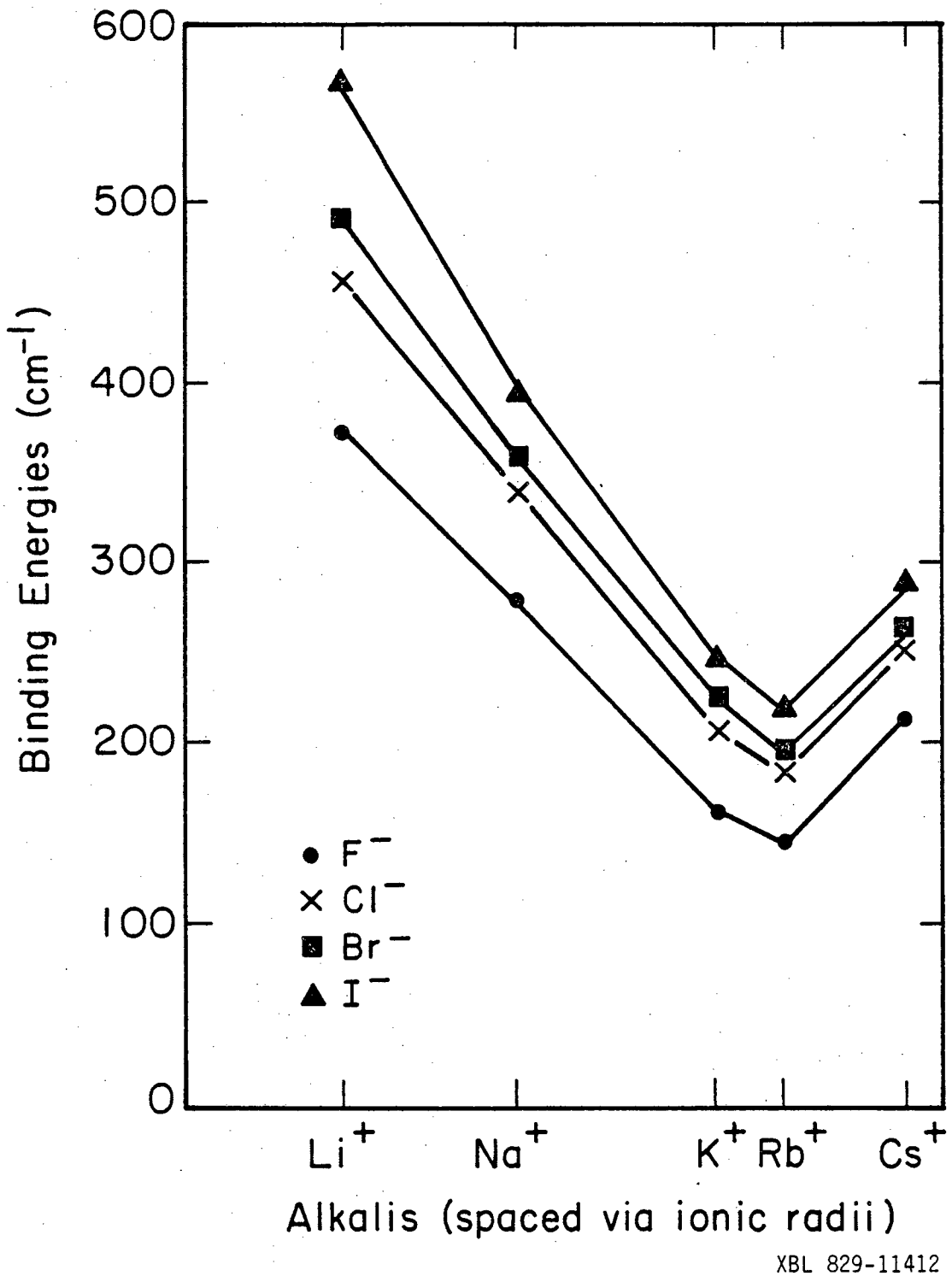

Figure 5.3. Binding energies of argon to the alkali halides.

Ar-MX binding energies, as defined in Equation (5.20). Because of the absolute error involved in the calculation of the dipole moments for the MX systems as typified in Table 5.4, we have presented in Table 5.5 the probably more meaningful differencesin the dipole moments ($\Delta\mu$) between ArMX and MX alone. The change in length of r_{MX} as one goes from MX to ArMX is generally on the order of +0.005 Å, and is therefore not a major contribution to these values of $\Delta\mu$. Table 5.6 gives the calculated values of the force constants, via Equations (5.21-5.23), and the rotational constants for the ArMX complexes. Figure 5.2 schematically illustrates the geometries of these molecules and again gives the binding energies.

As seen in Figure 2, in all of the ArMX minimum energy configurations, the Ar sits closer to the alkali cation. This is due largely to the smaller effective size of the alkali as governed by the repulsive term in the model potential. As the Ar atom can approach closer to the positive charge center than to the negative charge center, a larger dipole moment can be induced on the Ar atom, and correspondingly, the binding energy increases. Figure 5.3 illustrates this graphically, where D(Ar-MX) is plotted versus the alkali cations' ionic radii for each of the halide series. With increasing cation size, the binding energy generally decreases as the Ar is forced further from the positive charge center. This trend reverses for Cs^+, as its increased polarizability and dispersion energy contributions overcome the effect of its larger radius compared to Rb^+. As indicated in Table 5.1, Cs^+ is also "softer" than Rb^+. The increase in binding energy with increase in halide size is due primarily to their increasing polarizabilities. (This effect was also seen in variation 2 where the dispersion energy was surpressed,

Table 5.6

Calculated Force Constants for Ar-MX Motion (μdyne/Å) and Rotational Constant (GHz)

MX	f_R	f_θ	$f_{R\theta}$	B[b]
LiF	97.5	0.72	a	2.26
NaF	54.0	0.16	a	1.52
KF	22.8	0.67	3.88	13.40,1.41,1.28
RbF	16.4	0.42	0.54	6.98,1.31,1.11
CsF	27.6	1.75	5.07	5.82,1.22,1.01
LiCl	119.	0.78	a	1.34
NaCl	64.3	0.17	a	0.98
KCl	25.9	2.75	8.00	5.50,1.26,1.03
RbCl	20.4	1.21	3.07	2.95,1.24,0.87
CsCl	29.2	5.06	10.3	2.32,1.21,0.80
LiBr	127.	0.83	a	0.89
NaBr	68.0	0.17	a	0.65
KBr	35.5	5.22	11.3	5.02,0.80,0.69
RbBr	20.2	2.77	6.47	2.04,0.90,0.63
CsBr	32.0	3.58	8.60	1.44,0.93,0.56
LiI	148.	0.83	a	0.70
NaI	74.5	0.17	a	0.51
KI	25.7	8.18	14.1	4.16,0.65,0.57
RbI	20.7	4.98	9.05	1.81,0.67.0.49
CsI	32.1	6.54	12.5	1.35,0.63,0.43

[a] Vanishes by symmetry for linear complexes.

[b] Masses, in amu, for rotational constants are Li-7, Na-23, K-39, Rb-85, Cs-133, F-19, Cl-35, Br-80, I-127, Ar-40. Three rotational constants are given for nonlinear molecules.

discounting that term from influencing the characteristic change in D(Ar-MX)). Even more obvious from Figure 5.2 is the general geometry of the ArMX molecules -- linear for $M^+ = Li^+$ or Na^+, and triangular for the rest. If the potential energy surface for ArMX was dominated by the dispersion term Ar would generally bind in this latter configuration, as close to both of the MX nuclei as possible. Thus, one would suggest that the geometries of ArLiX and ArNaX are determined primarily from the electrostatic terms of our potential.

To better understand the potential fields, potential energy contour maps of ArLiCl and ArKCl are included as Figures 5.4 and 5.5. The method of preparation for these maps was described previously (under Eq. (5.20)). Again, the r_{MX} distance is held fixed at the ArMX potential minimum value, and the energies shown are the binding energies of Ar at those positions relative to an MX molecule at equilibrium. Thus, the 0. cm^{-1} contour is not at infinity. The darkened contour about LiCl and KCl represent the boundary determined by Eq. (5.19). The equilibrium position of Ar is indicated by a dot. The insert represents a spherical model of the ArMX complex, with the radii drawn to scale with the corresponding atomic and ionic radii. For ArLiCl (Fig. 5.4) there is a relatively localized potential well on the Li^+ side of LiCl, with a quickly rising repulsive wall as r_{Ar-Li^+} is reduced. There is virtually no potential trough on the Cl^- side. For ArKCl (Fig. 5.5), the well is shallower and less localized. The overall potential is significantly more isotropic.

To better see the relative effects of the electrostatic and dispersive potential energy terms, the results of the ArMX calculations using variation 2, with the dispersive term suppressed, is presented in Table 5.7, and the geometries summarized in Figure 5.6. The Li^+ and Na^+

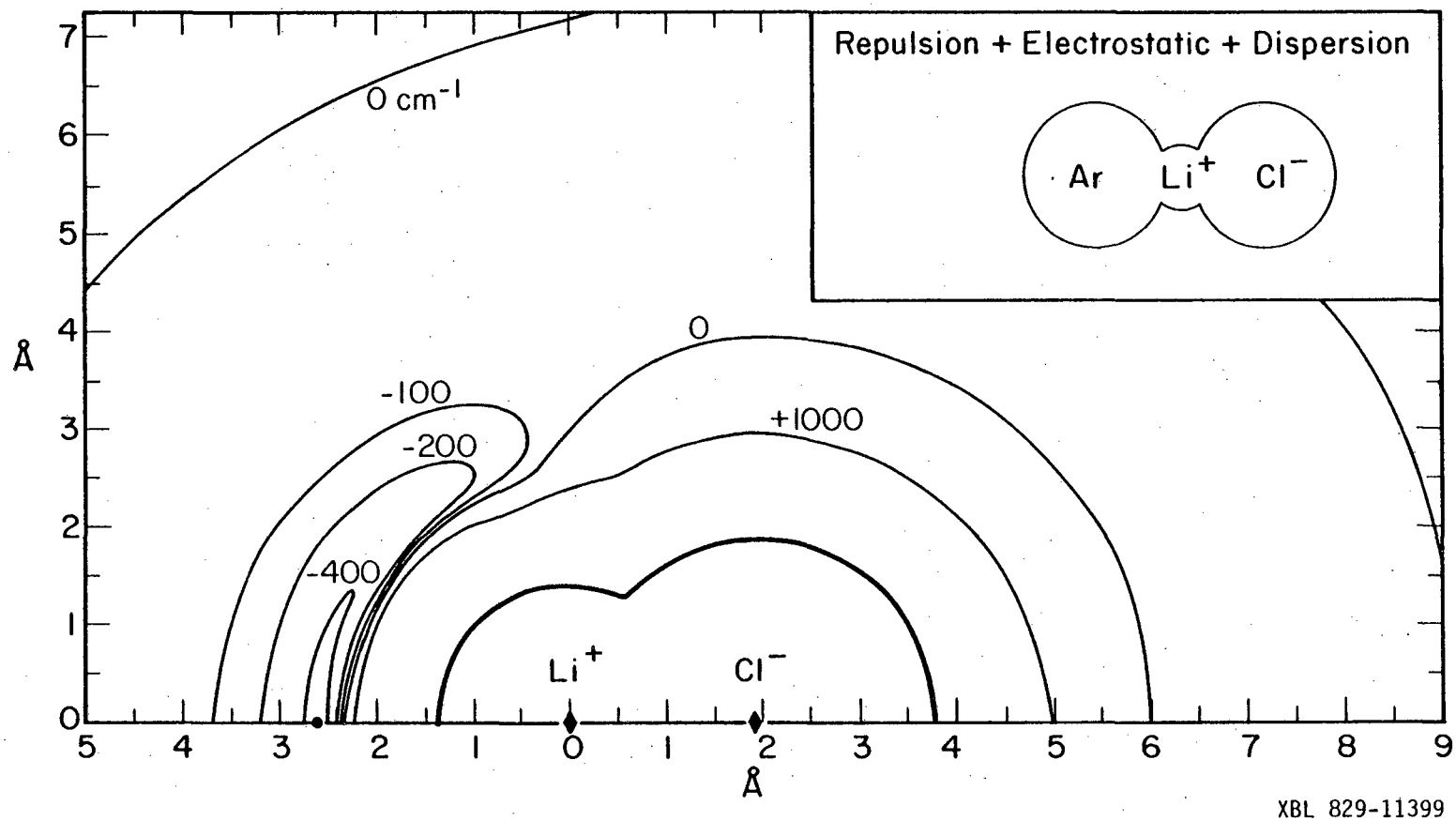

Figure 5.4. Energy contour map of argon in vicinity of LiCl (see text for description).

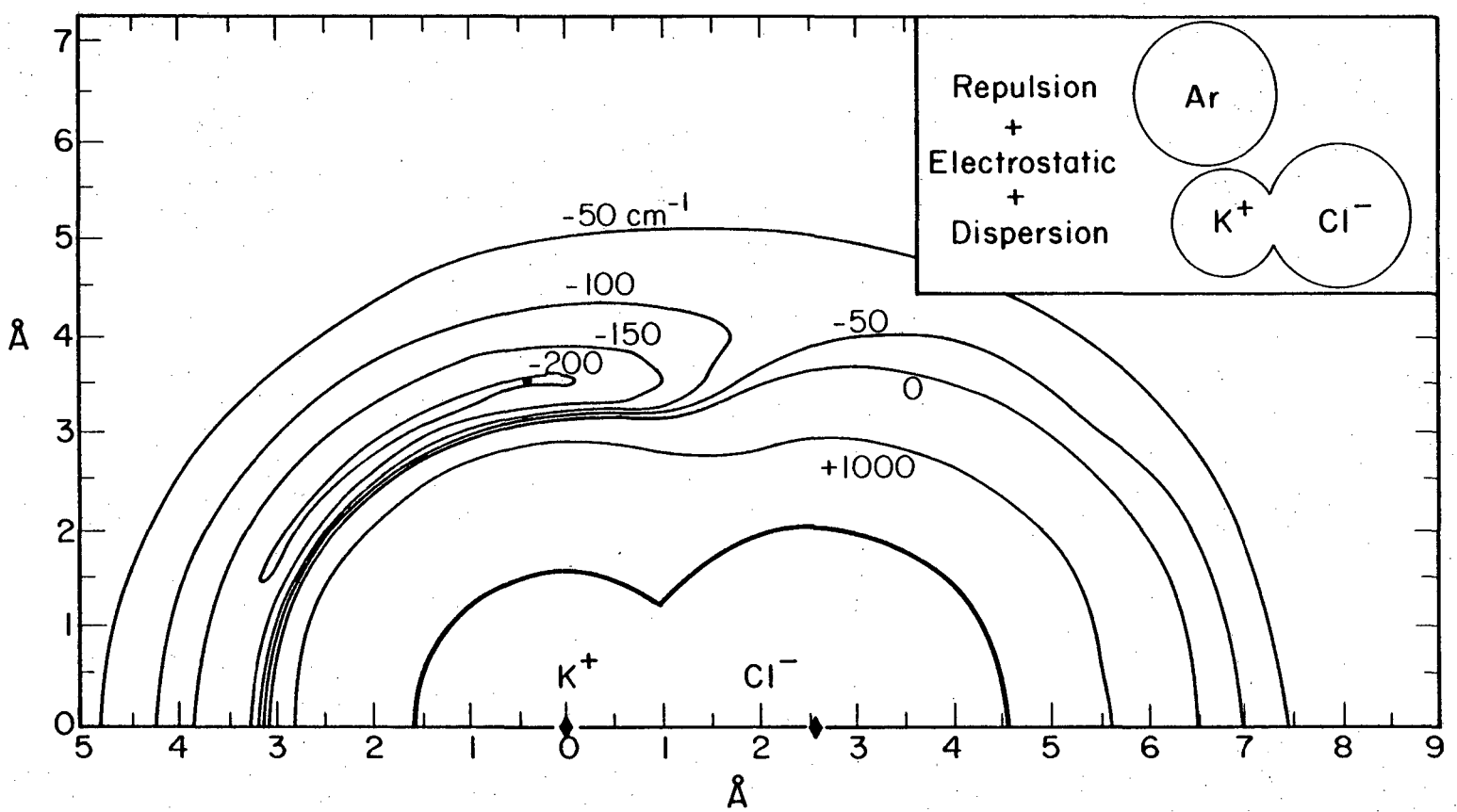

Figure 5.5. Energy contour map of argon in vicinity of KCl.

Table 5.7

ArMX Equilibrium Geometries and Ar-MX Binding Energies (cm^{-1}) via Variation 2[a]

	r_e(Ar-M)	r_e(Ar-X)	∢(Ar-M-X)	D(Ar-MX)
LiF	2.62	4.11	180	316
NaF	3.05	4.91	180	213
KF	6.42	4.27	0	26
RbF	6.52	4.26	0	27
CsF	6.64	4.23	0	28
LiCl	2.60	4.52	180	364
NaCl	3.02	5.32	180	251
KCl	3.61	6.23	180	102
RbCl	3.91	6.35	145	61
CsCl	3.94	5.52	107	56
LiBr	2.59	4.65	180	390
NaBr	3.00	5.44	180	267
KBr	3.59	6.36	180	112
RbBr	3.89	6.56	150	69
CsBr	3.93	5.73	110	62
LiI	2.57	4.86	180	461
NaI	2.99	5.66	180	295
KI	3.56	6.57	180	127
RbI	3.86	6.85	157	81
CsI	3.90	5.93	111	72

[a] No disposition term in potential. See text.

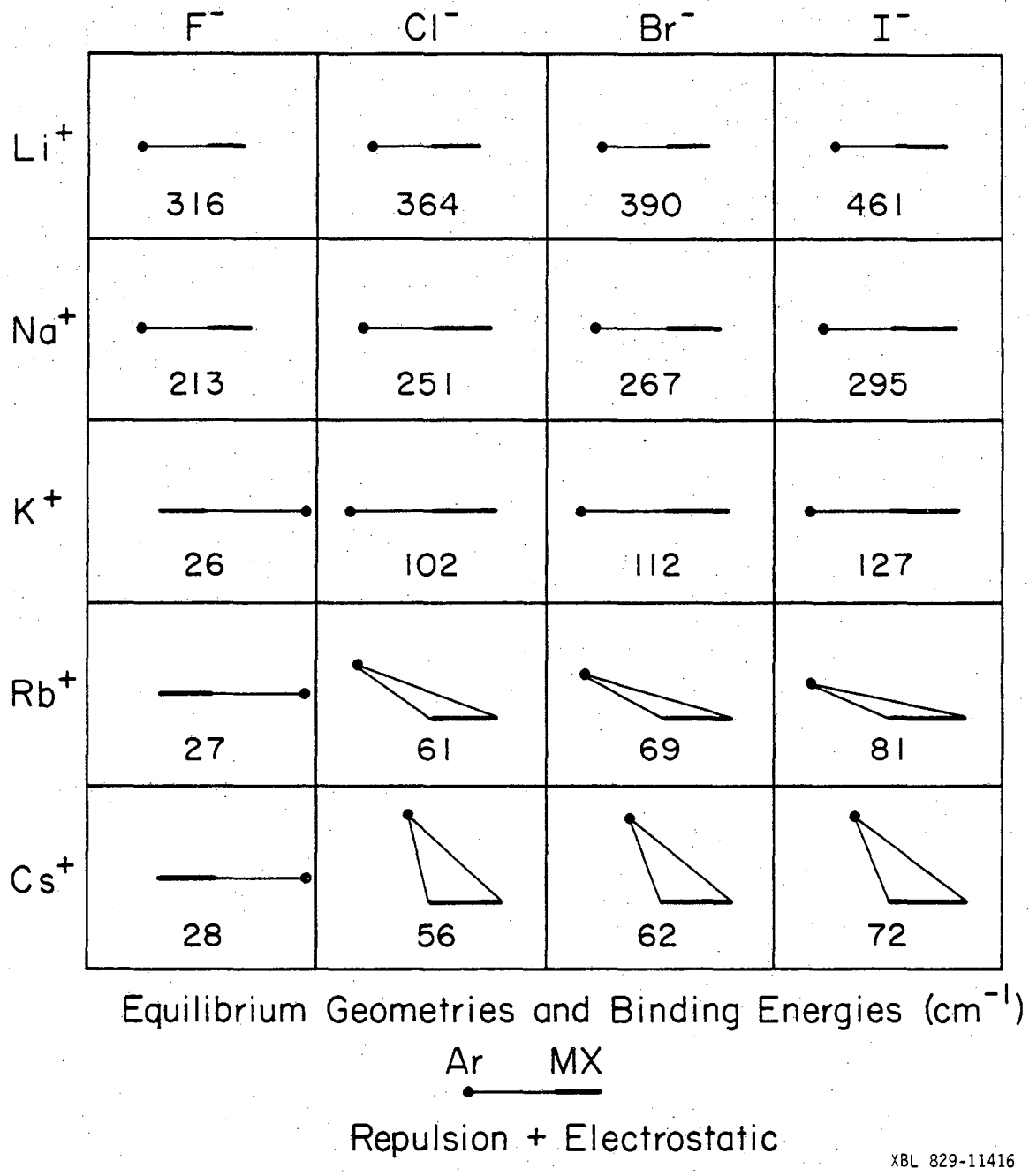

XBL 829-11416

Figure 5.6

complexes decrease only slightly in energy. The changes in the energies and geometries of the other molecules are more drastic. The K^+, Rb^+, and Cs^+ fluoride complexes are linear with the Ar on the F^- side, as the alkali cations are larger than the fluoride anion. The remaining complexes are now either linear or near linear, and all the K^+, Rb^+ and Cs^+ ArMX complexes are significantly reduced in binding energy. Contour maps of these molecules showed in general very shallow minima with elliptically shaped troughs about the MX. Figures 5.7 and 5.8 are contour maps of ArLiCl and ArKCl without the dispersive energy term, to parallel Figures 5.4 and 5.5. There is no potential minimum in the Cl^- vicinity for either complex. Little change has occurred in the region of the potential well near Li^+ for ArLiCl. The ArKCl potential, however, appears somewhat more anisotropic. We conclude that for the ArMX complexes in general, the Li^+ and Na^+ molecules at their equilibrium configuration are influenced primarily by electrostatic forces, while the remainder, particularly the Rb^+ and Cs^+ complexes, are influenced primarily by the more isotropic dispersive term.

The changes in dipole moment in Table 5.5 are largest in magnitude and positive for the linear ArMX complexes, and slightly negative for the remainder. The changes are predominantly due to the polarization of the Ar atom. The radial force constants, f_R, in Table 5.6 reflect the trend of the binding energies of Ar to the salt. The bending motion, reflected by the f_θ value, is generally lower in the linear complexes, as relatively no repulsion effect is experienced from the halide ions.

To give an indication of the sensitivity of the calculated equilibrium geometry to the choice of parameters for the potential energy, Table 5.8 summarizes calculations for ArLiCl, ArKCl and ArCsCl using

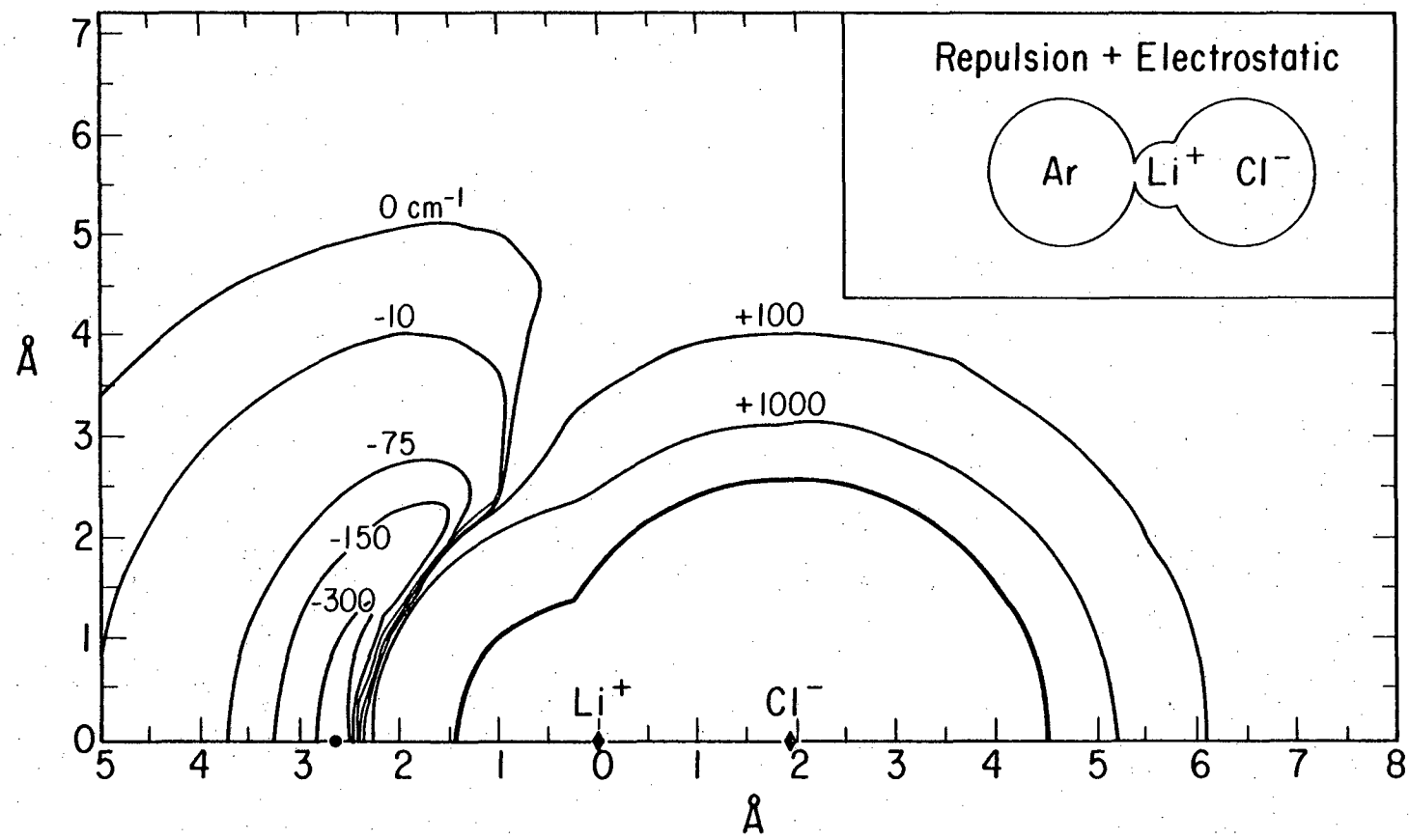

XBL 829-11397

Figure 5.7. Energy contour map of argon in vicinity of LiCl. Dispersion term suppressed.

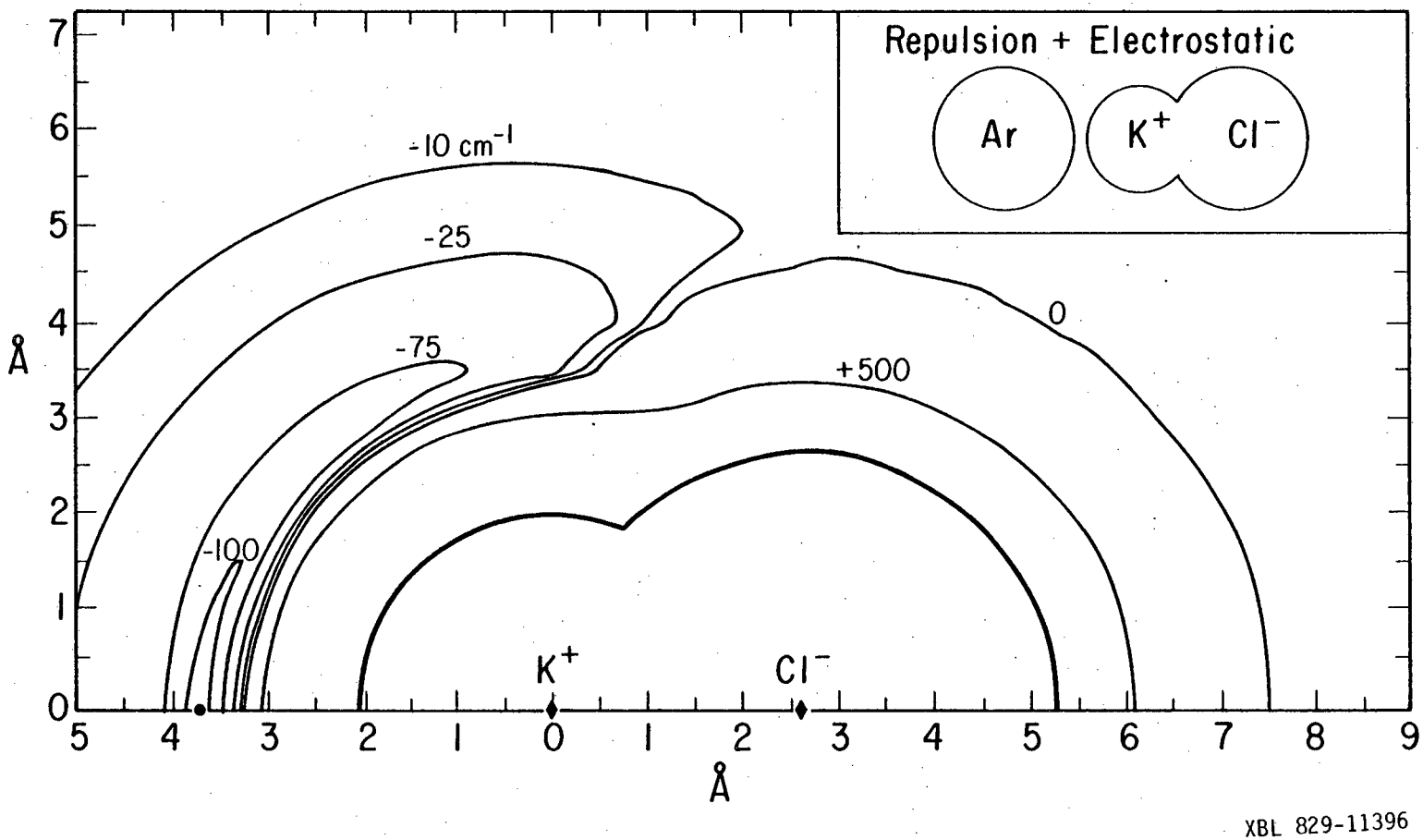

Figure 5.8. Energy contour map of argon in vicinity of KCl. Dispersion term suppressed.

Table 5.8

Equilibrium Geometries, Change in Dipole Moments (D) and Binding Energies (cm^{-1}) for Selected Ar-MX

	Variation	R(Ar-M)	R(Ar-X)	∢(Ar-MX)	Δμ(Ar-MX)	D(Ar-MX)
ArLiCl	0[a]	2.57	4.49	180°	0.75	453
	1	2.57	4.48	180°	0.75	472
	2	2.60	4.52	180°	0.74	364
	3	2.68	4.53	180°	0.56	187
	4[b]	2.54	4.51	180°	0.82	570
	5	2.57	4.49	180°	0.75	456
ArKCl	0	3.44	4.53	97°	-0.08	208
	1	3.42	4.23	89°	-0.15	246
	2	3.61	6.23	180°	+0.36	102
	3	3.59	6.16	180°	+0.36	87
	4	3.40	4.62	101°	-0.02	235
	5	3.44	4.53	97°	-0.08	209
ArCsCl	0	3.63	4.25	82°	-0.15	253
	1	3.61	4.08	78°	-0.18	296
	2	3.94	5.52	107°	+0.01	56
	3	4.39	7.28	180°	-0.18	30
	4	3.60	4.35	85°	-0.10	281
	5	3.63	4.25	82°	-0.15	252

[a] Variation 0-5 described in the text.

[b] Variation 4, no VDW, from Tessman, *et al.*,[27] $\alpha_{K^+} = 1.201$, $\alpha_{Cl^-} = 2.974$, $\alpha_{Li^+} = 0.029$, $\alpha_{Cs^+} = 3.137$.

the six different variations of models mentioned at the beginning of this section. Variations 0, 1, 4, and 5 change little the binding energy of ArMX or the change in dipole moment. Similarly, the geometries of these variants are quite alike. Variations 2 and 3 are both without dispersive terms, so that they differ from the rest in calculated results. Geometrically they differ somewhat from each other, indicating the strong effect of the choice of repulsive parameters. In short, we feel that errors introduced by the choice of polarizabilities and for the method of calculating the C_6 coefficients for the dispersive energy introduce relatively small calculation errors for the binding energy (~15%), structural angle and dipole moment differences (~10%), and less in the bond lengths (~5%). The possible errors due to the choice of repulsive parameters are less well characterized and are discussed more fully in the following section.

As a further test of our model, calculations were also performed for other classes of triatomic molecules. Table 5.9 indicates results for molecules of the form MAr_2^+ and XAr_2^-. FAr_2^- could not be calculated, due to the combined large polarizability of F^- and small repulsion for ArF^-. Figure 5.9 illustrates their predicted geometries. Our model predicted a bond length of 3.42 Å for free Ar_2, compared to the experimental value of 3.76 Å. Thus, for this class of molecules, only the geometry of $LiAr_2^+$ is predicted to be chiefly determined by electrostatic considerations. The larger dipoles induced in the Ar atoms near the small Li^+ increase their mutual repulsion. Table 5.10 gives calculated results for species of the type MX, X_2^- and M_2X^+, and some of these are also depicted in Figure 5.9. Of the negative ions, only CsF_2^- is predicted to be nonlinear, due to the combined largeness of the

Table 5.9

Calculated Properties of BAr_2 Ions ($B = M^+$ or X^-). Units are Å, Degrees, cm^{-1}, and μdyne/Å

	r_e (Ar-Ar)[a]	r_e (B-Ar)[b]	∢ (Ar-B-Ar)	D_e (Ar-BAr)	D_e ($B-Ar_2$)	f_R ($B-Ar_2$)	f_θ ($B-Ar_2$)	f_R (Ar-BAr)	f_θ (Ar-BAr)	f_R (Ar-BAr)
$LiAr_2^+$	4.76	2.38	180.0	2194	4438	--	--	497.	0.14	0
$NaAr_2^+$	3.71	2.78	83.7	1262	2468	225.	176.	142.	62.9	92.8
KAr_2^+	3.54	3.21	66.9	817	1503	128.	54.2	74.6	24.0	36.4
$RbAr_2^+$	3.51	3.40	62.2	694	1238	98.4	34.6	65.0	9.9	15.4
$CsAr_2^+$	3.50	3.46	60.8	748	1340	122.	41.1	64.6	25.8	33.6
$ClAr_2^-$	3.49	3.56	58.7	494	825	30.4	8.9	21.5	7.4	-4.9
$BrAr_2^-$	3.47	3.85	53.6	412	665	23.4	5.6	18.3	6.3	0.9
IAr_2^-	3.46	4.19	48.8	354	518	18.9	3.6	15.7	6.4	-7.5

[a] Ar-Ar separation in the triatomic. The calculated value for free Ar_2 was 3.42 Å, while the experimental value is 3.76 Å.

[b] B-Ar separation in the triatomic. The calculated values for free B-Ar were 0.01 to 0.02 Å less.

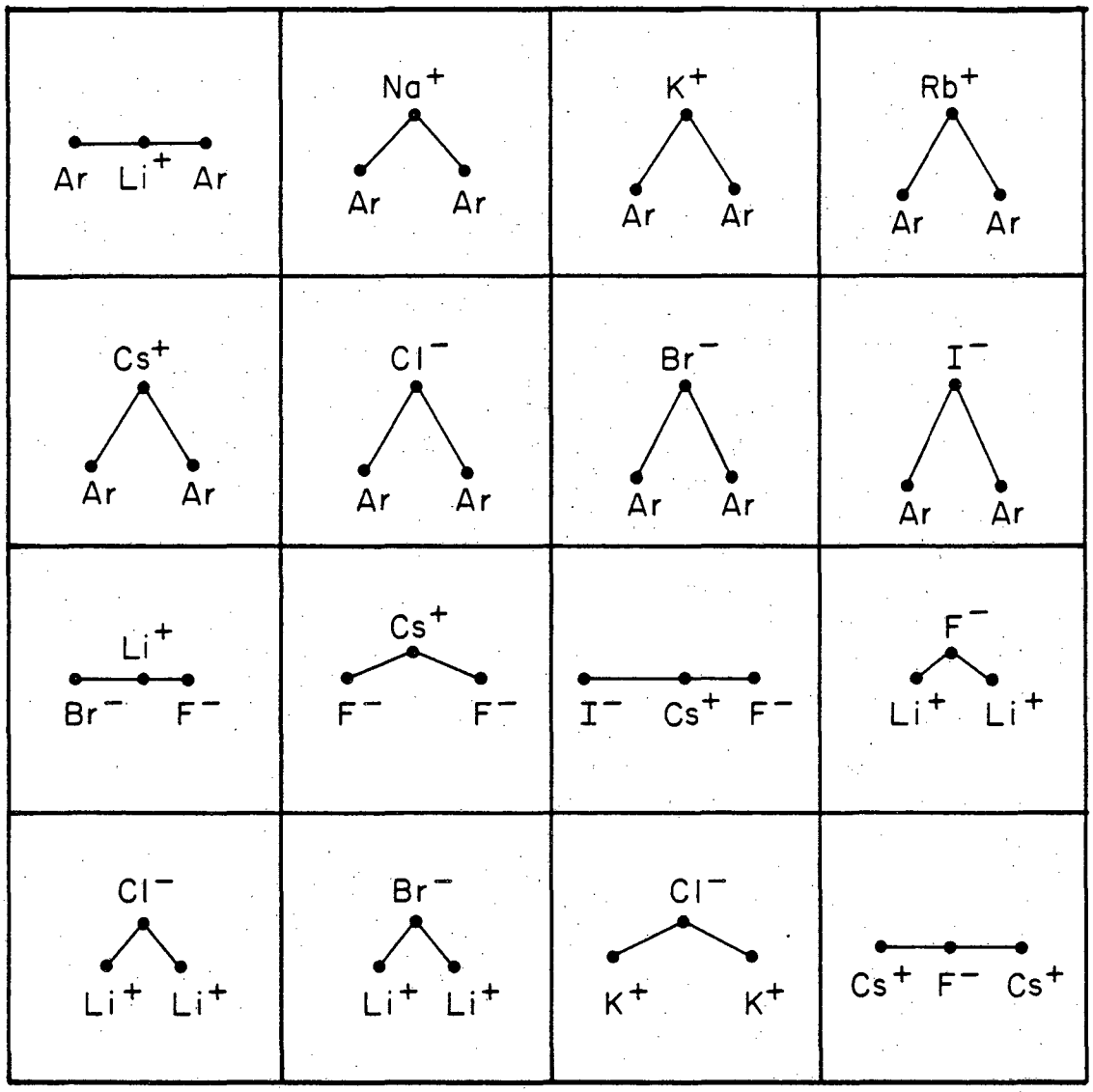

XBL 829-11413

Figure 5.9. Equilibrium geometries.

Table 5.10

Calculated Properties of ABC Ions (A,B,C - M^+ or X^-)
Units are Å, degrees and cm^{-1}

	r_e (A-B)	Δr_e (A-B)[a]	$\measuredangle$ (A-B-C)	D_e (AB-C)[b]
LiF_2^-	1.69	0.23	180°	-21,581
$LiCl_2^-$	2.15	0.24	180°	-16,963
LiI_2^-	2.53	0.25	180°	-14,873
$LiBrF^-$	2.40 (LiBr) 1.61 (LiF)	0.36 0.15	180°	-26,283 -12,845
KF_2^-	2.37	0.30	180°	-15,385
CsF_2^-	2.64	0.33	139.9°	-12,178
$CsCl_2^-$	3.12	0.33	180°	-11,595
$CsBr_2^-$	3.27	0.33	180°	-11,390
$CsIF^-$	3.70 (CsI) 2.53 (CsF)	0.41 0.22	180°	-17,991 - 7,289
RbF_2^-	2.51	0.37	180°	-13,328
Li_2F^+	1.67	0.21	109.1°	-16,477
Li_2Cl^+	1.96	0.05	78.2°	-17,750
Li_2Br^+	2.08	0.04	75.5°	-17,916
K_2Cl^+	2.84	0.29	125.7°	-11,484
Cs_2F^+	2.63	0.32	180°	-13,857

[a] Difference in bond length for (A-B) between ABC and AB. AB identity indicated where necessary.

[b] Difference in energy between ABC and AB.

alkali and relative smallness of the halides. The geometries of the M_2X^- calculated here are mostly bent with the angle again dependent on the relative sizes of the ions. Also indicated in this table are the calculated changes in the M^+-X^- bond lengths from the neutral salts.

D. Discussion

In this section, the errors incurred by our particular selection of parameters within the context of the electrostatic model will first be discussed. The question of the validity of any electrostatic model will then be addressed, followed by a brief comparison of our calculated results with other available data.

Though the values for polarizability we have used may be quite good for free ions, there is some question of their propriety in a model such as ours. As previously mentioned, Smith[33] indicated that by his distortion model, dipoles would be induced at the ion sites just through their repulsive overlap interaction. In our model, this would need to be rectified by a change in the effective polarizability as a function of ion or atom separation. In their perturbative treatment, Brumer and Karplus[10] derive a truncated Rittner potential energy expression, with their first correction to the basic Rittner model being bond distance dependent polarizabilities. This was derived from terms in their expansion that Murrell[11] referred to as exchange polarization energy and charge transfer energy. Brumer and Karplus indicate that the effective polarizability of positive ions should increase while that of the anions should decrease exponentially with decreasing bond distance. De Wijn[13] suggests the reduction of a free halide's polarizability by 2/3, in MX as of the six p electrons typically available for polarizing "excitation"

in X^-, only those four perpendicular to the MX axis will actually be free to "move toward the alkali". The lack of information on the change in polarizability of an ion in the presence of an atom like Ar precluded a similar treatment by us. As indicated by our results with variation 5, just modulating the polarizabilities of M^+ and X^- by the distance between them had little effect on the results for ArMX.

Our particular choice of repulsive parameters is probably the greatest contribution to calculation error. The values for ρ_{ii} and R_{ii} have been given in Table 5.1 and were adapted from data tabulated by Smith.[33] His estimated values for ρ_{Cl^-} and R_{Cl^-} were used to determine repulsive parameters for the alkali cations, which were in turn used to get averaged values of ρ_{ii} and R_{ii} for the remaining halides. Alkali parameters were then recalculated in a similar manner, and finally all of the halide parameters were reevaluated. The comparison of experimental ρ_{ij} and R_{ij} parameters with those calculated from values in Table 5.1, given in Table 5.2, showed good agreement, with the exception of K^+Ar.

Tabulated values for ρ_{ii}[37] found after doing our calculations differ mostly in their larger values for the alkali cations. As the ArMX complexes are predicted to have the Ar closest to the alkali, larger values of ρ_{m^+} would allow the rare gas atom slightly closer to the alkali nucleus. Thus, we predict that our binding potential wells may well be too shallow. The derived structural parameters, however, are not quite as sensitive to the repulsive parameters. On a side note, Lee and Kim[38] have recently compared the Smith combining rules with an arithmetic mean,geometric mean and a method of their own and found the Smith rules lacking in accuracy. However, they used electron gas

potentials as the potential energy form in testing these methods, whereas the Smith rules were derived for a two parameter potential like Equation (5.11), so that their criticism is poorly founded.

The electron gas model of Gordon and Kim[22] is particularly suited for binding between closed-shell systems as we have in ArMX. In essence, Hartree-Fock electron densities of the interacting individual atoms are left undistorted, but added up in the regions of overlap. The Coulomb interactions are then calculated, and added to density dependent functions for electron correlation, kinetic energy and exchange. Their calculations for MX are somewhat better than ours. Calculations for $(MX)_2$ systems[23] have given dissociation energies deviating from 6 to 13% from experimental values, not significantly better than other semi-empirical calculations based on a Rittner model. It would be of interest to follow the results of an electron gas calculation of ArMX systems in the future.

Significant criticism has been leveled against the basic soundness of electrostatic potential models.[2,3] It was suggested that the model violates the Pauli exclusion principle and lacks wavefunction antisymmetrization in its treatment of overlap, and that the virial theorem is violated with the lack of a direct appearance of an electron kinetic energy term in the nuclear potential energy surface. From the Born-Oppenheimer approximation and the Hellmann-Feynman theorem one can derive the general force equation

$$\frac{\partial U}{\partial r_{ij}} = \int \psi^*(\tau)\psi(\tau) \frac{\partial \hat{V}}{\partial r_{ij}} d\tau \qquad (5.24)$$

where U is the nucleus potential energy of a system; $\hat{V}$, the position

dependent potential energy operator; $\psi(\tau)$, the electronic wavefunction; and r_{ij}, a typical internuclear separation. The force acting on a nucleus, then, is dependent only on the electron density distribution and not directly on the electronic wavefunction. It is thus not unreasonable to view the electron distribution as a cloud of charges. As an aside, from (5.24) it appears significantly easier to determine the equilibrium geometry of a complex, where $\partial U/\partial r_{ij} = 0$, than to determine the actual value of the potential at that minimum. The actual use of a wavefunction is not incurred in our model. Klemperer's[3] criticism of the use of perturbation theory to derive interaction energies, as by Brumer and Karplus,[10] is well founded in that there is some electronic overlap at equilibrium which is not explicitly included in the perturbed Hamiltonian of Brumer and Karplus. However, only the form of their potential is used in the Rittner model. The values for the repulsion parameters are not calculated from their theory, but determined empirically. The data from scattering experiments automatically and correctly include the effects of electron overlap, exchange, kinetic energy and nuclear-nuclear repulsion. This in itself indicates that there really is no problem with a virial theorem violation at small internuclear distances. A small amount of electronic kinetic energy is also included in the polarization energy of the participating atoms in ArMX, but this contribution is minor compared to that in the Born repulsive term. The inclusion of the Pauli principle is somewhat implicit on the distortion model of Smith.

In our model, the relative size of the ions becomes the major criterion in determining if the electrostatic or dispersive term has the major influence on the ArMX equilibrium geometry. It is essentially a question of how closely the polarizable Ar atom can approach the ions'

nuclei, their center of charge. At first glance, such a model has very little to say correctly about such previously studied molecules as ArClF[39] and KrClF.[40] The equilibrium geometry of ArClF is indicated in Figure 5.4 of Ref. 39. It is found to be linear with the Ar on the electropositive chlorine side of ClF, 3.33 Å from the Cl nucleus, about 0.3 Å less than the sum of the van der Waals radii of Ar and Cl. As fluorine is typically viewed as the smaller of the two halogens, this result appears in opposition to our model. ArClF was found to have a dissociation energy D_e = 228 cm^{-1} and vibrational force constants f_R = 30.2 μdyne/Å and f_θ = 1.5 μdyne/Å. Placing point charges at the nuclei of ClF consistent with its dipole moment (0.888 D), our model would predict significantly lower values for D_e and f_R. Bond directionality, derived as the ratio of the bond stretching constant to the bond bending constant, is 20 for ArClF, while for linear ArMX complexes it is found to be from 135 and 152 for ArLiF and ArLiCl to 337 and 378 for ArNaF and ArNaCl. This indicates that the ArClF bending motion is relatively more restricted than for our complexes, again seemingly inconsistent with an electrostatic model. For these reasons and others it has been found better to describe van der Waals molecules such as ArClF with a Lewis acid-base model, with the Ar interacting here with the unoccupied σ* orbital on the chlorine.[39] The observed properties of ArClF could well be attributed to such a "chemical" bond.

The electrostatic model, however, may still have something to say about ArClF. Firstly, the figure of Ref. 39 may be misleading in denoting the relative "sizes" of the chlorine and fluorine atoms for the molecule ClF. With the electron density shifted toward the fluorine, it is not at all obvious that the chlorine atom is still larger. A more

subtle point is that if one associates a certain electron "cloud" to the chlorine atom in ClF, its center of charge would not fall on the chlorine nucleus, due to the distortion from the covalent bond. This, in turn, would shift the location of the effective center of charge to the chlorine side of ClF. If the effective nuclear charge is given by q^+ (for chlorine, this would be about 5 e, as only the five 3 p electrons are much delocalized), and if the effective electron charge by q^- (less than q^+ for chlorine), is shifted by a distance ε toward the other nucleus, then, to first order, the effective $q^+ - q^-$ charge center to a probe at a distance significantly greater than ε from the nucleus is located at a distance ε' from the nucleus toward the probe, where

$$\varepsilon' \sim \varepsilon \frac{q^+}{q^+ - q^-} . \tag{5.25}$$

Though this expression cannot be applied too literally, it still indicates that for ClF, the "charge center" on the chlorine side is further toward the end of the molecule than the chlorine nucleus. An electrostatic potential term would be determined by the location of this charge center, and so the predicted interaction of Ar with ClF would be correspondingly strengthened. The repulsive and dispersive energy terms would still be influenced primarily by the relative locations of the interacting nuclei (as, from Eq. (5.25), ε is typically much less than ε'). Thus, an equipotential contour near the equilibrium position of Ar would have a particularly smaller effective radius than a corresponding contour for a linear ArMX complex, and, as f_θ values are determined relative to the center of mass of the strongly bonded diatomic, ArClF would appear to have a significantly more directionalized van der Waals bond.

Such a qualitative model could be used to redescribe most van der Waals molecules presently described by the Lewis acid-base model. In general, it would also predict van der Waals bonding to an electropositive site of a covalent molecule, but would take more direct account of the rare gas' and closed-shelled species' polarizabilities. The use of such a model to predict quantitatively equilibrium properties of molecules such as ArClF, however, would be difficult without previous information on the charge distribution within the covalent molecule, as from *ab initio* calculations or as indicated by spectroscopic dipole and quadrupole coupling values. Repulsive parameters would also be difficult to find. The spectral values obtained for ArClF can be inversely used to give such information for ClF to predict geometries and energies for similar molecules, as KrClF. For ArMX system, the initial charge distribution about the MX nuclei is much less ambiguous. The ion induced polarization is a small perturbation to the binding effect of argon, and is in fact accounted for in the Rittner model.

From the Ar-LiF scattering experiments of Reed and Wharton,[4] a spherically averaged well depth of 206 ± 20 cm^{-1} is predicted at an argon-LiF separation of 3.8 Å. This was calculated by assuming that the width and location of their rainbow scattering peak could be modeled by a spherical averaging about the LiF potential surface. However, given the large anisotropy of this attractive potential and that rainbow scattering, in an unbalanced way, only probes those orientations of the Ar/LiF system where the argon experiences the attractive well, their higher complex binding energy relative to our prediction (with an angle averaged value of 102 cm^{-1} at 3.8 Å) is understood. The scattering work of Greene, et al.[6] suggest for the Ar/CsI system a well depth in the

range of 320 to 480 cm^{-1} with a bond length of 4 to 5 Å. In model calculations of Matzer and Fisk[41] to describe results in collision studies between vibrationally excited KBr and Ar,[7] their surface I gives good qualitative agreement to our contour surface for ArKBr, though they predict a somewhat greater binding energy of 450 cm^{-1} at a significantly smaller distance. These differences are attributed primarily to differences in our respective repulsive terms in the potential expressions. Inelastic scattering experiments for Ar with CsI, CsBr, RbI and KI by Tully, et al.[8] do not particularly probe the shallow potential wells about the alkali halides. That an impulsive kinetic model describes their observed ionic dissociation process does not oppose our results. Finally, it is of interest that the Ar-crystal calculations of House and Jaycock[42] predict that the Ar sits best over the Na^+ in NaCl crystal, but between the K^+ and Cl^- for KCl, consistent with our predictions.

Lin, Wharton and Grice[20] have done calculations similar to ours for M_2X^+ and MX_2^- systems. The equilibrium angles they calculate follow the same trend as ours, namely, that the larger the M^+ to X^- "size" ratio, the more linear the equilibrium molecule. Their generally more acute angles and larger binding energies (energies in their Table 5.1 should be in units of eV/mol) is due to their use of larger values of ρ_{ii} for the alkalis. The ab initio calculations of Rechsteiner et al.[43] on the other hand, predict linear equilibrium geometries for Li_2F^+, Na_2F^+, Li_2Cl^+, and Na_2Cl^+, with small bending coefficients. Their results indicate that the charge distribution of M_2X^+ complexes are not so obvious. Our calculations are consistent with those of Reck, et al.[21] for MX_2^- systems in that only CsF_2^- is found to be nonlinear. We have found no previous calculations for ArM_2^+ or ArX_2^- systems.

E. Conclusion

Using an electrostatic model, we have predicted the equilibrium geometries and potential fields for the general class of argon-alkali halide complexes. From this model it is found that the geometries of ArLiX and ArNaX are determined primarily from electrostatic considerations, while the remainder are shaped more strongly by the dispersive attractive interaction. The greatest error within the context of our model is probably from our choice of repulsive parameters. Objections to the validity of such a model have been addressed.

The ultimate test for our model would be by the actual determination of the geometric configurations of bound ArMX molecules from spectroscopic studies. Molecular beam electric resonance spectroscopy is a particularly well suited method for such measurements. Having an argon beam seeded with gaseous alkali halide monomers, determinations of geometry, change in dipole moment, vibrational constants, etc. can be made. The results of such work would better indicate whether or not van der Waals molecules need to be described by chemical forces more specifically than in the electrostatic model.

REFERENCES for CHAPTER V

1. B. L. Blaney and G. E. Ewing, Ann. Rev. Phys. Chem. 27, 553 (1976).
2. W. Klemperer, in Advances in Laser Chemistry, ed. by A. H. Zewail (Springer-Verlag, Berlin, 1978), 398.
3. W. Klemperer, J. Mol. Spec. 59, 161 (1980).
4. K. A. Reed and L. Wharton, J. Chem. Phys. 66, 3399 (1977).
5. H. J. Loesch and D. R. Herschback, J. Chem. Phys. 57, 2038 (1972).
6. E. F. Greene, R. B. Hall, and N. A. Sondergaard, J. Chem. Phys. 66, 3171 (1977).
7. F. F. Crim, M. S. Chou, and G. A. Fisk, Chem. Phys. 2, 283 (1973).
8. F. P. Tully, N. H. Cheung, H. Haberland, and Y. T. Lee, J. Chem. Phys. 73, 4460 (1980).
9. E. S. Rittner, J. Chem. Phys. 19, 1030 (1951).
10. P. Brumer and M. Karplus, J. Chem. Phys. 58, 3903 (1973).
11. J. N. Murrell, M. Randić, and D. R. Williams, Proc. Roy. Soc. (London) A284, 566 (1965); J. N. Murrell and G. Shaw, J. Chem. Phys. 46, 1768 (1967).
12. G. M. Rothberg, J. Chem. Phys. 34, 2069 (1961).
13. H. W. de Wijn, J. Chem. Phys. 44, 810 (1966).
14. C. Maltz, Chem. Phys. Lett. 3, 707 (1969).
15. C. T. O'Konski and W. I. Higuchi, J. Chem. Phys. 23, 1175 (1955).
16. T. A. Milne and D. Cubicciotti, J. Chem. Phys. 29, 846 (1958).
17. P. Brumer and M. Karplus, J. Chem. Phys. 64, 5165 (1976).
18. T. A. Milne and D. Cubicciotti, J. Chem. Phys. 29, 1625 (1958).
19. M. Guido and G. Gigli, J. Chem. Phys. 65, 1397 (1976).
20. S. M. Lin, J. G. Wharton, and R. Grice, Mol. Phys. 26, 317 (1973).
21. G. P. Reck, B. P. Mathor, and E. W. Rothe, J. Chem. Phys. 66, 3847 (1977).

22. R. G. Gordon and Y. S. Kim, J. Chem. Phys. 56, 3122 (1972); M. Waldman and R. G. Gordon, J. Chem. Phys. 71, 1325 (1979).

23. S. Trugman and R. G. Gordon, J. Chem. Phys. 64, 4625 (1976).

24. C. T. O'Konski, J. Chem. Phys. 23, 1174 (1955).

25. J. H. Goble, D. C. Hartman, and J. S. Winn, J. Chem. Phys. 67, (1977).

26. L. Pauling, Proc. Roy. Soc. (London) 114A, 181 (1927).

27. J. R. Tessman, A. H. Kahn, and W. Shockley, Phys. Rev. 92, 890 (1953).

28. R. A. Buckingham, Proc. Roy. Soc. (London) A160, 94 (1937).

29. I. Eliezer and P. Krindel, J. Chem. Phys. 57, 1884 (1972).

30. R. R. Teachout and R. T. Pack, Atomic Data, 3, 195 (1971).

31. M. Born and J. E. Mayer, Z. Physik, 75, 1 (1932).

32. T. L. Gilbert, J. Chem. Phys. 49, 2640 (1968).

33. F. T. Smith, in VII ICPEAC, Physics of Electronic and Atomic Collisions, ed. by T. R. Groves and F. J. de Heer, 1 (North-Holland, Amsterdam, 1972); F. T. Smith, Phys. Rev. A 5, 1708 (1972).

34. J. C. Slater and J. G. Kirkwood, Phys. Rev. 37, 682 (1931).

35. R. A. Buckingham, Proc. Roy. Soc. (London) A160, 113 (1937).

36. G. Starkschall and R. G. Gordon, J. Chem. Phys. 54, 663 (1971).

37. J. Shanker and D. P. Agrawal, J. Phys. Chem. Solids 41, 1003 (1980).

38. H. C. Lee and Y. S. Kim, J. Chem. Phys. 74, 6144 (1981).

39. S. J. Harris, S. E. Novick, and W. Klemperer, J. Chem. Phys. 61, 193 (1974).

40. S. E. Novick, S. J. Harris, K. C. Janda, and W. Klemperer, Can. J. Phys. 53, 2007 (1975).

41. M. K. Matzen and G. A. Fisk, J. Chem. Phys. 66, 1514 (1977).

42. W. A. House and M. J. Jaycock, J. Chem. Soc. Faraday Trans. I. 70, 1710 (1975).

43. C. E. Rechsteiner, R. P. Buck, and L. Pedersen, J. Chem. Phys. 65, 1659 (1976).

44. Alkali Halide Vapors - Structure, Spectra, and Reaction Dynamics, ed. by P. Davidovits and D. L. McFadden (Academic Press, N.Y., 1979) [A good general reference found after this writing. Particularly relevant to this work are Chapter 1 by M. Blander discussing thermodynamic properties of MX vapors, and Chapter 15 by K. D. Jordan on theoretical methods.]

APPENDIX

The Computer Program CLARNA

The listing to CLARNA has been printed on the microfiche appended to this thesis (see the Appendix to Chapter III). The plotting routines are currently outdated at LBL. Following the listing is a typical data file to be inputted with the program.

This report was done with support from the Department of Energy. Any conclusions or opinions expressed in this report represent solely those of the author(s) and not necessarily those of The Regents of the University of California, the Lawrence Berkeley Laboratory or the Department of Energy.

Reference to a company or product name does not imply approval or recommendation of the product by the University of California or the U.S. Department of Energy to the exclusion of others that may be suitable.

TECHNICAL INFORMATION DEPARTMENT
LAWRENCE BERKELEY LABORATORY
UNIVERSITY OF CALIFORNIA
BERKELEY, CALIFORNIA 94720